

Syracuse University

SURFACE

Dissertations - ALL

SURFACE

August 2018

Hybrid Electric Distributed Propulsion for Vertical Takeoff and Landing Aircraft

Andrew Voss Welles
Syracuse University

Follow this and additional works at: <https://surface.syr.edu/etd>



Part of the [Engineering Commons](#)

Recommended Citation

Welles, Andrew Voss, "Hybrid Electric Distributed Propulsion for Vertical Takeoff and Landing Aircraft" (2018). *Dissertations - ALL*. 943.
<https://surface.syr.edu/etd/943>

This Dissertation is brought to you for free and open access by the SURFACE at SURFACE. It has been accepted for inclusion in Dissertations - ALL by an authorized administrator of SURFACE. For more information, please contact surface@syr.edu.

Abstract

This research effort explores the interactions between aerodynamics and hybrid-electric power system (HEPS) design and control for vertical takeoff and landing (VTOL) aircraft applications. Specifically, this research focuses on embedded distributed electric propulsion systems, for which the aerodynamic forces and moments are inextricably linked to power input.

This effort begins by characterizing the performance of two similar embedded propulsion systems using computational fluid dynamics (CFD). From this initial analysis, a wind tunnel model is constructed and the systems are tested across the operating conditions required to characterize the performance of a VTOL aircraft, where $0 \text{ deg} \leq \alpha \leq 90 \text{ deg}$. One of these configurations is selected for evaluating the interaction with the hybrid-power system.

An experimental HEPS is constructed based on a small two-stroke internal combustion engine as well, with a rated continuous power output of $2kW$. This experiment is used to develop a validated dynamical HEPS model in MATLAB and Simulink, where the control systems are refined and the performance of the system is extended to accommodate the VTOL power demand during transitional flight. A robust control design is developed using a second order sliding mode controller (2-SMC), implemented using the super-twisting

algorithm and integrated with classical linear control schemes in an interleaved-cascade architecture. The resulting system has a variable voltage output and a robust response to rapid changes in power demand. Additionally, the HEPS is also demonstrated to fully utilize the mechanical power output capability of the two-stroke engine.

Ultimately, the HEPS is demonstrated, via the dynamical model, to be capable of supplying power for an embedded propulsion VTOL aircraft. This performance is further extended with the addition of an actively controlled slack bus, utilizing battery energy storage and a buck-converter integrated with the HEPS control system. In this configuration, the peak power demands of the system can exceed the maximum sustained power threshold (MSPT) of the HEPS.

Hybrid Electric Distributed Propulsion for Vertical Takeoff and Landing Aircraft

by

Andrew Voss Welles

Bachelor of Science, Syracuse University, 2008

Master of Science, Syracuse University, 2009

Dissertation

Submitted in partial fulfillment of the requirements for the degree of

Doctor of Philosophy in Mechanical and Aerospace Engineering

Syracuse University

August 2018

Copyright ©Andrew Voss Welles, 2018

All Rights Reserved

To my wife Jaclyn.

Whose love, support, and patience made this possible.

To my son Leo.

Who reminded me why I needed to keep going.

To Mom and Dad, Uncle Greg, Aunt Maureen, and Tom and Kathleen.

Who supported Jaclyn, Leo, and I every step of the way.

To Prof. Dang.

Whose influence has shaped my intellectual development for the past 14 years.

To Prof. Bujanovic.

For introducing me to the world of power systems.

Contents

- 0.1 Nomenclature xl
- 0.2 List of Abbreviations xliv

- 1 Introduction, Motivation, and Background 1**

 - 1.1 Introduction 1
 - 1.2 Current Aircraft Types 2
 - 1.3 VTOL Aircraft Configurations 3
 - 1.3.1 Helicopters, Multirotors, and Tilt Rotors 4
 - 1.3.2 Separate Lift and Thrust (SLT) 5
 - 1.3.3 Distributed Lift and Thrust (DLT) 7
 - 1.4 DLT VTOL Configurations 8
 - 1.5 Power Sources for Distributed Propulsion 9
 - 1.5.1 Benefits and Shortcomings of Battery Power for VTOL 10
 - 1.5.2 Benefits and Shortcomings of Hybrid-Electric Power Systems (HEPS) 11
 - 1.6 Historical Perspective on VTOL 11
 - 1.7 Literature Review 13
 - 1.7.1 Electric Aircraft Propulsion and VTOL Transition Control 13

1.7.2	Hybrid-Electric Power System (HEPS) Technology	17
1.7.3	Electrical Machines and Power Generation	19
1.7.4	Additional Discussion	21
1.8	Guiding Research Question and Original Contributions	23
1.8.1	Contributions to Aerodynamics and Propulsion	24
1.8.2	Contributions to Power Systems and Controls Engineering	24
1.9	Dissertation Road-map	25
2	ADP Experiment Results	29
2.1	Introduction	29
2.2	Experiment Design and Construction Summary	30
2.3	Data Acquisition and Analysis Summary	32
2.4	Data Summary	33
2.5	Aerodynamic Cruise Regime	39
2.5.1	c_v - the vertical net force coefficient	39
2.5.2	c_u - the horizontal net force coefficient	40
2.5.3	$c_{m_{c/4}}$ - the moment coefficient	40
2.5.4	Power Input and Jet Power	43
2.5.5	CFD Results in the ACR	43
2.6	Powered Lift Regime	50
2.6.1	c_v behavior - the vertical force net coefficient	51
2.6.2	c_u behavior - the horizontal force net coefficient	51
2.6.3	$c_{m_{c/4}}$ - the moment coefficient	52

2.6.4	Power Input and Jet Power	52
2.6.5	CFD Results in the PLR	52
2.7	Hover Breakdown Regime	64
2.7.1	c_v behavior - vertical net force coefficient	65
2.7.2	c_u behavior - horizontal net force coefficient	66
2.7.3	$c_{m_{c/4}}$ behavior - net moment coefficient	67
2.7.4	Power Input and Jet Power	67
2.7.5	CFD Results in the HBR	67
2.8	Summary Data for ACR and PLR	71
2.8.1	$c_v(\alpha c_p^*)$ behavior	71
2.8.2	$c_u(\alpha c_p^*)$ behavior	72
2.8.3	$c_u(c_v c_p^*)$ behavior	73
2.8.4	$c_{m_{c/4}}(\alpha c_p^*)$ behavior	74
2.8.5	$\underline{P}(\alpha c_p^*)$ behavior	76
2.9	Conclusions	77
3	CDP Experimental Results	78
3.1	Introduction	78
3.2	Data Summary	79
3.2.1	Mode 1 Description	81
3.2.2	Mode 2 Description	81
3.3	Dominant Mode 1 - CDP Results and Behavior Near $\alpha = 0$ deg	82
3.3.1	c_v Behavior near $\alpha = 0$ deg	82

3.3.2	c_v Behavior near $\alpha = 0$ deg	85
3.3.3	$c_{m_{c/4}}$ Behavior near $\alpha = 0$ deg	87
3.3.4	Jet Power Behavior near $\alpha = 0$ deg	88
3.4	Transitional Modes - CDP Results and Behavior Near $\alpha = 9$ deg	88
3.5	Examining a Particular Condition: $\alpha = 9$ deg and $\theta = 40$ deg	93
3.6	Conclusions	96
4	Hybrid Electric Power System (HEPS) Experiment Results	99
4.1	Introduction	99
4.2	Test Profiles	100
4.3	Step Response Tests	101
4.4	Ramp Response Tests	103
4.5	Results Summary and Critical Operating Regimes	108
4.5.1	Control Summary	108
4.5.2	Data Reduction	109
4.5.3	Measurement Noise - Servo Signals and RPM	110
4.6	Results - Loading Regime	115
4.6.1	Step Response Results	116
4.6.2	Ramp Response Results - Loading Regime	119
4.7	Results - Unloading Regime	123
4.7.1	Step Response - Unloading	123
4.7.2	Ramp Response - Unloading	126
4.8	Effect of The Slack Bus	131

4.8.1	On the 40V loading response	131
4.8.2	Effect of Voltage Setpoint on Slack Bus Support	131
4.9	Conclusions	136
5	HEPS Dynamical Model Development	138
5.1	Introduction	138
5.2	System Representation	139
5.2.1	Plant	139
5.2.2	Controller	154
5.2.3	Throttle Response Model	160
5.3	Model Tuning and Comparison With Experimental Data	172
5.3.1	Single-Step Response Characteristics	173
5.3.2	Multi-Step Response	176
5.3.3	Fast Ramp Response	181
5.4	Conclusions	186
6	Combined ADP VTOL and HEPS Simulation	188
6.1	Introduction	188
6.2	Part One - Developing the Aircraft Models	189
6.2.1	Developing 3-D Wing Estimates for C_L , C_D and C_M	189
6.3	Aircraft Design Parameters	197
6.3.1	Wing Loading, W_L	197
6.3.2	Power Loading, P_L	198

6.4	Evaluating the Power Demands for Straight, Level, Unaccelerated Flight, (SLUF)	206
6.5	Developing Transition Profiles	213
6.5.1	Hypothetical Aircraft Configuration and Assumptions	213
6.5.2	Hover Performance and System Efficiency	214
6.5.3	Inbound Transition	215
6.5.4	Outbound Transition Profile	220
6.6	Aborted Landing Profile	223
6.7	Part Two - Aircraft Control Objectives	225
6.8	Identifying Non-linear Plant Elements	225
6.9	Sliding Mode Controller Design	228
6.9.1	Generator Voltage as the q_1 State Observer	230
6.9.2	2nd Order Sliding Mode Control (2-SMC)	231
6.9.3	Implementation in the HEPS Model	233
6.10	Power Output Control	238
6.11	Voltage Setpoint Modulation	242
6.12	HEPS Extension Using a Slack Bus	248
6.13	Comments on Practical Implementation and Future Improvements	252
6.13.1	Aircraft state estimation for computing power demand.	252
6.13.2	Slack bus DC-DC converter type	253
6.14	Part Three - Aircraft/HEPS Transition Response Behavior Analysis	255
6.15	Defining the Power Loading Conditions	256
6.16	Loading Case 1 Results, $b_1 = 1.35m$	261

6.16.1	Results Discussion, $b_1 = 1.35m$	261
6.16.2	Results Figures, $b_1 = 1.35m$	264
6.17	Loading Case 2 Results, $b_2 = 1.97m$	266
6.17.1	Results Discussion, $b_2 = 1.97m$	266
6.17.2	Results Figures, $b_2 = 1.97m$	268
6.18	Loading Case 3 Results, $b_3 = 2.70m$	270
6.18.1	Results Discussion, $b_3 = 2.70m$	270
6.18.2	Results Figures, $b_3 = 2.70m$	272
6.19	Conclusions	273
6.19.1	Part 1	273
6.19.2	Part 2	274
6.19.3	Part 3	274
7	Conclusions and Next Steps	275
7.1	Concluding Remarks	275
7.2	Next Steps and Future Work	278
A	Wind Tunnel Data Acquisition	281
A.1	Pressure Data Acquisition	281
A.1.1	Introduction	281
A.1.2	Imaging Considerations	283
A.1.3	Image Processing	284
A.1.4	Extracting the Fluid-Column Height Data	286
A.1.5	Processing the Fluid-Column Height Data	292

A.1.6	Measurement Uncertainty Analysis	297
A.2	Power System and Control Data Acquisition	304
A.2.1	Introduction	304
A.2.2	Data Logger Design and Integration	305
A.2.3	Power Data Cleanup	306
A.2.4	Voltage and Current Measurement Uncertainty Analysis	309
A.3	Conclusions	313
B	Wind Tunnel Data Methods of Analysis	315
B.1	Introduction	315
B.2	System Geometry and Coordinate System Transformations	316
B.3	Force and Moment Coefficients	319
B.3.1	Lift	320
B.3.2	Drag	325
B.3.3	Moment	327
B.4	Force Calculations	328
B.4.1	Pressure Force and Moment Contributions	329
B.4.2	Fan Contributions	332
B.4.3	Estimating Critical Variables	341
B.5	Wind Tunnel Corrections	356
B.5.1	3-D Blockage Correction	356
B.5.2	Confined Flow Thrust Correction	357
B.5.3	Circulation-Induced Velocity Correction	360

B.6	Calculation Summary	361
B.7	Conclusions	363
C	HEPS Experiment Development and Construction	365
C.1	Introduction	365
C.2	System Configuration	366
C.3	Power System Design and Construction	369
C.3.1	Thermal and Exhaust Management Strategy	369
C.3.2	Engine	371
C.3.3	Generator	371
C.3.4	Power Electronics	374
C.3.5	Load Design	376
C.3.6	Slack Bus	381
C.4	Data Acquisition System	383
C.4.1	Architecture	383
C.4.2	Uncertainty Analysis	385
C.5	Control System	388
C.5.1	Architecture	388
C.5.2	Preliminary Linear Controls and Implementation	390
C.6	Conclusions	392

List of Figures

1.1	Light, fixed wing aircraft example, Vans RV-10 [3]	2
1.2	Helicopter example, Robinson R22 [49]	3
1.3	Multicopter drone example, 800mm DYS Quadcopter [20]	5
1.4	Tilt rotor example, V-22 Osprey [4]	5
1.5	Kittyhawk SLT example [33]	6
1.6	Lilium Jet DLT example [37]	7
1.7	Aurora Lightning Strike DLT example, ADP configuration [48]	8
1.8	Lilium Jet DLT example, CDP configuration [37]	9
1.9	Direct Transmission System Topology	10
1.10	Direct Transmission System Topology [52]	12
1.11	Hybrid aircraft propulsion topology proposed by Freidrich and Robert- son, [27]	18
1.12	Typical automotive hybrid configurations presented by Slivas, Hof- man, et. al. [51]	19
1.13	Research approach flowchart	26
2.1	Completed ADP/CDP wind tunnel experimental apparatus.	30

2.2	Completed ADP/CDP wind tunnel facility design.	31
2.3	ADP system pressure port numerical representation	33
2.4	The ADP system consists of axial fans embedded into bi-wing configuration whereby the upper and lower wings comprise the duct boundaries for each fan.	37
2.5	The control volume is defined as having the inlet boundary parallel to the outlet boundary, and perpendicular to the fan axis of rotation. The lateral boundaries are drawn along the inner surfaces of upper and lower fan duct.	38
2.6	Summary of the ADP force coefficients, including aerodynamic and fan-derived contributions vs. c_p^* , for cases from $\alpha = 0$ deg to $\alpha = 18$ deg.	41
2.7	Summary of the ADP electrical input power and jet power vs. c_p^* , including aerodynamic and fan-derived contributions for cases from $\alpha = 0$ deg to $\alpha = 18$ deg.	42
2.8	Contours of velocity magnitude for ADP where $\alpha = 0$ deg and $c_p^* \approx 3.52$.	48
2.9	Contours of velocity magnitude for ADP where $\alpha = 9$ deg and $c_p^* \approx 3.58$.	49
2.10	Contours of velocity magnitude for ADP where $\alpha = 0$ deg and $c_p^* \approx 3.55$.	50
2.11	Summary of the ADP force coefficients, including aerodynamic and fan-derived contributions vs. c_p^* , for cases from $\alpha = 27$ deg to $\alpha = 54$ deg.	53
2.12	Summary of the ADP electrical input power and jet power vs. c_p^* , including aerodynamic and fan-derived contributions for cases from $\alpha = 27$ deg to $\alpha = 54$ deg.	54

2.13	Contours of velocity magnitude for ADP where $\alpha = 27$ deg and $c_p^* \approx$ 3.54.	58
2.14	Contours of velocity magnitude for ADP where $\alpha = 36$ deg and $c_p^* \approx$ 3.83.	59
2.15	Contours of velocity magnitude for ADP where $\alpha = 45$ deg and $c_p^* \approx$ 4.08.	60
2.16	Time-series plot of $c_{u_{pres}}$, the integrated static pressure contribution to horizontal net force, for ADP where $\alpha = 45$ deg and $c_p^* \approx 4.08$	61
2.17	Time-series plot of U_{fan} , the fan actuator contribution to horizontal net force, for ADP where $\alpha = 45$ deg and $c_p^* \approx 4.08$	61
2.18	Contours of velocity magnitude for ADP where $\alpha = 54$ deg and $c_p^* \approx$ 5.08.	63
2.19	Time-series plot of U_{fan} , the fan actuator contribution to horizontal net force, for ADP where $\alpha = 54$ deg and $c_p^* \approx 5.08$	63
2.20	Summary of the ADP force coefficients, including aerodynamic and fan-derived contributions vs. c_p^* , for cases from $\alpha = 63$ deg to $\alpha = 90$ deg.	64
2.21	Summary of the ADP electrical input power and jet power vs. c_p^* , including aerodynamic and fan-derived contributions for cases from $\alpha = 63$ deg to $\alpha = 90$ deg.	65
2.22	Contours of velocity magnitude for ADP where $\alpha = 72$ deg and $c_p^* \approx 2.4$.	68
2.23	Contours of velocity magnitude for ADP where $\alpha = 72$ deg and $c_p^* \approx 2.4$.	69
2.24	Contours of velocity magnitude for ADP where $\alpha = 90$ deg and $c_p^* \approx$ 8.90.	70

2.25	Summary of the ADP vertical force coefficient data as a function of α for various values of $c_p^* = const$	71
2.26	Summary of the ADP horizontal force coefficient data as a function of α for various values of $c_p^* = const$. Negative values denote a net thrust.	73
2.27	Summary of the ADP horizontal force coefficient c_u data as a function of c_v , the vertical force coefficient, for various values of $c_p^* = const$. Negative values of c_u denote a net thrust.	74
2.28	Summary of the ADP pitching moment coefficient data as a function of α for various values of $c_p^* = const$. Negative values denote a net nose down pitching moment.	75
2.29	Summary of the ADP jet power data as a function of α for various values of $c_p^* = const$	76
3.1	CDP Experimental Conditions	79
3.2	CDP Experimental Conditions	80
3.3	Bi-modal response to power input for a given α	80
3.4	CDP Experimental Data Summary - Aerodynamic Coefficients	84
3.5	CDP Experimental Data Summary - Power Requirements	85
3.6	CDP Experimental Data Summary - Aerodynamic Coefficients	86
3.7	CDP Experimental Data Summary - Power Requirements	87
3.8	CDP Experimental Data Summary - Aerodynamic Coefficients	89
3.9	CDP Experimental Data Summary - Power Requirements	90

3.10	CDP Experimental Data Summary - Aerodynamic Coefficients . . .	91
3.11	CDP Experimental Data Summary - Power Requirements	92
3.12	Specific example condition where the transition between Mode 1 and Mode 2 is well defined, and the bi-modal response is easily observed for a constant input power.	94
3.13	Example points showing where each mode can occur at the same power setting.	95
3.14	Pressure coefficient distribution about the forward wing for Mode 1 and Mode 2 observed at a constant input power setting where c_p^* is near 0. Where Mode 1 is present, $c_p^* = -0.045$ and where Mode 2 is present $c_p^* = 0.258$	95
3.15	Pressure coefficient distribution about the upper and lower flap sur- faces for Mode 1 and Mode 2 observed at a constant input power setting where c_p^* is near 0. Where Mode 1 is present, $c_p^* = -0.045$ and where Mode 2 is present $c_p^* = 0.258$	96
4.1	Simliar to the ramp response cases, the duty cycle is a linear mul- tiple of the control signal for all time in this test protocol. Again, the ideal power $\underline{P}_{ideal} \propto D^2$	103
4.2	For all step response cases $s_{down} = -s_{up}$	103
4.3	The duty is a linear multiple of the control signal for all time in this test protocol. However, the ideal power $\underline{P}_{ideal} \propto D^2$	105
4.4	For all ramp response cases $R_{down} = -R_{up}$	106

4.5	For several separate sequential ramp response tests, the response of the system is shown to be very repeatable. This performance is consistently maintained throughout the experiment.	109
4.6	Similar to the ramp rate data, the step response data is shown to be very repeatable. Again, the mean value of several consecutive responses is assumed to represent the average behavior of the system.	110
4.7	The data logger and system control software are running in parallel on two separate microcontrollers.	111
4.8	PWM controlled servos utilize a 1-2ms pulse contained in a 20ms frame, resulting in a control refresh rate of 50Hz.	112
4.9	The signal noise in the RPM measurement is symmetric about a mean, and is assumed to be normally distributed.	115
4.10	The step response tests are designed to evaluate the response of the system to step changes in power demand throughout its working power band for a specific control voltage.	117
4.11	RPM Reductions appear to be sensitive to the ramp rate.	120
4.12	The loading ramp response of the system changes significantly depending on the ramp rate. Here, significantly more energy is drawn from the slack bus as the power demand increases.	122
4.13	The descending step response tests are characterized by power inversions for each descending step in the power band. <i>Note that the data series 'tails' in this plot are artifacts from manually ending an experimental run, and are not physically significant.</i>	125

4.14	The unloading ramp response of the system changes significantly depending on the ramp rate. Here, significantly the voltage overrun is significantly greater for high unloading rates. <i>Note that the data series 'tails' in this plot are artifacts from manually ending an experimental run, and are not physically significant.</i>	128
4.15	Depending on the rate at which the unloading process occurs, the output power response can temporarily invert, resulting in a short-term increase in power output prior to the desired decrease in power. <i>Note that the data series 'tails' in this plot are artifacts from manually ending an experimental run, and are not physically significant.</i>	130
4.16	The addition of the slack bus in the 40V case reduces the oscillation of the system during the loading ramp.	132
4.17	Increasing the control voltage from 33V to 40V has a significant effect on the response of the slack bus. Significantly more energy is drawn from the slack bus in the 40V case.	133
4.18	Increasing the control voltage from 33V to 40V has a significant effect on the response of the PID controller. Oscillation is clearly observed in the 40V case and absent in the 33V case.	134
5.1	Simplified block diagram for the hybrid power system and controller.	139
5.2	Simplified block diagram total hybrid power system plant.	140
5.3	Equivalent circuit for the PMSM plant and power electronics.	140

5.4	Equivalent circuit of the PMSM, DC representation	141
5.5	Functional block diagram for a PMSM motor/generator based on Eq. 5.10	143
5.6	The equivalent circuit for the generator system coupled to a PWM regulated RC load.	145
5.7	The equivalent circuit for the generator system coupled to a PWM regulated resistance load only.	146
5.8	The equivalent circuit for the generator system coupled to a variable resistor.	146
5.9	Functional block diagram for the applied voltage V_c based on Eq. 5.26	149
5.10	Functional block diagram for the PMSM operating as a generator and regulated by the load PWM duty cycle with the T2 term included.	150
5.11	Functional block diagram for the PMSM operating as a motor/generator and regulated by the load PWM duty cycle with the T2 term omit- ted. Note that the current feedback loop present in Fig. 5.10 is gone.	150
5.12	Functional block diagram for the mechanical PMSM components based on Eq. 5.31	151
5.13	Functional block diagram for the mechanical PMSM components based on Eq. 5.32	152
5.14	Functional block diagram for the mechanical PMSM components based on Eq. 5.32. The T_2 current loop is included here for com- pleteness.	153

5.15	Plant MIMO subsystem representation, only critical inputs and output are visible here, though others can be used to monitor the model.	153
5.16	Bode Diagram of the open loop and closed loop system with the parameter values defined for the experimental apparatus.	157
5.17	The PID controller is implemented in the model of the power system with the ability to specify the initial torque, load duty cycle, and voltage setpoint.	159
5.18	Comparison between a model where $T2$ is omitted, and a model where $T2$ is included. These are models 1 and 2 respectively in the plot legends.	160
5.19	The model torque response predictably follows the current response.	161
5.20	Example of power and torque curves for a two stroke engine, taken from the commonly used Rotax 582 [13].	162
5.21	Parametric Bezier power curve and conversion to normalized power curve. Note that the control points do not necessarily fall on the generated curve.	165
5.22	Scaled engine model developed from the Zenoah G320PUM two-stroke used in this experiment	167
5.23	Schematic representation and CFD results for the flow through a throttle body [Bordjane and Chalet].	168
5.24	The path between the minimum and maximum torque is defined by shape parameter a , to create a concave, linear, or convex path for any angular velocity.	169

5.25 Torque response surface model for the Zenoah G320PUM engine used in this experiment where $a = 0.5$	170
5.26 Torque response surface model implemented in Simulink	171
5.27 Torque response surface model implemented in the complete power system model.	171
5.28 Simplified block diagram for the engine-driven hybrid power system.	172
5.29 System model results for single step up.	174
5.30 Throttle trajectory results for single step up.	175
5.31 System model results for single step down.	176
5.32 Throttle trajectory results for single step down.	177
5.33 System model results for the multi-step duty-cycle profile.	178
5.34 Experiment results for multi-step duty-cycle profile for comparison.	179
5.35 Throttle trajectory results for multi-step duty-cycle profile.	180
5.36 Power results for multi-step duty-cycle profile.	180
5.37 Model power output results for the fast-ramp duty-cycle profile. . .	181
5.38 System model results for the fast-ramp duty-cycle profile.	183
5.39 Experimental results for the fast-ramp duty-cycle profile. <i>Note that the data 'tails' in this figure are due to the manual shutoff of an experimental protocol, as well as data processing, and are not physically significant.</i>	184
5.40 Model throttle trajectory results for the fast-ramp duty-cycle profile.	185

6.1	Normalized circulation distribution for rectangular planform wings for different aspect ratios. For $AR = \infty$, the result is the circulation induced by the 2D airfoil section.	190
6.2	Three-dimensional vortex filament, [39]	191
6.3	A finite wing modeled as a superposition of an infinite number of horseshoe vortex elements, [creditAnderson].]	192
6.4	Comparison between c_l and C_L for the ADP propulsion system, AR = 8]	195
6.5	Comparison between c_d and C_{Di} the induced drag coefficient, for the ADP propulsion system, AR = 8]	196
6.6	Comparison between c_m and C_M for the ADP propulsion system, AR = 8]	196
6.7	Control volume drawn around each embedded fan in the ADP system.]199	
6.8	SLUF operating conditions for the ADP system with increasing wing loading.	209
6.9	Power loading for SLUF operating conditions with increasing wing loading.	210
6.10	Power loading for SLUF operating conditions with increasing wing chord.	211
6.11	CL model and SLUF response trajectory.	211
6.12	CDi model and SLUF response trajectory. Note that SLUF conditions cannot be achieved with this system for $C_{Di} \geq -c_{d0}$	212
6.13	ADP system efficiency as a function of α and c_p^*	215

6.14	Assumed bi-Wing ADP aircraft configuration, relative to the DARPA Lightning Strike sub-scale prototype.	216
6.15	The vertical velocities for both the inbound and outbound transition require closed loop control.	216
6.16	Both the horizontal and vertical forces are functions of only α and c_p^* .	218
6.17	The inbound transition velocity profile	219
6.18	The inbound transition power loading P_L and c_p^* profiles.	220
6.19	The outbound transition velocity profile	222
6.20	The outbound transition power loading P_L and c_p^* profiles.	222
6.21	The baseline aborted landing maneuver power loading profile.	224
6.22	Simplified block diagram representation of the HEPS voltage con- trol system.	225
6.23	Equivalent circuit representation of the HEPS voltage control system.	226
6.24	Expanded simplified block diagram representation of the HEPS voltage control system.	226
6.25	First order sliding mode control example (1-SMC). Note that the control u 'chatters' about the σ manifold.	232
6.26	Second order sliding mode control example (2-SMC). Note that the control u chattering is reduced.	234
6.27	2-SMC controller implemented in the HEPS voltage control system.	234
6.28	PID vs. 2-SMC controller system response implemented in the HEPS voltage control system and subjected to the multi-step load profile for a constant voltage setpoint.	236

6.29	PID vs. 2-SMC controller tracking error implemented in the HEPS voltage control system and subjected to the multi-step load profile for a constant voltage setpoint.	237
6.30	Servo rate response requirements based on 2-SMC controller with a timestep of $\Delta t = 0.0025sec$	238
6.31	Simplified MIMO block diagram including the power PI controller.	240
6.32	Power tracking behavior using a PI controller to update the load regulator duty cycle D	240
6.33	System summary behavior using a PI controller to update the load regulator duty cycle D	241
6.34	HEPS engine power and torque trajectories under the power-tracking multi-step load profile, for a constant voltage setpoint, $V_{setpt} = 33V$.	242
6.35	HEPS engine power and torque trajectories under the power-tracking multi-step load profile, for a constant voltage setpoint, $V_{setpt} = 33V$. Note that when the voltage is restricted to a constant value, the system will be unable to deliver the required power beyond a certain point.	243
6.36	HEPS engine power and torque trajectories under the power-tracking multi-step load profile, for a constant voltage setpoint, $V_{setpt} = 33V$. The power target cannot be satisfied as the HEPS trajectory approaches the maximum throttle boundary.	244
6.37	Simplified block diagram including the voltage setpoint controller.	245

6.38	When the operating voltage is permitted to float, the response to high power demands is much more robust.	246
6.39	The HEPS trajectory is capable of more fully utilizing the power and torque available in the engine.	246
6.40	The voltage setpoint response increases with power demand, then decreases as power is reduced.	247
6.41	HEPS equivalent circuit with Buck converter battery attached. . .	248
6.42	HEPS equivalent circuit with Buck converter represented as a controlled voltage source.	249
6.43	HEPS only collapse under large transient power demand.	251
6.44	Current output comparison between the slack bus supplemental current, the armature current, and the load current.	252
6.45	Battery comparison, Specific Power vs. Specific Energy [41]	254
6.46	Maximum sustained power threshold (MSPT) for the un-augmented HEPS.	257
6.47	System collapse for constant torque.	258
6.48	Maximum sustained power threshold (MSPT) system response summary for the un-augmented HEPS.	259
6.49	Power loading cases taken from the aborted landing maneuver profiles	260
6.50	Summary data from the transition profile simulation where $b_1 = 1.35$	264
6.51	HEP trajectory results from the transition profile simulation where $b_1 = 1.35$	265
6.52	Summary data from the transition profile simulation where $b_2 = 1.97$	268

6.53	HEP trajectory results from the transition profile simulation where	
	$b_2 = 1.97$	269
6.54	Summary data from the transition profile simulation where $b_3 = 2.70$	272
6.55	HEP trajectory results from the transition profile simulation where	
	$b_3 = 2.70$	273
A.1	Functional block diagram of the wind tunnel data acquisition system.	282
A.2	Layout of the manometer panel, showing the primary panel, tunnel conditions, fan outlet subpanel, and vertical length scale.	286
A.3	The raw manometer panel images are scaled to include both the main panel and sub panel, the scale reference, and notes regarding the current model configuration and operating condition.	287
A.4	Original image showing the pixel index locations used for cropping this and all subsequent images during data processing	287
A.5	Primary manometer panel imaged cropped to reference locations, converted to grey-scale with contrast adjusted to improve pressure data extraction from the image. The approximate center of each fluid column is marked as well. Image aspect ratio is true to scale.	288

A.6 Manometer sub-panel imaged cropped to reference locations, converted to grey-scale, though displayed using RGB wights, with contrast adjusted to improve pressure data extraction from the image. *Note that when displayed in this manner, the meniscus of the fluid column is clearly visible as the darkest patch at the top of each column.* The approximate center of each fluid column is marked as well. Image aspect ratio has been adjusted to display within this document. 289

A.7 Taken from ADP test data, the first 20 pressure taps are not used, as can be clearly seen. The identified column center indexes are augmented by taking measurements along adjacent additional pixels. The resulting measurement is the median of the row indexes identified by the algorithm. 290

A.8 Examining $\frac{\partial}{\partial m} C_j$ shows a distinct minimum value. This is interpreted as the transition between the light and dark regions of the fluid column, i.e. the height of the fluid in the column. 291

A.9 Collating the column height estimates from each fluid column produces a complete data set comprised of all 58 individual pressure taps. This sparse data set is shown for clarity, only the data from a few images included. 291

A.10 Typically, data is extracted from between 70 and 100 photos in order to characterize the performance for a given configuration. . . 292

A.11 The scaling factor used to compensate for the planar offset between the scale-reference and the manometer tubes is the ratio between the total distance of each to the camera lens focal point.	294
A.12 Tap ID Reference	295
A.13 Depending on the lens optics and the overall FOV of the lens, straight features in an image can appear to be curved or warped, particularly near the edges of the frame.	298
A.14 Method for estimating the uncertainty due to optical image warping	299
A.15 Method for estimating the uncertainty due to optical image warping applied to actual manometer panel images.	300
A.16 The Arduino Pro-Micro features both analog and digital I/O pins, as well as USB communication. The micro-SD card breakout board enables direct data logging.	304
A.17 This module can measure $\pm 30A$ when placed in series with the DC power supply circuit.	305
A.18 Schematic representation of the data logging system developed for the wind tunnel experiments.	307
A.19 Considerable signal noise is evident in the unfiltered power signal data.	308
A.20 Signal noise is significantly reduced by simply taking the mean of all samples with a specific record index.	310
A.21 Functional block diagram of the ASC712-30A sensor chip, [5]. . . .	311
A.22 Flow of information through the power data acquisition system. . .	312

B.1	CDP vs. ADP Experiment Configurations. ADP is a sub assembly of the CDP system.	317
B.2	The wind tunnel models are represented as a series of panels between pressure taps.	317
B.3	Coordinate systems for transforming the wing and flap geometries for each model configuration.	318
B.4	This figure shows the lift and moment coefficients, c_l and $c_{m_{c/4}}$ as a function of angle of attack, α , as well as the drag coefficient, c_d as a function of c_l . The $c_l(\alpha)$ curves with and without flaps are parallel until very near stall. Note the corresponding change in moment coefficient at stall, both with and without flaps.	321
B.5	The wind tunnel model has static pressure taps surrounding nearly the entire perimeter of each aerodynamic surface.	329
B.6	The wind tunnel models have static pressure taps surrounding nearly the entire perimeter of each aerodynamic surface.	329
B.7	The static pressure measurements at each tap are shown as an example, arrow length indicates the relative magnitude.	331
B.8	Resulting forces are applied at the cell-center position, the midpoint between each pressure tap.	332
B.9	In order to develop a fan thrust estimate, a control volume is drawn around fan #3, and is assumed to be representative of all fans in the experiment. For all cases, it is assumed that the total fan force contribution acts along the fan's axis of rotation.	335

B.10 URANS CDF results, CDP configuration with moderate flap deflection, showing the instantaneous stream-tube passing through the fan.	338
B.11 For both the CDP and ADP configurations, the fan axis is offset from the flap reference by angle $\beta = 4.85$ deg.	339
B.12 Fan #3 is instrumented with eight total pressure taps positioned in the fan outlet on the measurement plane.	344
B.13 Wall static pressure taps in the fan #4 duct are used for reference when estimating the velocity at each total pressure probe.	347
B.14 Example of a case where recirculating region was identified for removal from the thrust estimate.	347
B.15 Example showing the u and v thrust components estimated for an ADP configuration at $\alpha = 0$ deg	348
B.16 An example case showing the computed u and v components of thrust - ADP at $\alpha = 0$ deg. Note that the net thrust is negative for cases where $c_p^* \lesssim 0$	353
B.17 The pressure distributions on surfaces ③ and ④ are measured and the areas of each surface is known.	354
B.18 Example showing a valid power balance for all conditions in a specific configuration, in this case ADP at $\alpha = 0$ deg. Also note that the high efficiency early in the test corresponds to zero electrical power input.	355

B.19	Example showing the velocity correction due to the u-thrust component in a confined flow-field for a specific configuration, in this case ADP at $\alpha = 0$ deg.	358
B.20	Example showing the net velocity correction due to the 3D blockage and thrust u-thrust component in a confined flow-field for a specific configuration, in this case ADP at $\alpha = 0$ deg.	359
B.21	Example showing the convergence of the velocity correction due to thrust in a specific configuration, in this case ADP at $\alpha = 0$ deg. . .	360
B.22	Example showing the force and moment coefficients for a specific configuration, in this case ADP at $\alpha = 0$ deg.	362
C.1	This configuration applies to the power systems required for both the ADP and CDP propulsion configurations.	366
C.2	For this experiment, only a single PWM controlled load is applied to the system. Also, note that the battery or slack-bus can be connect or removed from the system.	367
C.3	Hybrid power system experiment installed in a fume hood in the Syracuse Center of Excellence.	369
C.4	Water cooling is used to remove heat from the engine as well as the power diodes, rectifier, and the primary system load.	370
C.5	A Zenoah model G320PUM, liquid cooled engine is use as the prime-mover for this hybrid system.	371

C.6 The Zenoah G320PUM, is coupled directly to a three-phase BLDC generator. The generator is mounted rigidly to the output shaft of the engine, and supported by polymer vibration-absorbing mounts. 372

C.7 The Leopard Hobbies LC6362-10T is a three-phase PMSM motor with the phases connected in a delta configuration. 373

C.8 A delta-connected generator is preferable for this airborne application, the neutral reference required for a wye connected system presents significant challenges for un-grounded systems. (<http://electrical-engineering-portal.com/3-phase-transformer-connections>.) 373

C.9 The MDS-100A three-phase rectifier is a low cost COTS device capable of handling 100A forward rectified DC current. 375

C.10 The IXYS DSS2x101-015A Schottky Diode is a low cost COTS device capable of handling 100A forward DC current with the additional benefit of being packaged in a double configuration. 375

C.11 The DC load consists of two water heating elements, each with a resistance of 1.536Ohms, connected in parallel. 378

C.12 The tubular heat exchanger constructed for this experiment provided a safe, compact design, where heating elements were shielded from contact with any external surface. 378

C.13 The PWM motor controller breaks the DC input voltage into discrete square wave pulses in order to control power output. Shown here are the measured waveforms at duty cycles of $D_{mid} = 0.375$ and $D_{low} = 0.125$ 379

C.14	The PWM controller used in this experiment uses an array of MOS-FETs operating at a constant switching frequency of 15kHz to generate the controlled square wave pulses required for regulating the DC load.	380
C.15	The slack bus used in this experiment consists of COTS power supply and conditioning equipment. The Output voltage from DC power supply is boosted to the working voltage of the system. . . .	382
C.16	The data acquisition system developed for this experiment is based on the same microcontroller and SD card data logging as the wind tunnel data acquisition system.	384
C.17	This current sensor is designed to measure AC, DC and Pulsed current. The digital display provides a convenient means of visual feedback during testing.	387
C.18	The experiment control software runs on a dedicated microcontroller, in parallel with the data logging microcontroller. Shown here is the architecture of the system as it pertains to the experiment controller only.	389

List of Tables

2.1	ADP Experiment Summary Table	36
2.2	ADP Experiment Summary Table - ACR	48
2.3	ADP Experiment Summary Table - PLR	56
2.4	ADP Experiment Summary Table - HBR	67
4.1	Step Test Condition Summary	101
4.2	Ramp Test Summary	106
4.3	Step Response Test - Voltage Drop	116
4.4	Step Response Test - Slack Bus Energy Contribution	119
4.5	Ramp Test Response Summary - Voltage Lag	121
4.6	Ramp Response Test - Slack Bus Energy Contribution	121
4.7	Step Response Test - Voltage Jump	124
4.8	Step Response Test - Power Inversion	126
4.9	Ramp Response Test - Voltage Lead	127
4.10	Ramp Response Test - Power Inversion	129
4.11	Ramp Response Test - Slack Bus Energy Contribution	135
5.1	Experimental Apparatus Parameters	156

5.2	Phase Margin Improvement with PID Control	158
6.1	Aborted Landing Maneuver Parameters	224
B.1	Forward wing pressure tap locations, given in the forward wing reference frame.	333
B.2	Upper flap pressure tap locations, given in the flap reference frame	333
B.3	Lower flap pressure tap locations, given in the flap reference frame	334
C.1	Zenoah G320PUM Specifications	372
C.2	Leopard LC6362-10T 210kV Specifications	374
C.3	MDS-100A Rectifier Specifications	375
C.4	IXYS DSS2x101-015A Schottky Diode Specifications	376
C.5	PWM Switching DC Motor Controller Specifications	381
C.6	Venom ProPower DC Power Supply Specifications	382
C.7	DROK DC-DC Buck-Boost Controller	383

List of Algorithms

1	Numerical Lifting Line Algorithm	194
2	SLUF Condition Calculation Algorithm	208
3	Photo processing and raw column height data extraction	285
4	Simultaneously take a photo and store 50 data samples.	306
5	Remove recirculating regions from thrust and power estimates	346
6	Compute inlet velocity such that continuity is satisfied over the fan control volume, Fig. B.9	351
7	Iterative scheme for refining velocity and thrust estimates	359

Symbols and Nomenclature

0.1 Nomenclature

As this work spans the disciplines of Mechanical, Aerospace, and Electrical Engineering, careful attention must be paid to the context in which specific variables are used. The common nomenclature practices of each discipline are followed to the greatest extent possible.

A [m^2]	flow area	c_d	section drag coefficient
a, b	fitting parameters	C_D	..	finite wing total drag coefficient
A, B	fitting parameters	c_{d0}	parasite drag coefficient
α [deg]	...	geometric angle of attack	C_{D_i}	induced drag coefficient
α_i [deg]	induced angle of attack	c_l	section lift coefficient
AR	wing aspect ratio	C_L	finite wing lift coefficient
b [m]	.	wing span or viscous damping	$c_{m_{c/4}}$	moment coefficient
b_n [m]	scaling coefficients	C_M	...	finite wing moment coefficient
β	coefficient substitution	c_p^*	dimensionless parameter

c_p^{*l}	dimensionless parameter	Γ [m^2/s]	circulation
c_u	horizontal force coefficient	\hat{x}_n	a state observer
c_v	vertical force coefficient	i_a [A]	armature current
D [N]	drag force, or duty cycle	I, i [A]	current
d, d_1, d_2 [m]	fan diameter	i, j, k	indices
\dot{m} [kg/s]	mass flow rate	i_s [A]	supplemental current
e	tracking error	J [$kg * m^2$]	rotational moment of inertia
e_a [V]	electromotive force (back emf)	k_E	voltage constant
ϵ	a sigmoid parameter	k_T	torque constant
η	efficiency	L [N]	lifting force
f [Hz]	a frequency	l, dl [m]	vortex filament length
f_{model} [Hz]	model solver frequency	λ	2-SMC controller parameter
f_r	frequency ratio	l, m, n	indices
f_{sw} [Hz]	switching frequency	n_b	number of fans per unit span
F_x [N]	horizontal force	N_{poles}	number of poles
FOM	figure of merit	$\omega, \omega_1, \omega_2$	angular velocity
$G(s), etc.$	Laplace transform result	\bar{A}, \bar{B}	fitting parameters

p [Pa]	pressure	T	throttle setting
P [Pa]	pressure	T_1, T_2	equation term reference
P_s [Pa]	local static pressure	τ, tau [N-m]	torque
P, \underline{P} [W]	power	TEO [Wh]	total energy output
P_L [W/m]	power loading	$\theta, \dot{\theta}, \ddot{\theta}$	angular motion
Ψ	energy output ratio	u	control variable
Pwr [W]	power	u_e [m/s]	..	exit velocity from fan duct
q_∞ [Pa]	.	free stream dynamic pressure	U	control constant
q_n, \dot{q}_n	state variables	v	a voltage
r [m]	radial distance	V_c [V]	control voltage
R [ohms]	a resistance	V_{in} [V]	input voltage
ρ [kg/m^3]	density	V_∞ [m/s]	free stream velocity
s	Laplace variable	v_o [V]	output voltage
S [m^2]	wing area	v_s [V]	slack bus output voltage
SBO [Wh]	slack bus output	V_{stall} [m/s]	stall velocity
σ	sliding variable	V, v [V]	voltage
t [s]	time	w [m/s]	down-wash velocity, or controller parameter

W	2-SMC controller parameter	x_n, \dot{x}_n	controller state variables
W_L	$[N/m^2]$	wing loading	y, \dot{y}, \ddot{y}	$[m, m/s, m/s^2]$ lateral motion
$w(y_0)$	downwash at a specific wing station		y, y_0	wing spanwise coordinate
ω , omega	$[\text{rad/s}]$	angular velocity	y, y_{des}	system output variable and setpoint
x, \dot{x}, \ddot{x}	$[m, m/s, m/s^2]$..	horizontal motion	z, \dot{z}, \ddot{z}	$[m, m/s, m/s^2]$... vertical motion

0.2 List of Abbreviations

ACR	aerodynamic cruise (regime)
ADC	analog to digital converter
ADP	articulated distributed propulsion
C++	programming language
CDP	compound distributed propulsion
CFD	computational fluid dynamics
DEP(S)	distributed electric propulsion (system)
DoF	degrees of freedom
DTML	direct transmission to multiple loads
FOM	figure of merit
HBR	hover breakdown (regime)
HEPS	hybrid electric power system
MSPT	maximum sustained power threshold
MTOW	maximum takeoff weight
PLR	powered lift (regime)
PPM	pulse position modulation

PWM pulse width modulation

RANS Reynolds-averaged Navier-Stokes, steady state solver is implied

Star-CCM+ commercial CFD code, RANS and URANS solvers

URANS unsteady Reynolds-averaged Navier-Stokes

VTOL vertical takeoff and landing

xPLP transition power loading profile

Chapter 1

Introduction, Motivation, and Background

1.1 Introduction

The objective of this chapter is to present the motivation for the present research effort in the context of the current state of the art of aircraft propulsion and power systems. A summary of the relevant segments of the aircraft industry will be presented to provide the background information and motivation for vertical takeoff and landing (VTOL) aircraft development. Additionally, the specific VTOL concepts investigated in this research will be compared to existing aircraft technologies and to competing VTOL configurations. Later, the relevant literature will be reviewed and compared to the scope of the present effort. This leads ultimately to the guiding research question for this work and the primary contributions to the fields of Aerodynamics and Propulsion, and Power Systems

and Controls that will be developed throughout the course of this dissertation. Finally, a road-map summary of the contents of this dissertation will be provided at the end of this chapter.

1.2 Current Aircraft Types

There are two primary types of aircraft currently in use, fixed wing aircraft and rotorcraft, otherwise known as helicopters. An example of a light fixed-wing aircraft is shown in Fig. 1.1 and an example of a helicopter is shown in Fig. 1.2. These aircraft fill two distinct roles in the current aviation ecosystem. Fixed wing aircraft are typically used for long range transportation, while helicopters are typically used for short range applications, such as point-to-point transportation and aerial imaging and surveillance.



Figure 1.1: Light, fixed wing aircraft example, Vans RV-10 [3]

These roles are respectively determined by the particular performance attributes of aircraft and rotorcraft. These attributes are summarized as follows:

- **Fixed Wing Aircraft Attributes**



Figure 1.2: Helicopter example, Robinson R22 [49]

Pro - Fast and efficient

Con - Requires large and complex airport infrastructure to operate

- **Rotorcraft Attributes**

Pro - Can operate with minimal infrastructure due to VTOL capability

Con - Slow and inefficient

Based on these high-level attributes, a VTOL-capable fixed wing aircraft represents the best of these two aircraft categories.

1.3 VTOL Aircraft Configurations

VTOL aircraft have been an area of significant interest periodically for the past 50 years. The most recent resurgence in VTOL interest began in approximately 2010, with the commercialization of accurate semiconductor accelerometers and gyroscopes for controlling the

attitude of small scale aircraft, as well as batteries capable of delivering flight power for short periods of time. While these technologies were developed for the consumer electronics industry, this led to the growing popularity of consumer drones used for aerial photography beginning in 2010 and continuing through present day. These adjacent technologies have resulted in renewed interest in VTOL as critical enabling technologies have been provided by these adjacent industries. While innumerable configurations have been proposed, they fall into one of three primary categories.

- Helicopters, Multirotors, and Tilt Rotors
- Separate Lift and Thrust (SLT)
- Distributed Lift and Thrust (DLT)

1.3.1 Helicopters, Multirotors, and Tilt Rotors

This category of VTOL system is the most established. These vehicles are primarily rotorcraft, intended for operating in vertical flight modes. Primarily designed for hover, the large rotor-disk area of these rotorcraft give these configurations a distinct advantage over other VTOL configurations in terms of hover endurance. Due to low disk loading, these designs have the lowest power requirement for operating in hover. This category includes light helicopters, as shown previously in Fig. 1.2, as well as multirotor drones, shown in Fig. 1.3 and tilt rotor aircraft shown in Fig. 1.4.



Figure 1.3: Multirotor drone example, 800mm DYS Quadcopter [20]



Figure 1.4: Tilt rotor example, V-22 Osprey [4]

1.3.2 Separate Lift and Thrust (SLT)

SLT configurations are characterized by separate propulsion systems used for vertical thrust (rotor-lift) and horizontal propulsion. The most notable of these configurations is being

developed by Kittyhawk, a Silicon Valley startup company. Their SLT concept aircraft is shown in Fig. 1.5.



Figure 1.5: Kittyhawk SLT example [33]

This VTOL configuration uses an array of lifting rotors driven by electric motors that operate while the aircraft is in transition or in hover, and that shut down when the aircraft has sufficient forward velocity to achieve wing-borne flight. While this design is relatively simple and provides significant redundancy in the event of a power failure, it is tremendously inefficient in hover, transition, and cruise. In hover, the lifting rotors incur the weight penalty of the additional, idle, forward propulsion system. In transition, the lifting system must overcome adverse interactions between the lifting rotors and the wing. Further complicating this, the rotor-induced downwash along the wing will dramatically increase the power required to maintain a particular flight condition. Finally, in cruise, the forward propulsion must overcome the drag penalty imposed by the idle lifting rotor system. As a consequence, the lifting system and the forward propulsion system must be significantly oversized relative to the hover and cruise conditions alone.

1.3.3 Distributed Lift and Thrust (DLT)

DLT configurations represent an elegant integration of lifting and propulsion systems that serve to augment each other, resulting in a cohesive system that leverages interactions between the aircraft aerodynamics and propulsion systems to deliver significant performance enhancements for each system. Understanding and leveraging these interactions is an objective of this present research effort. Though complex, these systems have the highest potential for advancing the state of the art in aircraft design and propulsion.

As the disk loading is the highest for the DLT systems, these will have the highest hover power requirements. However, since the propulsion system augments the circulatory lift about the aerodynamic surfaces, this power demand will decrease significantly and rapidly as the vehicle accelerates through transition, providing for fast and efficient cruise performance. An example of a DLT configuration studied in this research is shown in Fig. 1.6.



Figure 1.6: Lilium Jet DLT example [37]

1.4 DLT VTOL Configurations

There are two DLT configurations that are studied in this research effort. The first of these is embodied in the Aurora Flight Sciences concept known as Lightning Strike [48]. This aircraft is shown in Fig. 1.7. Since the wing is articulated, able to tilt through a 90 deg arc, from hover to cruise, this concept shall be known as articulated distributed propulsion (ADP) for this research. The second configuration considered herein is under development by Lilium GmbH [37], a German aerospace startup. This configuration is shown in Fig. 1.8 and previously in Fig. 1.6. As this configuration consists of a compound wing-flap system, where the flap can rotate through a 90 deg arc, this system is known as compound distributed propulsion (CDP) for the purposes of this research.



Figure 1.7: Aurora Lightning Strike DLT example, ADP configuration [48]

As of the publication of this dissertation, Aug. 2018, no publications regarding either of these propulsion systems had been made by either of the developing entities. As a result, the geometries and behaviors of these systems were reverse-engineered and characterized as a part of this research effort.



Figure 1.8: Lilium Jet DLT example, CDP configuration [37]

1.5 Power Sources for Distributed Propulsion

Both the ADP and CDP propulsion systems are characterized by an array of small ducted fans distributed along the span of the main wing and canard wing. It is impractical and inefficient to mechanically shaft power to each of these systems. As such, small permanent magnet synchronous motors (PMSMs) are used to drive the distributed ducted fans. Therefore, an electrical power distribution system is required for each of these propulsion systems. As a result, the ADP and CDP systems are powered by airborne micro power grids. This power distribution system is shown in Fig. 1.9. This direct transmission to multiple loads (DTML) topology is similar to a system proposed by NASA for large turbo-electric microgrids in 2015 [8].

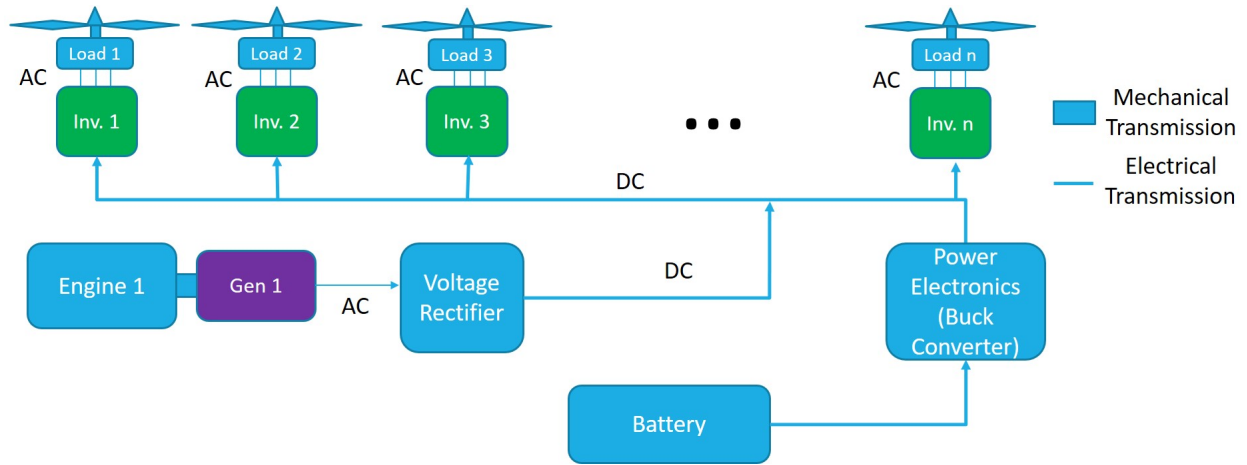


Figure 1.9: Direct Transmission System Topology

1.5.1 Benefits and Shortcomings of Battery Power for VTOL

Since these propulsion technologies require an electrical power distribution system, the initial source of this electrical power must be addressed. Current battery technologies are able to provide the power required to operate these propulsion systems. However, their energy storage capacity is not capable of providing the endurance required for most aircraft operations. While controlling these battery systems is very simple, when using battery power alone, the endurance of these aircraft is typically less than 30 minutes. Therefore, battery power only is not sufficient for most aircraft applications. Further, given the recent commercial development of battery technologies, it is unlikely that battery technology with sufficient energy density will be available in the foreseeable future, approximately 10-20 years.

1.5.2 Benefits and Shortcomings of Hybrid-Electric Power Systems (HEPS)

Since hybrid-electric power systems use a chemical fuel as their primary energy source, they are readily capable of delivering the power required for VTOL flight as well as storing sufficient energy for acceptable flight endurance. However, since these use dynamic electromechanical systems, i.e. engine-generator systems, for converting stored chemical energy into electrical energy, the control of these systems and processes is critically important. Additionally, the system architecture must be refined to ensure a robust response to potential input disturbances.

1.6 Historical Perspective on VTOL

Given the potential benefits and broad applications of a VTOL aircraft, this concept has been in development for nearly 60 years. One of the earliest attempts can be attributed to Curtiss-Wright in the early 1960s. Since then, more than 45 major defense programs in the U.S. and abroad were undertaken to achieve this capability, with very few resulting in service-worthy aircraft. Of these few marginal success are the V-22 Osprey, the F-35B, the Yak-38, and Harrier [52]. The American Helicopter Society compiled the VTOL wheel, shown in Fig. 1.10.

Studying these programs reveals several critical lessons about VTOL flight throughout history. Many of these aircraft could hover and many of these aircraft could fly, but all

1.7 Literature Review

This section presents a summary of the relevant literature in the critical subject areas involved in this research. As such, the literature in each of the subject areas is treated separately. These areas include VTOL aircraft propulsion and transition control, hybrid powertrain technology, and electrical machines and power generation. Literature is drawn from these seemingly disparate areas of mechanical, aerospace, and electrical engineering because, as of the date of this dissertation, Aug. 2018, the author is not aware of another attempt to cohesively evaluate the performance and stability of hybrid-electric aircraft propulsion system, notwithstanding the application to VTOL transition dynamics.

1.7.1 Electric Aircraft Propulsion and VTOL Transition Control

The literature in this area can be more finely segmented into two sub-categories, that dealing with distributed electric propulsion, and that addressing VTOL transition specifically. Nothing in the literature specifically addresses either the ADP or CDP configurations.

Distributed Electric Propulsion (DEP)

First, in 2014 Nalianda and Singh [42] published a high-level review of the opportunities benefits and challenges associated with large scale turbo-electric distributed propulsion (TeDP) for large transport-category aircraft. This paper presents TeDP as a potential solution for easing airport congestion and making the transportation industry more environmentally sustainable and posits that use of this type of propulsion system could enable improved

propulsion system packaging and integration with the airframe to realize potential energy utilization and aircraft performance benefits. These proposed benefits include more efficient structural design and boundary layer ingestion for improved propulsion efficiency and reduced emissions. Specifically, this paper considers the potential for implementation of superconducting electrical systems using cryogenic fuels to maintain superconductivity, such as liquid hydrogen. Further, it finds that the practical implementation of such superconducting technologies represents a significant challenge to deploying distributed electric propulsion in the next generation of large transport category aircraft. Through the e-Thrust conceptual development project Airbus and Rolls-Royce are working on solving these problems [2].

Next, also published in 2014, in a collaborative effort between the NASA Langley Research Center and Joby Aviation, Moore, Stoll, et. al., propose using distributed electric propulsion as a means of drag reduction for improved cruise performance on a general aviation aircraft [54]. This paper details a specific DEP configuration, the Leading Edge Asynchronous Propellers Technology or LEAPTech. In this system, many small propellers are distributed spanwise along the wing, creating a blown wing system where the dynamic pressure over the wing is increased significantly. Consequently, the wing area can be reduced without the need for structurally complex multi-element high lift devices. This leads to a significant drag reduction in cruise and decreased gust sensitivity due to higher wing loading. NASA's LEAPTech is the basis for the MRTR configuration that NASA has evaluated as part of their Greased Lightning VTOL test program.

VTOL Modeling and Control

There is an abundance of literature involving the development, control, and testing of V-22-type bi-rotor tiltrotor aircraft. In this body of work, consisting of research into the control system of XV-15 research aircraft and the V-22 Osprey conducted by NASA, Bell, and Boeing primarily, large scale modelling and wind tunnel testing methods are developed and analyzed. However, this configuration is not considered in the scope of the present research, as to do so would be redundant. This body of work will be consulted regarding the development of specific experimental protocols for wind tunnel testing and vehicle system analysis.

In a 2015 publication, Diekmann and Hahn detail the effect of an active high-lift system failure during landing approaches [19]. In this analysis, a propeller blown flap is assumed to fail at various stages during a simulated approach to landing. The high lift region is assumed to be in the slipstream of the wing mounted engine on a CS-25 transport aircraft. While not a VTOL aircraft, this work presents a method for simulating the failure of active high-lift devices, in this case a blown flap, during a landing approach, including a method for solving a 6-DoF aircraft model in MATLAB/Simulink. This approach uses modeled data from the aircraft generated a priori for simulating the system dynamics during before during and after the high lift system failure. Further, this analysis presents the dynamic response of a CS-25 Aircraft to the failure of the lifting system and from published data on that aircraft, concludes that certain failure points are recoverable while others are determined to be catastrophic.

Also in 2015, Yoon, Lee, and Pulliam [59] researchers at NASA Ames Research Center published a computational analysis of large-scale multirotor flows [2]. In this analysis, a Detached Eddy Simulation (DES) turbulence model is used in conjunction with a three-dimensional unsteady Navier-Stokes solver to model the rotor-rotor and rotor-aircraft interactions in a large conceptual quad-tilt rotor aircraft. This analysis used the rotor system from an XV-15, with a 25-foot diameter, fixed in a hover configuration. The performance degradation of the rotors is presented as a function of the distance between the rotors and normalized by the performance of a single rotor operating independently. Also, the relative contributions of the rotor wings and fuselage are presented as well, with the wings contributing -18.8% normalized downforce relative to rotor thrust.

Finally, in 2016, Yuksek, Vuruskan, et. al. published an analysis of the transitional flight phase for a tilt-rotor VTOL UAV [61]. This work presents a 6-DoF model of a tilt rotor UAV in MATLAB/Simulink, including the aerodynamic effects of the propeller induced slipstream and its effect on the wing aerodynamic forces and moments as a function of cruise speed tilt angle and angle of attack. The development of a 6-DoF aircraft model is developed in detail as is the design of the transition profile. Here, the estimated performance data are embedded in lookup tables derived from modified force and moment coefficients and applied to the rotor-affected areas based on simplified velocity vector approximations. These are later verified using a combination of a Vortex Lattice method and a 3D CFD model with actuator disk rotor approximations for quasi-steady operation. In this analysis, the method for hover-to-cruise and cruise-to-hover transitions are prescribed. Both scenarios are designed and state-scheduled, these schedules are ultimately used as a feedforward state for the flight control system. A flying UAV testbed was constructed and inbound and outbound transitions

were demonstrated successfully. This provides a basis for the design of a 6-DoF aircraft model and corresponding flight controller.

1.7.2 Hybrid-Electric Power System (HEPS) Technology

In 2000, Baumann, Washington, et. al. published “Mechatronic Design and Control of Hybrid Vehicles.” [11] In this analysis, an approach for developing a hybrid powertrain model and controller for dynamic simulation, where the engine model is developed using known engine performance data, particularly net efficiency as a function of rpm and engine torque. In this case, a VW 1.9L TDI (Turbo-diesel) is used as the power source. This model is developed from the perspective of automotive hybrid system design, with an emphasis on improving fuel economy. Here the model development strategies are of primary interest to the present research effort.

In 2015, Friedrich and Robertson published an analysis and design of a hybrid electric propulsion system for aircraft [27]. This analysis specifically focused on the detailed analysis, development, and experimental validation of a parallel hybrid system for use in a midscale, 235kg GTOW fixed-wing aircraft. This paper presents the modelling and analysis efforts behind the design of the hybrid topology and component sizing for this aircraft. Further, this analysis also presents an approach for scaling the analytical and experimental results down to a 20kg UAV and up to a 50-ton intercity airliner. The architecture of this system is shown in Fig. 1.11.

In 2017, Silvas, Hofman, et. al. published a comprehensive review of systems-level design and optimization strategies for hybrid electric vehicles [51]. Initially, this work presents

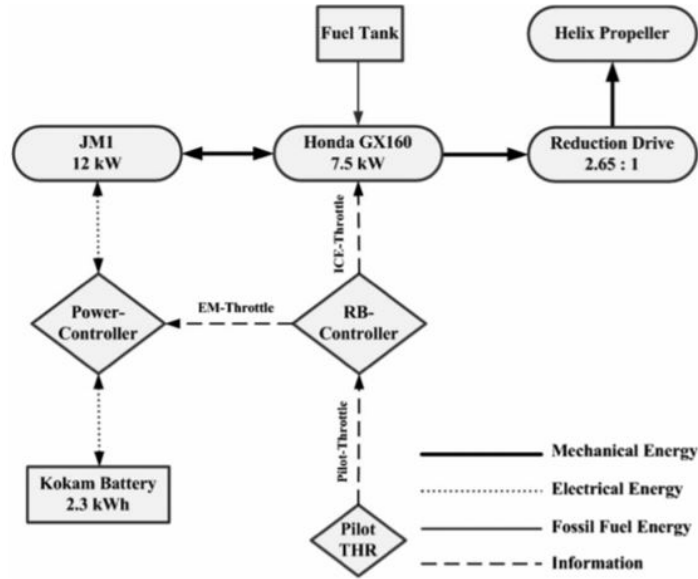


Figure 1.11: Hybrid aircraft propulsion topology proposed by Freidrich and Robertson, [27]

a summary of the primary hybrid topologies used in the automotive industry. Also, a comprehensive analysis of non-linear optimization strategies for the independent and concurrent design of hybrid power systems and controllers, with an emphasis on fuel use optimization is presented, as is a framework for system-wide optimal design, again with the objective of optimal fuel utilization. This framework consists primarily of three design levels, topology selection, component sizing, and controller design. Though this work is presented from the perspective of automotive design, the strategies presented for topology generation, system design and optimization are applicable to aircraft hybrid-electric system design, as shown in Fig. 1.12.

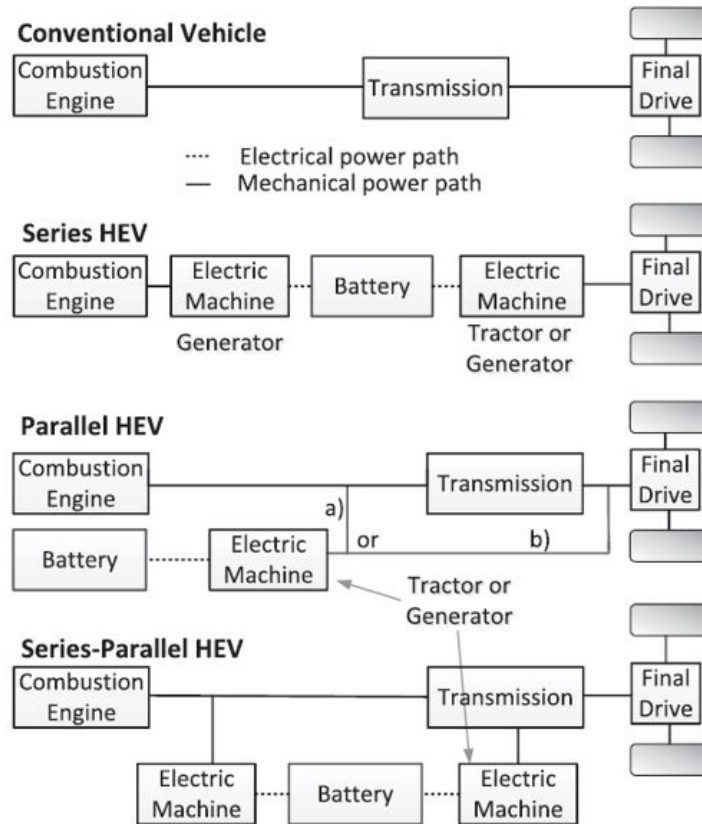


Figure 1.12: Typical automotive hybrid configurations presented by Slivas, Hofman, et. al. [51]

1.7.3 Electrical Machines and Power Generation

In 2007, Zhu and Howe present a comparative analysis of electrical machines for used in hybrid vehicles [62]. This analysis presents the performance and operation characteristics of induction machines, switched reluctance machines, and permanent magnet machines. Both induction and switched reluctance machines can deliver the required performance characteristics, however, the permanent magnet machines off higher efficiency and torque density. Further, this work described the critical difference in the back-EMF and phase current waveforms of BLAC and BLDC machines. Both BLAC and BLDC machines are determined to be suitable for use in aircraft hybrid-electric systems for the present research effort, with

the primary distinction between them being the use of sinusoidal and trapezoidal phase current waveforms respectively. These will collectively be referred to as permanent magnet synchronous machines (PMSMs) for the purposes of this analysis, as these designs have identical equivalent circuits.

In 2008, W.L. Soong presented a briefing document that described a simplified method for estimating the size of an electrical machine given a specific torque and speed requirement. This method uses the configuration of the machine as well as the magnetic flux-density to approximate the size of the rotor and stator components [53]. This method was extended by the author of the present work to design a PMSM for a specific operating condition, and estimate the performance characteristics of this machine across the full operating range.

In 2009, J.P.C Kleijnen presented a review of Kriging metamodeling in simulation [34]. Metamodels are otherwise known as response surface models, are extended to Kriging models with the addition of process noise to the system. The Universal Kriging model is defined as:

$$w(d) = \mu + \delta(d) + \epsilon(d) \tag{1.1}$$

Where, μ is an arbitrary, but typically low-order regression model of the system; $\delta(d)$ is additive white noise forming a stationary covariance process; and $\epsilon(d)$ has zero mean and an unknown covariance. Therefore, the Kriging predictor is no longer an exact interpolator of the data used to construct the regression model. These Kriging models are used to extend metamodels in dynamic simulation applications, as well as optimization schemes, so that they exhibit some of the random process characteristics of real systems.

Finally, in 2014 Lei, Wang, et. al. published a deterministic approach for the design optimization of the electrical drive systems [36]. Here, single level and multi-level optimization methods are applied to the design of a PMSM motor and controller. Most importantly for the present research, a simplified Kriging motor model was used in place of a Finite Element Magnetic (FEM) model to reduce the computational cost of the optimization. The Kriging model was developed using FEM to calculate critical parameters of the PM design under specific conditions, primarily the motor core loss under no-load conditions and the stator winding flux. This model, constructed from limited simulation data, can then be used in subsequent optimization calculation. The construction and implementation of this Kriging model can be adapted for use to several of the subsystems in the present analysis, though initially simple regression models will be used.

1.7.4 Additional Discussion

This section seeks to place the present research effort in the context of the prior work identified in the literature. The present work will be considered relative to the comparable and foundational work identified.

Relative to Diekmann and Hahn [19], this work presents a method for simulating the failure of an active high-lift device during landing approach. Here, aerodynamic data are incorporated into a dynamic simulation model where the aircraft undergoing the perturbation is modeled as a 6-DoF system. The method and analytical framework shown here for simulation the aircraft under normal conditions and under perturbed conditions are directly applicable to the present research effort. This work serves as a model for developing the

aircraft motion framework, implementing subsystem and aerodynamic metamodels in the simulation, and developing the normal and perturbed flight profiles of the aircraft during approach to landing. This work will be extended by the present effort in two specific ways. First, this work focuses on the CS-25 aircraft where the engines are independently operated, wing-mounted gas turbines. Therefore, the effects of a failure near one engine does not impact the performance of the other engine so the engine response to such perturbation need not be considered in detail, however, given the DTML parallel hybrid topology, all propulsion systems are coupled so aircraft perturbations affect the entire system. Second, given that the present research considered a VTOL system in transitional flight, normal transition operations result in large changes in power demand, which is compounded by the addition of external perturbations superimposed on the transition profiles.

Relative to Yuksek, et. al. [61], this work presents a framework for integrating the effects of aerodynamic phenomena related to aircraft-propulsion interactions into a Simulink dynamical model. Additionally, it also proposes prescribing the transition profile as a means for simplifying the simulation and describes the design of a flight controller for doing so. The present work can build on this analysis, using it as a model for the process of integrating transient aerodynamic effects into dynamical simulation. Also, the present work will extend this approach to include the interactions of the hybrid-electric powertrain with the power demands of the aircraft and the transient control response to the transition process and imposed perturbations.

Relative to Freidrich and Robertson [27], this work presents a model for developing and analyzing the design of a hybrid-power system topology. Here, a typical parallel hybrid topology directly applied to a single propeller mid-size aircraft. Additionally, the scaling

analysis presented herein can be used as a model for development of the scaling analysis in the present research. The present work will extend this research by developing a new hybrid-electric topology suited to applications with DEPs. The proposed DTML topology eliminated the mechanical transmission link between the engine and the loads. In so doing, the dynamic characteristics of the hybrid system are significantly altered. Also, the emphasis of the Friedrich and Robertson publication is on long-range fuel economy, while the emphasis of the present work is on VTOL transition performance and the short-term stability of the hybrid powertrain under rapid changes in power demand.

1.8 Guiding Research Question and Original Contributions

Examining the technical and historical context surrounding the problem of VTOL aerodynamics and transition control, the following guiding research question emerges:

Given the range limitations imposed by battery systems on electric VTOL aircraft, what is required for an internal combustion engine-based hybrid-electric power system (HEPS) to satisfy the power demands of a VTOL aircraft in transitional flight.

The research question above serves to guide the present multidisciplinary research effort.

Addressing this question through this dissertation has led to original contributions to the fields of aerodynamics and propulsion as well as power systems and controls engineering.

1.8.1 Contributions to Aerodynamics and Propulsion

At present, no research has been published in the academic literature or otherwise detailing either the computational analysis or experimental investigation of the performance attributes of the ADP and CDP embedded propulsion systems. This research explores both of these systems computationally and experimentally, with the objective of characterizing each system and determining which is best suited for use in a VTOL aircraft utilizing hybrid-electric power. Both systems are evaluated, though ultimately ADP provides the most robust VTOL characteristics, based on these results.

Additionally, a methodology is developed for estimating the transition power loading required for VTOL operation using an embedded propulsion system. In conducting this analysis, new methods for characterizing embedded propulsion systems are developed as well. Ultimately, an enhanced analytic framework for evaluating their performance is presented. This methodology extends conventional aircraft performance analysis to include the influence of power input on circulatory lift, drag, and moments.

1.8.2 Contributions to Power Systems and Controls Engineering

Most hybrid power system literature is focused on improving fuel economy in automotive or aircraft applications, and therefore assumes that the power system is operating at various steady states, with little attention paid to short-term transient behaviors. In this research,

an experimental HEPS is constructed to provide validation data to inform the development of a detailed dynamic HEPS simulation. This model employs manifold regression meta-models to estimate the response of the engine to changes in load, angular velocity, and throttle setting. This validated simulation enables the development of improved control designs and an enhanced system architecture that provides robust disturbance response characteristics.

Also, the addition of a controlled slack-bus to the system allows the HEPS to sustain power demands significantly in excess of its maximum sustained power threshold (MSPT). Ultimately, the transition power loading profile is applied to the HEPS simulation, augmented by this slack-bus, and a robust response is demonstrated for several peak power conditions. This control strategy and architecture has several direct applications to any airborne power system, from those used in small unmanned aircraft to those proposed for small passenger aircraft.

1.9 Dissertation Road-map

The objective of this section is to provide a high-level perspective on the contents of this document. The research approach is represented visually in Fig. 1.13. Essentially, two parallel experiments are required to address this research question; one to represent the propulsion systems considered and another to represent the hybrid power system.

For the purposes of this research, the aircraft scale is constrained based on the approximate takeoff mass of the aircraft. Here, we will consider only aircraft with masses between 5kg and 1000kg. This restricts the analysis to aircraft from small unmanned systems to light passenger aircraft, and practically restricts powerplant considerations to reciprocating inter-

nal combustion engines. Also, for the purposes of this analysis, only conventional two-stroke and four-stroke engines are considered in the present research effort.

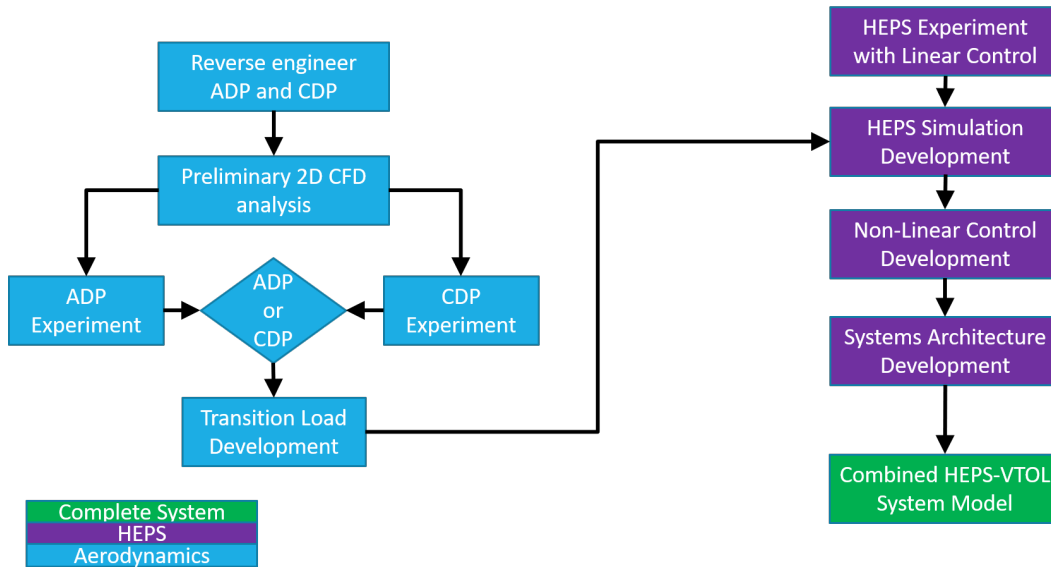


Figure 1.13: Research approach flowchart

In chapter one, the motivations behind the interest in VTOL aircraft are presented, as are the adjacent innovations that make VTOL and distributed propulsion possible. These innovations are set in the context of the relevant academic literature, representing the present state of the art. Finally, the primary original contributions of this work are summarized and present alongside this dissertation road-map.

In chapter two, the results of the ADP wind tunnel experiment are presented in the context of the operating regimes observed in the experimental data. The data acquisition and methods of analysis are presented in Appendix A and Appendix B respectively.

In chapter three, a brief summary is provided for the CDP system and experimental results. Additional discussion, as well as a justification for proceeding with ADP only for the remainder of the analysis is provided as well.

In chapter four, the results from the HEPS experiment are presented. This experiment evaluated the dynamic response characteristics of the HEPS using a linear PID controller. The response characteristics are presented for later use in tuning the HEPS simulation. A detailed discussion of the design and construction of this experiment are included in Appendix C.

In chapter five, the experimental data presented in chapter four are used to develop an accurate, validated model of the experimental HEPS system. In this chapter, the PID control system used in the experiment is duplicated, and the model's dynamic parameters are tuned to accurately approximate the experimental results.

In part one of chapter six, the ADP section data are used to estimate the finite wing performance for a given aircraft configuration. These results are then used to estimate the transition power loading profile (xPLP) for an aborted landing maneuver, consisting of an inbound transition to hover, hover operations, and finally an outbound transition to forward flight.

Given the complex loading profile the HEPS must sustain during transition, significant improvements to the control system are required. These improvements are developed in part two of chapter six. The voltage tracking controller improved using a second order sliding mode controller, the power output of the system is actively tracked, dynamically adaptive voltage modulation is introduced, and a controlled slack-bus is introduced to extend the performance.

In part three of chapter six, the xPLP is applied to the HEPS model with the controls and architecture developed in Part 2. This loading profile is scaled to various levels relative to the MSPT of the system. In all cases, the HEPS response is shown to be robust.

Finally, in chapter seven, the original contributions of this work are discussed in the context of the present state of the art in aerodynamics and power systems. Also, several recommendations are made for how this work might be improved in future efforts as well as how this work may be extended by incorporating additional power generating technologies into the system architecture.

Chapter 2

ADP Experiment Results

2.1 Introduction

The objective of this chapter is to present a summary of the results from the ADP wind tunnel experiment. These results are presented in terms of directional net force and moment coefficients, c_u , c_v , and $c_{mc/4}$. The fan thrust estimates are presented as well, and are resolved into contributions from surface forces on the fan control volume and the momentum flux contributions through the control volume. This data is presented in two contexts as $f(c_p^*|\alpha)$ and $f(\alpha|c_p^*)$. Three distinct operating regimes are identified and discussed in comparison with CFD results. Response surface models are developed for each c_u , c_v , $c_{mc/4}$ and jet power are developed from the data as a function of α and c_p^* .

2.2 Experiment Design and Construction Summary

Given the complexity of the both the CDP and ADP propulsion systems and the computational expense associated with exploring the performance of these systems, an experiment is constructed to enable thorough testing. As has been discussed previously, the ADP propulsion system is a subassembly of the CDP propulsion system. Therefore, construction of an instrumented CDP experiment system would enable testing of both propulsion configurations, Fig. 2.1.

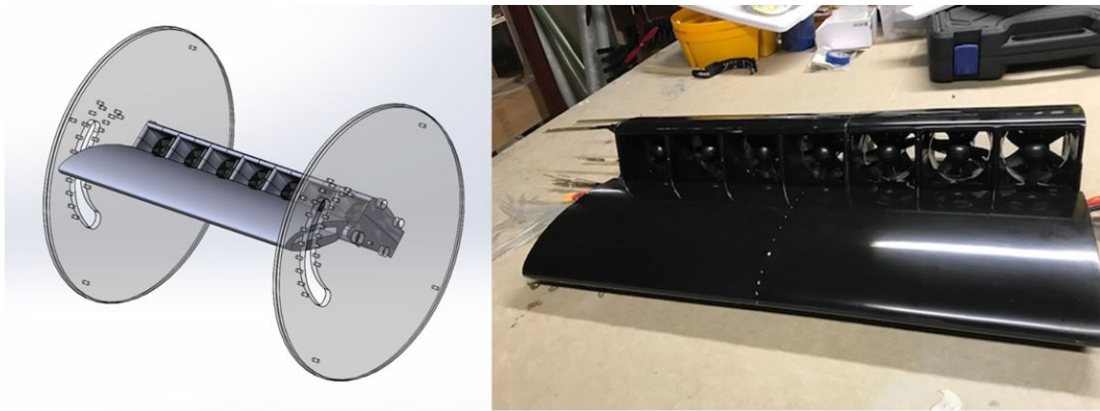


Figure 2.1: Completed ADP/CDP wind tunnel experimental apparatus.

Both the CDP and ADP configurations need to be represented in the construction of a single apparatus. This apparatus is designed to span the test section of the wind tunnel and represent a two-dimensional wing section of the CDP and ADP configurations. This apparatus must therefore be capable of all angles of attack and flap angles encountered by these configurations during normal VTOL operation. As such, both the flap angle and the angle of attack need to be varied.

The basic concept of this installation is that the entire CDP assembly is mounted between two round polycarbonate endplates. These end plates are mounted on a set of bearings

in the wall of the wind tunnel, thereby permitting the angle of the entire assembly to be varied through a 360deg rotation without restriction. Further, the ADP portion of the assembly is fixed to the endplates with the forward wing section able to move with respect to the flap. In this manner, all required operation conditions can be achieved with minimal complexity. Indexed pin locations are provided to align and secure the forward wing at 10deg intervals relative to the flap from 0 to 90 degrees. The extreme degree of flow turning under these conditions required that a dedicated low speed wind tunnel facility be constructed to facilitate the experiment. The design of this tunnel is shown in Fig. 2.2.

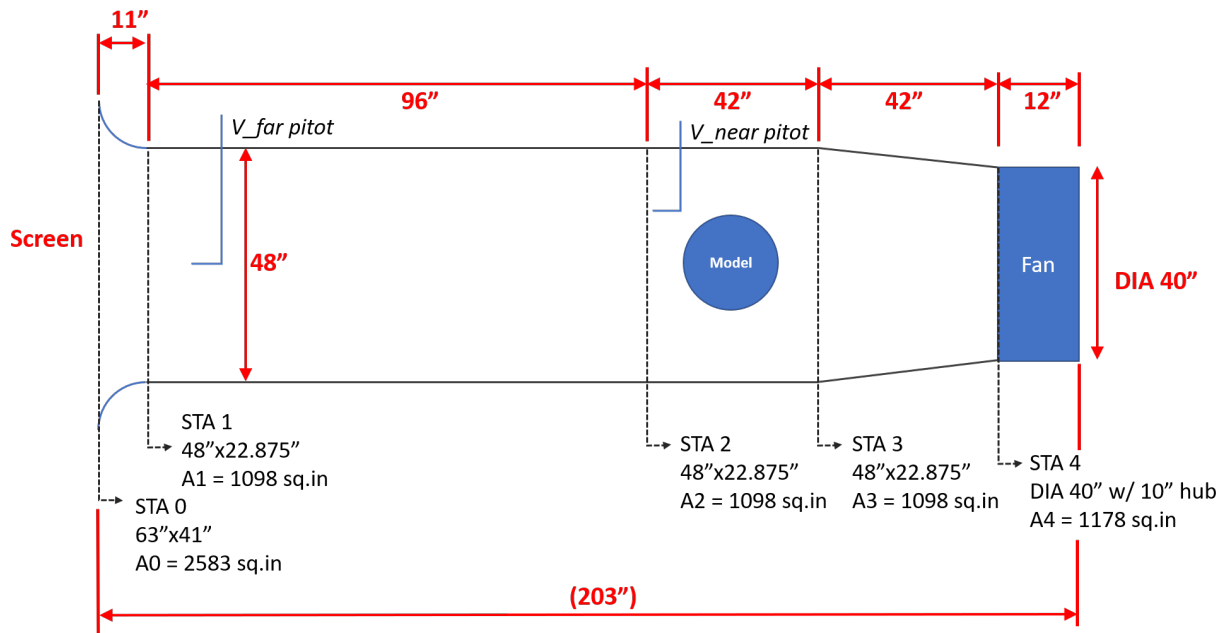


Figure 2.2: Completed ADP/CDP wind tunnel facility design.

The precise and complex geometries of the ducted fan flap assembly requires that the housing parts be machined using, at a minimum, a 3-axis CNC machine. A 3-axis CNC router was available for the construction of this experiment, and as such, the materials of construction needed to be compatible with this machine and well suited for use in the experiment. As the manufacturing equipment available was compatible with soft materials such

as wood, tooling foams and plastics, the list of potential materials was limited. Several critical materials attributes were identified to ensure both compatibility with the manufacturing process as well as the end use in the experiment. Ultimately, the experimental apparatus is machined from high density PVC foam due to its low cost and excellent machinability.

2.3 Data Acquisition and Analysis Summary

The ADP wind tunnel experiment spans the entire wind tunnel test section and is therefore assumed to represent a two-dimensional, infinite-span, wing section. The experimental apparatus is fitted with an array of static pressure taps coinciding with the vertical center-plane of the wind tunnel test section. Since the flow is two-dimensional, it is assumed that the pressure distribution captured by these static pressure taps is representative of the pressure distribution at all wing stations. Additionally, an array of stagnation pressure measurements are taken at the outlet of one the embedded fans. Detailed descriptions of the data acquisition and analysis processes are provided in Appendix A and Appendix B respectively.

The aerodynamic forces on the system are computed from of the integrated static pressure distribution taken from the static pressure taps, as well as a control volume analysis of the fan duct based on the stagnation pressure distribution measured at the fan outlet. The inlet conditions are estimated from the wind tunnel freestream measurements, as well as the inlet static pressure conditions measured by the wall static ports.

The wind tunnel model geometry is well represented numerically by the array of static pressure ports installed in the model. This is shown in Fig. 2.3.

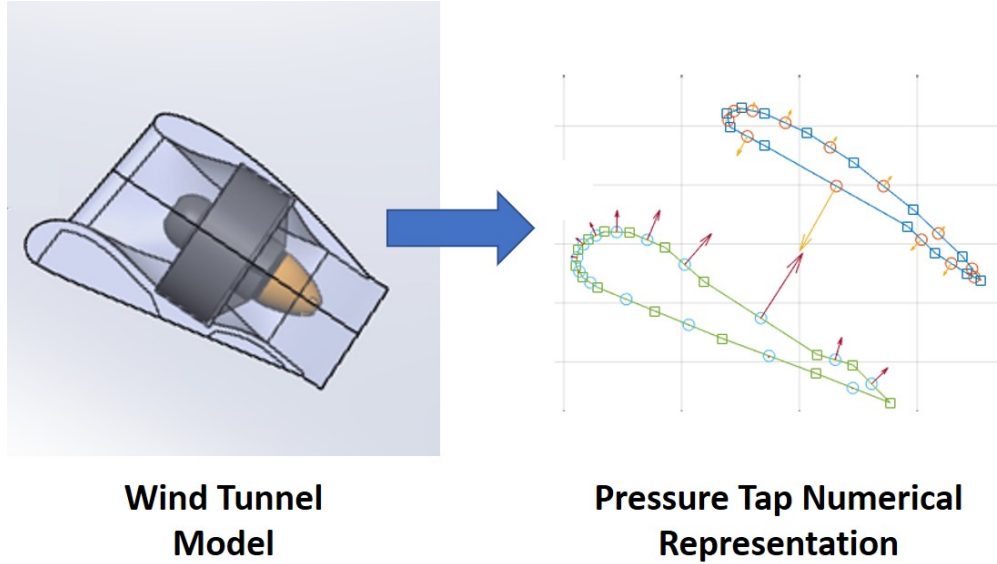


Figure 2.3: ADP system pressure port numerical representation

2.4 Data Summary

The ADP experiment consists of only the integrated propulsion assembly, as shown in Fig. 2.4. In this system, an array of axial fans are integrated into a stacked bi-wing configuration whereby the upper and lower wings form the boundaries of the fan duct. The ducts themselves proceed from rectangular to round and back to rectangular from inlet to outlet. In this manner, circular axial fans can be integrated into the assembly with acceptable blade tip clearance.

As discussed previously, the net forces acting on the ADP wind tunnel experiment are of primary concern. This experiment spans the entire wind tunnel during testing and will therefore be treated as a two-dimension wing during this experiment.

The net forces on this system are due to the integrated static pressure distribution around the aerodynamic surfaces, and from the surfaces forces and momentum flux acting on a control volume defined around the fan as shown in Fig. 2.5.

For all cases, the resultant force from the fan is assumed to act along the rotational axis of the fan. Further, the static pressure distribution around the aerodynamic surfaces are taken about the center-plane of the wind tunnel model. Given the assumption of nominally two-dimensional flow, this is assumed to represent the flow at all stations along the span of the model. Also, fan #3's outlet pressure distribution is well instrumented. Since each fan is identical and calibrated to the same input control signal, the data from this fan is assumed to be representative of the performance of all fans in the model.

For applications in VTOL aircraft, the ADP system must operate at all conditions between cruise and hover. This implies that the ADP system will experience conditions from $\alpha = 0$ deg to $\alpha = 90$ deg during all typical operations. As a result, an array of possible conditions across this operating range must be explored in order to fully characterize ADP performance in a VTOL application.

Typically, angle of attack α is increased in 9 deg increments from cruise condition at $\alpha = 0$ deg to hover $\alpha = 90$ deg. In some case, finer increments are applied where changes in behavior are observed.

Here it is convenient to recall the definition of the dimensionless parameter

$$c_p^* \equiv \frac{\Delta P_{fan}}{P_{dyn\infty}} \quad (2.1)$$

This parameter is derived from dimensional analysis where power is included in the dimensional group defining the net forces and moment on this system.

$$c_p^* = \frac{P_{T_{out}} - P_{T_{in}}}{P_{dyn\infty}} = \frac{P_{T_{out}}^{gauge}}{P_{dyn\infty}} = \frac{P_{dyn_{out}} + P_{s_{out}}}{P_{dyn\infty}} \quad (2.2)$$

Since the free-stream stagnation pressure is the gauge reference pressure, $P_{s_{out}} + P_{dyn_{\infty}} = P_{T_{in}} = 0$, therefore,

$$P_{s_{out}} = -P_{dyn_{\infty}} = -1/2\rho V_{\infty}^2 \quad (2.3)$$

$$c_p^* = \frac{P_{dyn_{out}}}{P_{dyn_{\infty}}} - \frac{P_{dyn_{\infty}}}{P_{dyn_{\infty}}} \quad (2.4)$$

$$c_p^* = \frac{V_{out}^2}{V_{\infty}^2} - 1 \quad (2.5)$$

These relationships will be used for delineating between the different operating regimes of the ADP system throughout its flight regime.

Consider the ideal jet power, \underline{P}

$$\underline{P} = Q_{fan} \Delta P_{fan} = 1/2\rho A_{fan} V_{fan}^3 \quad (2.6)$$

Since the flow area change from the fan to the outlet is small and the flow is incompressible, then by continuity the velocity at the plane of the fan is approximately equal to the velocity at the duct outlet.

$$V_{fan} \approx V_{out} \quad (2.7)$$

So the jet ideal power is proportional to the cube of the outlet velocity. This approximation is well supported by the data in the aerodynamic cruise regime and the powered lift regime, which will be discussed in detail later in this chapter.

$$\underline{P} \propto V_{out}^3 \quad (2.8)$$

ADP Experiment Summary Table			
Angle of Attack, deg	Input Power Range, W	Observed Range	c_p^* Operating Regime
$\alpha = 0.0$	0 to 980	-1.8 to 8.7	Aero-Cruise
$\alpha = 4.5$	0 to 930	0.2 to 9.3	Aero-Cruise
$\alpha = 9.0$	0 to 800	-0.6 to 8.5	Aero-Cruise
$\alpha = 18.0$	0 to 800	-1.9 to 8.8	Transitional 1
$\alpha = 27.0$	0 to 980	-1.1 to 8.4	Powered Lift
$\alpha = 36.0$	0 to 950	-1.3 to 8.4	Powered Lift
$\alpha = 45.0$	0 to 889	-1.3 to 8.4	Powered Lift
$\alpha = 54.0$	0 to 800	-1.3 to 7.2	Powered Lift
$\alpha = 63.0$	0 to 925	-3.4 to 4.7	Transitional 2
$\alpha = 67.5$	0 to 900	-3 to 6.2	Transitional 2
$\alpha = 72.0$	0 to 850	-3.8 to 3.5	Hover Break- down
$\alpha = 81.0$	0 to 950	-3.7 to -1.0	Hover Break- down
$\alpha = 90$ deg	0 to 800	-4.6 to -0.7	Hover Break- down

Table 2.1: ADP Experiment Summary Table

Since $c_p^* \propto V_{out}^2$, the jet ideal power is proportional to $c_p^{*3/2}$

$$\boxed{\underline{P} \propto c_p^{*3/2}} \quad (2.9)$$

Further, since c_p^* is the dimensionless group formed from considering that $F_{net}(\underline{P})$, these proportional relationships will hold under conditions where the jet power is the dominant influence on the system for the experimentally determined \underline{P} , c_v , and c_u .

Each condition in this experiment was conducted using a constant wind tunnel fan angular velocity. The tunnel is set to $\omega = 1080rpm \pm 10rpm$, which results in a free stream velocity of $\sim 9.0m/s$. The free stream velocity is a function also of the power applied to the model, as well as the operating condition of the model. Therefore, wind tunnel corrections

are applied to the measured free-stream velocity in order to properly estimate the test section velocity.

The experimental conditions investigated here can be resolved into three categories based on the characteristic behaviors of the vertical and horizontal force coefficient responses to increasing in propulsion c_p^* as well as the observed maximum c_p^* that for a given maximum power input to the system.

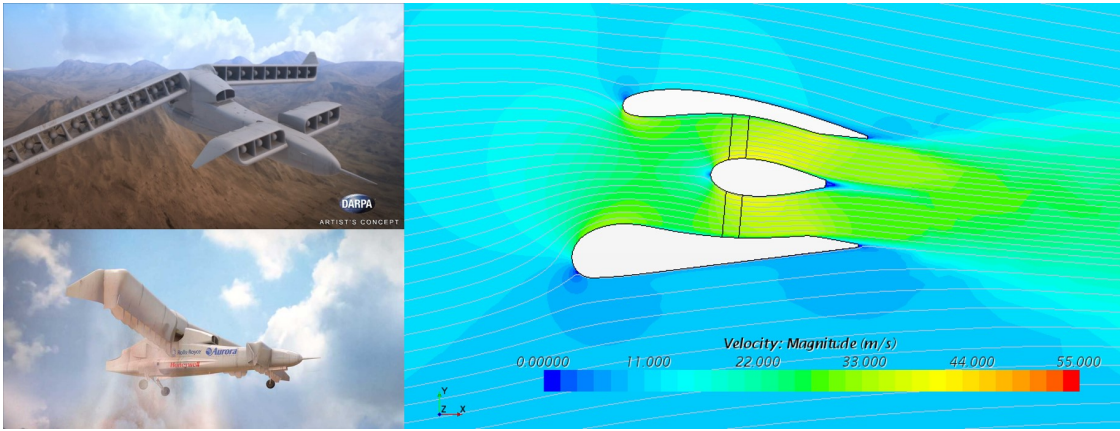


Figure 2.4: The ADP system consists of axial fans embedded into bi-wing configuration whereby the upper and lower wings comprise the duct boundaries for each fan.

- **Aerodynamic Cruise Regime (ACR):** These conditions are characterized by the behaviors

$$c_u \propto c_p^*$$

and

$$\underline{P}_{jet} \propto c_p^{*3/2}$$

This is observed when $0 \text{ deg} \leq \alpha \leq \sim 18 \text{ deg}$, where $\alpha \approx 18 \text{ deg}$ is the upper limit of this condition.

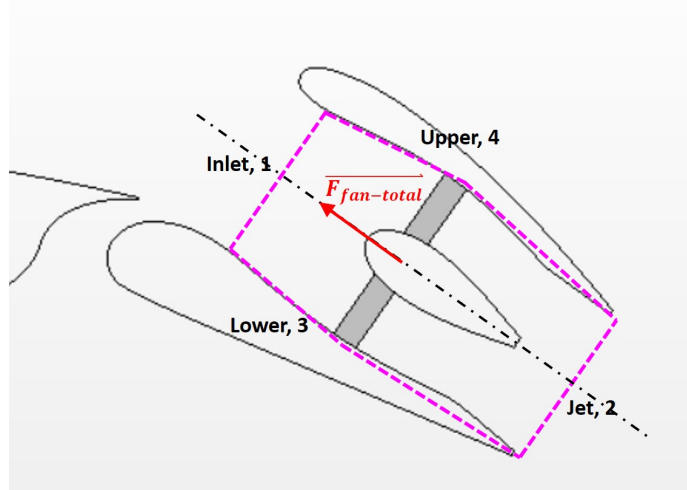


Figure 2.5: The control volume is defined as having the inlet boundary parallel to the outlet boundary, and perpendicular to the fan axis of rotation. The lateral boundaries are drawn along the inner surfaces of upper and lower fan duct.

- **Powered Lift Regime (PLR):** These conditions are characterized by the behavior

$$c_v \propto c_p^*$$

and

$$\underline{P}_{jet} \propto c_p^{*3/2}$$

This is observed when $\sim 18 \text{ deg} \leq \alpha \leq \sim 63 \text{ deg}$, whereupon the maximum c_p^* that is achieved for a given maximum input power begins to decrease.

- **Hover Breakdown Regime (HBR):** These conditions are characterized by the breakdown of the previous linearly proportional relationships between c_u , c_v and c_p^* as well as the breakdown of $\underline{P}_{jet} \propto c_p^{*3/2}$. This is observed where $\alpha \geq 72 \text{ deg}$ though

the transition out of PL and into HB appears to be quite broad, essentially from $\sim 63 \text{ deg} \leq \alpha \leq 72 \text{ deg}$.

Each of the operating regimes will be discussed in greater detail later in this chapter.

2.5 Aerodynamic Cruise Regime

- **Defining Characteristics**

- vertical force coefficient, $c_u \propto c_p^*$, for $c_p^* \geq 0$
- jet power, $\underline{P}_{jet} \propto c_p^{*3/2}$, for $c_p^* \geq 0$

- **Observed Range**, $0 \text{ deg} \leq \alpha \leq \sim 18 \text{ deg}$

The characteristic behaviors that define this regime are most readily observed when examining the results as a function of the parameter c_p^* . Here, summary data is presented for each condition determined to meet the criteria for operating in the ACR. The force and moment coefficients are presented along with a summary of the electrical input power and computed jet power.

2.5.1 c_v - the vertical net force coefficient

The force coefficient c_v is analogous to the commonly used aerodynamic force coefficient c_l , in that it is a non-dimensional expression of the vertical force component acting on a two-dimensional lifting system. The critical distinction in this case is that c_v includes contributions from the embedded propulsion system, both in terms of fan thrust in the vertical direction, and in terms of augmented circulation about the system.

For cases from $\alpha = 0$ deg to $\alpha = 9$ deg, the square root behavior of the $c_v(c_p^*|\alpha)$ is readily observed. For $\alpha = 18$ deg, this behavior is less evident, with the system transitioning between the ACR and PLR, as shown in Fig. 2.6. In all cases, c_v is observed to follow the power law relationship described above, shown in Fig. 2.7.

2.5.2 c_u - the horizontal net force coefficient

The force coefficient c_u is analogous to the aerodynamic force coefficient c_d , in that it is a non-dimensional expression of the horizontal force component acting on a two-dimensional lifting system. Here again, the coefficient c_u captures contributions from propulsion system. Because of these contributions, in the ACR, c_u is typically negative for most values of c_p^* . Here, negative values indicate a net thrust force as opposed to a net drag force, as shown in Fig. 2.6.

Because the total thrust on the system is linearly proportional to c_p^* , the relationship $c_u(c_p^*|\alpha)$ is seen to be approximately linear for all cases in the ACR.

The case where $\alpha = 18$ deg appears to deviate the most from this linear behavior. This is likely due to the onset of flow separation from the upper surface of the ADP fan duct and the associated increased prevalence of aerodynamic pressure drag on the net horizontal force on the system.

2.5.3 $c_{m_{c/4}}$ - the moment coefficient

The moment coefficient $c_{m_{c/4}}$ is a dimensionless expression of the moment about the quarter chord of the ADP lower surface. The moment in these cases is due primarily to fan

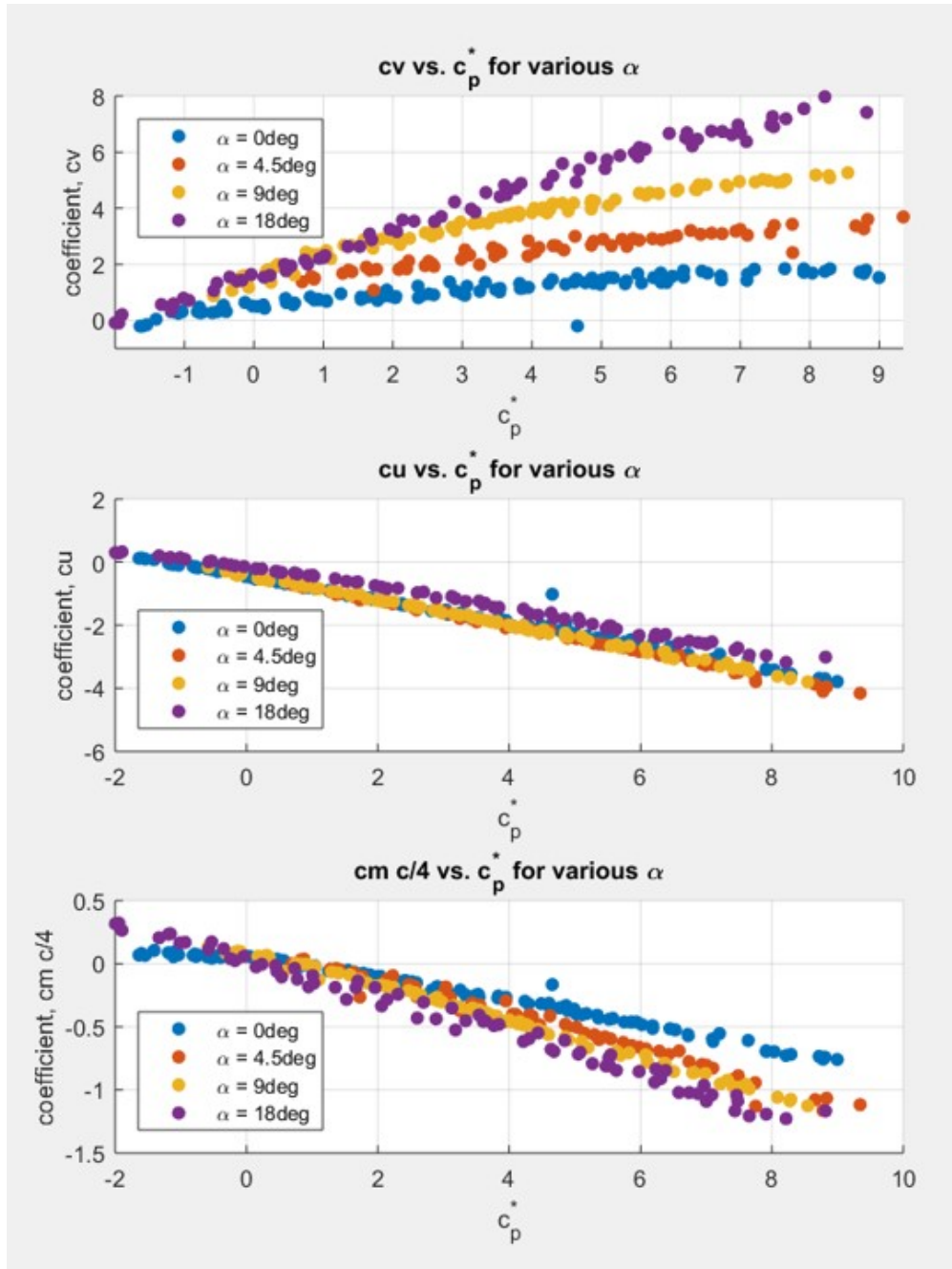


Figure 2.6: Summary of the ADP force coefficients, including aerodynamic and fan-derived contributions vs. c_p^* , for cases from $\alpha = 0$ deg to $\alpha = 18$ deg.

thrust, through contributions from the integrated static pressure distributions around the aerodynamic surfaces play a larger role here than in the c_u case.

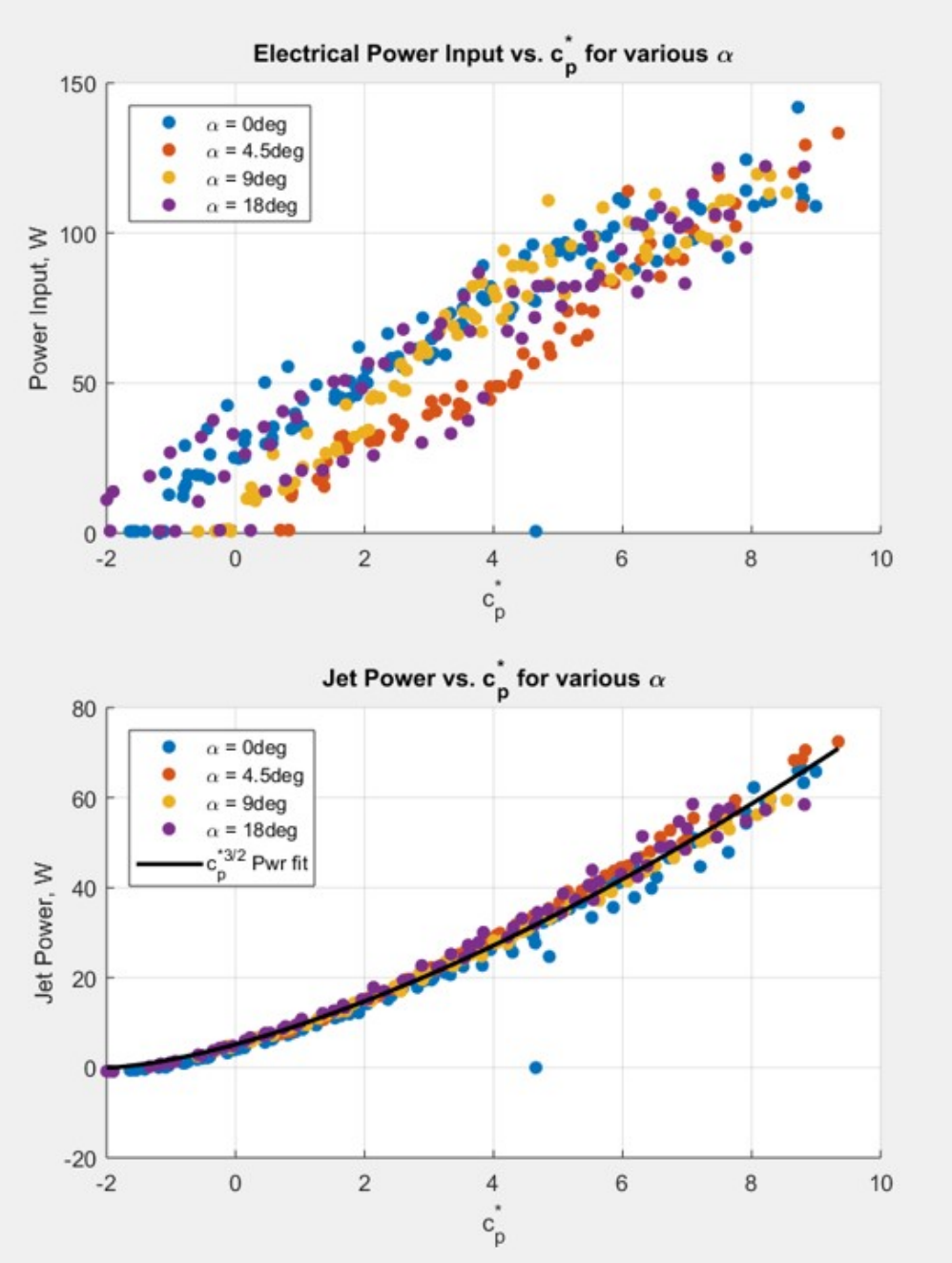


Figure 2.7: Summary of the ADP electrical input power and jet power vs. c_p^* , including aerodynamic and fan-derived contributions for cases from $\alpha = 0\text{ deg}$ to $\alpha = 18\text{ deg}$.

Here negative values indicate a net nose-down pitching moment about the reference point, with larger negative moments associated with higher c_p^* , as shown in Fig. 2.6.

2.5.4 Power Input and Jet Power

As shown in Fig. 2.7, the electrical input power increases approximately linearly with increasing c_p^* , though the results show considerable scatter in the data. The resulting jet ideal power \underline{P} however is tightly grouped and reflects the characteristic behavior of the ACR. The following fit function was applied to the data in the ACR

$$f(c_p^*|\alpha = [0, 4.5, 9, 18] \text{ deg}) = A * (c_p^* - \min(c_p^*))^b \quad (2.10)$$

The detail of this fitting function are summarized here:

- the mean of A is $\bar{A} = 1.828$ with the 95% confidence interval(1.7, 1.957)
- the mean exponent b is $\bar{b} = 1.506$ with the 95% confidence interval (1.473, 1.539)
- $R^2 = 0.98$

The relative scatter in the electrical power data is likely due to short term fluctuations in electrical power as captured by the 400Hz data logging system. The jet power estimates are calculated primarily from manometer panel data, which has significant viscous damping and therefore acts as a low pass filter, attenuating the appearance of any fluctuation whose period is ≤ 1 or 2 sec.

2.5.5 CFD Results in the ACR

Significant insight can be gained by examining the CFD analysis of a two-dimensional ADP system. In this context the CFD analysis will be used to illustrate the dominant aerodynamic phenomena governing the ADP system in the ACR. In order to examine both the CFD

analysis and experimental data in the same context, we must establish a methodology for scaling between them.

The reference chord length for the CFD case and the wind tunnel ADP model are identical.

$$c_{CFD_{ADP}} = c_{exp_{ADP}} = 0.153m \quad (2.11)$$

The vertical spacing between the upper and lower duct surfaces are also identical. Since the ADP model spans the entire wind tunnel test section, it can reasonably be considered a two-dimensional experimental representation of the system. The primary difference between these systems is that effective flow area of the fan-section per unit span are significantly different. This means that for a given \dot{m} , the values of c_p^* will be different. Since the data in this experiment is presented in terms of c_p^* and α , we need to develop a method for scaling c_p^* between the experimental data and CFD results. Since this is a two-dimensional simulation and an effectively two-dimensional experiment, α will not require additional scaling.

Angle of attach α is affected somewhat by the constraints imposed by the model operating in a confined stream tube. The effective angle of attack is increased from geometric angle of attack due to induced up-wash caused by the confinement of the test section stream-tube within the tunnel walls, which are not present in the CFD simulation.

In the CFD analysis, all quantities are computed in terms of unit depth, $d = 1m$. The resulting flow area through the fan per unit depth is

$$A_{fan_{CFD}} = 0.0466m^2 \quad (2.12)$$

In comparison, the total flow area of the fans in the experiment per unit depth is

$$A_{fan_{exp}} = 0.0367m^2 \quad (2.13)$$

Since the flow is incompressible and assuming $V_{out} \approx V_{fan}$, by continuity we have

$$\frac{V_{out_{CFD}}}{V_{out_{exp}}} = \frac{A_{fan_{exp}}}{A_{fan_{CFD}}} = 0.787 \quad (2.14)$$

Since it has been previously established in this chapter that, in the PLR

$$c_p^* \propto c_v \quad (2.15)$$

We can say that

$$\frac{c_{p_{CFD}}^*}{c_{p_{exp}}^*} \propto \frac{c_{v_{CFD}}}{c_{v_{exp}}} \quad (2.16)$$

Therefore, the CFD analysis can be compared directly to the experimental data on the basis of the similarity relationship between c_p^* in each case.

$$\boxed{c_{p_{exp}}^* \sim c_{p_{CFD}}^*} \quad (2.17)$$

Since the similarity of c_p^* is used as the basis for comparing the CFD results to experimental data, the similarity in the outlet velocity is implied as well, based on the control volume in Fig. B.9, and continuity, the ratio of the mass flow rate through the control volume in the experiment to the mass flow rate through a similar control volume in the CFD

analysis is

$$\frac{\dot{m}_{exp}}{\dot{m}_{CFD}} = \frac{A_{fan_{exp}}}{A_{fan_{CFD}}} = 0.787 \quad (2.18)$$

Since the thrust in the ACR is dominated by the fan jet, the force coefficient contribution from the fan in the CFD analysis should be scaled according to this ratio to accurately represent the thrust in the experimental case.

Recall that the net force on this system has contributions from both the static pressure distribution around the wing as well as forces due to the pressure and momentum flux calculated for the fan control volume, as do the coefficients in the vertical and horizontal directions

$$F_{total} = F_{aero-surfaces} + F_{pres-CV} + F_{support-CV} \quad (2.19)$$

$$C_{u_{total}} = C_{u_{aero-surfaces}} + C_{u_{pres-CV}} + C_{u_{support-CV}} \quad (2.20)$$

$$C_{v_{total}} = C_{v_{aero-surfaces}} + C_{v_{pres-CV}} + C_{v_{support-CV}} \quad (2.21)$$

The force due to the pressures on the control volume are proportional to the areas of the inlet and outlet surfaces

$$F_{pres-CV} \propto A_{1,2} \quad (2.22)$$

Also, the force due to the momentum flux through the control volume is proportional to the mass flow through the volume, given similar c_p^* .

$$c_{u_{scl}} \approx 0.787(c_{u_{pres-CV,CFD}} + c_{u_{support-CV,CFD}}) = 0.787c_{u_{CV,CFD}} \quad (2.23)$$

$$c_{v_{scl}} \approx 0.787(c_{v_{pres-CV,CFD}} + c_{v_{support-CV,CFD}}) = 0.787c_{v_{CV,CFD}} \quad (2.24)$$

for an example case where $\alpha = 0$ deg, $c_{u_{CV,CFD}} = -2.46$. When this scaling relationship is applied to the data for this case, we have

$$c_{u_{scl}} \approx 0.787 * -2.46 = -1.91 \quad (2.25)$$

which closely approximates the measured value of $c_u = -1.82$ from the experiment.

Additionally, rather than comparing the CFD data to a fitted curve passing through the experimental data, the comparison is made using the mapping $c_{p_{CFD}}^* \rightarrow c_{p_{nearest}}^*$, the nearest measured data point in the relevant set of experimental data, as shown in Table 2.2.

The behavior of the CFD model compared to the experimental system can be summarized as follows:

The CFD analysis in the ACR are set up to enforce $\dot{m} = 1kg/s$ through the fan actuator surfaces, as shown in Fig. 2.8. This is accomplished within Star-CCM+ by applying and controlling an additional body force term acting normal to the fan actuator surface, until the desired mass flow is reached through each surface. This is measured in this analysis as $c_p^* \geq 0$. In the ACR this body force results in $c_p^* \approx 3.55$. For all cases in this regime, c_p^*

ADP Experiment Summary Table - ACR			
Angle of Attack	$c_{PCFD}^* \rightarrow \text{nearest}[c_{pexp}^*]$	$c_{v_{scl}}, c_{u_{scl}}$, from CFD	c_v, c_u , from Exp.
$\alpha = 0$ deg	3.52→3.82	$c_v = 1.27,$ $c_u = -1.91$	$c_v = 1.32,$ $c_u = -1.82$
$\alpha = 9$ deg	3.58→3.54	$c_v = 3.20,$ $c_u = -1.86$	$c_v = 3.69,$ $c_u = -1.86$
$\alpha = 18$ deg	3.55→3.61	$c_v = 4.25,$ $c_u = -1.60$	$c_v = 4.42,$ $c_u = -1.34$

Table 2.2: ADP Experiment Summary Table - ACR

remains nearly constant, indicating that the additional body force required to achieve the target \dot{m} through the fan does not vary significantly in this regime.

CFD Results $\alpha = 0$ deg

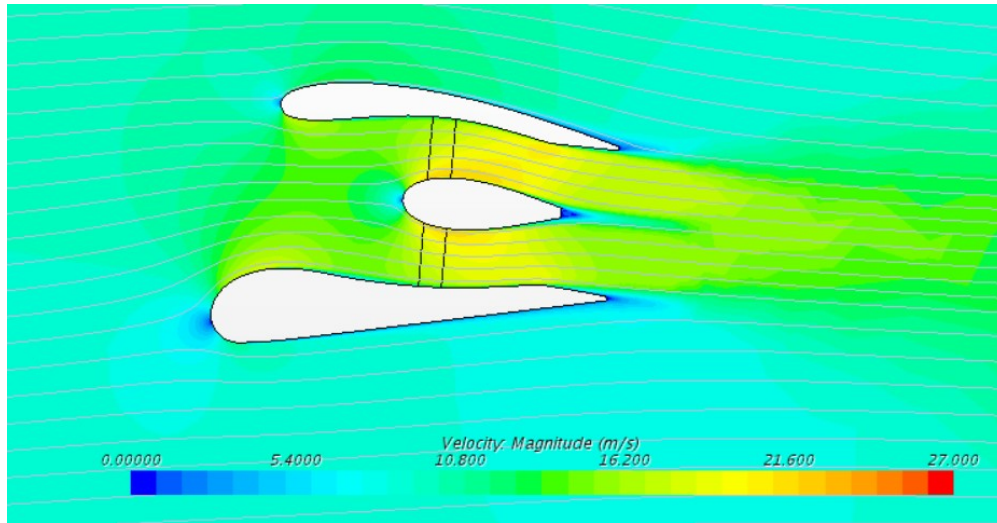


Figure 2.8: Contours of velocity magnitude for ADP where $\alpha = 0$ deg and $c_p^* \approx 3.52$.

In this case, where $\alpha = 0$ deg, the flow around the ADP system is clean. The wake behind the aerodynamic surfaces is filled in by the fan jet. Here where $c_p^* \geq 0$, the system is producing a net forward thrust. In this case, the CFD analysis accurately predicts the

measured vertical and horizontal forces on the ADP system. The corrections based on the area and mass flow rate ratios between the CFD model and the experiment are shown here to enable this comparison. This corroborates both the capability of a simple two-dimensional CFD model to predict the performance of the ADP system at $\alpha = 0$ deg, as well as the validity of the thrust estimation methodology presented previously in this dissertation.

CFD Results $\alpha = 9$ deg

At $\alpha = 9$ deg, the flow is beginning to separate from the trailing edge of the suction surface of the upper wing, as show in Fig. 2.9. Otherwise the flow through the fan duct remains fully attached to both the upper and lower surfaces of the fan duct. Again, the CFD shows excellent correlation with the experimental data when the mass flow rate and area ratio corrections are applied.

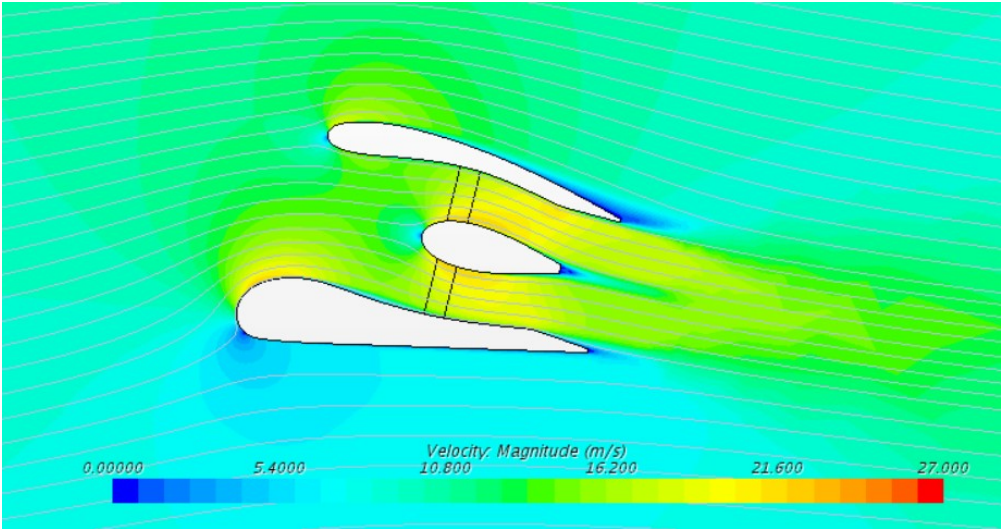


Figure 2.9: Contours of velocity magnitude for ADP where $\alpha = 9$ deg and $c_p^* \approx 3.58$.

CFD Results $\alpha = 18$ deg

At $\alpha = 18$ deg, the flow is fully separated from the suction surface of the upper wing, as shown in Fig. 2.10. This likely accounts for the deviation of the experimental $c_u(c_p^*)$ data at this condition deviating somewhat from the linear response expected. Also, the flow is beginning to separate from the inlet lip of the lower wing. This separated region is expected to expand with further angle of attack increases. As with the other ACR cases presented, the CFD model shows excellent correlation with the experimental data when the mass flow rate and area ratio corrections are applied.

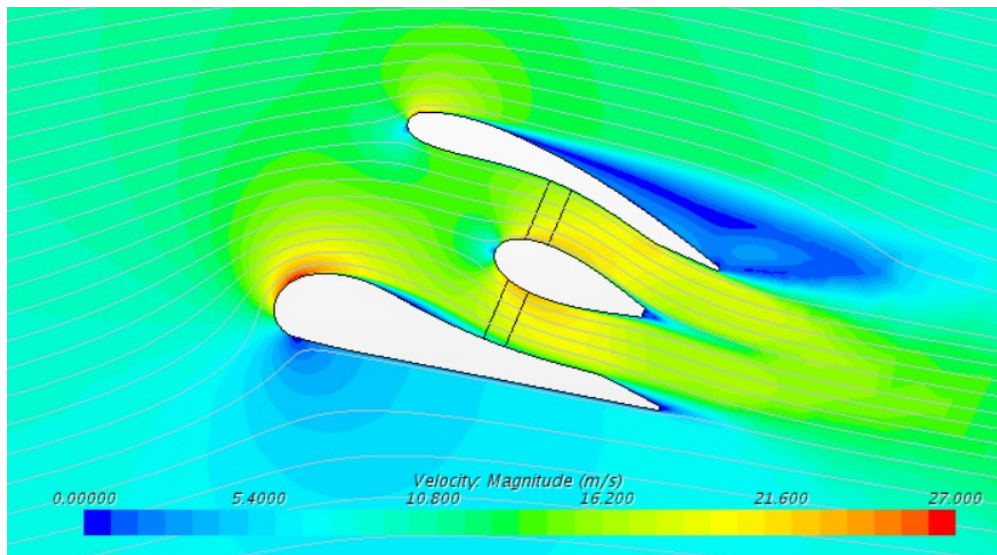


Figure 2.10: Contours of velocity magnitude for ADP where $\alpha = 0$ deg and $c_p^* \approx 3.55$.

2.6 Powered Lift Regime

- Defining Characteristics

- vertical force coefficient, $c_v \propto c_p^*$, for all c_p^*

– jet power, $Pwr_{jet} \propto c_p^{*3/2}$, for $c_p^* \geq 0$

- **Observed Range**, $27 \text{ deg} \leq \alpha \leq \sim 63 \text{ deg}$

The powered lift regime develops between $\alpha = 27 \text{ deg}$ and $\alpha = 63 \text{ deg}$ and is characterized by a linear proportionality between c_p^* and c_v .

2.6.1 c_v behavior - the vertical force net coefficient

Here the behavior of $c_v(c_p^*|\alpha)$ is linear for $\alpha = [27, 36, 45, 54] \text{ deg}$. Therefore since this proportionality is maintained for these cases, we can assert that the jet power is the dominant contribution to the net vertical force, both through fan thrust and augmented circulatory lift. Additionally, there is no change in the slope of the $c_v(c_p^*)$ curve with increasing α from 27 deg to 54 deg. Rather, the curve is simply shifted vertically for each 9 deg increment from $\alpha = 27 \text{ deg}$ to $\alpha = 45 \text{ deg}$, with a small decrease when $\alpha = 54 \text{ deg}$.

2.6.2 c_u behavior - the horizontal force net coefficient

Here the behavior of $c_u(c_p^*|\alpha)$ is approximately linear for $\alpha = [27, 36, 45] \text{ deg}$ with a departure from this behavior for $\alpha = 54 \text{ deg}$. Unlike the cases presented in the ACR, for cases in PLR, the slope of $c_u(c_p^*)$ is increasing with each successive increase in α . Positive c_u 's are increasingly prevalent in this regime and ultimately, where $\alpha = 54 \text{ deg}$, $c_u(c_p^*) \approx 2$ for all measured c_p^* , indicating that the influence of the jet power on horizontal force is significantly diminished.

2.6.3 $c_{m_{c/4}}$ - the moment coefficient

The behavior of $c_{m_{c/4}}(c_p^*|\alpha)$ is approximately linear for $\alpha = [27, 36, 45, 54]$ deg. The slope of this response does not change significantly with increasing α , and the values of $c_{m_{c/4}} \leq 0$ for $c_p^* \geq 0$, indicating that a nose down pitching moment is maintained throughout the PLR.

2.6.4 Power Input and Jet Power

As shown in Fig. 2.12, the electrical input power increases approximately linearly with increasing c_p^* , though the results show considerable scatter in the data. The resulting jet power however is tightly grouped and reflects the characteristic behavior of the ACR. The following fit function is applied to the data in the ACR

$$f(c_p^*|\alpha = [27, 36, 45, 54] \text{ deg}) = A * (c_p^* - \min(c_p^*))^b \quad (2.26)$$

The detail of this fitting function are summarized here:

- the mean of A is $\bar{A} = 1.821$ with the 95% confidence interval(1.705, 1.937)
- the mean exponent b is $\bar{b} = 1.515$ with the 95% confidence interval (1.484, 1.545)
- $R^2 = 0.98$

2.6.5 CFD Results in the PLR

The CFD analysis in the PLR are specified to enforce $\dot{m} = 1kg/s$ through the fan actuator surfaces, as in the previous ACR cases. Here however, the additional body force imposed on

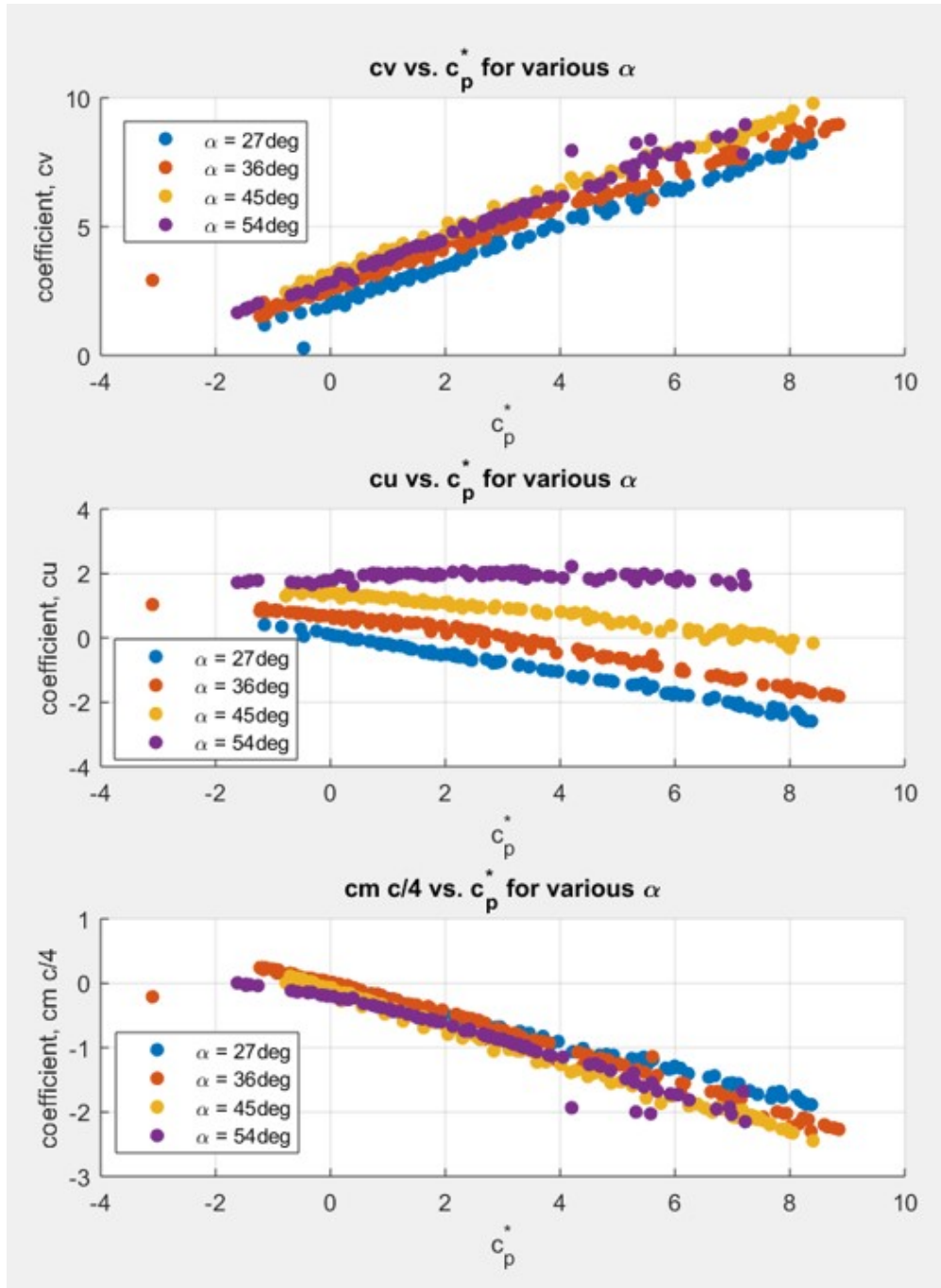


Figure 2.11: Summary of the ADP force coefficients, including aerodynamic and fan-derived contributions vs. c_p^* , for cases from $\alpha = 27deg$ to $\alpha = 54deg$.

the flow at the fan actuator boundary must increase significantly in order to maintain the target \dot{m} through the fan actuator.

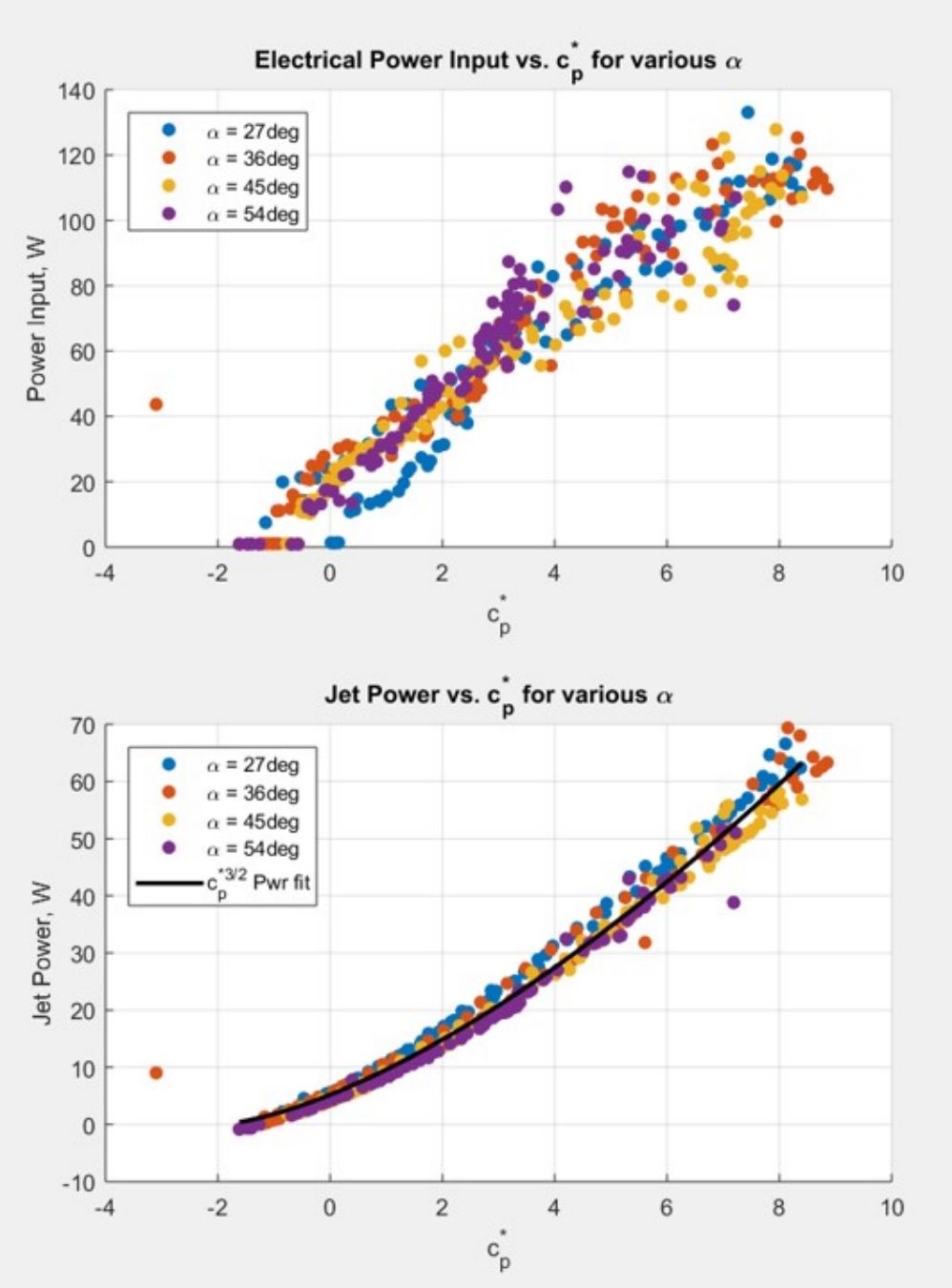


Figure 2.12: Summary of the ADP electrical input power and jet power vs. c_p^* , including aerodynamic and fan-derived contributions for cases from $\alpha = 27$ deg to $\alpha = 54$ deg.

Each case included in the PLR is discussed in this section since there is a notable departure in the behavior of $c_u(c_p^*|\alpha)$ in the CFD model relative to the experimental data for

cases where $\alpha = 45$ deg and $\alpha = 54$ deg. Here, the CFD model initially appears to predict a dramatically lower net drag force than the experimental model when all surfaces, including the 2-D fan hub are included in the CFD coefficient estimates.

In the case where $\alpha = 45$ deg, the predicted c_u is experimentally measured to be $c_{u_{exp}} = 0.75$, while the CFD predicts a net thrust $c_{u_{CFD}} = -0.21$. A larger discrepancy is observed where $\alpha = 54$ deg, with the measured and CFD predicted values are $c_{u_{exp}} = 1.98$ and $c_{u_{CFD}} = 0.17$ respectively. However, the presence of the inlet separation induces a negative incidence on the 2-D fan-hub approximation, thereby breaking the symmetry that has existed about this body up to this point.

Though the 2-D hub occupies approximately the same ratio of the flow area through the fan duct as does the real fan hub, the 2-D hub has an infinite aspect ratio and is therefore able to contribute significantly to the lift and drag forces on the system when experiencing asymmetric loading. Therefore, for cases where $\alpha \geq 45$ deg, this hub geometry is removed from the calculation. Making this adjustment for $\alpha = 45$ deg and $\alpha = 54$ deg yields $c_{u_{CFD}} = 1.49$ and $c_{u_{CFD}} = 2.8$ respectively, with the c_v results in both cases again showing excellent agreement with experimental results.

Conversely, cases where $\alpha = 27$ deg and $\alpha = 36$ deg show excellent agreement between the CFD model and experimental data. This divergence in the estimated c_u coincides with the prevalence of separated flow from the lower inlet lip of the fan duct.

Now, the CFD model appears to over-predict the drag on the system. However this likely due to highly three dimensional surfaces present in the interior of the fan-duct in the experiment. In the CFD case, the effect of the asymmetric pressure loading on the interior of the fan duct are amplified as the CFD model is assumed to be two-dimensional.

ADP Experiment Summary Table - PLR			
Angle of Attack	$c_{pCFD}^* \rightarrow \text{nearest}[c_{pexp}^*]$	c_{vscl}, c_{uscl} , from CFD	c_v, c_u , from Exp.
$\alpha = 27$ deg	3.54→3.46	$c_v = 4.22,$ $c_u = -1.10$	$c_v = 4.61,$ $c_u = -0.90$
$\alpha = 36$ deg	3.83→3.81	$c_v = 5.17,$ $c_u = -0.64$	$c_v = 5.58,$ $c_u = -0.47$
$\alpha = 45$ deg	4.08→3.89	$c_v = 6.67,$ $c_u = 1.49$	$c_v = 6.44,$ $c_u = 0.75$
$\alpha = 54$ deg	5.08→5.14	$c_v = 7.23,$ $c_u = 2.8$	$c_v = 7.30,$ $c_u = 1.98$

Table 2.3: ADP Experiment Summary Table - PLR

For all cases, $c_v(c_p^*|\alpha)$ behavior shows excellent agreement between the CFD analysis and experimental measurements. Here, the experimentally measured c_v values are slightly higher, in some cases, than those predicted by the CFD analysis. This discrepancy can likely be attributed to the discrepancy between the force resulting from two-dimensional asymmetric pressure loading in the CFD case, and the highly three-dimensional fan duct in the experiment. Additionally, recall from the ACR discussion, the comparison is made using the mapping c_{pCFD}^* to $c_{pnearest}^*$, the nearest measured data point in the relevant set of experimental data.

The behavior of the CFD model compared to the experimental system in this regime can be summarized as follows:

CFD Results $\alpha = 27$ deg

The flow for $\alpha = 27$ deg is characterized by the full separation and stall of the suction surface of the upper wing. Also note that very little separation is present from the lower inlet lip of

the fan duct, and as a result, the flow passing through the fan is minimally distorted, with none of the separated region passing through the fan actuator surface as shown in Fig. 2.13.

Further this CFD analysis was run using the URANS solver, as the significant flow separation from the upper wing prevented convergence using the steady state solver. The unsteady case parameters are:

- **Solver:** Star-CCM+ Implicit-Unsteady, 1st-order in time
- **Turbulence Model:** Spalart-Allmaras
- **Time Step:** $\Delta t = 425\mu s$
- **Iterations per Time Step:** 15
- **Convergence:** $\leq 10^{-4}$
- **Flow Time:** 0.17 seconds
- **Comments:** Force and coefficient monitors converged to a constant value after approximately 0.05s of flow time. No periodicity was observed.

CFD Results $\alpha = 36$ deg

The flow for $\alpha = 36$ deg is characterized by the full separation and stall of the suction surface of the upper wing. Again note that although initial separation is present from the lower inlet lip of the fan duct, the flow is re-attached in the vicinity of the fan actuator plane, and as a result, the flow passing through the fan is minimally distorted, with none of the separated region passing through the fan actuator surface as shown in Fig. 2.14.

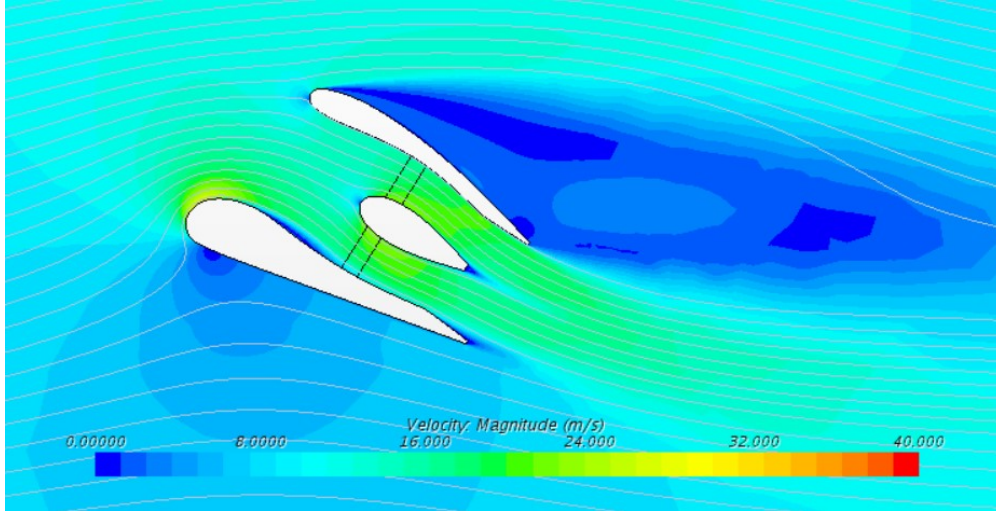


Figure 2.13: Contours of velocity magnitude for ADP where $\alpha = 27$ deg and $c_p^* \approx 3.54$.

Further this CFD analysis was run using the URANS solver, as the significant flow separation from the upper wing prevented convergence using the steady state solver. The unsteady case parameters are:

- **Solver:** Star-CCM+ Implicit-Unsteady, 1st-order in time
- **Turbulence Model:** Spalart-Allmaras
- **Time Step:** $\Delta t = 425\mu s$
- **Iterations per Time Step:** 15
- **Convergence:** $\leq 10^{-4}$
- **Flow Time:** 3.1 seconds
- **Comments:** Force and coefficient monitors converged to a constant value after approximately 0.05s of flow time. No periodicity was observed, although the case was allowed to run for extended flow times.

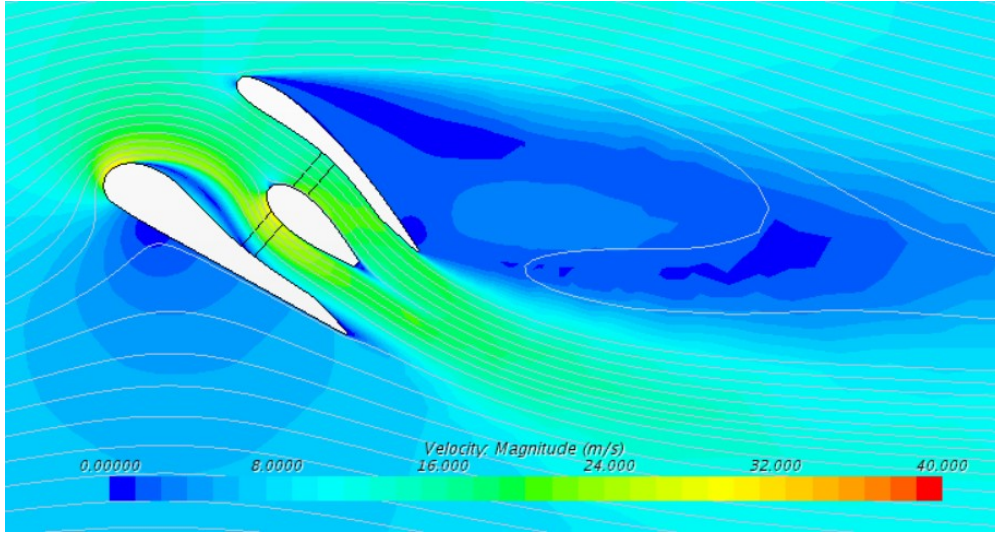


Figure 2.14: Contours of velocity magnitude for ADP where $\alpha = 36$ deg and $c_p^* \approx 3.83$.

CFD Results $\alpha = 45$ deg

The flow for $\alpha = 45$ deg is characterized by the full separation and stall of the suction surface of the upper wing as well as a large separated region developing beyond the lower inlet lip. Here note that this separated region is large and the flow does not re-attach in the vicinity of the fan actuator plane, and as a result, the flow passing through the fan is very distorted, with much of the separated region passing through the fan actuator surface as shown in Fig. 2.15.

This CFD analysis was also run using the URANS solver, as the significant flow separation from the upper wing prevented convergence using the steady state solver. The unsteady case parameters are:

- **Solver:** Star-CCM+ Implicit-Unsteady, 1st-order in time
- **Turbulence Model:** Spalart-Allmaras

- **Time Step:** $\Delta t = 425\mu s$
- **Iterations per Time Step:** 15
- **Convergence:** $\leq 10^{-4}$
- **Flow Time:** 3.1 seconds
- **Comments:** Large periodic variations are observed for all coefficients and parameters monitored.

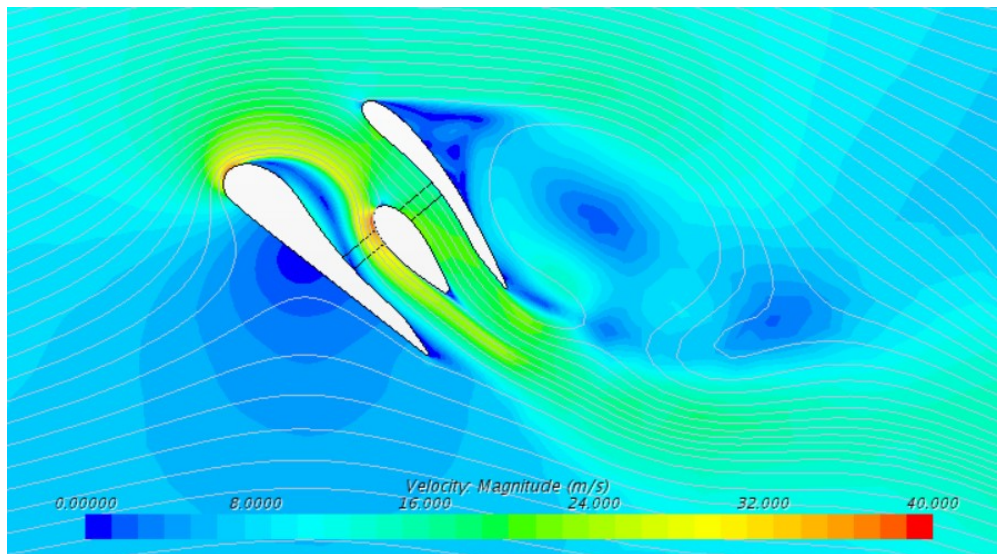


Figure 2.15: Contours of velocity magnitude for ADP where $\alpha = 45 \text{ deg}$ and $c_p^* \approx 4.08$.

This strong periodicity is observed in both the aerodynamic surface force contributions as well as the fan force contributions as shown in Fig. 2.16 and Fig. 2.19. This fundamental frequency of this oscillation is measured to be $f_0 = 18.2Hz$ with a higher harmonic observed in the behavior of the fan force contribution. This is estimated to be $f_2 \approx 2f_0 \approx 36.4Hz$. These are most likely due to the development of a periodic vortex shedding phenomenon developing between $\alpha = 36 \text{ deg}$ and $\alpha = 45 \text{ deg}$ in the CFD simulation. These frequencies

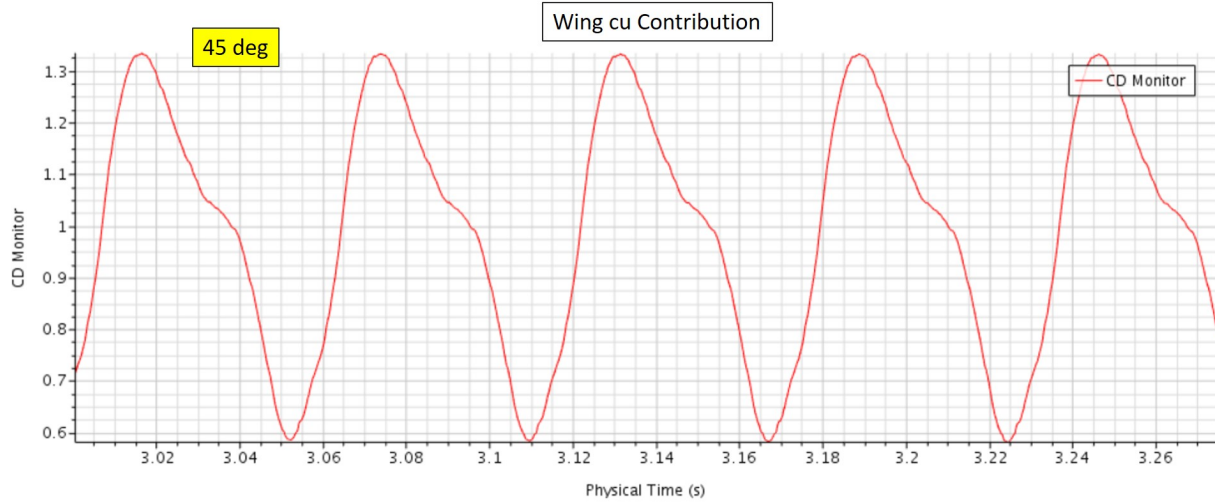


Figure 2.16: Time-series plot of $c_{u_{pres}}$, the integrated static pressure contribution to horizontal net force, for ADP where $\alpha = 45 \text{ deg}$ and $c_p^* \approx 4.08$.

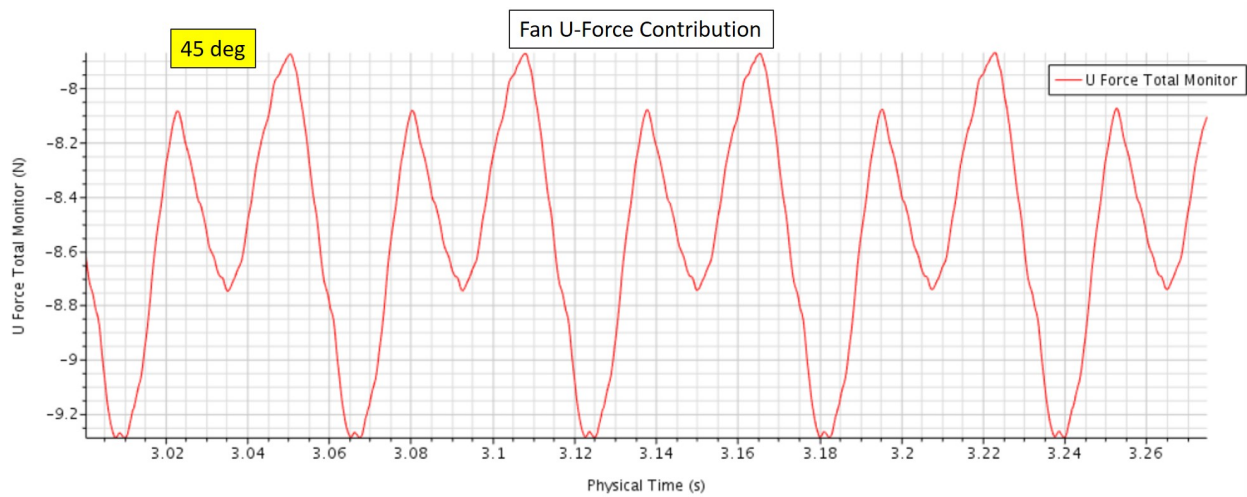


Figure 2.17: Time-series plot of U_{fan} , the fan actuator contribution to horizontal net force, for ADP where $\alpha = 45 \text{ deg}$ and $c_p^* \approx 4.08$.

are too high to be captured using the manometer pressure dataq acquisition method, but may contribute to the noise about the mean power data captured during the experiment, given that the data logging system operates at 400Hz. Time-averaged parameters from the CFD results are therefore used for comparison to the experimental results in this case.

CFD Results $\alpha = 54$ deg

The flow for $\alpha = 54$ deg is again characterized by the full separation and stall of the suction surface of the upper wing as well as a large separated region developing beyond the lower inlet lip. As with $\alpha = 45$ deg, this separated region is large and the flow does not re-attach in the vicinity of the fan actuator plane, and as a result, the flow passing through the fan is very distorted, with much of the separated region passing through the fan actuator surface as shown in Fig. 2.18.

Further this CFD analysis was run using the URANS solver, as the significant flow separation from the upper wing prevented convergence using the steady state solver. The unsteady case parameters are:

- **Solver:** Star-CCM+ Implicit-Unsteady, 1st-order in time
- **Turbulence Model:** Spalart-Allmaras
- **Time Step:** $\Delta t = 425\mu s$
- **Iterations per Time Step:** 15
- **Convergence:** $\leq 10^{-4}$
- **Flow Time:** 2.7 seconds
- **Comments:** Periodic variations are observed when $\alpha = 45$ deg are later eliminated when $\alpha = 54$ deg for all coefficients and parameters monitored in this CFD analysis.

Here the vortex shedding phenomena that dominated the $\alpha = 45$ deg is no longer present when $\alpha = 54$ deg. The mechanisms driving this phenomena for the ADP propulsion system

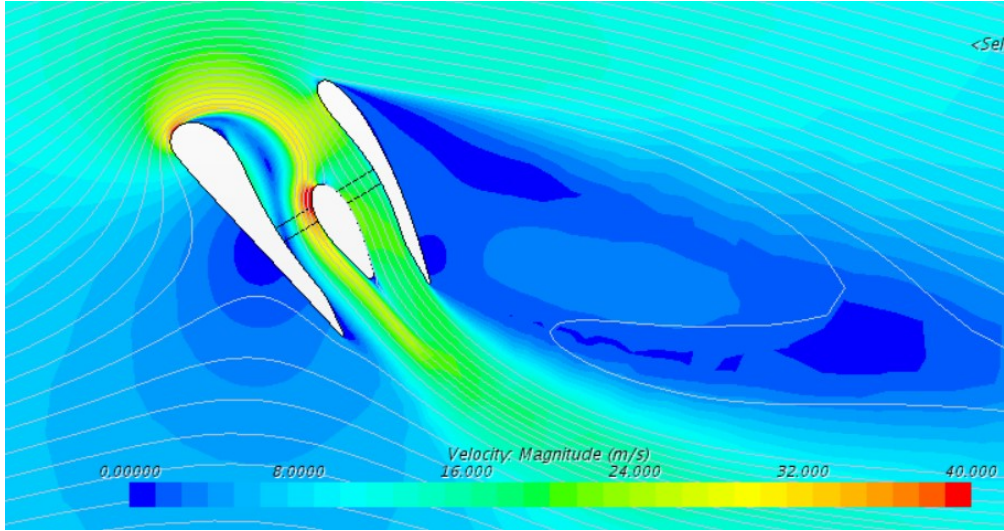


Figure 2.18: Contours of velocity magnitude for ADP where $\alpha = 54 \text{ deg}$ and $c_p^* \approx 5.08$.

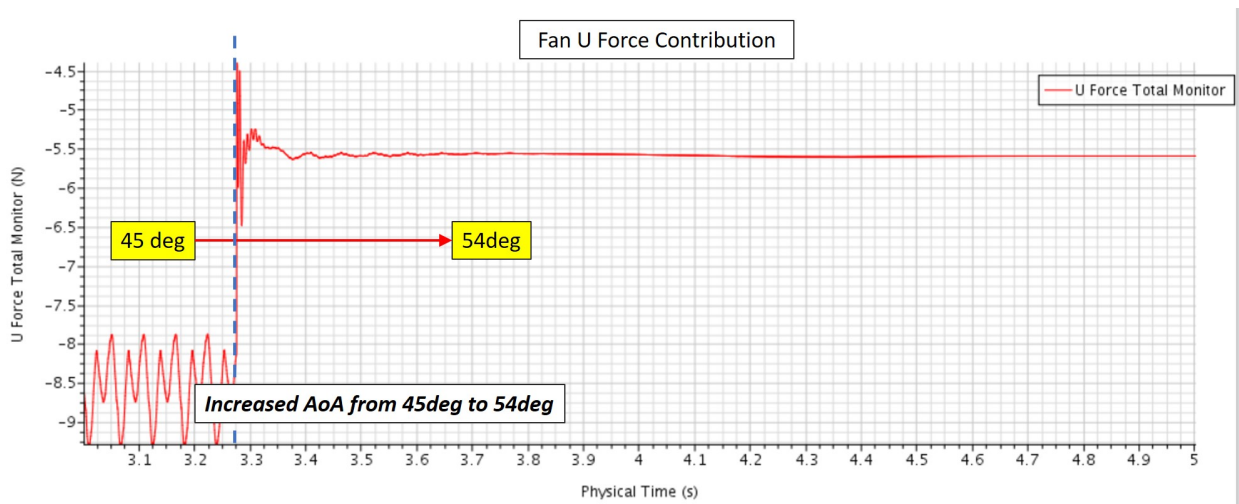


Figure 2.19: Time-series plot of U_{fan} , the fan actuator contribution to horizontal net force, for ADP where $\alpha = 54 \text{ deg}$ and $c_p^* \approx 5.08$.

are not well resolved in this analysis. This is recommended for further research following the conclusion of the present research effort.

2.7 Hover Breakdown Regime

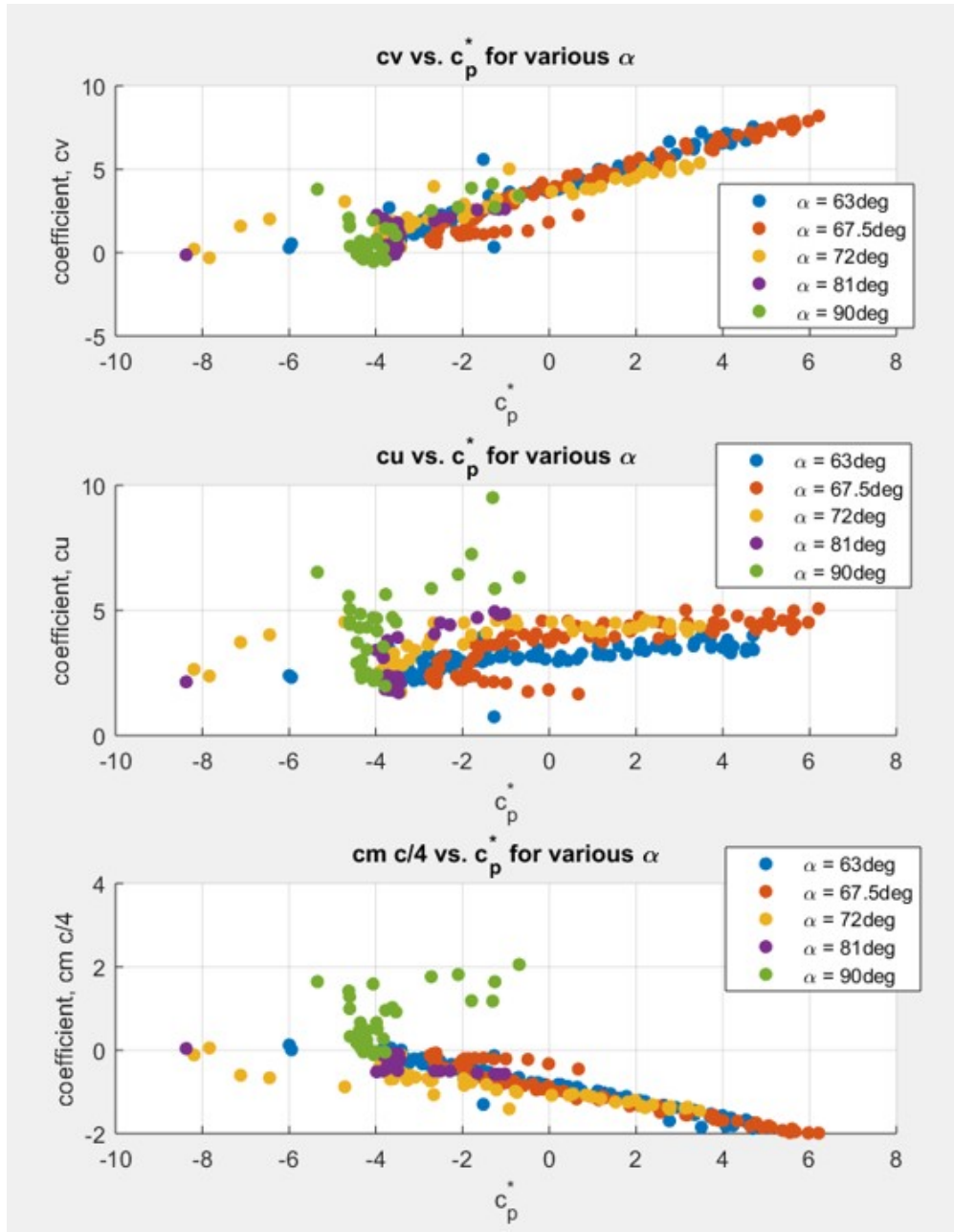


Figure 2.20: Summary of the ADP force coefficients, including aerodynamic and fan-derived contributions vs. c_p^* , for cases from $\alpha = 63deg$ to $\alpha = 90deg$.

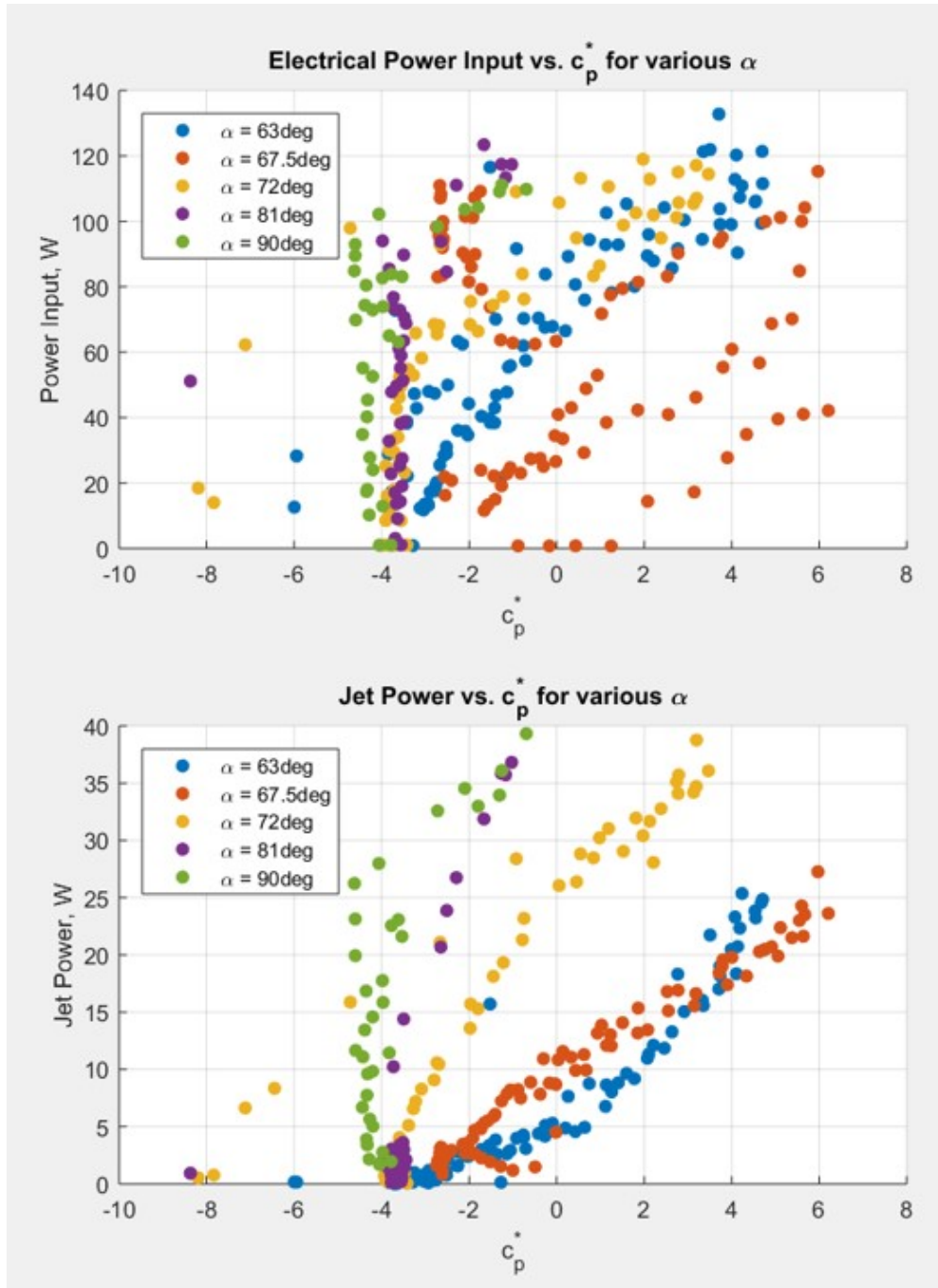


Figure 2.21: Summary of the ADP electrical input power and jet power vs. c_p^* , including aerodynamic and fan-derived contributions for cases from $\alpha = 63\text{ deg}$ to $\alpha = 90\text{ deg}$.

2.7.1 c_v behavior - vertical net force coefficient

Cases where $\alpha = 63\text{ deg}$ and $\alpha = 67.5\text{ deg}$ are considered to comprise the transition between the PLR and HBR. This is due to the observation that the response $c_v(c_p^*|\alpha = [63, 67.5]\text{ deg})$

remains primarily linear. Once $\alpha \geq 72$ deg this linear response is no longer observed. The linear proportional relationship between c_p^* and force coefficients dominated by the influence of the fan jet is no longer observed at this point. While the static pressure taps around the aerodynamic surfaces can be integrated to yield a net force component, the estimated contributions from the fan are no longer reliable for $\alpha = 81$ deg and $\alpha = 90$ deg. As such these contributions will not be included when compiling the final response surface model of the ADP system from the experimental data.

Additionally, a qualitative observation of the experiment operating in these conditions revealed extremely unsteady flow. For example, the walls of the wind tunnel test section buffet violently during these conditions. Also, at high power setting, the fan rpm was audibly unsteady, accelerating and decelerating under an unsteady aerodynamic load.

2.7.2 c_u behavior - horizontal net force coefficient

Findings regarding the behavior of c_u proceed in a similar manner to c_v . Cases where $\alpha = 63$ deg and $\alpha = 67.5$ deg are considered to be transitional between the PLR and HBR. This is again due to the observations that $c_v(c_p^*|\alpha = [63, 67.5] \text{ deg})$ remains primarily linear. Where $\alpha \geq 72$ deg, this behavior is no longer observed. For cases where $\alpha = 81$ deg and $\alpha = 90$ deg, c_u is observed to increase with c_p^* and is positive for all α and c_p^* in this regime. This is likely due to the breakdown of methods for estimating the force contributions of the fan to the system.

ADP Experiment Summary Table - HBR			
Angle of At-tack	$c_{PCFD}^* \rightarrow$ $nearest[c_{pexp}^*]$	$c_{v_{scl}}, c_{u_{scl}},$ from CFD	$c_v, c_u,$ from Exp.
$\alpha = 72$ deg	2.40→2.39	$c_v = 4.00,$ $c_u = 1.73$	$c_v = 4.79,$ $c_u = 4.54$

Table 2.4: ADP Experiment Summary Table - HBR

2.7.3 $c_{m_{c/4}}$ behavior - net moment coefficient

2.7.4 Power Input and Jet Power

The observations for $c_{m_{c/4}}$ are consistent with those for both c_u and c_v . Cases where $\alpha = 63$ deg and $\alpha = 67.5$ deg are considered to be transitional between the PLR and HBR. This is again due to the observations that $c_v(c_p^*|\alpha = [63, 67.5] \text{ deg})$ remains primarily linear. Cases where $\alpha \geq 72$ deg are again observed to break down.

2.7.5 CFD Results in the HBR

In this regime, the predictable behaviors that characterize both the ACR and PLR break down. At $\alpha = 72$ deg, the experimental data shows $c_p^* \geq 0$. However, for cases where $\alpha \geq 81$ deg, $c_p^* \geq 0$ was not able to be achieved with the input power available during the experiment. Since $\alpha = 63$ deg and $\alpha = 67.5$ deg are considered to be transitional cases, a comparison between CFD results and HBR experimental data will only be made for $\alpha = 72$ deg.

Again, the c_v results in both cases are reasonably similar, given the extreme flow separation that characterizes both the CFD results and experimental data. Additionally, the 3/2 power proportionality between c_p^* and jet power that is readily apparent in both the ACR

and PLR, is distinctly absent beyond $\alpha = 63$ deg. In this case, we can no longer assume that the control volume estimation methods defined for the experimental system are necessarily valid. Additionally, the CFD results are also suspect, given the prevalence of extreme flow separation in these conditions. Given the extreme electrical power input that would be required for the wind tunnel model, these conditions where $\alpha = 81$ deg and $\alpha = 90$ deg will be evaluated as a hover condition when developing the final response surface models. This analysis will be presented in that context in a later chapter of this document.

CFD Results for $\alpha = 72$ deg

The case where $\alpha = 72$ deg was set to achieve a target $\dot{m} = 0.5 \text{ kg/s}$ this results in a $c_p^* = 2.40$. The flow in this case is characterized by extreme flow separations as well as periodic vortex shedding from the upper wing suction surface as well as from the lower inlet lip. Also, this flow is highly periodic, requiring the use of the URANS solver, set up in the same manner as the previous URANS cases discussed in this chapter.

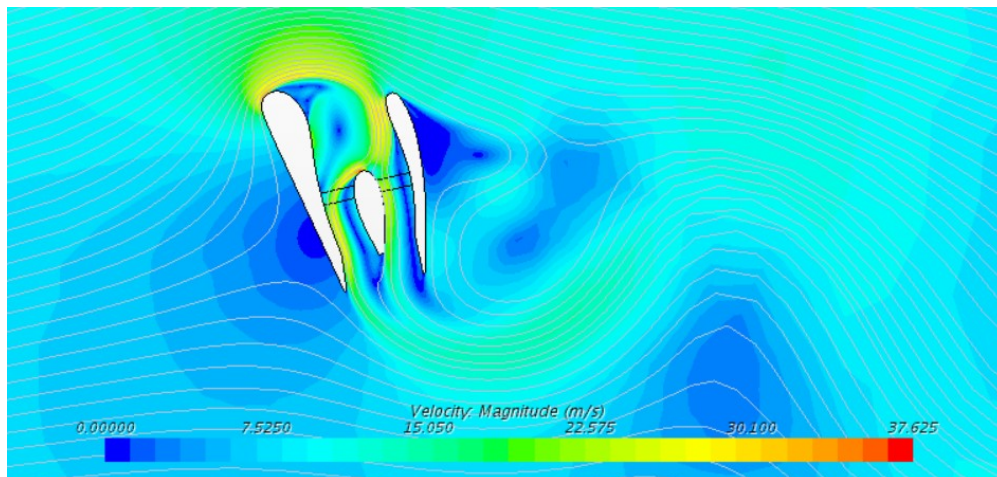


Figure 2.22: Contours of velocity magnitude for ADP where $\alpha = 72$ deg and $c_p^* \approx 2.4$.

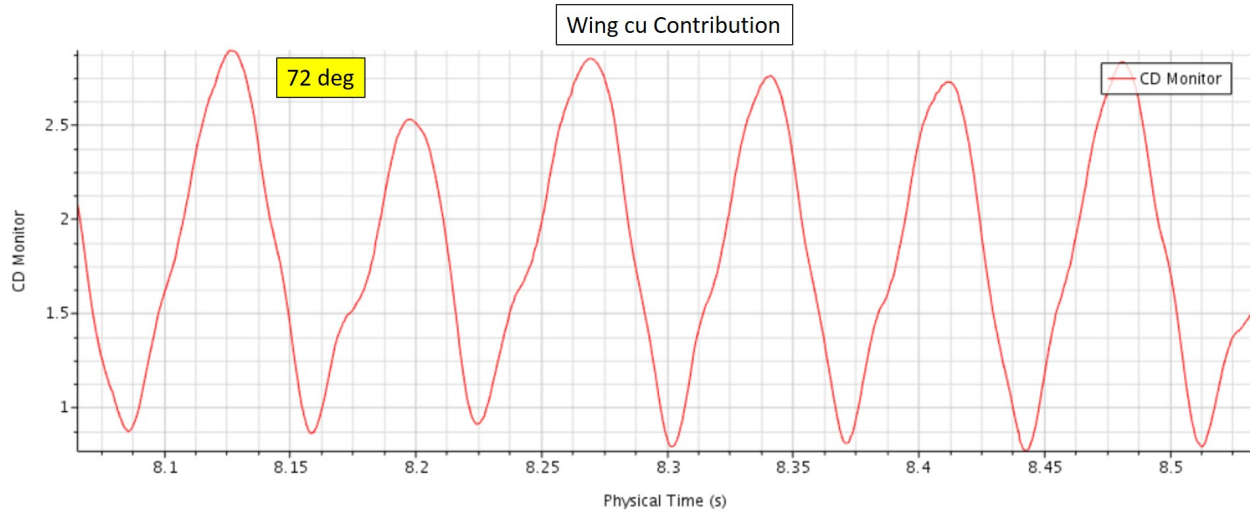


Figure 2.23: Contours of velocity magnitude for ADP where $\alpha = 72$ deg and $c_p^* \approx 2.4$.

CFD Results for $\alpha = 90$ deg

The CFD results shown in Fig. 2.24 represent an $\dot{m} = 1\text{kg/s}$ and a resulting $c_p^* = 8.90$. However, no direct comparison can be made with experimental data, as $c_p^* \geq 0$ was not achieved with approximately 950W of input electrical power. As a result, these conditions will be evaluated as a hover condition when constructing the final response surface model of the ADP system. This analysis will be presented in this context in a later chapter of this document.

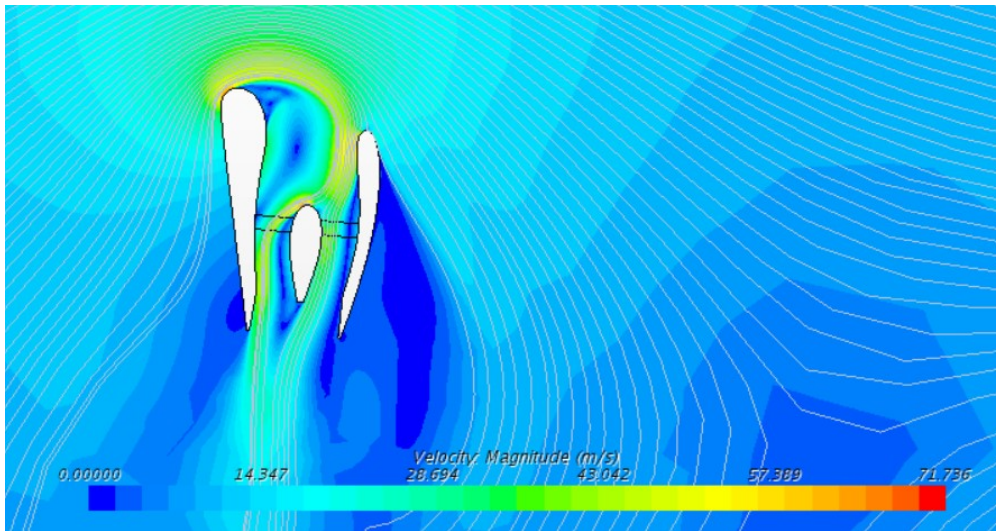


Figure 2.24: Contours of velocity magnitude for ADP where $\alpha = 90$ deg and $c_p^* \approx 8.90$.

2.8 Summary Data for ACR and PLR

It is also informative to examine the data as $f(\alpha|c_p^* = \text{const})$. Here we will use $f(\alpha|c_p^* = [0, 1, 3, 5, 7])$. This method of examining the data has the effect of revealing more conventional aerodynamic behaviors such as the lift curve slope for each c_p^* condition.

2.8.1 $c_v(\alpha|c_p^*)$ behavior

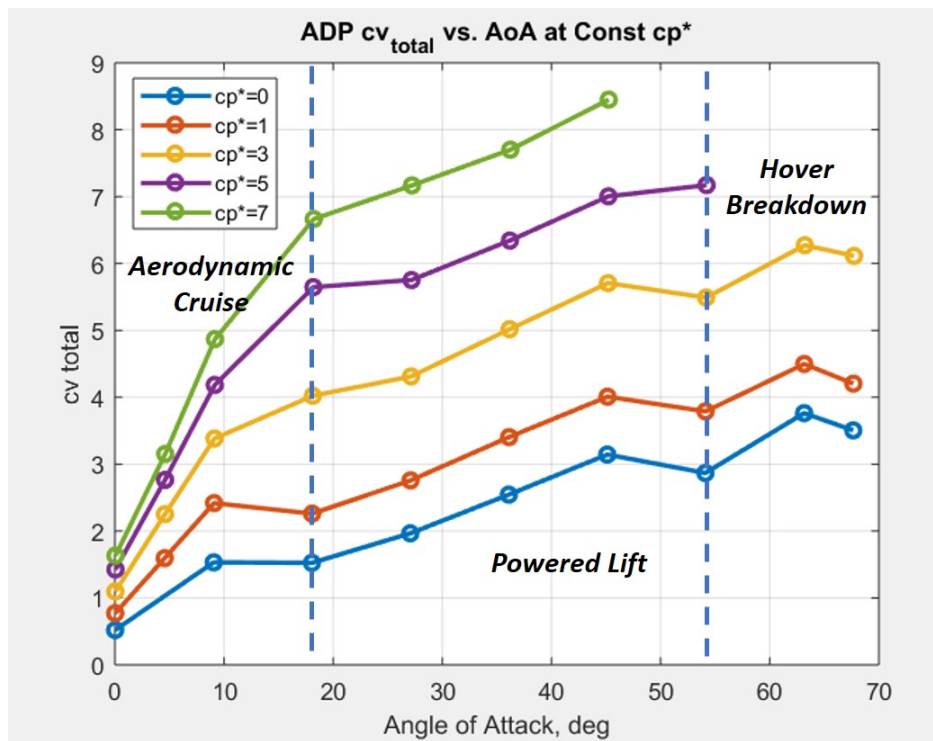


Figure 2.25: Summary of the ADP vertical force coefficient data as a function of α for various values of $c_p^* = \text{const}$

The lift curve slope is observed to be linear for each $c_p^* = \text{const}$ plotted here. However, the slope of $c_v(\alpha|c_p^*)$ increases as c_p^* increases. Where $c_p^* = 0$, the lift curve slope is

$$\alpha_{0_{c_p^*=0}} = 0.11 \text{ per degree} \quad (2.27)$$

Recall that thin airfoil theory predicts a two dimensional wing to have a lift curve slope of

$$\alpha_0 = 2\pi \text{ per radian, or } 0.11 \text{ per degree} \quad (2.28)$$

This match indicates that when the fan is not augmenting the total pressure of the flow passing through the propulsion system, the ADP propulsion system behaves like a typical wing.

Further, when $c_p^* \geq 0$, the initial lift curve slope where $0 \text{ deg} \leq \alpha \leq 9 \text{ deg}$, increases beyond the thin airfoil theory prediction, also as expected when adding significant energy to the flow. The maximum slope occurs at maximum c_p^* , here $c_p^* = 7$. This results in

$$\alpha_{0_{c_p^*=7}} = 0.36 \text{ per degree} \quad (2.29)$$

more than three times the thin airfoil theory result.

The behavior of $c_v(\alpha|c_p^*)$ when $9 \text{ deg} \leq \alpha \leq 18 \text{ deg}$ indicates the relative influence of the flow separation from the suction surface of the upper wing on the resulting c_v . Here, the effect is significantly more pronounced for lower values of c_p^* .

2.8.2 $c_u(\alpha|c_p^*)$ behavior

Examining the behavior of $c_u(\alpha|c_p^*)$, reveals the steadily increasing forward thrust produced by the system in the ACR. Note the slight increase in net thrust with increasing angle of attack for $c_p^* \geq 1$. This is due to the increase in the thrust component due to the pressure distribution around the aerodynamic surfaces.

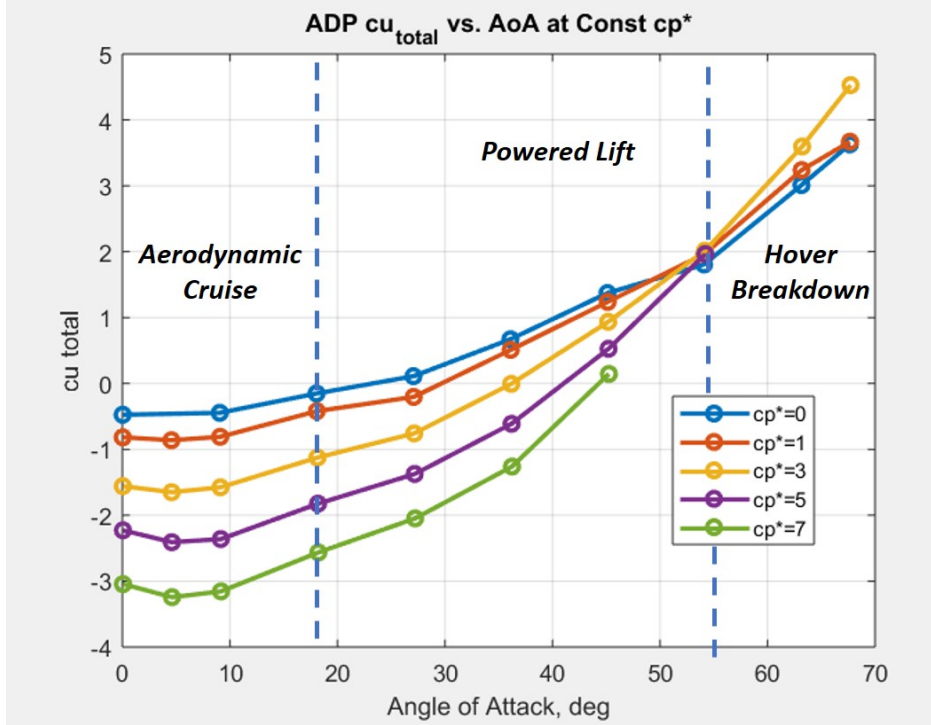


Figure 2.26: Summary of the ADP horizontal force coefficient data as a function of α for various values of $c_p^* = const.$ Negative values denote a net thrust.

The powered lift region is characterized by increasing $c_u(\alpha)$ for all c_p^* . Also, for all c_p^* , at $\alpha = 54$ deg the $c_u(\alpha|c_p^*)$ curves intersect.

2.8.3 $c_u(c_v|c_p^*)$ behavior

Examining the behavior of $c_u(c_v|c_p^*)$ shows the response of changes in c_u resulting from changes in c_v are generally smooth throughout much of the ACR and PLR. This indicates that strong non-linear behaviors will be limited to regions where flow separation is prevalent, as highlighted in Fig. 2.27. Fortunately, these phenomena occur at low c_p^* , and therefore can likely be recovered from with the addition of power, should they be encountered during operation.

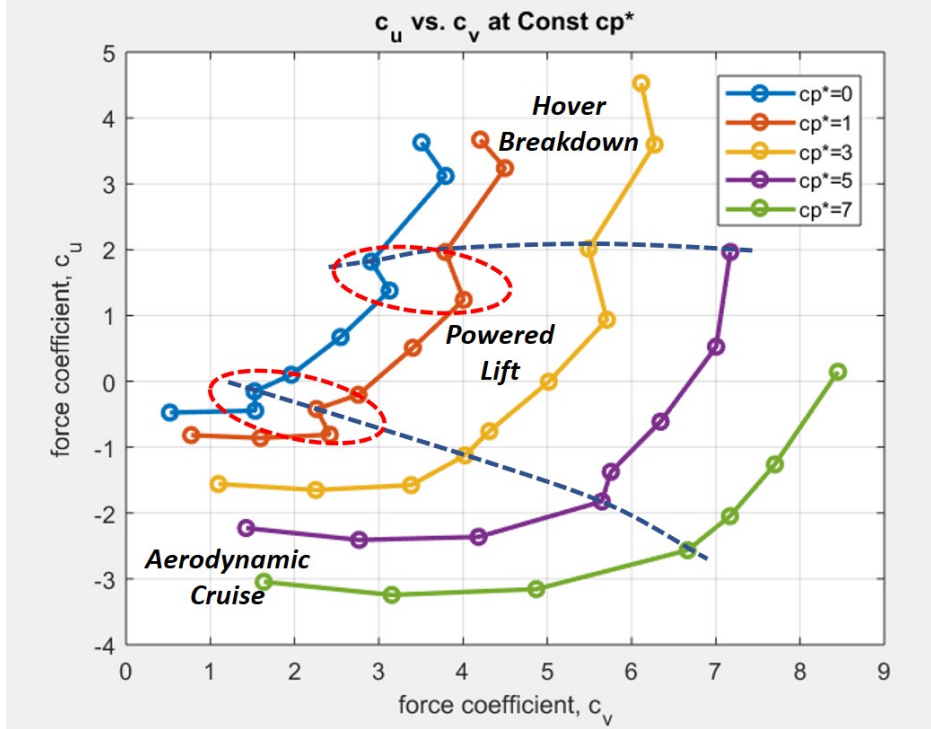


Figure 2.27: Summary of the ADP horizontal force coefficient c_u data as a function of c_v , the vertical force coefficient, for various values of $c_p^* = const.$ Negative values of c_u denote a net thrust.

2.8.4 $c_{m_{c/4}}(\alpha|c_p^*)$ behavior

The moment coefficient calculation about the quarter chord of the lower wing assumes that the fan thrust force acts through and parallel to the rotational axis of the fan. Fan asymmetric loading would modify the moment arm estimate and therefore the calculated moment coefficient in these cases. However, in the absence of the precise and detailed velocity measurements inside the fan duct, such as those obtained by PIV techniques, the previously stated assumption is maintained throughout this analysis.

For cases in the ACR and into the PLR, this assumption is likely reasonable for $\alpha \leq 36$ deg. As observed in the CFD cases, for $\alpha \geq 45$ deg the flow is separated from the lower inlet lip, and potentially introducing flow asymmetry at the fan. This effect is likely less

pronounced in the experiment, given the presence of physical fan blade and a low aspect ratio, cylindrical hub region.

The transitional cases where $\alpha = 63$ deg and $\alpha = 67.5$ deg show an abrupt change in the moment trends that developed for $\alpha \leq 54$ deg. These changes may indicate that the flow asymmetry seen in the CFD model at $\alpha = 45$ deg manifests later in the experiment at $\alpha = 63$ deg.

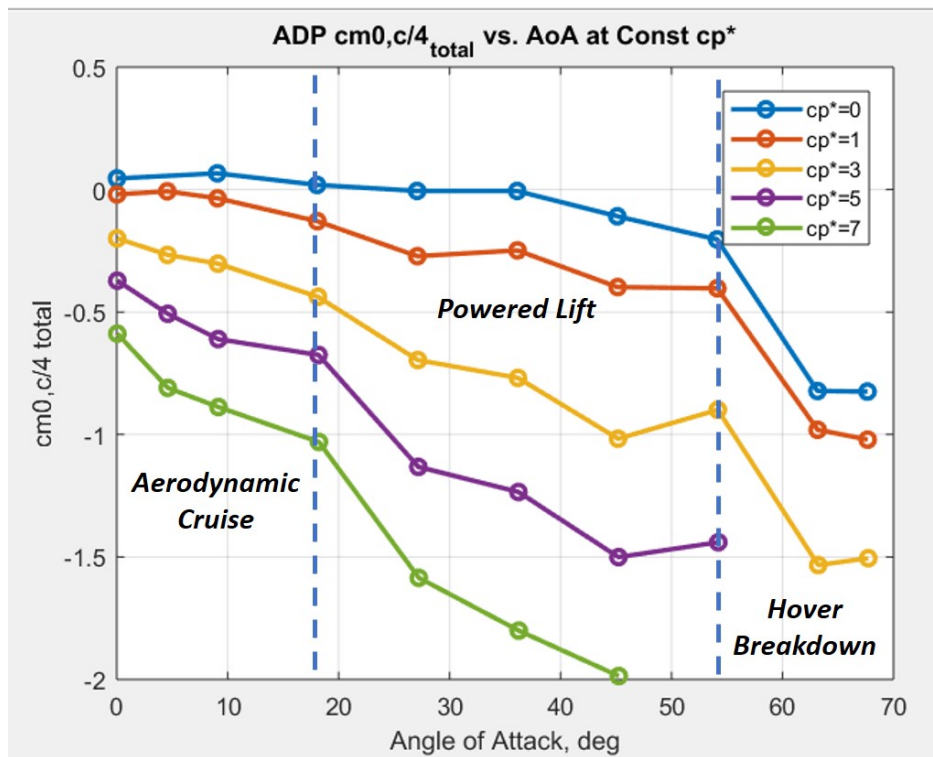


Figure 2.28: Summary of the ADP pitching moment coefficient data as a function of α for various values of $c_p^* = const$. Negative values denote a net nose down pitching moment.

2.8.5 $\underline{P}(\alpha|c_p^*)$ behavior

As stated in the previous sections, the jet power \underline{P} in the ACR and PLR are characterized primarily by the proportional relationship

$$\underline{P} \propto c_p^{*3/2} \quad (2.30)$$

While more difficult to observe, when the data is presented in this manner, this proportional relationship is nonetheless present. Additionally, we can observe that the ideal power of the jet remains essentially constant for a given c_p^* for all α in the ACR and PLR.

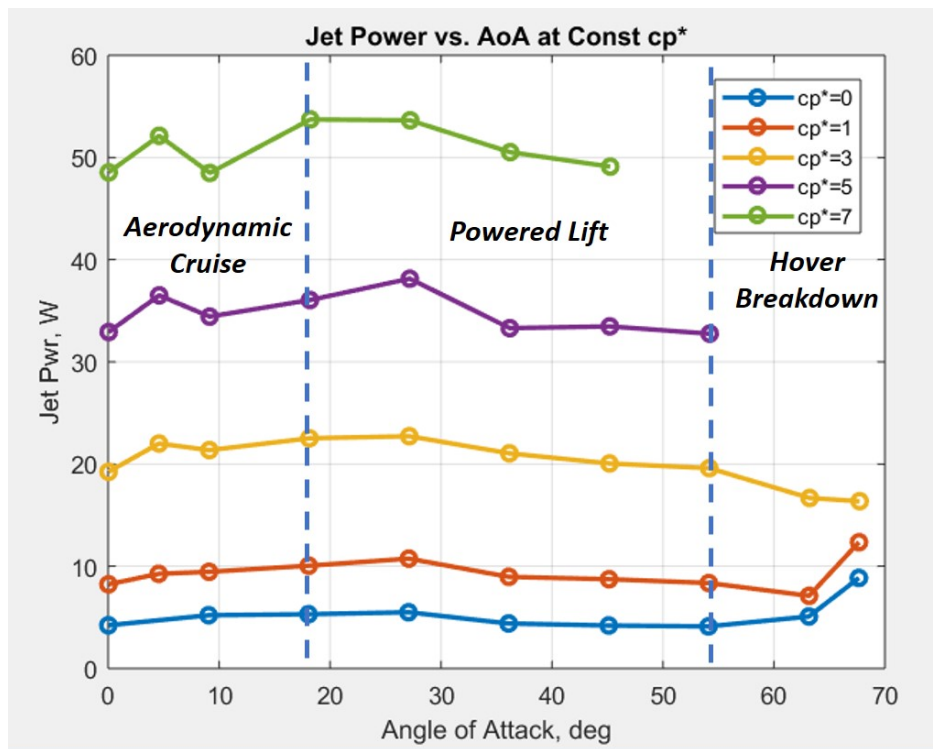


Figure 2.29: Summary of the ADP jet power data as a function of α for various values of $c_p^* = const.$

2.9 Conclusions

This chapter presented a summary of the ADP experimental data as well as illustrative comparisons with CFD analysis to help visualize the critical flow phenomena that characterize the performance of the system. From the experimental data, three operating regimes were identified: Aerodynamic Cruise (AC), Powered Lift (PL), and Hover Breakdown(HB). The ACR and PLR were shown to follow predictable proportional relationships to the dimensionless parameter c_p^* , while in the HBR, these relationships were observed to break down.

Cases where $\alpha \leq 36$ deg were shown to have excellent agreement with the CFD analysis for both $c_u(\alpha|c_p^*)$ and $c_v(\alpha|c_p^*)$, while cases where $\alpha \geq 45$ deg in the PL and lower HB regime were shown only to agree regarding $c_v(\alpha|c_p^*)$. This is likely due a departure from symmetric pressure loading on the inside of the fan duct and two-dimensional nature of the CFD model when compared to the three-dimensional ducts in the wind tunnel experiment.

Generally, the experimental data provides an excellent representation of the performance of the ADP system up to $\alpha = 72$ deg. For cases beyond this where $\alpha = 81$ deg and $\alpha = 90$ deg, the power input to the wind tunnel model is insufficient to generate $c_p^* \geq 0$. Therefore, these extreme cases will be treated as though the aircraft is in hover.

Chapter 3

CDP Experimental Results

3.1 Introduction

This chapter will present a summary of the experimental and computational results for the CDP system. As with the ADP results, these results are presented in terms of the directional net force and moment coefficients, c_u , c_v , and $c_{m_{c/4}}$. These results are presented in the context $f(c_p^*|\alpha, \theta)$. The CDP system as designed for this experiment, exhibits a bi-modal response to power input for some combinations of the input variables c_p^* , α , and θ , where the flow over the suction surface of the forward wing will separate, artificially increasing the camber of the wing, and dramatically increasing the drag on the system. Since the primary objective of this research effort is to characterize the interactions between a hybrid power system and distributed electrical propulsion systems, the CDP system will not be considered beyond this summary chapter. However, the CDP system has considerable promise as a VTOL propulsion system if this

bi-modal response to power input is well understood. While beyond the scope of the present effort, this phenomena provides considerable opportunity for further research.

3.2 Data Summary

For the purposes of this experiment, the angle α is defined as the angle of attack with respect to the chord reference line of the forward wing. The angle θ refers to the geometric deflection angle of the CDP fan-embedded flap. And finally, the angle Φ describes the nominal jet angle, assuming that the jet remains attached to the walls of the duct and that the flow is in the direction parallel to the fan axis. This is shown in Fig. 3.1.

The CDP system was evaluated experimentally for several forward wing angles of attack α for each flap setting θ . These conditions are summarized in Fig. 3.2.

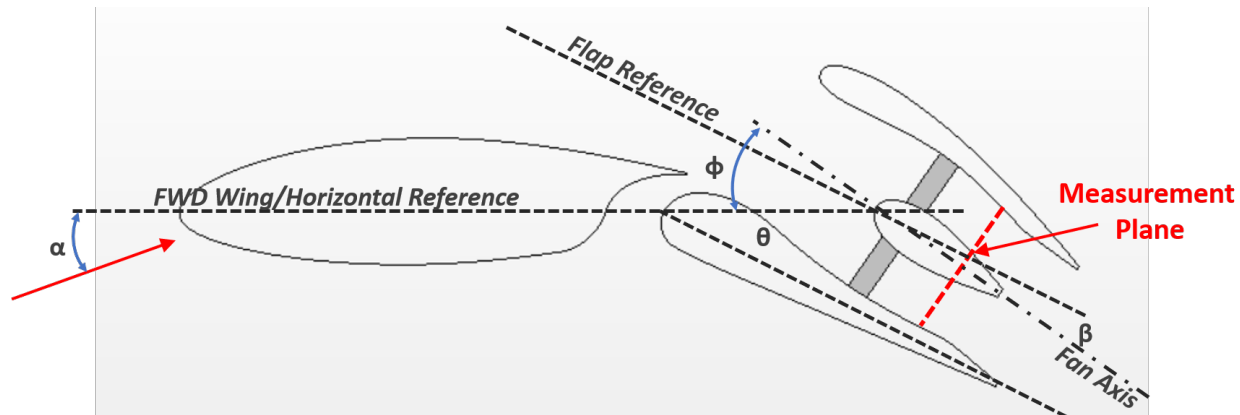


Figure 3.1: CDP Experimental Conditions

The aerodynamic phenomena observed during this experiment are presented in the context of the bi-modal power response mentioned above. This stall-like phenomena is absent when the system is operating in the range $0 \text{ deg} \leq \alpha \leq 4.5 \text{ deg}$ with the transition

CDP Experimental Condition Summary					
Flap Angle	Fwd Wing Angle	Flap Angle	Fwd Wing Angle	Flap Angle	Fwd Wing Angle
0 deg (closed)	-4.5	20 deg	0.0	60 deg	0.0
	0.0		4.5		4.5
	4.5		9.0		9.0
	9.0		13.5		13.5
	13.5		18.0		18.0
	18.0				
0 deg (open)	0.0	30 deg	0.0	70 deg	0.0
	4.5		4.5		4.5
	9.0		9.0		9.0
	13.5	40 deg	13.5	80 deg	-4.5
	18.0		18.0		0.0
10 deg	0.0	40 deg	4.5	90 deg	4.5
	4.5		9.0		-4.5
	9.0		13.5		0.0
	13.5	50 deg	18.0		4.5
	18.0		0.0		
			4.5		
			9.0		
			13.5		
			18.0		

Figure 3.2: CDP Experimental Conditions

between both modes response observed most prominently where $\alpha = 9$ deg in the available data set. The difference between each mode is sketched in Fig. 3.3.

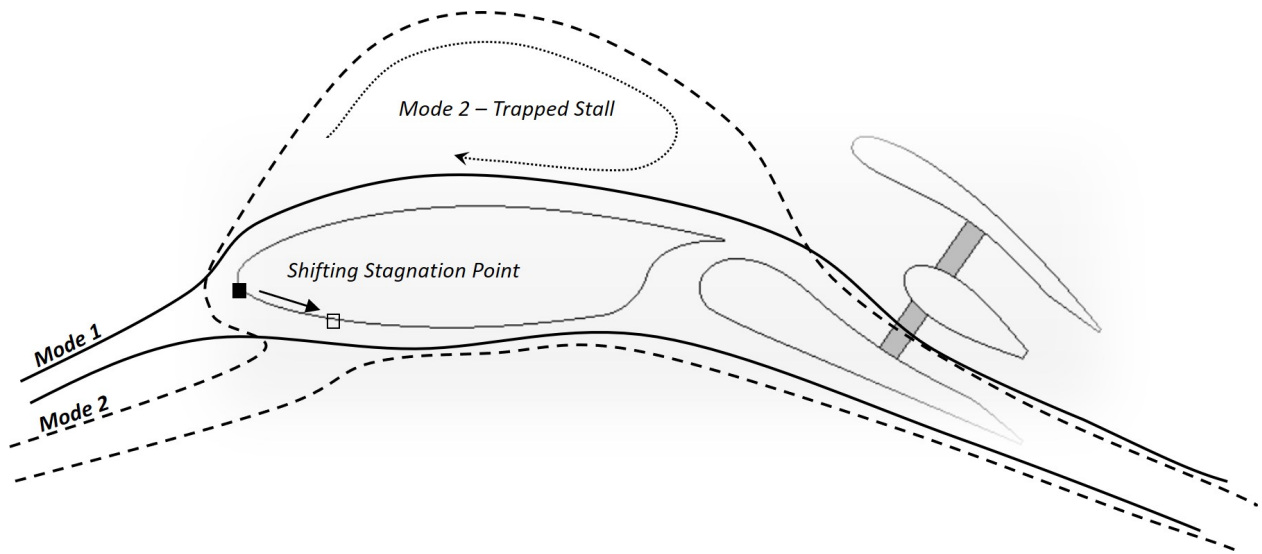


Figure 3.3: Bi-modal response to power input for a given α .

3.2.1 Mode 1 Description

The first mode of the bi-modal power response is characterized by attached flow long the suction surface of the forward wing. In this case, the stagnation point is near the leading edge of the wing. This is observed to occur experimentally at lower power settings, and corresponding lower values of c_p^* . The precise range where Mode 1 is dominant depends upon both the angle of attack α and flap angle θ .

3.2.2 Mode 2 Description

The second mode of the bi-modal power response is characterized by fully separated flow over the suction surface of the wing. The stagnation point moves aft, along the pressure surface of the forward wing. Once separated from the wing, the flow is then unconstrained by the wing geometry and influenced only by near-field pressure gradients, largely dominated by the embedded fans. Ultimately, the flow that separated from the leading edge of the forward re-attaches in the interior of the fan duct, and passes through the embedded-fan. The separated region above the the suction surface of the forward wing becomes trapped by the surrounding flow. This trapped stall condition appears to be stable when Mode 2 is the dominant mode in the flow field.

Therefore, the data for these will be presented for conditions where only Mode 1 is present, and where a transition occurs between Mode 1 and Mode 2.

3.3 Dominant Mode 1 - CDP Results and Behavior

Near $\alpha = 0$ deg

The data summary for the CDP system operating near $\alpha = 0$ deg includes both the section aerodynamic coefficients and power consumption requirements. Operating at these conditions is characterized entirely by Mode 1, where the flow over the suction surface of the forward wing remains fully attached.

The trends and behaviors observed for each force coefficient as well as the power consumption will be discussed individually.

3.3.1 c_v Behavior near $\alpha = 0$ deg

Generally, when Mode 1 is dominant, the vertical force coefficient c_v is proportional to c_p^* .

$$c_v \propto c_p^* \quad (3.1)$$

Operating range $0 \text{ deg} \leq \theta \leq 30 \text{ deg}$

The vertical force coefficient in this range is a strong function of the flap angle θ , particularly for $0 \text{ deg} \leq \theta \leq 20$. As the flap angle increases, the slope of the c_v response to increasing c_p^* also increases.

$$\frac{dc_v}{dc_p^*} \propto d\theta \quad (3.2)$$

This dependence on θ begins to diminish at $\theta = 30$ deg, as shown in Fig. 3.4. The behavior of the power response is shown in Fig. 3.5.

Operating Range $40 \text{ deg} \leq \theta \leq 80 \text{ deg}$

In this range, the slope of the c_v response curve $dv c_v c_p^*$ is no longer a function of θ . Rather, $c_v(c_p^*|\theta)$ is shifted toward greater c_v for increasing θ , as shown in 3.6. The power response of the system at these conditions is shown in Fig. 3.7.

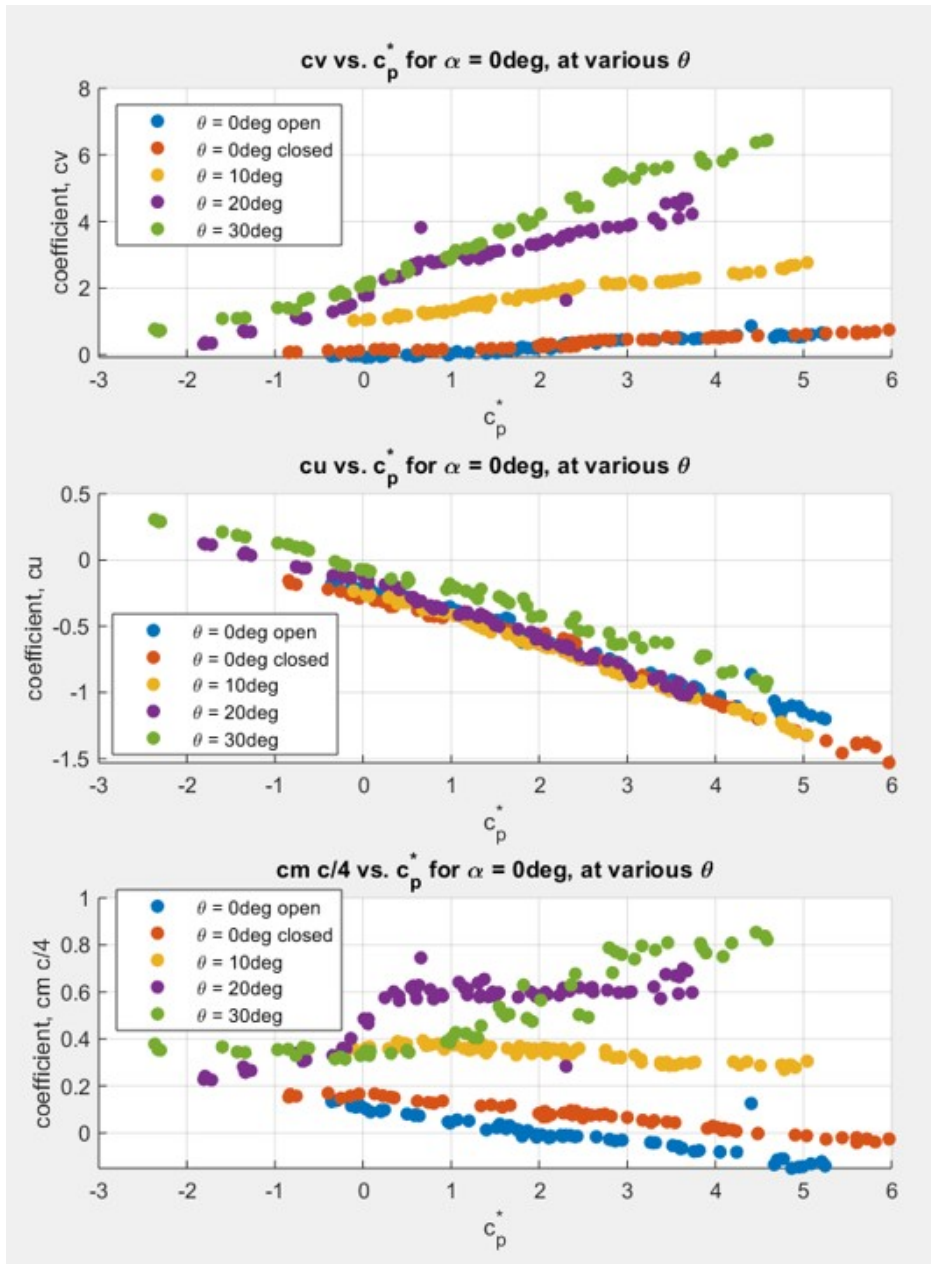


Figure 3.4: CDP Experimental Data Summary - Aerodynamic Coefficients

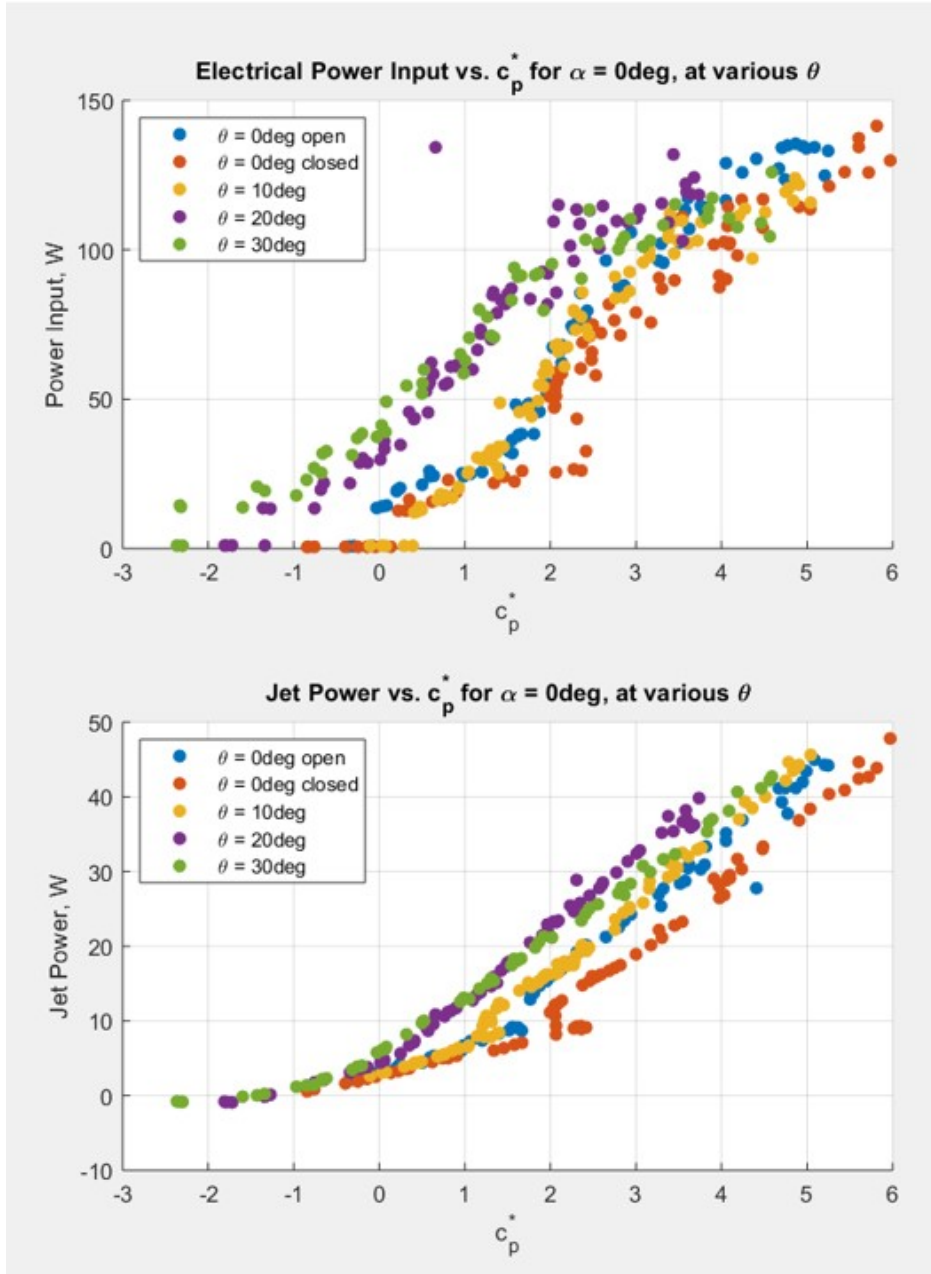


Figure 3.5: CDP Experimental Data Summary - Power Requirements

3.3.2 c_v Behavior near $\alpha = 0\text{ deg}$

Generally, when Mode 1 is dominant, the horizontal force coefficient c_u is proportional to c_p^*

$$c_u \propto c_p^* \quad (3.3)$$

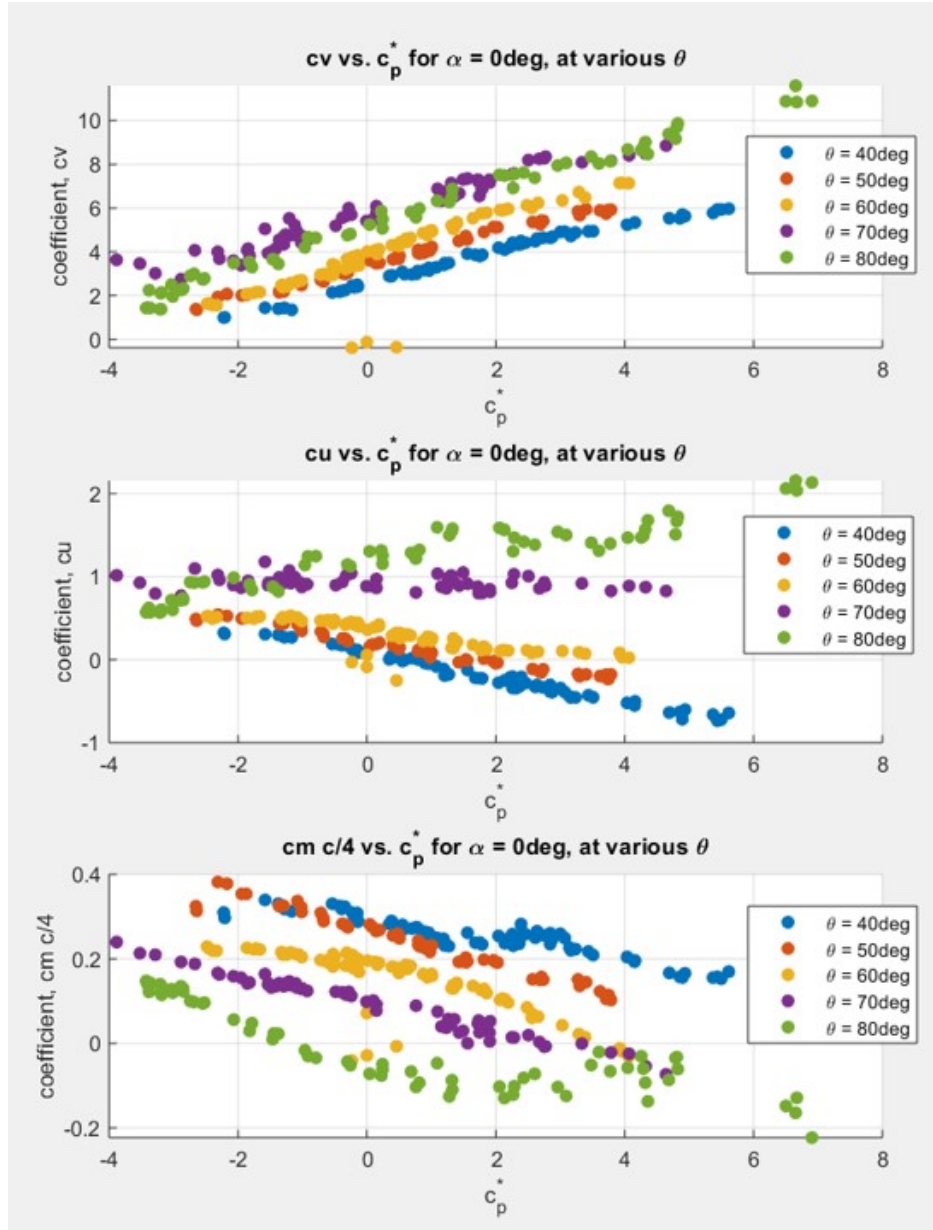


Figure 3.6: CDP Experimental Data Summary - Aerodynamic Coefficients

Additionally, the slope of $c_u(c_p^*|\theta)$ is typically negative for most flap angles.

$$\frac{dc_u}{dc_p^*} < 0, \text{ for } 0 \text{ deg} \leq \theta \leq 60 \text{ deg} \quad (3.4)$$

This is not the case where $\theta \geq 70$ deg, as shown in Fig. 3.4 and 3.6 respectively.

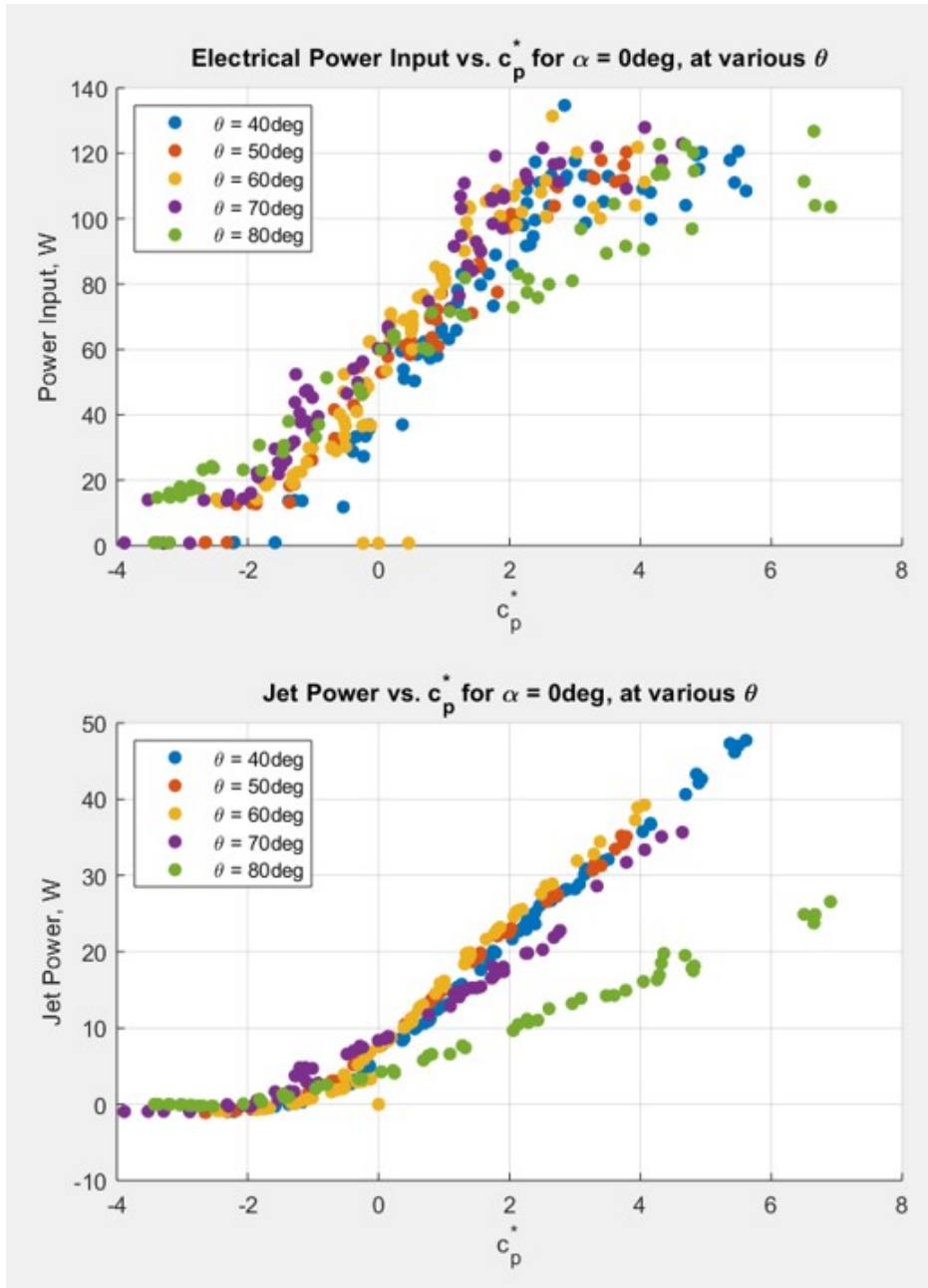


Figure 3.7: CDP Experimental Data Summary - Power Requirements

3.3.3 $c_{m_{c/4}}$ Behavior near $\alpha = 0\text{deg}$

For $\theta \leq 30\text{deg}$, the system moment behavior is dominated by the moments about the quarter chord due to the pressure distribution around the forward wing and the fan flap. Under these conditions, the majority of lift in the system is generated near the leading edge

of the forward wing. Because the circulation around the wing is controlled primarily by the embedded fans, the slope of the pitching moment response $c_{mc/4}(c_p^*|\theta)$ is observed to increase with increasing flap angle, reaching a maximum where $\theta = 20$ deg before decreasing again for negative and small c_p^* where $\theta = 30$ deg, as shown in Fig. 3.4. Additionally, where $\theta = 30$ deg the approximately linear response of pitching moment to increasing c_p^* observed in most other cases, is not present.

Beyond this point, for $\theta \geq 40$, the pitching moment response is dominated by fan thrust, and the negative slope and linear proportionality with c_p^* are restored.

3.3.4 Jet Power Behavior near $\alpha = 0$ deg

As shown previously in this research, the jet ideal power should be proportional to $c_p^{*3/2}$.

$$\text{Jet Ideal Power} \propto c_p^{*3/2} \quad (3.5)$$

This is approximately observed for operating conditions in the range $0 \text{ deg} \leq \theta \leq 70 \text{ deg}$. Beyond this range, this proportionality is observed to break down.

3.4 Transitional Modes - CDP Results and Behavior

Near $\alpha = 9$ deg

In this operating range, only flap angles up to $\theta = 70$ deg were tested. This was motivated partially by the fact that any aircraft fitted with CDP is unlikely to be operating with non-negligible forward velocity with a flap angle beyond this, and partially due to a desire to

preserve the integrity of the wind tunnel model as operation under these conditions are likely to damage the experimental apparatus. Additionally, for clarity, the results for $\theta = 30$ deg are included in both Fig. 3.8 and Fig. 3.9.

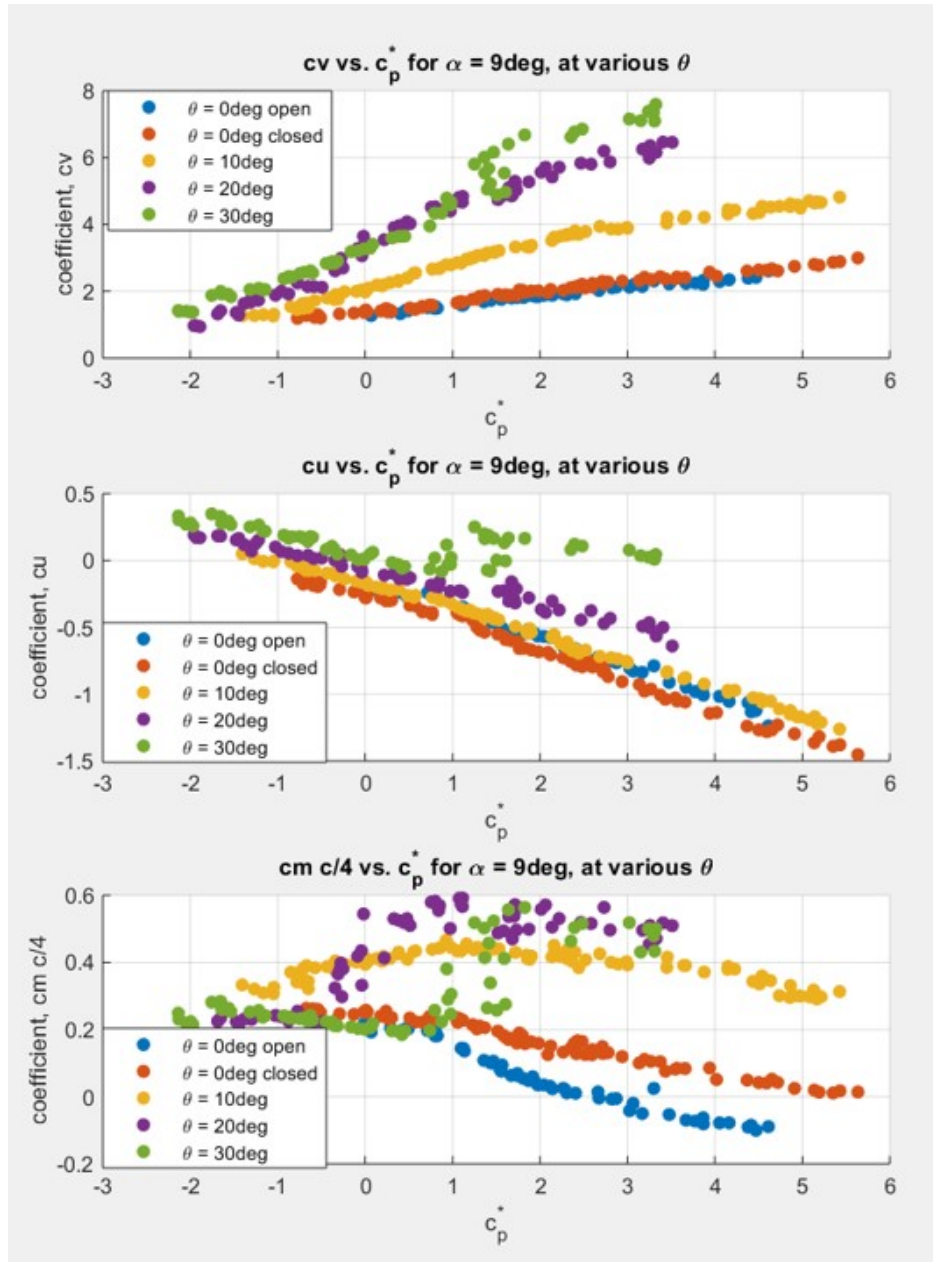


Figure 3.8: CDP Experimental Data Summary - Aerodynamic Coefficients

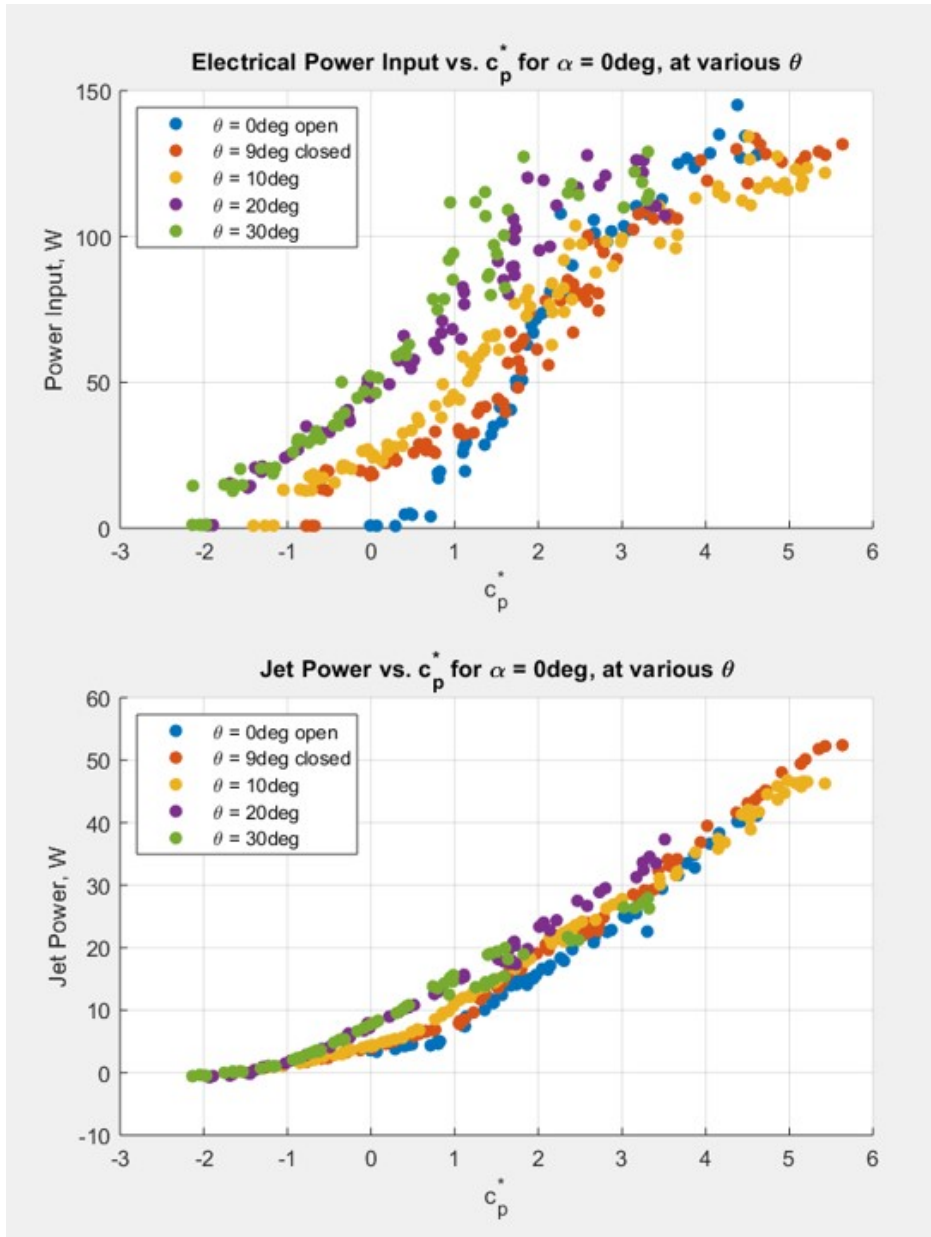


Figure 3.9: CDP Experimental Data Summary - Power Requirements

Here, rather than individually discussing the evolution of the aerodynamic force coefficients as a function of c_p^* and θ , the discussion will focus on the appearance and evolution of the bi-modal response of central concern to the viability of the CDP system, as shown in Figs. 3.10 and 3.11.

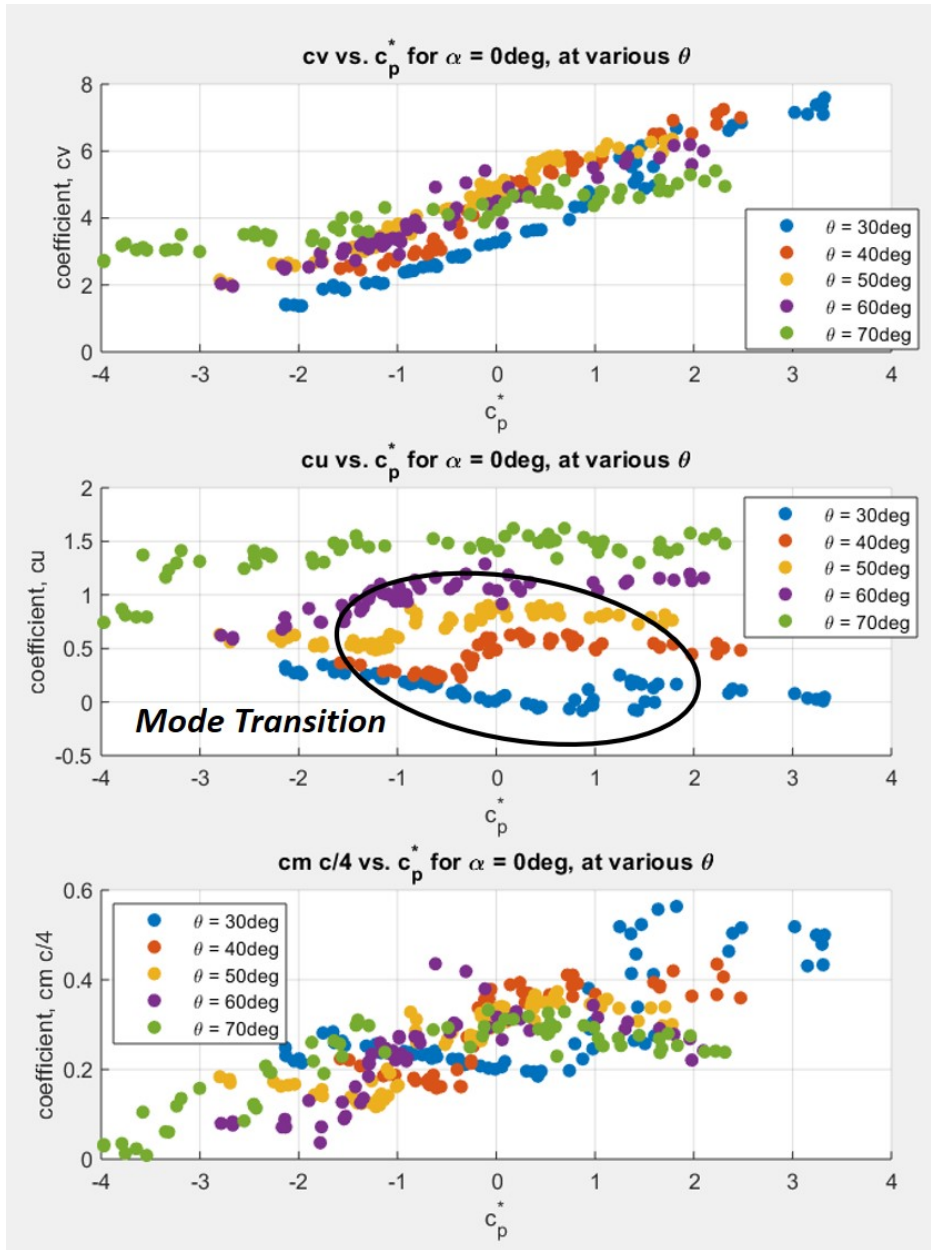


Figure 3.10: CDP Experimental Data Summary - Aerodynamic Coefficients

A bi-modal power response is first observed in the pitching moment behavior where $c_{m_{c/4}}(c_p^*)|_{\theta=20}$. In this case, at $c_p^* \approx -0.3$, the pitching moment begins to exhibit the characteristic behavior of the bi-modal power response, a dramatic departure from an established trend, followed by stabilization on a second trend, as shown in Fig. 3.8.

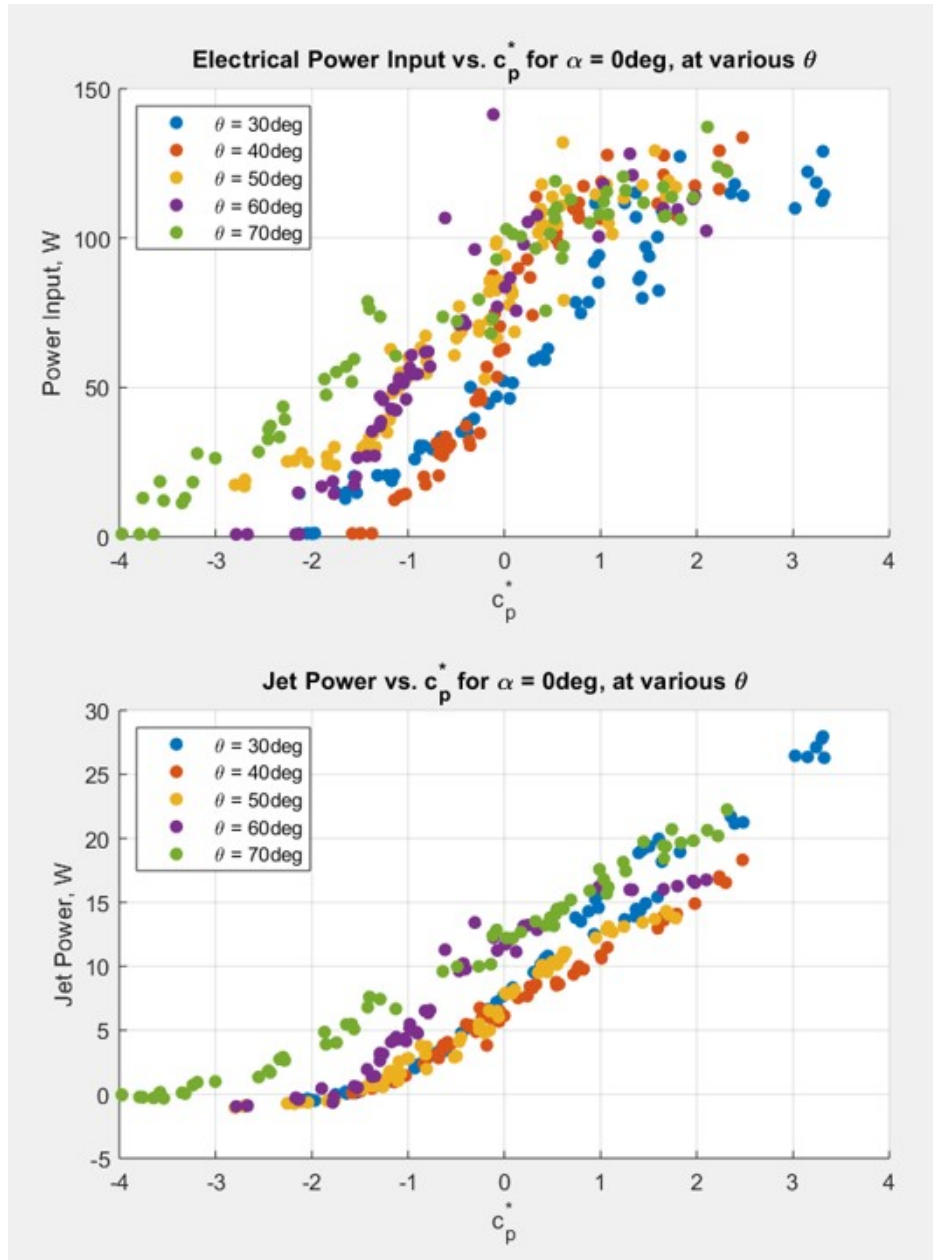


Figure 3.11: CDP Experimental Data Summary - Power Requirements

When the flap angle is in the range $30\text{deg} \leq \theta \leq 60\text{deg}$ this bi-modal response is observed to some extent for all aerodynamic coefficients, as shown in Fig. 3.11. To further clarify this phenomena, a single illustrative case is selected.

3.5 Examining a Particular Condition: $\alpha = 9 \text{ deg}$ and

$$\theta = 40 \text{ deg}$$

The bi-modal response of the CDP system to a given power input is particularly well defined for $\alpha = 9 \text{ deg}$ and $\theta = 40 \text{ deg}$. Therefore, this operating point is used to further illustrate this phenomenon.

The aerodynamic coefficients as well as input power and jet ideal power are presented in Fig. 3.12. Here, the characteristic bi-modal response is clearly observed for all aerodynamic coefficients.

For low c_p^* , an initial trend is clearly established for all aerodynamic force coefficients. As the CDP system enters the dual mode region, both modes are able to occur, and the system successively alternates between each mode, with the data points in Fig. 3.13 representing the time averaged response of the system.

In order to demonstrate the fact that each mode can occur for a constant power setting, two time averaged data points are selected that illustrate this behavior, as shown in Fig. 3.13. The pressure profiles are then extracted for all aerodynamic surfaces to enable a direct comparison. The results of this comparison for the forward wing as well as the upper and lower flap surfaces are shown in Fig. 3.14 and Fig. 3.15 respectively.

The pressure profile around the forward wing in Mode 1 is characterized by a well-defined suction peak as would be expected around a lifting airfoil. This suction peak then decreases when moving from leading to trailing edge. For Mode 1 operation the pressure coefficient range on the suction surface is $-9.2 > c_p > -4.0$. In contrast, Mode 2 operation is characterized by a much more uniform pressure distribution without a distinct suction peak.

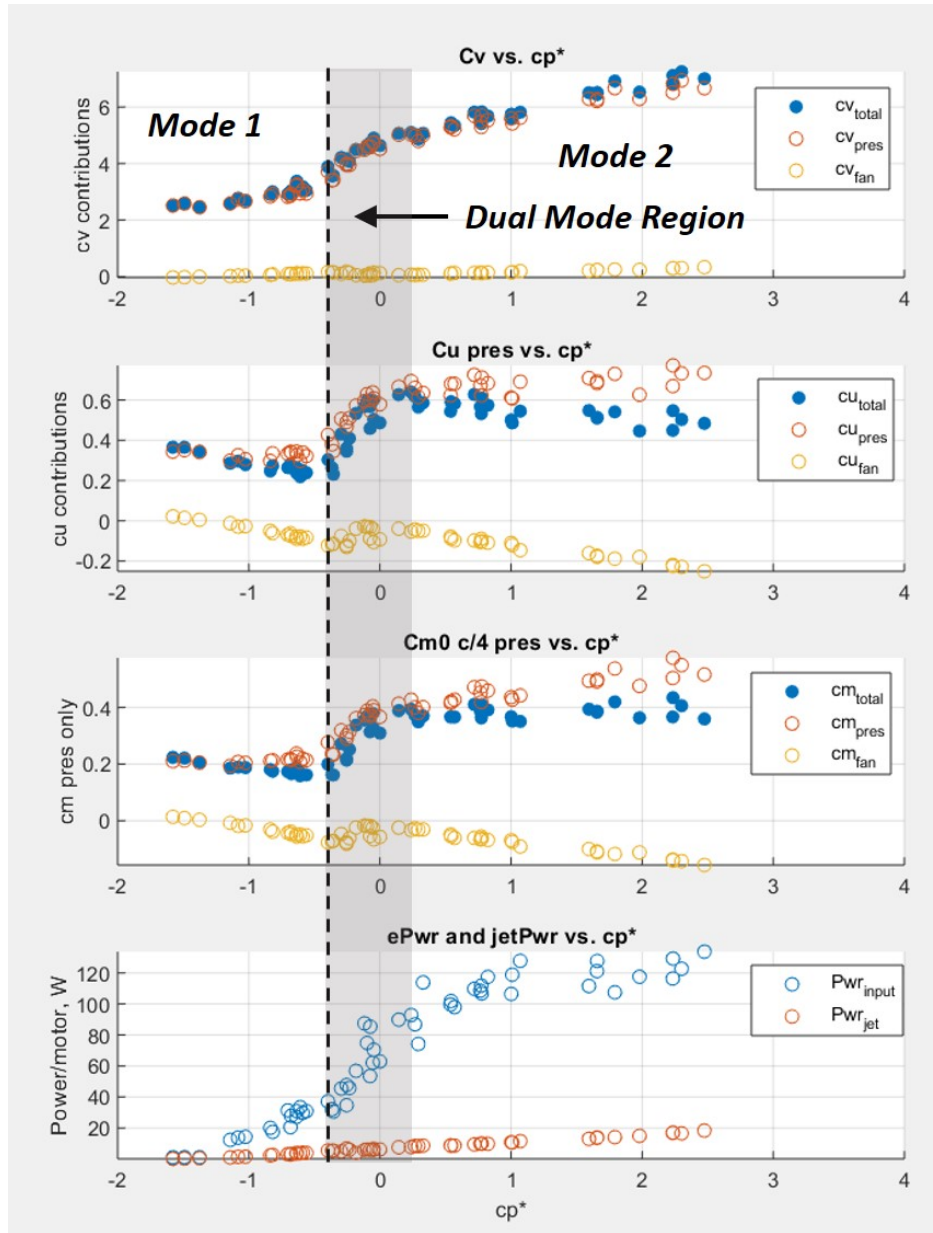


Figure 3.12: Specific example condition where the transition between Mode 1 and Mode 2 is well defined, and the bi-modal response is easily observed for a constant input power.

Also, for Mode 2 operation the pressure coefficient range on the suction surface pressure taps is $-7.3 > c_p > -5.2$.

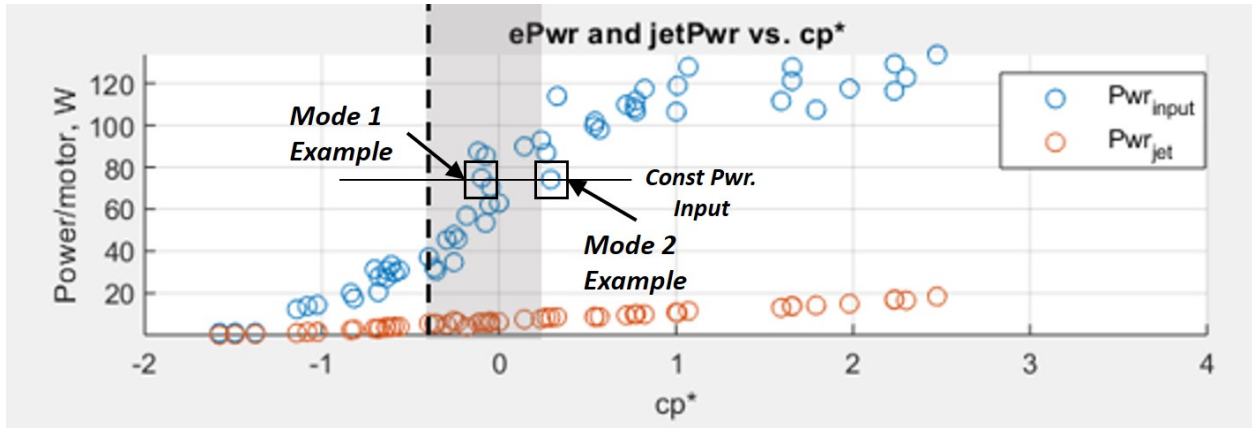


Figure 3.13: Example points showing where each mode can occur at the same power setting.

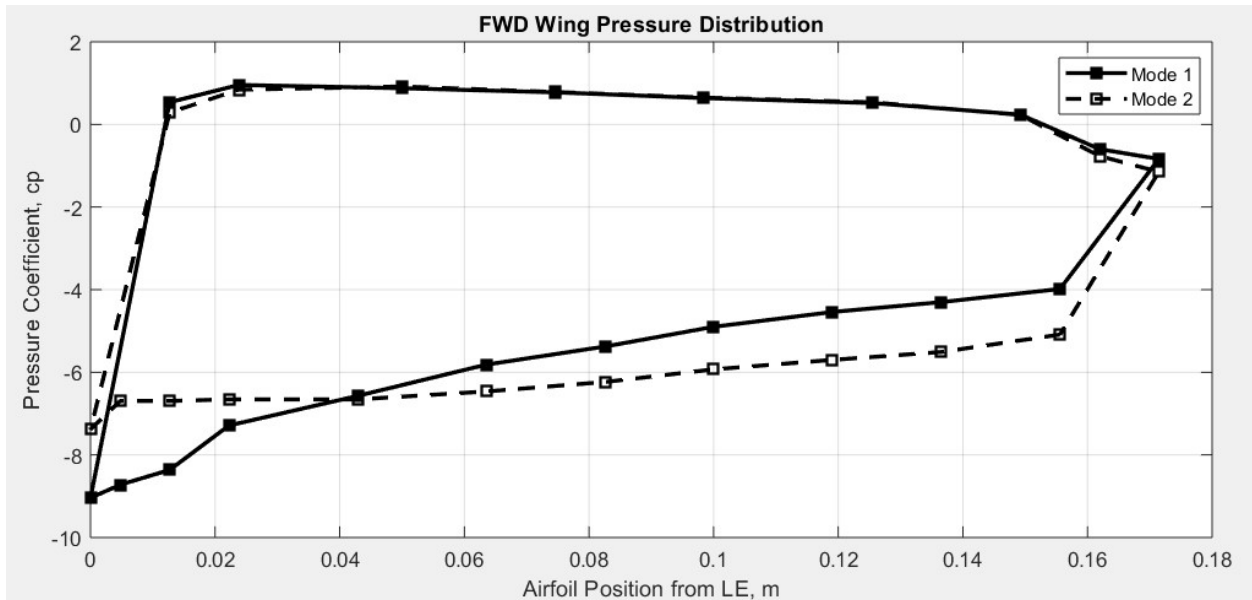


Figure 3.14: Pressure coefficient distribution about the forward wing for Mode 1 and Mode 2 observed at a constant input power setting where c_p^* is near 0. Where Mode 1 is present, $c_p^* = -0.045$ and where Mode 2 is present $c_p^* = 0.258$.

Significant changes to the pressure distribution around the upper and lower flap surfaces are also observed. These changes are consistent with the effective increase in c_p^* observed as well. With constant power input, $c_p^*|_{Mode1} = -0.05$ while $c_p^*|_{Mode2} = -0.258$.

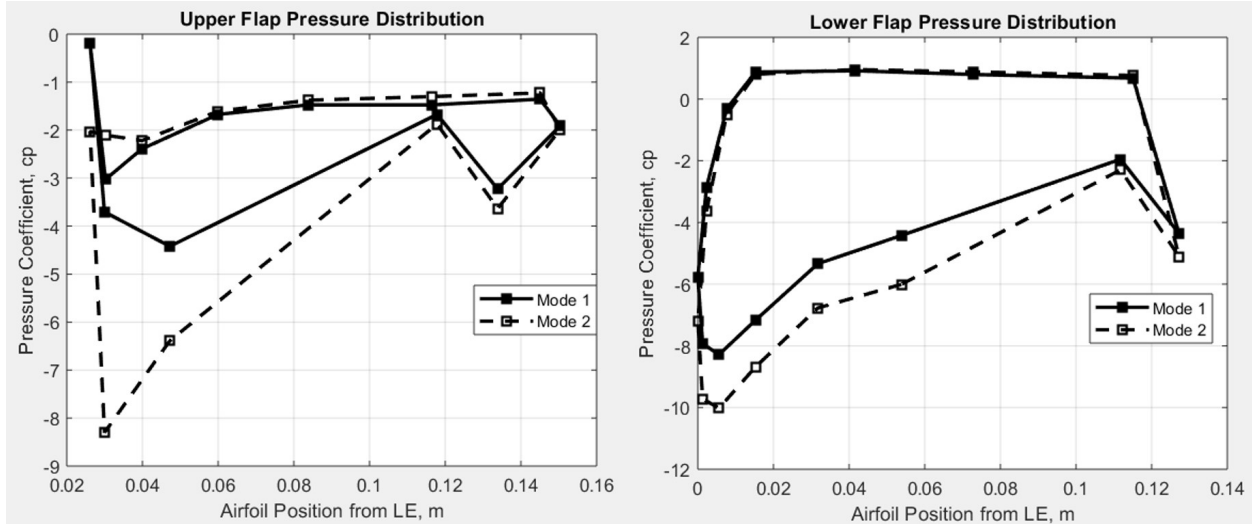


Figure 3.15: Pressure coefficient distribution about the upper and lower flap surfaces for Mode 1 and Mode 2 observed at a constant input power setting where c_p^* is near 0. Where Mode 1 is present, $c_p^* = -0.045$ and where Mode 2 is present $c_p^* = 0.258$.

Qualitatively, during the experiment, the pressure profile was readily observable on the manometer bank. As the CDP system alternated between Mode 1 and Mode 2, the changing pressure distribution was observed as well. Ultimately, beyond the dual mode region, the pressure profile was observed to stabilize and sustain Mode 2 operation.

3.6 Conclusions

The bi-modal response of the CDP system is presented in this chapter. The onset of this behavior appears to be a function of the flap angle θ as well as the forward wing angle α . Mode 1 is characterized by fully attached flow over the suction surface of the forward wing with linear proportionality with c_p^* retained for most operating conditions. In contrast, Mode 2 operation is characterized by fully separated flow over the suction surface of the forward wing, where this flow is ultimately ingested by the embedded fan system, as shown

in Fig. 3.3. This creates a *trapped stall* condition that artificially increased the camber of the wing section. This condition appears to be stable in the context of the 2D wind tunnel experiment, given that sufficient power is applied, increasing c_p^* beyond the dual mode region for a specific operating condition.

Because this bi-modal behavior influences all aerodynamic coefficients, it has potentially disastrous implications for aircraft stability and control. This markedly non-linear response to applied power occurs in the regime where VTOL aircraft are most susceptible to control loss, the transition between forward flight and hover.

Consider for example a transition approach (or departure) where $\alpha = 9$ deg and $\theta = 40$ deg. Since each mode can occur at the same power setting, assume that that both wings are operating in Mode 1, and the aircraft is in straight, level, and unaccelerated flight (SLUF). Now consider that the right wing enters Mode 2 operation, while the left wing is maintains Mode 1. In this condition, the aircraft will immediately roll to the left, due to the increase in lift associated with Mode 2 operation on the right wing. The increased drag also associated with Mode 2 will cause the aircraft to yaw to the right, creating a cross-controlled condition. Further complicating the situation, the aircraft will experience an increase in pitching moment, causing the nose to pitch up. These changes will be large, aggressive, and unpredictable in the dual mode region for a specific operating condition. For a conventional aircraft, this situation is identical to the control inputs for a violent aerobatic maneuver known as a snap-roll, where the aircraft rotates rapidly about all control axes. These maneuvers are spectacular under controlled conditions, but are catastrophic if entered accidentally during near-ground operations, such as landing approach or departure.

As the bi-modal response of the CDP system presents significant challenges for aircraft operations, it will not be considered in the remainder of this research effort. The entirety of the CDP experimental data is included as an appendix to this document. A thorough evaluation of the bi-modal transition is required before this system can be successfully applied to manned or unmanned applications, and is an area for future research. Additionally, while Mode 2 operation appeared to be stable given sufficiently large c_p^* for the two-dimensional wing section studied in the wind tunnel experiment, it is unknown whether a finite CDP wing will exhibit this same stability.

Chapter 4

Hybrid Electric Power System (HEPS) Experiment Results

4.1 Introduction

The objective of this chapter is to discuss the test methodology for identifying and characterizing significant attributes of the dynamic response of the hybrid power system to changes in power demand, as well as the results from these experiments. These tests will be performed both with and without the support of a slack bus to quantify the differences in the dynamic response. This will additionally assist in developing an understanding of the sizing and design requirements of such a slack bus for airborne applications. The testing of this system is fully automated with prescribed test protocols executed by the system control processor. These protocols produce very repeatable results and therefore

provide an accurate representation of the electrical and mechanical dynamics of the system.

4.2 Test Profiles

In order to ensure repeatable results, automated test protocols are designed to evaluate the dynamic response of the hybrid system to specific changes in power demand. No specific testing procedures are discussed in the applicable literature. As such, the presented procedures represent an original contribution to the testing, standardization, and evaluation methods for small hybrid-electric power systems. These tests can be grouped into two categories.

- **Step Response** Step response tests are designed to evaluate the response of the system to discrete step changes in power demand from zero power to full power and from full power to zero power, also while maintaining a constant voltage set point.
- **Ramp Response** Ramp response tests are designed to evaluate the response of the system during a ramp from zero power to full power, then from full power to zero power, while maintaining a constant voltage set point.

Additionally, more context for these tests, as well as the rating data for the components used in this experiment are provided in detail in Appendix C.

Slack Bus Usage

Typically all cases are performed using the support of the slack bus. However, as mentioned previously specific cases are performed without slack bus support to determine the impact of

the slack bus on the overall performance of the system. Also, given the forward voltage drop of the power diodes, the control voltage for the slack bus is set one volt below the voltage set point in the controller.

$$V_{slk} = V_{spt} - V_f \quad (4.1)$$

For these experiments, $V_f \approx 1V$ with a test operating at a $33V$ set point. The slack bus is set for $32V$ so that when the generator output voltage is within $\pm V_f$ of the desired set point, the power diode will not conduct.

4.3 Step Response Tests

The step response test is run by an automated protocol. Here, the step response of the system is investigated throughout the operating range of the engine at a specific voltage set point.

The automated test protocol used to evaluate the step response of this system uses the following procedure.

- 1 Begin with the engine at idle

Step Response Test Condition Summary				
No. Steps	Hold Time, sec/step	Control Voltage, V	Slack Bus Voltage, V	Runs
4, $350\mu s/step$ or $22.5\%/s$	10 sec/step	33	—	4
4, $350\mu s/step$ or $22.5\%/s$	10 sec/step	33	32	4
5, $280\mu s/step$ or $22.5\%/s$	10 sec/step	33	32	4

Table 4.1: Step Test Condition Summary

- 2 Start the test protocol
- 3 The engine controller will activate and the engine will accelerate to its target generator output voltage
- 4 Hold this constant-voltage, zero-power condition for the specified time
- 5 Step up the load control command the specified distance, either $280\mu s/step$ or $350\mu s/step$.
- 6 Hold each condition for the specified duration of 10 seconds.
- 7 Repeat this process until the maximum allowed duty cycle is reached, $D_{max} = 0.9$ with a load signal command of $2200\mu s$
- 9 Step back down to the zero-power condition using the step sizes and conditions given in ⑤ and ⑥
- 8 Hold this condition until the test is manually stopped

The step-up and step down loading profiles are shown in Figs. 4.1 and 4.2 respectively.

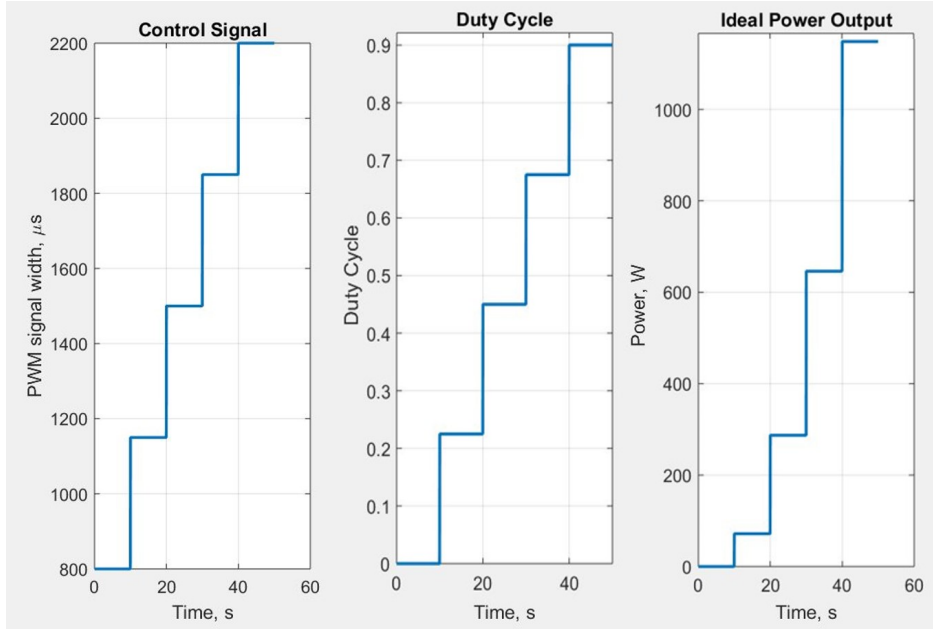


Figure 4.1: Similar to the ramp response cases, the duty cycle is a linear multiple of the control signal for all time in this test protocol. Again, the ideal power $P_{ideal} \propto D^2$.

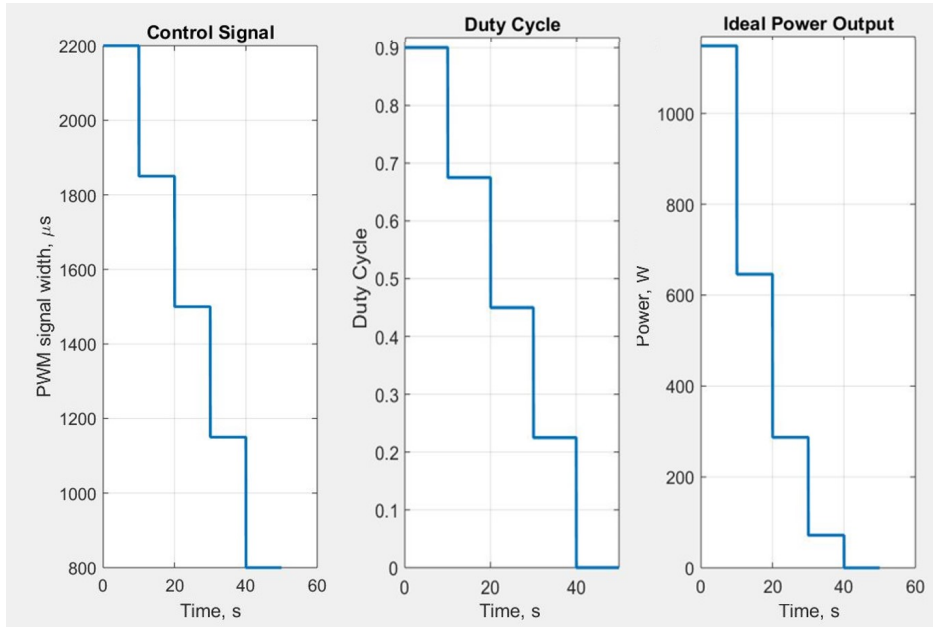


Figure 4.2: For all step response cases $s_{down} = -s_{up}$.

4.4 Ramp Response Tests

In order to evaluate the ramp response of the hybrid system, several different test protocols were devised. These test are all comprised of the same key elements and process steps.

- 1 Begin with the engine at idle
- 2 Start the test protocol
- 3 The engine controller will activate and the engine will accelerate to its target generator output voltage
- 4 Hold this constant-voltage, zero-power condition for the specified time, about 10 seconds
- 5 Ramp up the load control command at the specified rate until maximum allowed duty cycle is reached, $D_{max} = 0.9$
- 6 Hold $D = 0.9$ for specified duration, typically between 15 and 20 seconds.
- 7 Ramp back down to the constant voltage, zero-power condition
- 8 Hold this condition until the test is manually stopped, about 10-15 seconds

For characterizing the ramp response, two ramp rates were evaluated

$$R_{slow} = 108\mu s/s \rightarrow \Delta D_{slow} = 0.069/s \rightarrow 13.04s \quad (4.2)$$

$$R_{fast} = 216\mu s/s \rightarrow \Delta D_{fast} = 0.138/s \rightarrow 6.52s \quad (4.3)$$

With perfect conductance, the nominal DC output voltage from the PWM controller is given by

$$\bar{V}_{PWM_{out}} = DV_{in} \quad (4.4)$$

Since this PWM duty cycle is controlled by an external servo-driven potentiometer, where the angular position of the potentiometer is linearly proportional to the input signal to the servo

$$D = A\theta_{pot} = B\theta_{servo} = C(\text{servo}_{PWMsig}) \quad (4.5)$$

Where A , B , and D are proportionality constants.

Therefore the following relationship with ideal load is developed as a function of duty cycle

$$\underline{P}_{ideal} = I.^2 R_{load} = \left(\frac{\bar{V}_{PWMout}}{R_{load}} \right)^2 R_{load} = \frac{(DV_{in})^2}{R_{load}} \quad (4.6)$$

The ramp-up and ramp-down loading profiles are shown in Fig. 4.3 and 4.4 respectively.

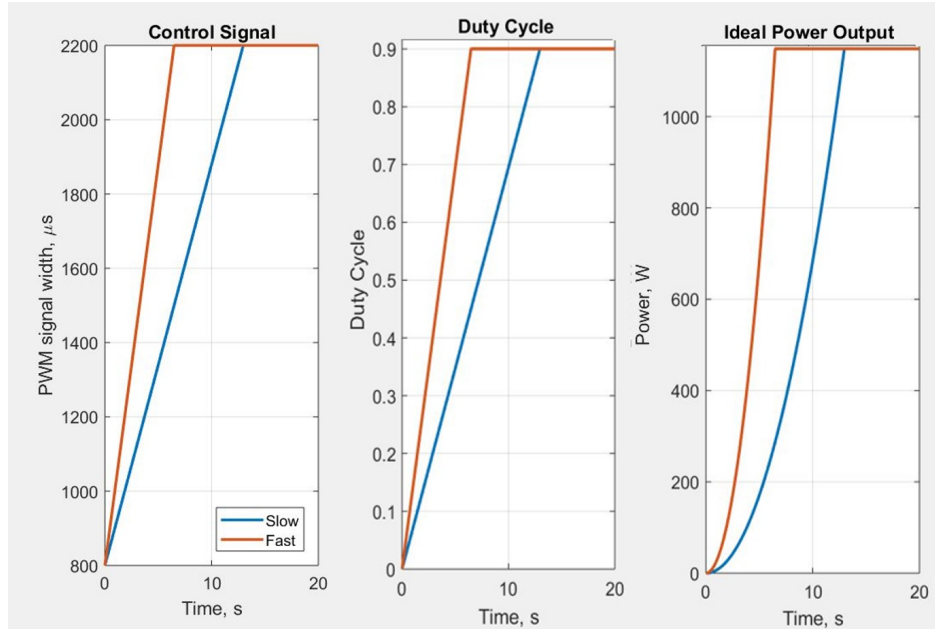


Figure 4.3: The duty is a linear multiple of the control signal for all time in this test protocol. However, the ideal power $\underline{P}_{ideal} \propto D^2$.

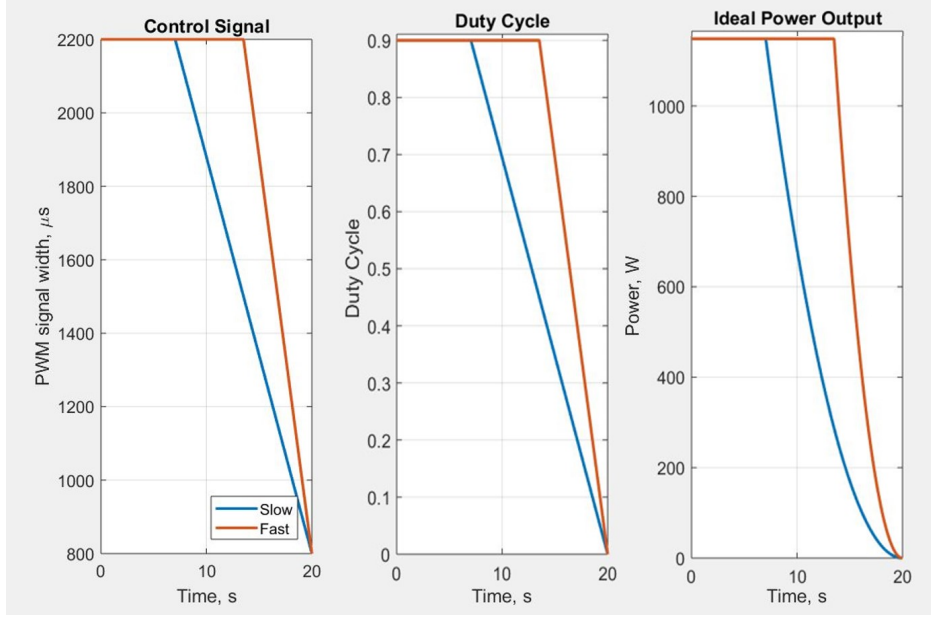


Figure 4.4: For all ramp response cases $R_{down} = -R_{up}$.

As shown in Table. 4.2, the tests emphasized the 33V operating setpoint with the fast and slow ramps. Other conditions were tested to verify the consistency of the results and to establish behavioral trends.

The ramp response test cases are typically run at 33V and 40V. This is to shift where the electrical loading relative to the maximum torque response of the engine. Depending on

Ramp Response Test Condition Summary				
Rate, $\mu s/s$ or $\%D/s$	Hold Time, sec at $D = 0.90$	Control Voltage, V	Slack Bus Voltage, V	No. of Runs
108 or 6.9	20	33	—	4
108 or 6.9	20	40	—	3
108 or 6.9	20	40	39	2
108 or 6.9	20	33	32	12
216 or 13.8	20	33	32	8
216 or 13.8	20	40	—	3

Table 4.2: Ramp Test Summary

the maximum power the engine can produce in a specific rpm range, the requirements from slack bus may be significantly altered.

4.5 Results Summary and Critical Operating Regimes

This series of experiments explores the dynamic response of the system to both ramped and stepped changes in power demand. Here two different ramp rates are evaluated, $216\mu s/s$ and $108\mu s/s$. These will simply be referred to as the 'fast' and 'slow' ramps respectively. Each step response experiment consists of four discrete steps, both increasing and decreasing between zero power and maximum load power dissipation at the specific control voltage. As a point of reference, the maximum continuous current output from the generator is $\sim 40A$ throughout the operating range of the engine. The detailed specification of the HEPS design and components are provided in Appendix C.

4.5.1 Control Summary

For all tests in this experiment, the same PID control implementation and gain values are used. The controller is implemented as

$$u_k = k_p e + k_i \sum_{k=0}^k e \Delta t + k_d \frac{e_k - e_{k-1}}{\Delta t} \quad (4.7)$$

The derivative gain k_d though small has a significant effect on the response of the system as observed in preliminary testing, accelerating the response and preventing overshoot. The measurement noise prevents the use of larger values of k_d .

The loading and unloading phases of the ramp rate experiment provide insight into each associated operating regime of the system, i.e. the loading regime response, and the unloading regime response.

4.5.2 Data Reduction

Since control of these experiments is fully automated, the results from each set of tests are very repeatable. Typically a set of tests consists of at least three sequential runs of the test protocol. As shown in Fig. 4.5 and Fig. 4.6, the dynamic response of the system is nearly identical for each separate run. Therefore, when comparing behaviors between different operating conditions, such as those between fast and slow ramp rates or with and without the slack bus, the response of the system will be estimated by taking the average response from all individual runs at a particular condition.

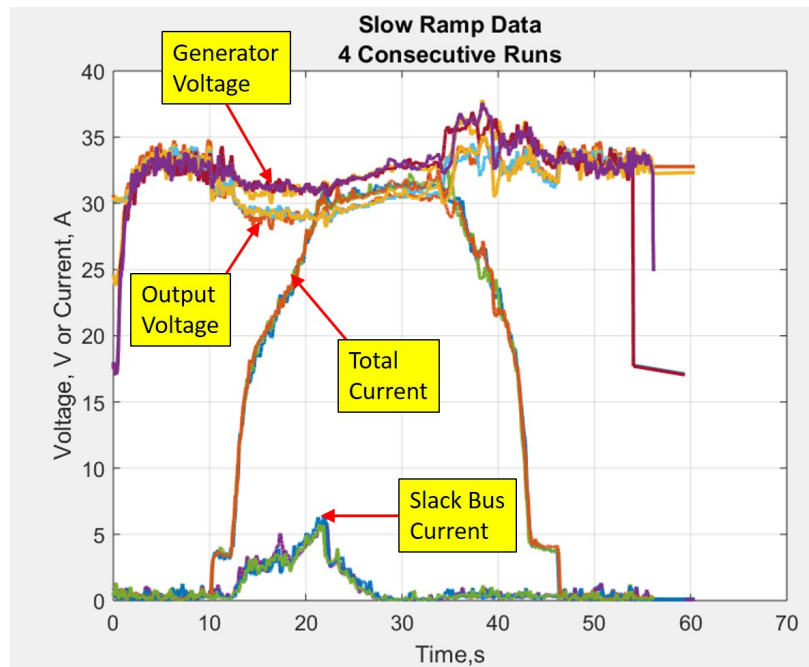


Figure 4.5: For several separate sequential ramp response tests, the response of the system is shown to be very repeatable. This performance is consistently maintained throughout the experiment.

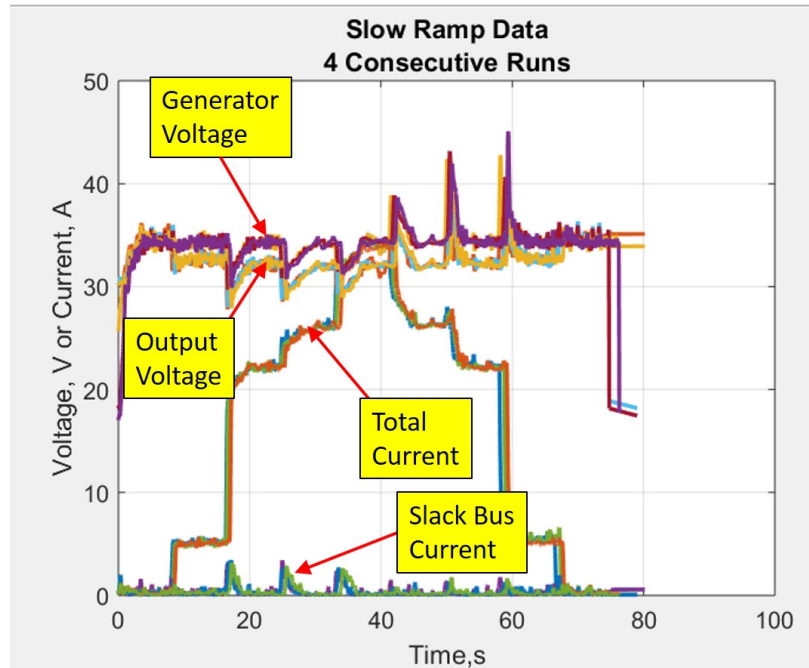


Figure 4.6: Similar to the ramp rate data, the step response data is shown to be very repeatable. Again, the mean value of several consecutive responses is assumed to represent the average behavior of the system.

4.5.3 Measurement Noise - Servo Signals and RPM

The visible noise in the recorded control signals needs to be addressed before proceeding to evaluate the results. This noise is due to the manner in which the control signals for the load and the throttle servo were recorded. The architecture of the power system controller and data acquisition system is shown in Fig. C.16.

The data logging software and system control software are running in parallel on two separate microcontrollers. This is due to the fact that these are single thread processors and the serial communication protocols used to write data to the SD card are also used to write the PWM output signals used to control external analog devices, such as the load and throttle servos. Attempting to perform both tasks from the same single thread processor results in corrupting both the data stream to log file, and the control signal to the servo.

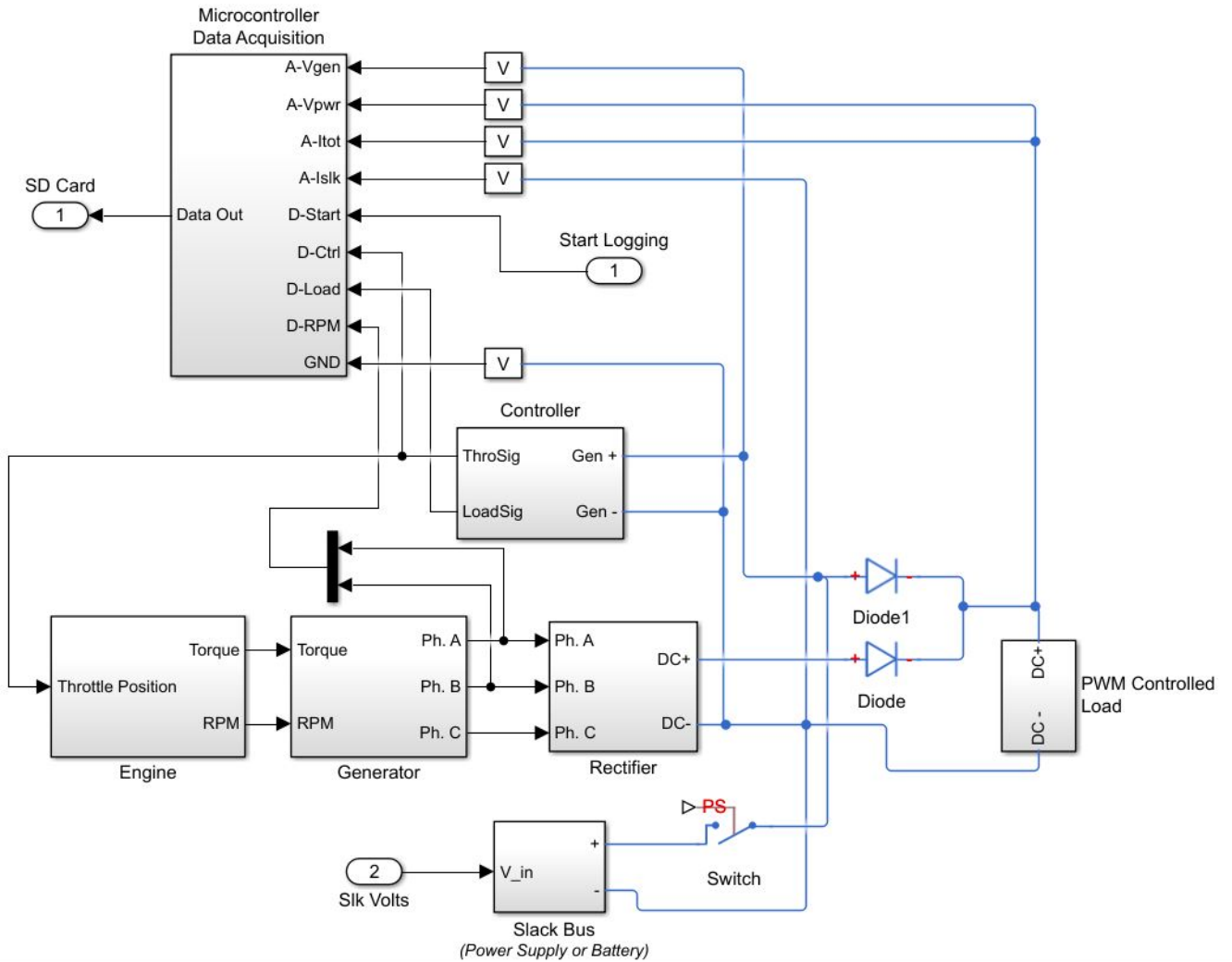


Figure 4.7: The data logger and system control software are running in parallel on two separate microcontrollers.

As a result the only way to log the system control signals to the SD card log file is to measure the width of the PWM pulses for each signal and record them indirectly from the data logging microcontroller.

Since this experiment seeks to capture the characteristic transient behaviors of hybrid power system, the rate of data logging is important for this experiment. Therefore, the fastest way to measure these PWM signals is to use a technique known as processor interrupts. This technique continuously polls each designated interrupt pin for a specific type of change. For

example, when measuring a PWM control signal, as shown in Fig. 4.8, we would like to know how long the pin state is HIGH.

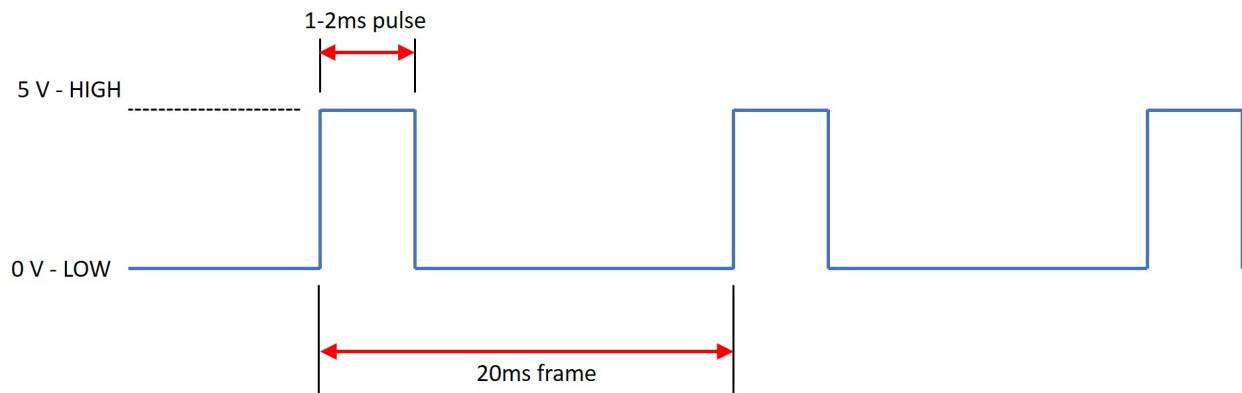


Figure 4.8: PWM controlled servos utilize a 1-2ms pulse contained in a 20ms frame, resulting in a control refresh rate of 50Hz.

In this case, the interrupt pins were monitored for a change in their digital state.

```
pinMode(interruptPinLoad, INPUT_PULLUP);  
  
attachInterrupt(digitalPinToInterrupt(interruptPinLoad), readLoad, CHANGE);
```

When a change was detected, all other processes were suspended and the following function `readLoad()` was executed.

```
void readLoad() {  
  
    loadTime = micros();  
  
    elapsedTimeLoad = loadTime - loadTime_old;  
  
    loadTime_old = loadTime;  
  
    if (elapsedTimeLoad < 2500 && elapsedTimeLoad > 790){ //a signal not a space  
  
        loadMeas = elapsedTimeLoad;  
  
        //lastReadL = 0;
```

```
}  
  
}
```

Also, these interrupt functions are suspended when the commands to write the data to the log file are being executed and are re-enabled immediately after as shown in the snippet.

```
noInterrupts();  
  
    logfile.print(m);           // milliseconds since start  
  
    logfile.print(", ");  
  
    logfile.println(dataString);  
  
interrupts();
```

Recall that the datalogger program is fully executed at approximately 400Hz, or every 2-3ms, with the processor operating at 16MHz. Also recall that a standard servo PWM frame updates at 50Hz. Because there are small differences in the length of each log entry due to changing character configurations in the data string, logging duration is not precisely constant. Also, due to the periodic execution of processor interrupt commands, the logging frequency is not constant. As a result, there is significant potential for task phasing when measuring and logging the PWM signals coming from the system control processor. This task phasing is the most likely cause of the noise observed in the measured servo signals, though the actual output signals to the servos have very low noise.

Additionally, the RPM signals are measured using a similar processor interrupt technique. In this case the AC voltage of a generator phase is monitored using a pulse position monitoring (PPM) device, whereby a pulse is emitted whenever the phase voltage exceeds the logic level voltage of the sensor. The emitted pulses are constant width and approx-

imately $100\mu s$ in duration, the time between these pulses can be related to the generator rpm, given the winding configuration of the generator.

- **Stator** - 12 slot armature
- **Rotor** - 14 pole permanent magnet rotor
- **Winding Scheme** - Aa bB Cc aA Bb cC

Where A, B, and C denote the phase wound clockwise around the armature tooth, and a, b, and c denote the phase wound counter-clockwise around the tooth. This gives the following relationship between generator angular frequency and phase angular frequency

$$\omega_{Phase} = \frac{N_{poles}\omega_{mech}}{2} \quad (4.8)$$

Which implies that

$$\omega_{mech} = \frac{2}{N_{poles}\Delta t_{PPM}} \quad (4.9)$$

Where Δt_{PPM} is the time measured between PPM pulses. These results are shown in Fig. 4.9. Several unfiltered data samples are included in this example. The heavy black line is the filtered results.

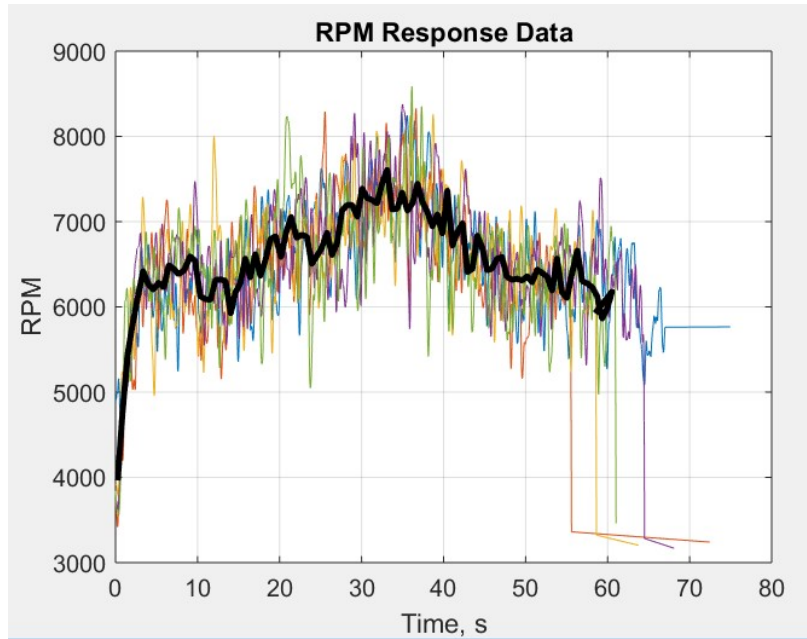


Figure 4.9: The signal noise in the RPM measurement is symmetric about a mean, and is assumed to be normally distributed.

4.6 Results - Loading Regime

For the purposes of this discussion, when the power demand on the hybrid system is increasing, the response is said to fall in the *Loading Regime*(LR). The response of the system in this regime is characterized by the following:

- **Step Response Characteristics**

- **Voltage Drop** - Voltage initially drops with the step increase in load.
- **Asymptotic Voltage Recovery** - Voltage recovers to the control target over a period of time and does not overshoot.
- **Slack Bus Support** - Slack bus conducts to temporarily supplement the load demand as the voltage from the generator lags under the increasing load.

- **Ramp Response Characteristics**

Step Response Test - Voltage Drop						
Step No.	Voltage Drop	Current Jump	Power Jump	Total I	Total Power	Time Const.
1	0.72 V	5.36 A	174 W	5.36 A	174 W	1.79s
2	4.01 V	17.01 A	558 W	22.37 A	732 W	1.29s
3	2.80 V	4.03 A	122 W	26.4 A	854 W	2.13s
4	2.52 V	8.03 A	243 W	34.43 A	1097 W	1.71s

Table 4.3: Step Response Test - Voltage Drop

- **RPM Reduction** - RPM initially falls below zero-load point.
- **Voltage Lag** - Voltage falls below control set point, and does not recover until the full power steady state demand is reached.
- **Slack Bus Support** - Slack bus conducts to temporarily supplement the load demand as the voltage from the generator lags under the increasing load.

Each of these conditions will be discussed in this section.

4.6.1 Step Response Results

Voltage Drop

The voltage is observed to drop sharply due to nearly instantaneous increase in power demand. This is due to both the reduced system rpm and increased conduction losses with increasing torque and current loads.

Given a voltage setpoint of 33V and the use of the slack bus set for 32V, for each step in the sequence the voltage drop is given below and shown in Fig. 4.10. These results are further summarized in Table. 4.3.

Asymptotic Voltage Recovery

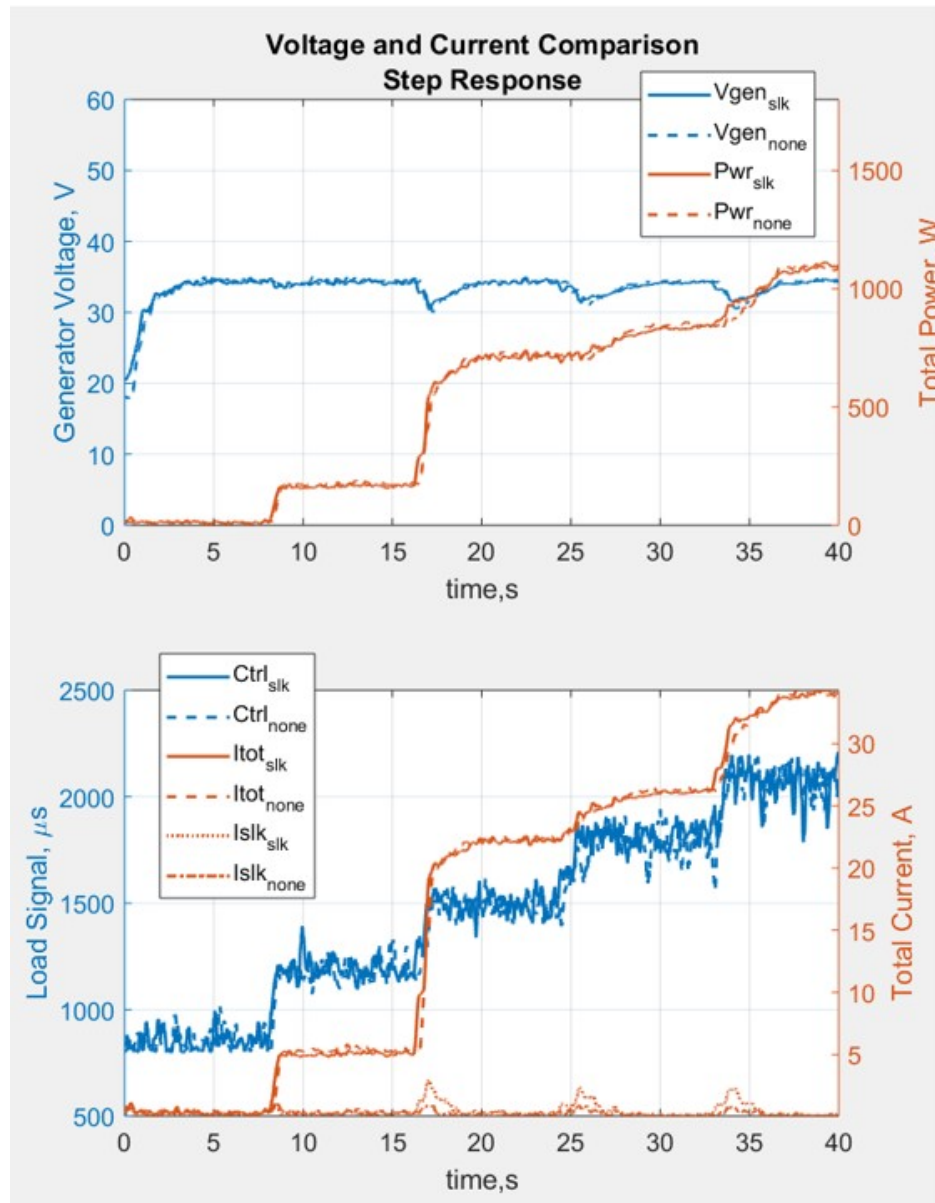


Figure 4.10: The step response tests are designed to evaluate the response of the system to step changes in power demand throughout its working power band for a specific control voltage.

The PID gains for this experiment are set up such that the controller response is robust and does not overshoot the setpoint voltage target, making it a simple matter to estimate the time-constant of the response across the power band of the engine. The time constant

will be defined as the time after the minimum voltage is measured where the voltage has recovered 63% of the measured voltage drop.

$$t_{min} \equiv t, \text{ when } V(t) = V_{min}, \text{ for a given step} \quad (4.10)$$

$$\Delta V = V_{set} - V_{min}, \text{ for a given step} \quad (4.11)$$

$$t_{63\%} \equiv t, \text{ when } V(t) = V_{min} + 0.63\Delta V, \text{ for a given step} \quad (4.12)$$

$$\tau \equiv t_{63\%} - t_{min} \quad (4.13)$$

These results are summarized for the step response data where the slack bus was utilized at 32V in the preceding table.

Slack Bus Support

The relative magnitude of the demands on the slack bus can be estimated throughout the engine power band by examining the peak current and energy draw from the slack bus for each step change in load power. The addition of a slack bus to the system represents added weight, which is detrimental for an airborne system. However, this addition may be able to extend the operating regime of the HEPS well beyond the operating regime of the engine-generator system alone. In this context, the addition of a slack-bus may be worth the additional weight penalty incurred.

Step Response Test - Slack Bus Energy Contribution				
Step No.	Conducting Duration	Slack Bus Voltage	Energy Output	Peak Current
1	$\sim 2sec$	32 V	0.008 Wh	1.11 A
2	$\sim 5sec$	32 V	0.035 Wh	2.97 A
3	$\sim 5sec$	32 V	0.035 Wh	2.34 A
4	$\sim 5sec$	32 V	0.033 Wh	2.28 A

Table 4.4: Step Response Test - Slack Bus Energy Contribution

4.6.2 Ramp Response Results - Loading Regime

RPM Reduction

While the reduction of system rpm upon initially loading the system is related directly to the increase in generator required torque as current demand increases, it is nonetheless important for characterizing the behavior of the system, as shown in Fig. 4.11. Particularly when the engine is operating at low power with low available torque, a rapid increase in current demand could stall the engine, causing the system to collapse.

Here we observe that the RPM initial drops as the load power demand increases.

The magnitude of the rpm reduction appears to be sensitive to the ramp rate.

- **Slow Rate** -650 rpm; from 6590 rpm to 5940 rpm
- **Fast Rate** -800 rpm; from 6550 rpm to 5750 rpm

The noise in the RPM measurement data prevents a more precise comparison. However, given the repeatability of the experiments, the magnitude of this speed reduction will help in model calibration.

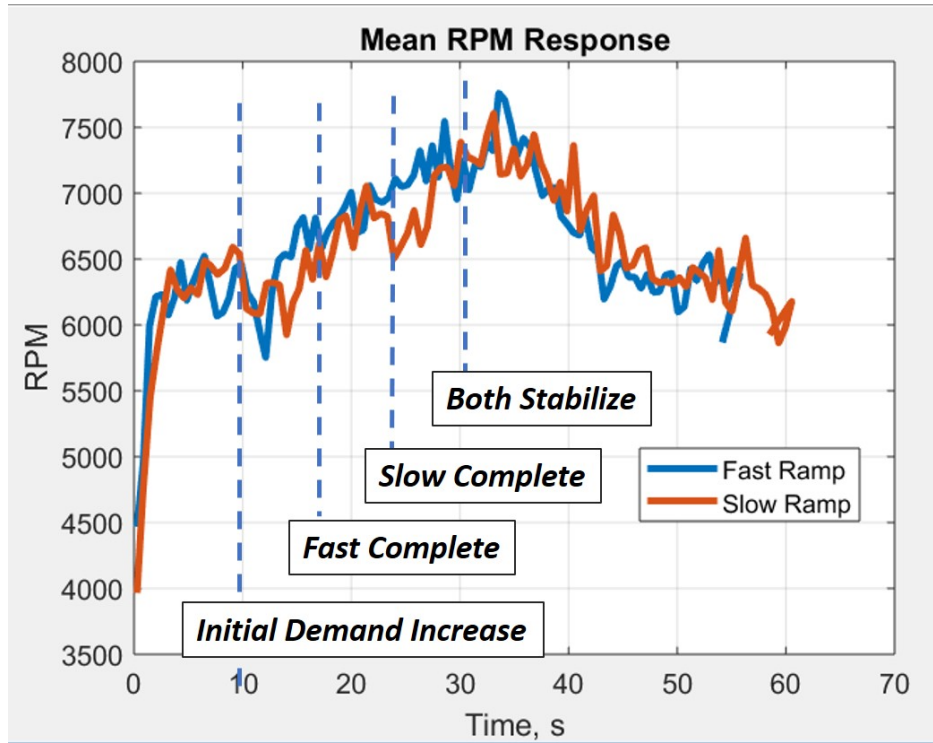


Figure 4.11: RPM Reductions appear to be sensitive to the ramp rate.

Voltage Lag

When the load is increasing, the PID controller only responds to the error in the voltage measurement. Recall that

$$e = V_{Set} - V_{meas} \quad (4.14)$$

Therefore, when the load is increasing the PID will typically lag behind the setpoint, particularly when the controller gains are setup for robust performance, limiting both overshoot and oscillation. Therefore it is convenient to describe this performance attribute in terms of maximum voltage deviation in a manner similar to the previous discussion of RPM reduction and in the time to stabilize *after* peak power demand is reached.

For a constant voltage setpoint of 33V, the voltage Lag is also sensitive to the ramp rate.

Ramp Response Test - Voltage Lag			
Rate	Min Voltage	Max Deviation	Recovery Time
Fast, $216\mu s/s$	29.86 V	3.14 V	12.95 sec
Slow, $108\mu s/s$	30.69 V	2.31 V	6.13 sec

Table 4.5: Ramp Test Response Summary - Voltage Lag

Ramp Response Test - Slack Bus Energy Contribution				
Rate	Conducting Duration	Slack Bus Voltage	Energy Output	Peak Current
Fast, $216\mu s/s$	$\sim 18sec$	32 V	0.494 Wh	8.80 A
Slow, $108\mu s/s$	$\sim 15sec$	32 V	0.179 Wh	2.64 A

Table 4.6: Ramp Response Test - Slack Bus Energy Contribution

Slack Bus Support

The slack bus support requirements are related to the voltage lag and rpm reduction, in that whatever load demand is not satisfied by the generator must be supported by the slack bus. Here it is convenient to describe this support in terms of conducting duration, peak current, and total energy drawn from the slack bus and shown in Fig. 4.12 and Table 4.6.

For a constant voltage setpoint of 33V, the slack bus support is also sensitive to the ramp rate.

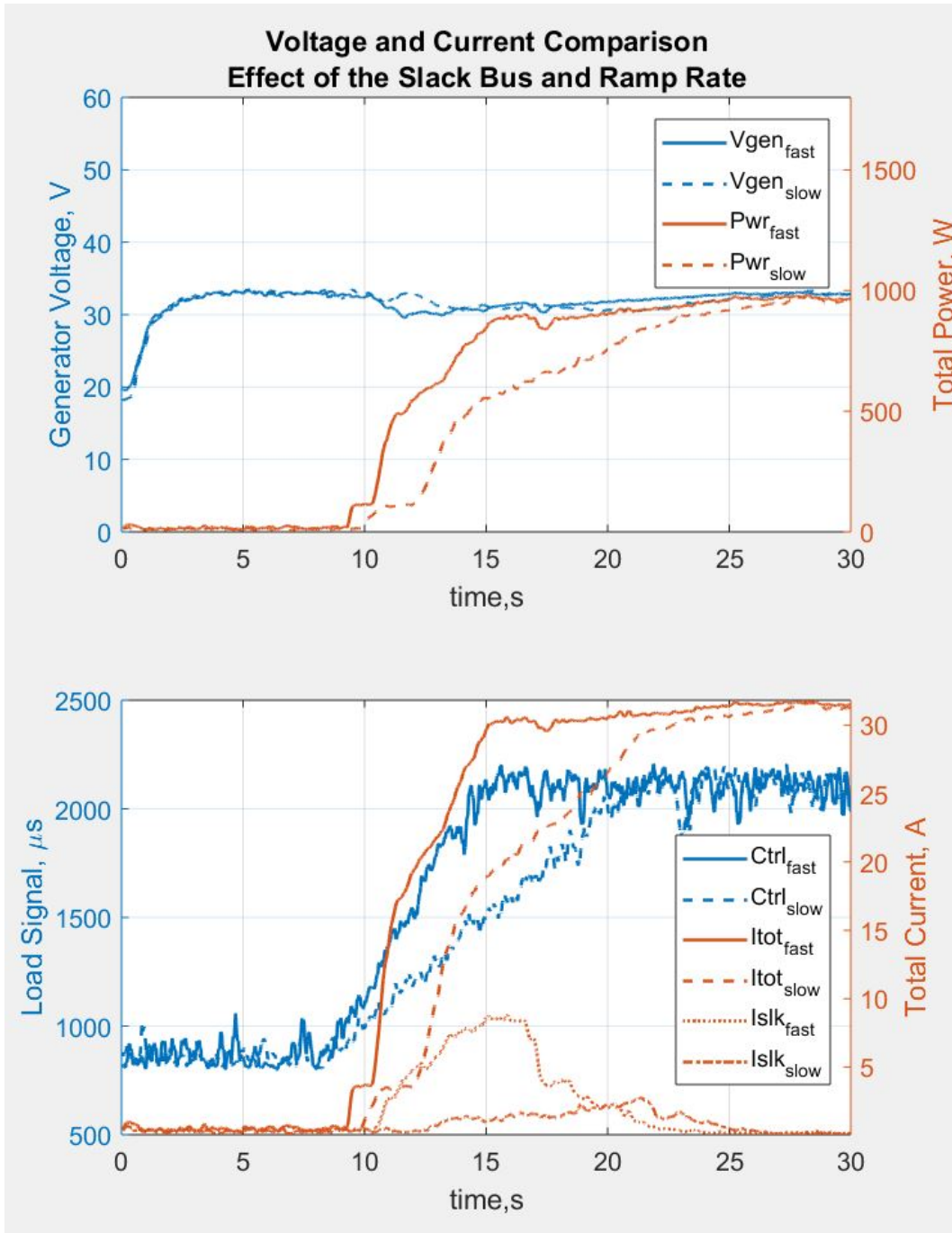


Figure 4.12: The loading ramp response of the system changes significantly depending on the ramp rate. Here, significantly more energy is drawn from the slack bus as the power demand increases.

4.7 Results - Unloading Regime

For the purposes of this discussion, when the power demand on the hybrid system is decreasing, the response is said to fall in the *Unloading Regime*(UR). The response of the system in this regime is characterized by the following:

- **Step Response Characteristics**

- **Voltage Jump** - Voltage initially jumps with the step decrease in load.
- **Asymptotic Voltage Recovery** - Voltage recovers to the control target over a period of time and does not overshoot.
- **Power Inversion** - Power transmitted to the load temporarily increases.

- **Ramp Response Characteristics**

- **Voltage Lead** - Voltage rises above the control set point, and does not recover until the zero power steady state demand is reached.
- **Power Inversion** - Power transmitted to the load temporarily increases.

Each of these conditions will be discussed in this section.

4.7.1 Step Response - Unloading

Voltage Increase and Asymptotic Recovery

As with the loading regime step response cases, the unloading regime tests were conducted only using a voltage setpoint of 33V. Upon each unloading step, the voltage was observed to increase dramatically before the controller recovered the voltage output to the desired

Step Response Test - Voltage Jump						
Step No.	Voltage Jump, V	Current Jump, A	Power Jump, W	Init. I, A	Init. Power, W	Time Const., sec
1	0.79	5.36	174	5.36	174	1.25
2	5.39	17.01	558	22.37	732	0.94
3	5.02	4.03	122	26.4	854	1.52
4	3.5	8.03	243	34.43	1097	1.91

Table 4.7: Step Response Test - Voltage Jump

setpoint. The discussion of both the voltage spike and the recovery time constant will be presented together in this regime.

The magnitude of the voltage jump and the recovery time constant are observed to be a function of the system output power as in the loading case. This behavior is shown in Fig. 4.13 and Table 4.7. While this behavior is observed in the experimental system, it is not observed in the simulation. As a result, the root cause of this phenomena is not well understood.

These cases are presented in order of ascending power to more directly compare with the loading regime step response cases.

The time constant will be defined in this regime as the time after the maximum voltage is measured where the voltage has recovered 63% of the measured voltage jump.

$$t_{max} \equiv t, \text{ when } V(t) = V_{max}, \text{ for a given step} \quad (4.15)$$

$$\Delta V = V_{max} - V_{set}, \text{ for a given step} \quad (4.16)$$

$$t_{37\%} \equiv t, \text{ when } V(t) = V_{min} + 0.37\Delta V, \text{ for a given step} \quad (4.17)$$

$$\tau \equiv t_{37\%} - t_{max} \quad (4.18)$$

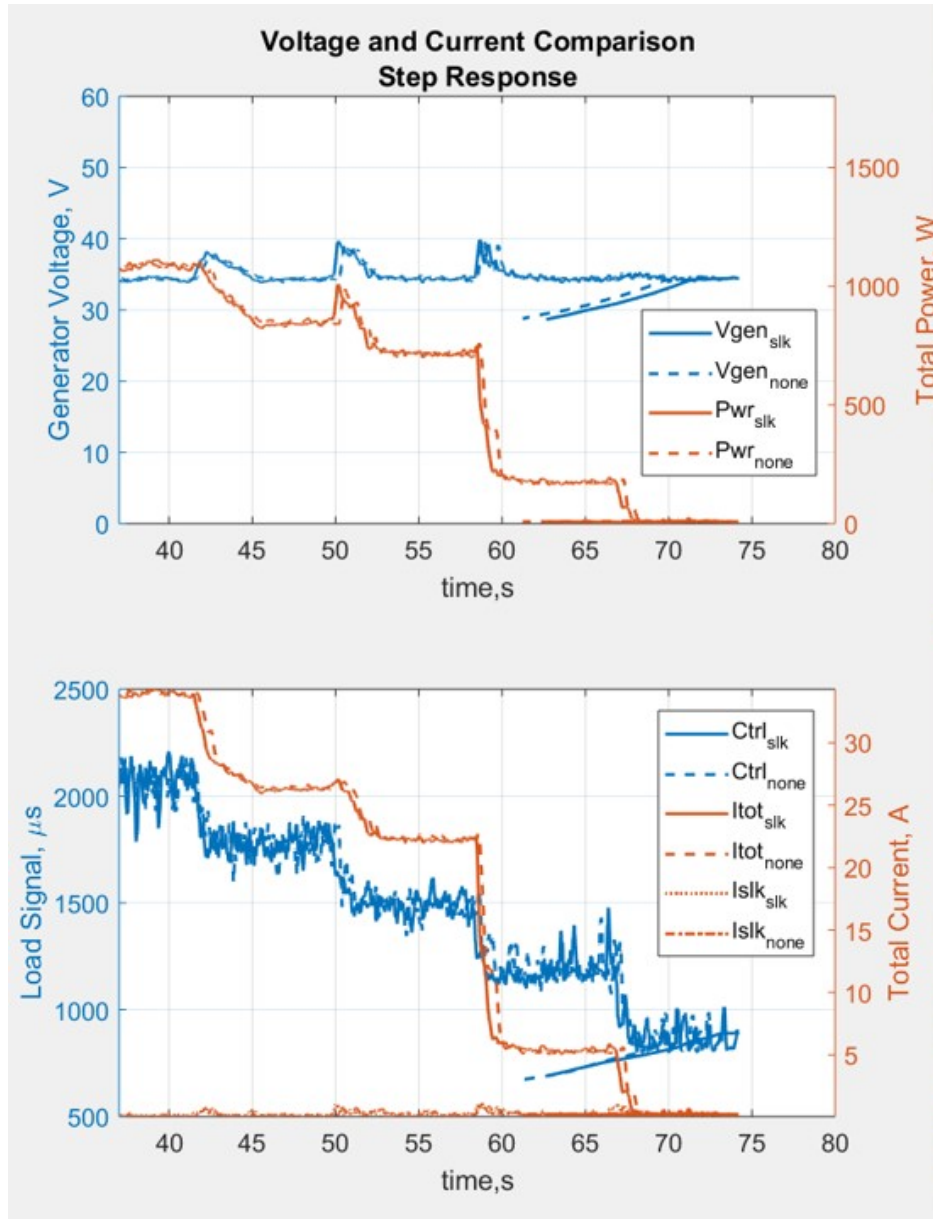


Figure 4.13: The descending step response tests are characterized by power inversions for each descending step in the power band. *Note that the data series 'tails' in this plot are artifacts from manually ending an experimental run, and are not physically significant.*

Step Response Test - Power Inversion				
Step No.	Steady Power	Peak Power	Max Deviation	Duration
1	174 W	195 W	21 W	0.6 sec
2	716 W	756 W	40 W	0.7 sec
3	848 W	1008 W	160 W	1.7 sec
4	1092 W	1092 W	0 W	0 sec

Table 4.8: Step Response Test - Power Inversion

Power Inversion

For each unloading step, the power system experiences some degree of power inversion. Though as stated previously, the mechanisms involved in this phenomena are not well understood. Further research is recommend to understand the phenomena driving this behavior and to develop fuel/air induction systems that effectively eliminate it.

These power inversions are characterized by the steady state power, peak power and duration. In this case the duration is measured from the time the power departs from steady state, to a maximum power, until it descends through the original steady state threshold. These cases were conducted with a control voltage setpoint of 33V.

4.7.2 Ramp Response - Unloading

Voltage Lead

As the system load is reduced, the net torque on the system due to the current load on the generator is reduced. This creates a net torque on the engine-generator system causing them to accelerate. While it is important to characterize both the initial rpm reduction in the loading regime as well as the voltage behavior, the change in rpm in this regime is not of

Ramp Response Test - Voltage Lead			
Rate	Max Volt- age	Max Deviation	Recovery Time
Fast, $216\mu s/s$	55.98 V	15.98 V	12.52 sec
Slow, $108\mu s/s$	49.61 V	9.61 V	4.57 sec

Table 4.9: Ramp Response Test - Voltage Lead

particular interest. This is due to the engine having minimal excess torque at low power and is therefore at risk of stalling. When the power is high, it is known that the excess torque with a reduction in load will cause the system to accelerate temporarily when using the PID controller discussed previously. However, this simultaneous unloading and acceleration creates a large transient voltage increase related both to the increase in rpm and decrease in conductive losses under the reduced current load. These voltage 'spikes' can cause damage to other components in the system, if not carefully managed.

Here the control voltage is increased to 40V and the magnitude of the voltage spike is observed to be sensitive to the unloading ramp rate, as shown in Fig 4.14 and Table 4.9.

Power Inversion

As a consequence of the voltage increase as well as the rpm increase, the power system often exhibits a temporary power inversion. Essentially, when the load is initially reduced, the power temporarily increases. This is characterized in terms of the steady state power output and the transient power peak, as shown in Table 4.10.

Again this is observed to be a function of the unloading ramp rate as shown in Fig. 4.14.

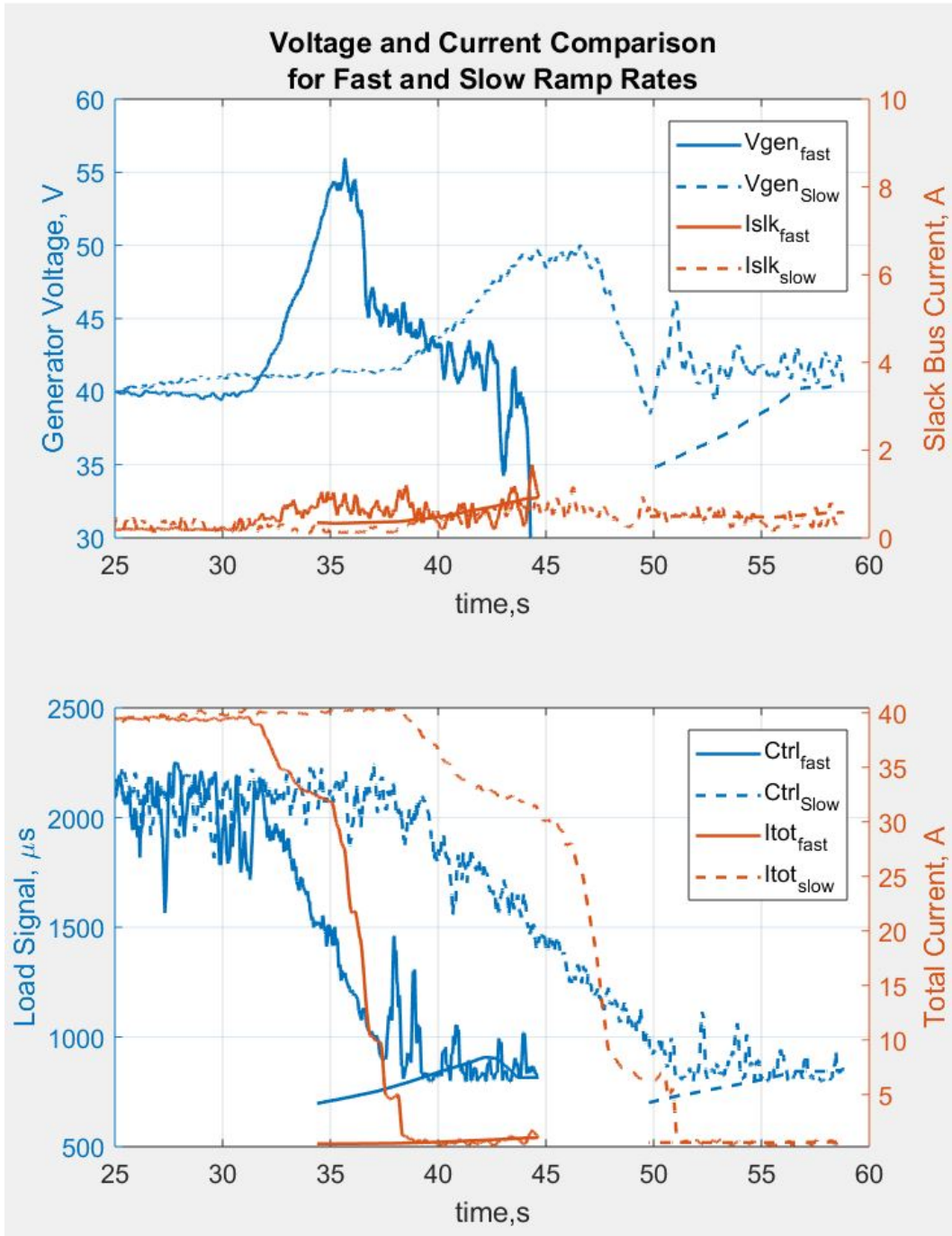


Figure 4.14: The unloading ramp response of the system changes significantly depending on the ramp rate. Here, significantly the voltage overrun is significantly greater for high unloading rates. *Note that the data series 'tails' in this plot are artifacts from manually ending an experimental run, and are not physically significant.*

Ramp Response Test - Power Inversion			
Rate	Steady Power	Peak Power	Max Deviation
Fast, $216\mu s/s$	1480 W	1650 W	170 W
Slow, $108\mu s/s$	1500 W	—	—

Table 4.10: Ramp Response Test - Power Inversion

When the slow ramp was applied to unload the system, the power output did not dramatically invert, as was the case when the fast ramp rate was applied. Rather, the system maintained an approximately constant power output before sharply declining, as shown in Fig. 4.15.

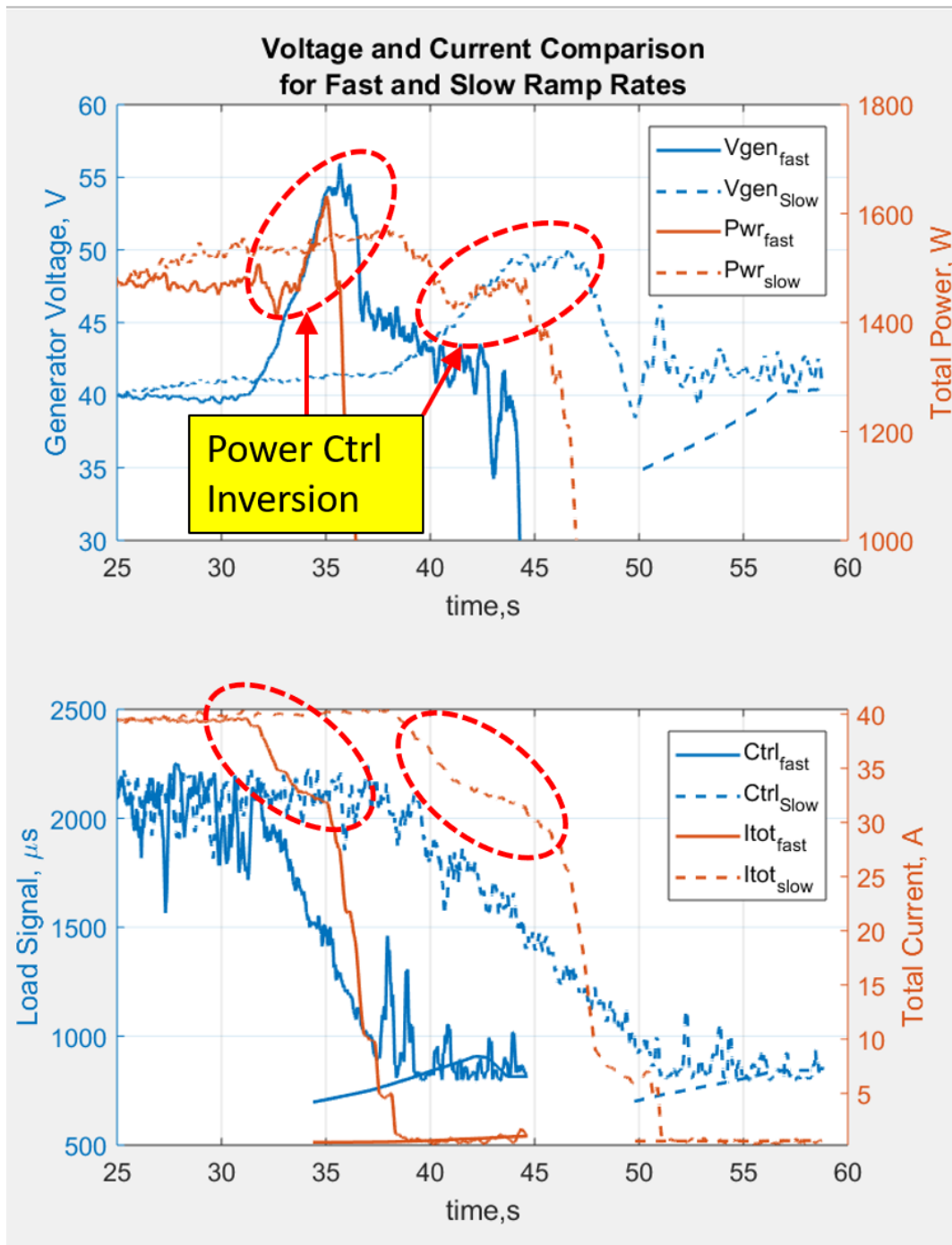


Figure 4.15: Depending on the rate at which the unloading process occurs, the output power response can temporarily invert, resulting in a short-term increase in power output prior to the desired decrease in power. *Note that the data series 'tails' in this plot are artifacts from manually ending an experimental run, and are not physically significant.*

4.8 Effect of The Slack Bus

4.8.1 On the 40V loading response

In this experiment, the slack bus can only provide additional power when the generator output voltage falls below the power diode voltage threshold, it cannot absorb excess power from the system. As a result, only the loading regime responses are impacted by the use of the slack bus.

Given a constant voltage setpoint of 40V, the system is examined both with and without the slack bus power available. At this condition, the slack is observed to reduce the oscillation of the power response when the system is undergoing the slow ramp rate test series. The change in this oscillatory behavior is shown in Fig. 4.16.

4.8.2 Effect of Voltage Setpoint on Slack Bus Support

The slow ramp rate test profile is applied when the system voltage setpoint is changes from 33V to 40V, with the slack bus supply voltage set to 32V and 39V respectively. Here, the higher voltage setpoint demands significantly more energy from the slack bus, despite the much more rapid power response shown in Fig. 4.17.

Additionally, the system was also tested under these same conditions without the slack bus applied in either case. The 40V setpoint is found to oscillate when the load is initially applied, whereas the 33V case does not, as shown in Fig. 4.18 and Table 4.11. While the addition of the slack bus works to damp these oscillations in this regime, the change in the response characteristics of the engine-generator system to a change in the operating voltage suggests that a fixed-gain controller is likely only a viable option if the controller is tuned

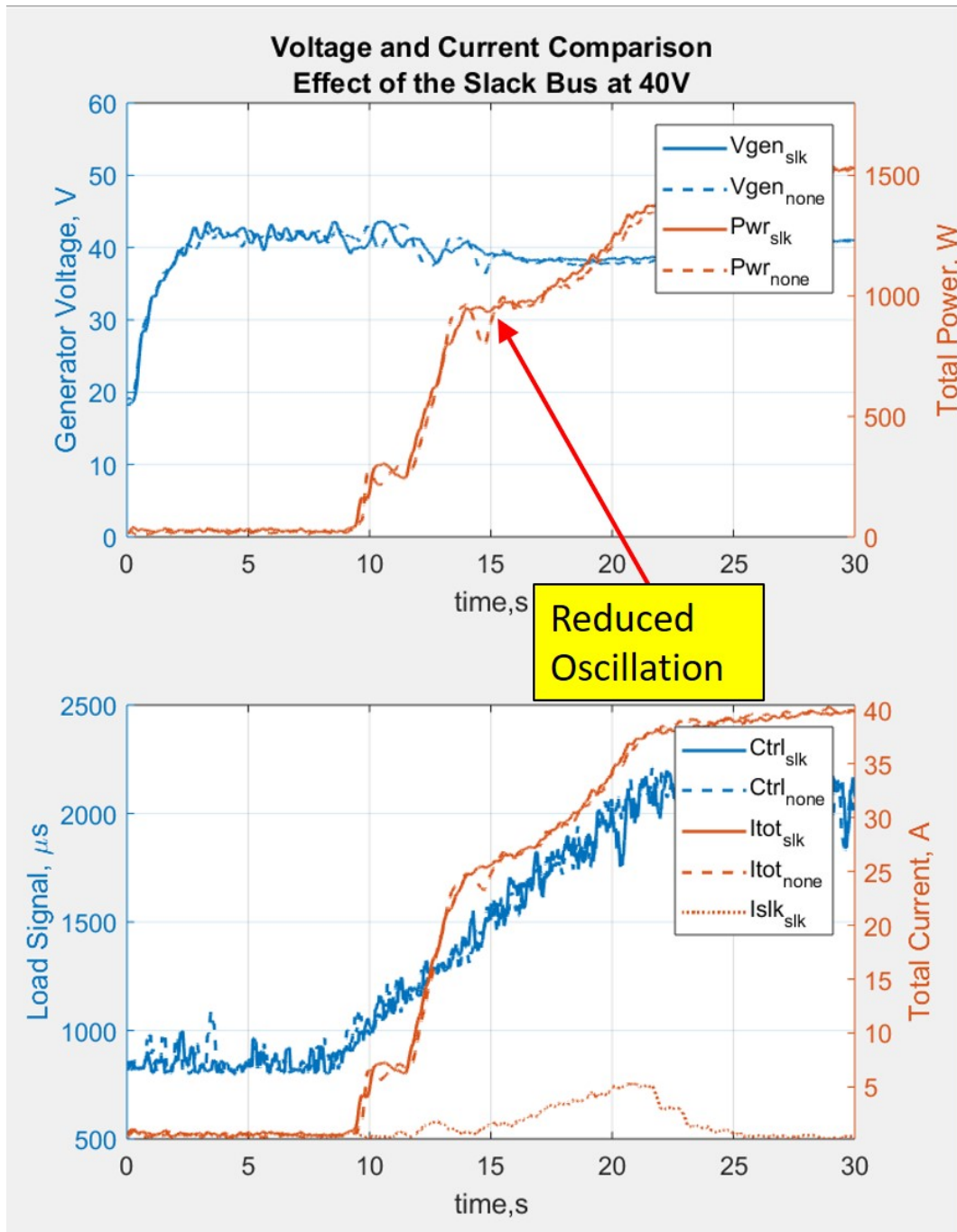


Figure 4.16: The addition of the slack bus in the 40V case reduces the oscillation of the system during the loading ramp.

for one specific operating voltage, which indicates a need for a more robust control strategy. This is explored later in this document, utilizing a dynamically adaptive voltage modulation design.

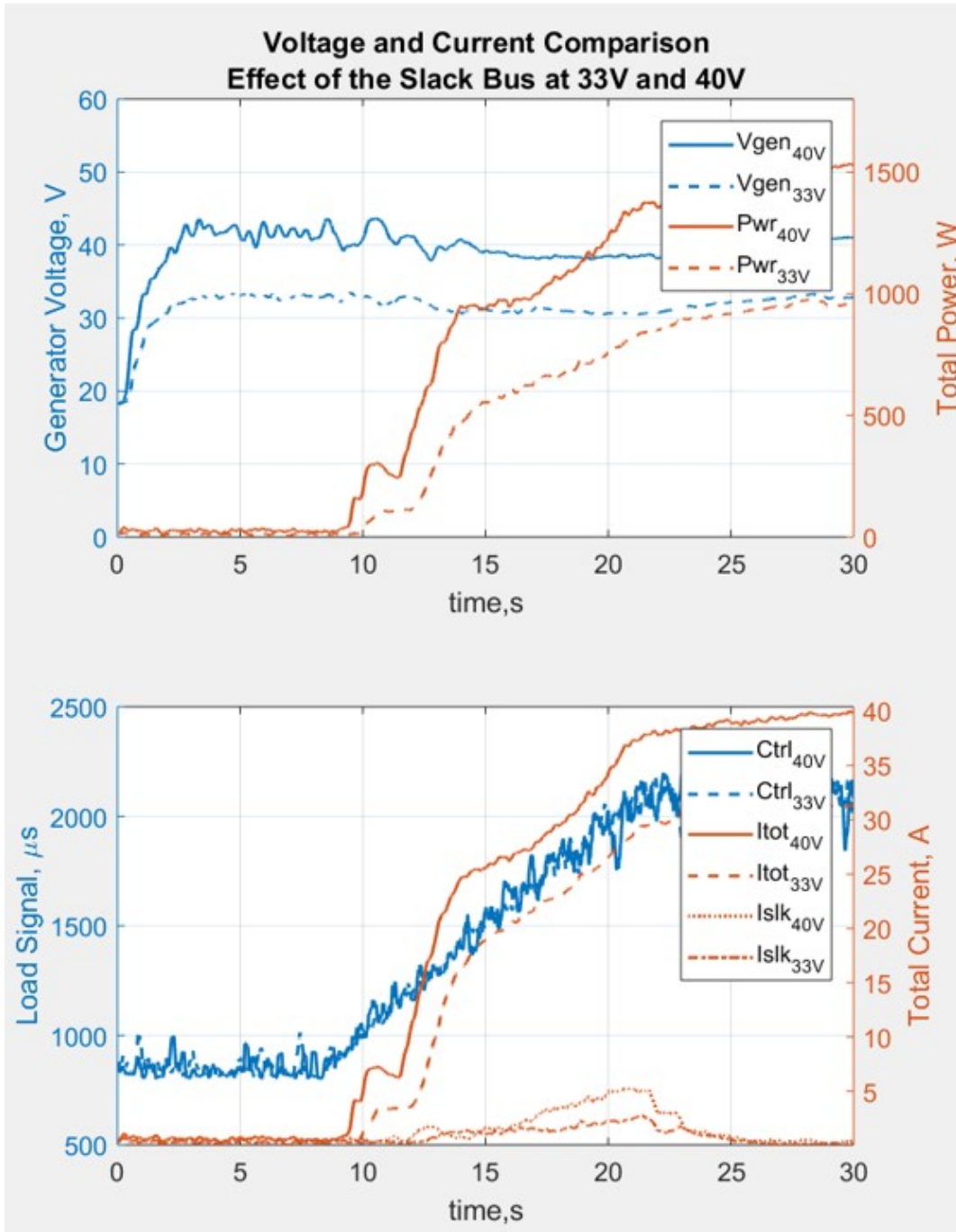


Figure 4.17: Increasing the control voltage from 33V to 40V has a significant effect on the response of the slack bus. Significantly more energy is drawn from the slack bus in the 40V case.

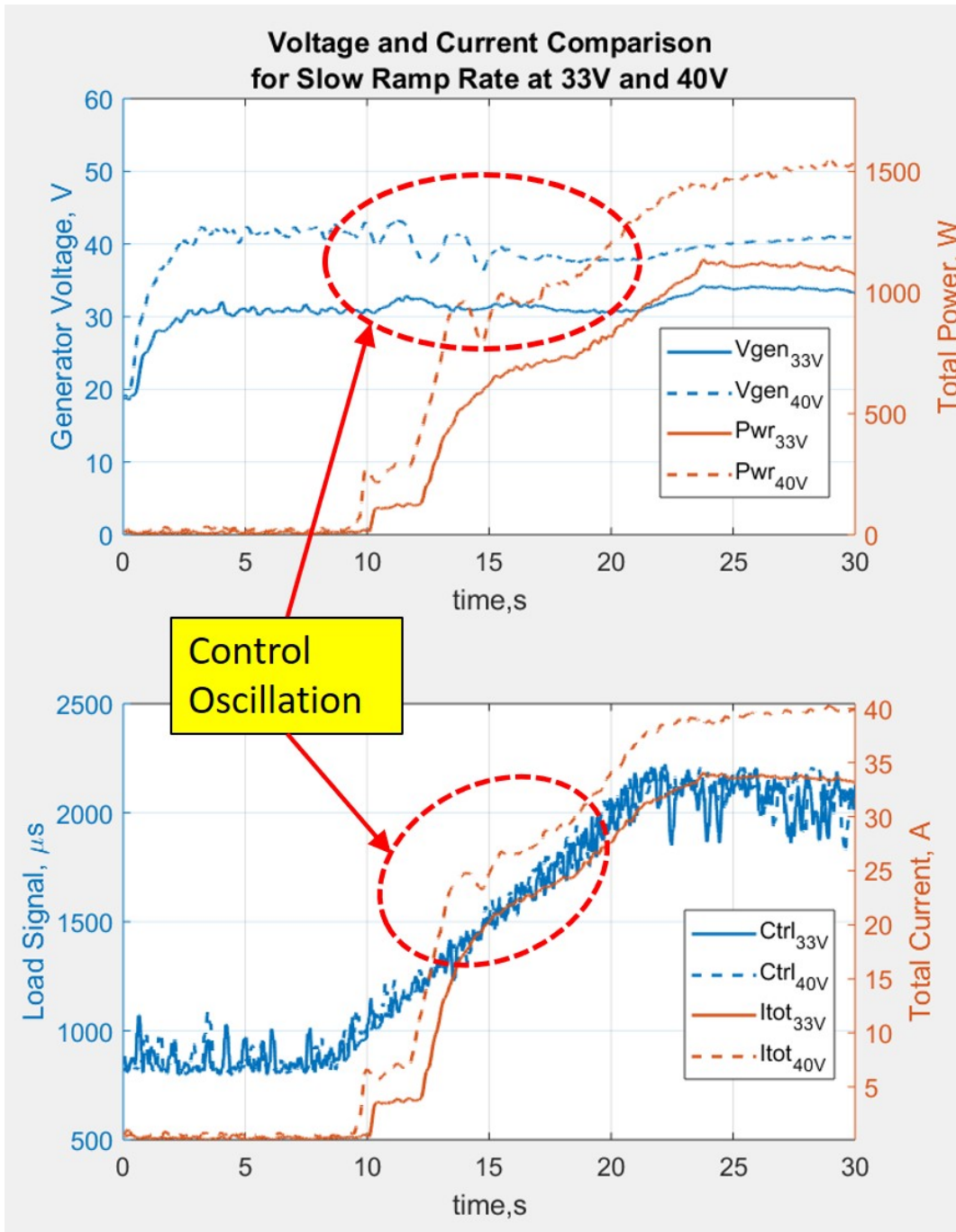


Figure 4.18: Increasing the control voltage from 33V to 40V has a significant effect on the response of the PID controller. Oscillation is clearly observed in the 40V case and absent in the 33V case.

Ramp Response Test - Slack Bus Energy Contribution				
Conducting Duration - $\sim 18sec$, both cases				
Ramp Rate	Max. Total. Current, A	Slack Bus Voltage, V	Energy Output, Wh	Slack Bus Peak, A
Slow, $108\mu s/s$	39.7	39.0	0.385	6.37
Slow, $108\mu s/s$	31.8	32.0	0.179	2.64

Table 4.11: Ramp Response Test - Slack Bus Energy Contribution

4.9 Conclusions

The objective of this experiment is to identify and characterize the attributes of the dynamic response of a hybrid generator system powered by a carbureted two-stroke internal combustion engine. This experiment illustrated that two distinct operating regimes exist for this type of system. These can be categorized simply as the loading and unloading regimes. Generally, the inverse of the behaviors in one regime are observed in the other regime. For instance, the loading regime is characterized by voltage drops in response to increasing power, while the unloading regime is characterized by large voltage increases when the load is reduced. In the loading regime, the voltage drop when subjected to step increases through the engine's power band are typically 2-4V, while the voltage increases for identical decreases in power are typically 3-5V.

The ramp rate and operating voltage were both found to have significant effects on the support required from the slack bus. For a given operating voltage, the slack bus was required to supply $\sim 2.75x$ more energy and deliver $\sim 3.3x$ more peak current than when the ramp rate is reduced by half. When the operating voltage was increased from 33V to 40V, the slack bus is required to supply $\sim 2.15x$ more energy and deliver $\sim 2.41x$ more peak current.

In closing, this experiment provides valuable insight in to the real dynamic characteristics of a two-stroke based hybrid power system. The attributes of the dynamic response to increases and decreases in power loading, as well as the approximate magnitudes of these attributes will enable an accurate dynamical model of this system to be constructed. Fur-

ther, the varied response of the PID controller design used in this experiment to changes in operation voltage indicates that more robust control techniques are required.

Chapter 5

HEPS Dynamical Model Development

5.1 Introduction

The objective of this chapter is to develop a dynamical model of the hybrid power system in Simulink. The model is tuned to reflect the attributes of the experimental power system using the results discussed in the previous chapter. Single-step, multi-step, and ramp responses will be evaluated and compared with the experimental results to develop a baseline model of the system.

To develop the model, this chapter proceeds through the development of the plant, controller, and load, developing the block diagrams and transfer functions for each. A baseline PID controller is developed for the system, with the phase margin of the open loop and closed loop systems are evaluated and significant improvements are shown.

Modeling the torque response of the engine presents a particular challenge to this simulation. Therefore, a method is developed to represent any arbitrary engine configuration based on a response surface model of the engine power and torque as a function of angular

velocity and throttle position, $\tau(\omega, T)$. Where ultimately, this dynamic model is compared to the experimental results for a comparable system, showing excellent agreement regarding the critical attributes of the dynamic response.

5.2 System Representation

The hybrid power system studied in the present research effort is a feedback control system. This can be represented using the simplified block diagram in Fig. 5.1.

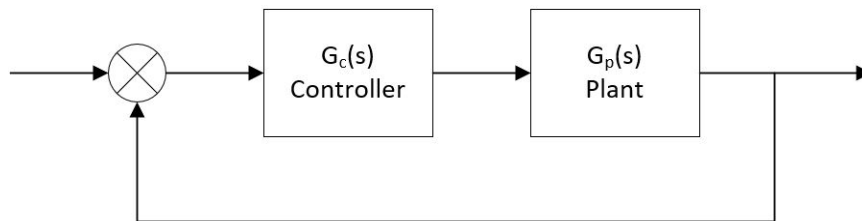


Figure 5.1: Simplified block diagram for the hybrid power system and controller.

This system can be represented as a controller and plant connected in a single feedback loop.

5.2.1 Plant

The plant in this case consists of the electrical and mechanical components of the hybrid power system, as well as the fuel regulation and load . Initially, we will assume that this system includes only the engine and a PMSM generator. This plant is represented in Fig.

5.2

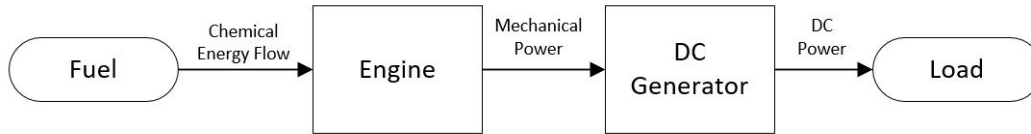


Figure 5.2: Simplified block diagram total hybrid power system plant.

Basic Representation of a PMSM as a DC Machine

The motor/generator is a three-phase delta connected permanent magnet synchronous machine (PMSM) running as a generator where the AC output is immediately converted to DC using a full-wave diode bridge rectifier. The complete generator circuit is shown in Fig. 5.3.

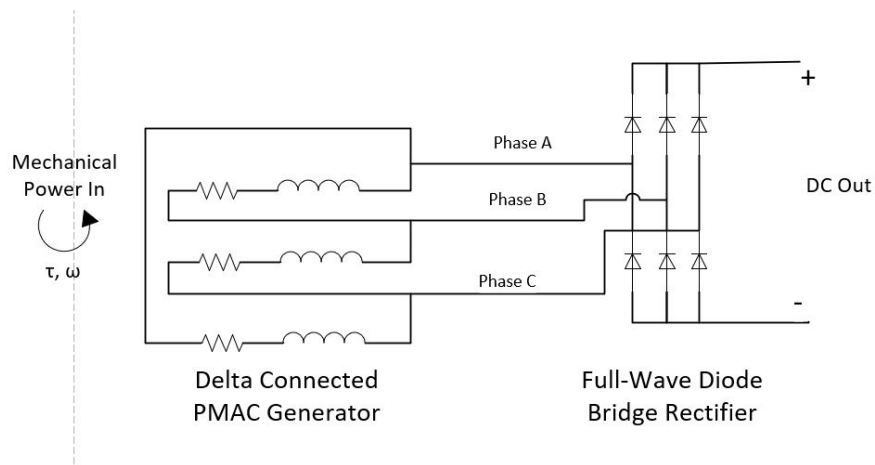


Figure 5.3: Equivalent circuit for the PMSM plant and power electronics.

This can be simplified and represented using the equivalent circuit for a PMSM, as shown in Fig. 5.4.

Here, L_{eq} is the parallel phase inductance of the armature windings and R_{eq} is the equivalent resistance of the conductive path through the phase winding and diode bridge

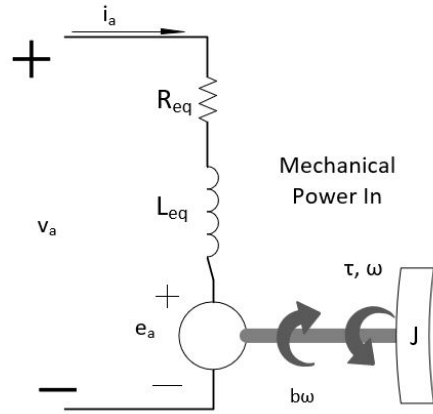


Figure 5.4: Equivalent circuit of the PMSM, DC representation

rectifier.

$$L_{eq} = L_{phase} = L \quad (5.1)$$

$$R_{eq} = R_{phase} + R_{rect} = R \quad (5.2)$$

The electromotive force induced by the motors' rotation, i.e. the back emf, is equal to

$$e_a = k_E \omega_m \quad (5.3)$$

The torque due to this electromotive force is similarly related to the motor torque constant k_T .

$$\tau_{em} = k_T i_a \quad (5.4)$$

For a PMSM machine, we will assume

$$k_E = k_T \quad (5.5)$$

Now the governing equations for this system can be written using Newton's 2nd Law and Kirchoff's Voltage Law.

$$J\ddot{\theta} + b\dot{\theta} = \tau_{em} = k_T i_a \quad (5.6)$$

$$L \frac{di_a}{dt} + R i_a = v_a - e_a = v_a - k_E \dot{\theta} \quad (5.7)$$

Then, taking the Laplace Transform of both equations we have

$$\dot{\Theta}(s)(Js + b) = k_T \dot{\Theta}(s) \quad (5.8)$$

$$I(s)(Ls + R) = V(s) - k_E \dot{\Theta}(s) \quad (5.9)$$

The transfer function for the plant is the ratio of the output $\dot{\Theta}(s)$ to the input $V(s)$.

We find this by eliminating $I(s)$ from both transformed equations.

$$G_p(s) = \frac{\dot{\Theta}(s)}{V(s)} = \frac{k_T}{(Js + b)(Ls + R) + k_T k_E} \quad (5.10)$$

This can be represented by the functional block diagram shown in Fig. 5.5.

In this case, the block diagrams for a PMSM motor and PMSM generator are identical, since a PMSM can operate as both a motor or a generator depending on the applied voltage and torque load. When operating as a motor, the applied voltage v_a must overcome the back emf e_a generated by the rotation of the system. The equilibrium of the system occurs when the loading torque τ_{mech} is equal to the torque due to the electromotive force τ_{em} . When the net torque is zero, the system is operating at steady state.

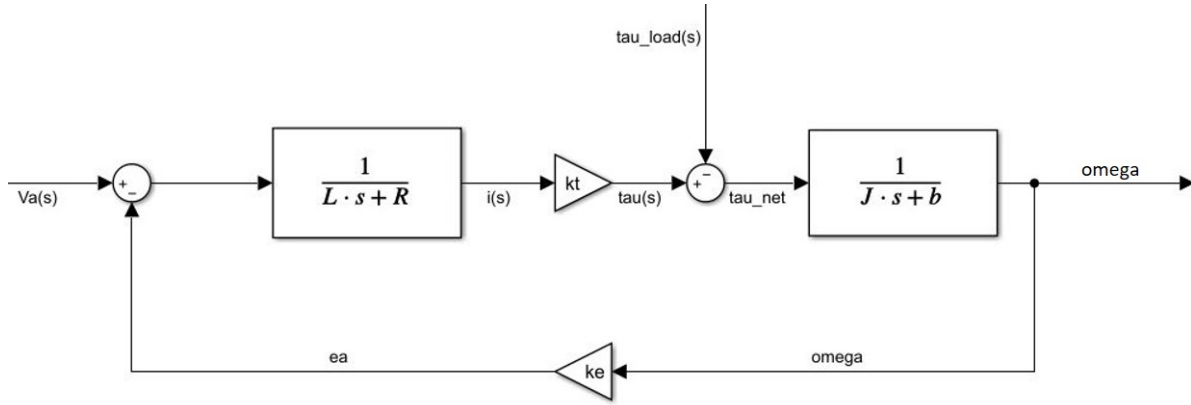


Figure 5.5: Functional block diagram for a PMSM motor/generator based on Eq. 5.10

$$\tau_{net} = \tau_{em} - \tau_{mech} = 0 \quad (5.11)$$

Stated in terms of current i_a ,

$$\tau_{em} = k_T i_a \quad (5.12)$$

$$\tau_{net} = k_T i_a - \tau_{mech} = 0 \quad (5.13)$$

Assuming slow changes in current i_a , $\frac{di_a}{dt} \approx 0$ so we can say that,

$$\tau_{em} \approx k_T \frac{v_a - e_a}{R} \quad (5.14)$$

For this approximation, we can see that increasing v_a will increase the electromotive torque. For a motor, power is supplied by an external source and the resulting electromotive torque is used to drive a load.

The inverse is true when operating as a generator. In this case, a mechanical torque is provided. The system accelerates until the resulting electromotive torque balances the mechanical input, and the system reaches steady state. The governing equations are identical, however the signs of the mechanical and electromotive torques are reversed, as is the sign of the current i_a .

$$\tau_{net} = -\tau_{em} + \tau_{mech} = 0 \quad (5.15)$$

Again assuming slow changes in current, $\frac{di_a}{dt} \approx 0$.

$$\tau_{em} \approx k_T \frac{v_a - e_a}{R} \tau_{em} \approx k_T (-i_a) \quad (5.16)$$

The negative current implies that the generator is supplying current to another electrical load. This arises from the fact that, in order to generate current, $e_a > v_a$. Here, the applied voltage v_a is used to regulate the current output from the generator system.

Modeling the PWM controlled resistance load

The experimental apparatus discussed in the previous chapter uses a water-cooled resistor bank to provide a load for the power generated by the hybrid power system. The output from the generator is coupled to a PWM-regulated resistance load. This load is modeled as a 'DC Transformer,' though in fact this is a MOSFET-based, switching DC current regulator. The resulting system is modeled as shown in Fig. 5.6

For the system considered in this experiment, the time constant of the Thevenin equivalent load circuit is given by

$$\tau_{ThevEq} = R_{ThevEq} * C_t \quad (5.17)$$

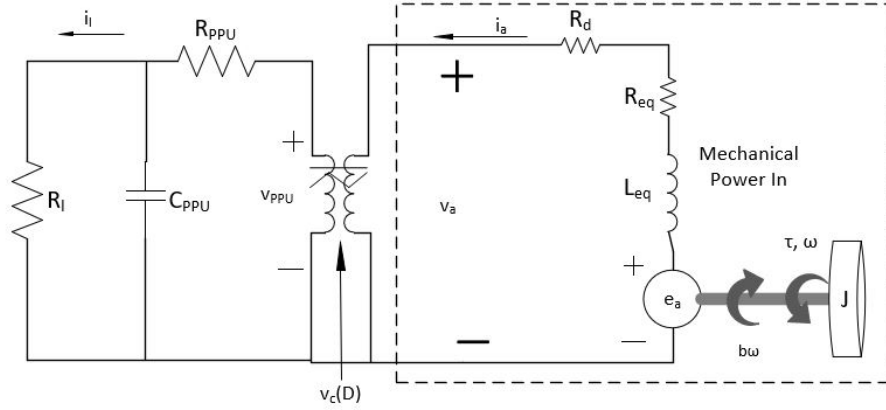


Figure 5.6: The equivalent circuit for the generator system coupled to a PWM regulated RC load.

while the time constant of the motor/generator system is given by

$$\tau_{gen_{RL}} = \frac{L_{eq}}{R_{eq}} \quad (5.18)$$

In this case, given the design parameters of this system, $R_l = 0.768\Omega$, $R_t \approx 0$, $R_{Thev_{Eq}} \approx 1$, $C_t \approx 2200\mu F$, $R_{ph} = 0.0328\Omega$, and $L_{eq} = 0.295H$,

$$\begin{aligned} \tau_{gen_{RL}} &>> \tau_{Thev_{Eq}} \\ \frac{L_{eq}}{R_{ph}} &>> R_{Thev_{Eq}} * C_t \\ &\sim 889ms >> \sim 2.2ms \end{aligned}$$

Therefore, the capacitance of the PWM switching regulator will be neglected in this model. The equivalent circuit for the model system is shown in Fig. 5.7.

The DC transformer in this case represents a PWM regulated DC-DC power processing unit (PPU). The generator system and the PPU are coupled such that the magnitude of the

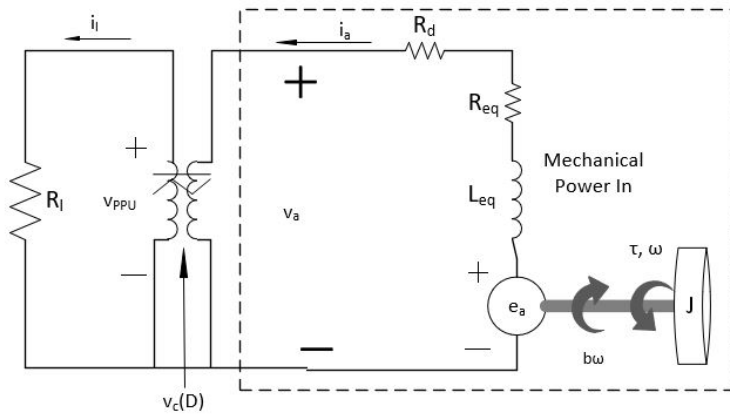


Figure 5.7: The equivalent circuit for the generator system coupled to a PWM regulated resistance load only.

load current is equal to that of the armature current.

$$-i_a = i_l \quad (5.19)$$

The PPU-load system therefore behaves as a variable resistor, where the current flow is controlled by the PWM duty cycle D . This simplified equivalent circuit is shown in Fig. 5.8.

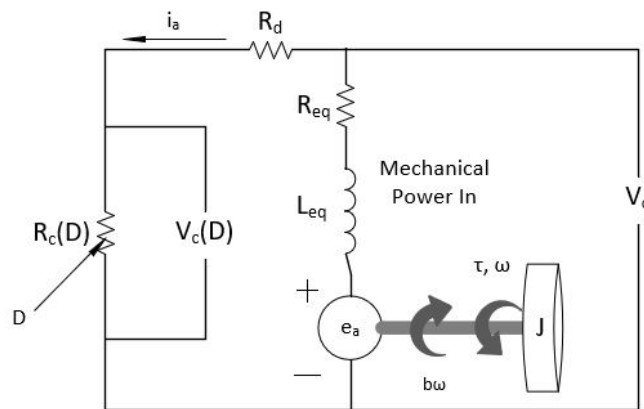


Figure 5.8: The equivalent circuit for the generator system coupled to a variable resistor.

Here, V_o is the voltage output from the hybrid generator system, and $V_c(D)$ is the controlled voltage required to drive i through the controlled resistor $R_c(D)$.

Proceeding with this model, the control voltage v_c , used to control the current output of the system, can be written in terms of the generator back emf and the voltage loss mechanisms in the system.

$$V_c(D) = ea - R_{eq}i - R_d i - L \frac{di}{dt} \quad (5.20)$$

Where the voltage losses are due to resistance and inductance. Assuming steady state, or slow changes in current, $\frac{di}{dt} \approx 0$.

$$V_c(D) = ea - R_{eq}i - R_d i \quad (5.21)$$

The current passing through the controlled resistor is a function of the controlled voltage and duty cycle.

$$i_l = i = \frac{V_c(D)D}{R_l} \quad (5.22)$$

Where R_l is the load resistance. This gives the implicit form of the controlled voltage function. For clarity, when $V_c(D)$ appears on the RHS of the equation, we will use V_c .

$$V_c(D) = e_a - \frac{V_c D}{R_l} i - R_d i \quad (5.23)$$

Here we will replace V_c on the RHS with the steady-state expression in Eq. 5.21.

$$V_c(D) = e_a - D \frac{R_{eq}}{R_l} (e_a - R_{eq}i - R_d i) \quad (5.24)$$

Making the substitution $R_c = R_{eq} + R_d$, we have

$$V_c(D) = e_a - e_a D \frac{R_{eq}}{R_l} + D \frac{R_{eq} R_c}{R_l} i - R_d i \quad (5.25)$$

Which can be simplified to

$$\boxed{V_c(D) = e_a \left(1 - D \frac{R_{eq}}{R_l}\right) + \left(D \frac{R_{eq} R_c}{R_l} i - R_d i\right)} \quad (5.26)$$

A block diagram can be constructed from this expression and is shown in Fig. 5.9.

Examining the relative magnitudes of each of the terms on the RHS of Eq. 5.26 reveals their contribution to the control voltage.

$$T_1 = e_a \left(1 - D \frac{R_{eq}}{R_l}\right)$$

$$T_2 = D \frac{R_{eq} R_c}{R_l} i - R_d i$$

If $R_l > R_c$ and $R_l > R_{eq}$, then $R_{eq}/R_l \gg (R_{eq} R_c)/R_l$ when $\mathbf{O}(i_a D) \approx \mathbf{O}(e_a D)$. Using the parameters defined for this system

$$\frac{|T_1|}{|T_2|} \approx 128 \quad (5.27)$$

Additionally, the term $T2$ creates an additional current feedback loop, which introduces additional complexity into the model, as shown in Fig. 5.10. When this term is removed, the resulting system is significantly simplified, as shown in Fig. 5.11.

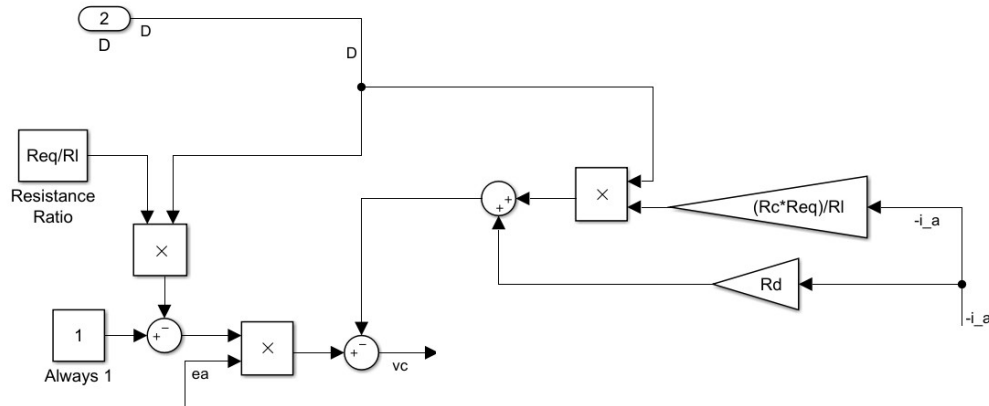


Figure 5.9: Functional block diagram for the applied voltage V_c based on Eq. 5.26

Applying this to the PMSM with the block diagram shown in Fig. 5.10, we can regulate the output current from the PMSM generator by varying the duty cycle of the PWM load controller.

The significance of $T2$ and the associated current feedback loop will be evaluated later in this chapter.

Representing an engine-powered system

Since the hybrid power system considered in this research effort is powered by an internal combustion engine, then while the engine is running, the angular velocity of the system must be non-zero. Specifically, the engine will have some finite idle speed, where the engine is

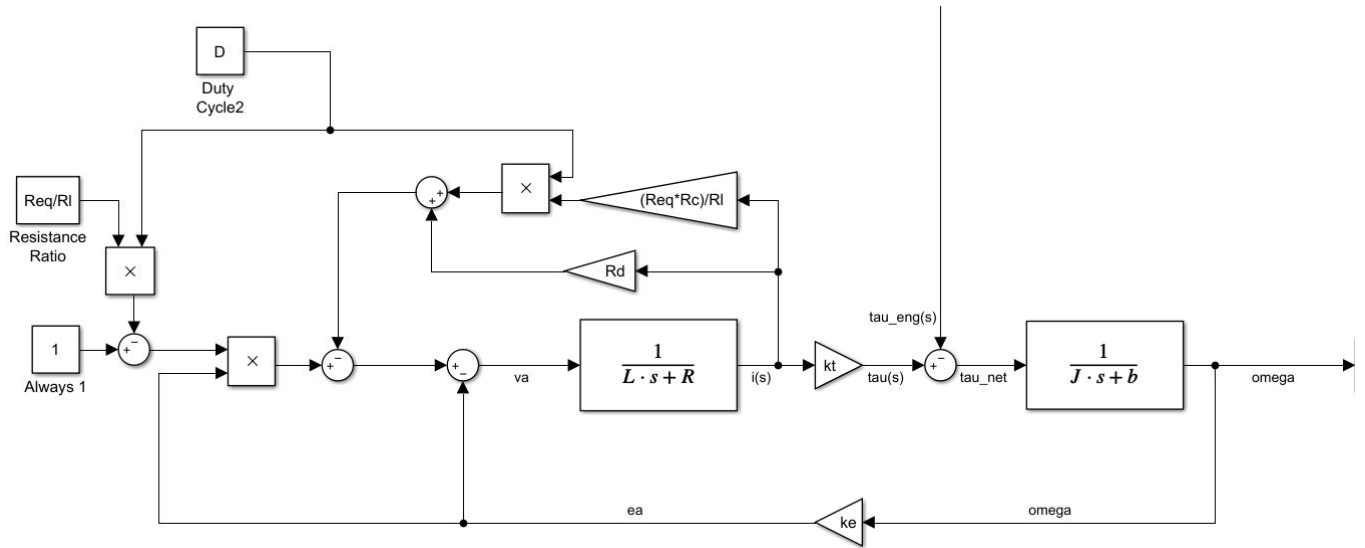


Figure 5.10: Functional block diagram for the PMSM operating as a generator and regulated by the load PWM duty cycle with the T2 term included.

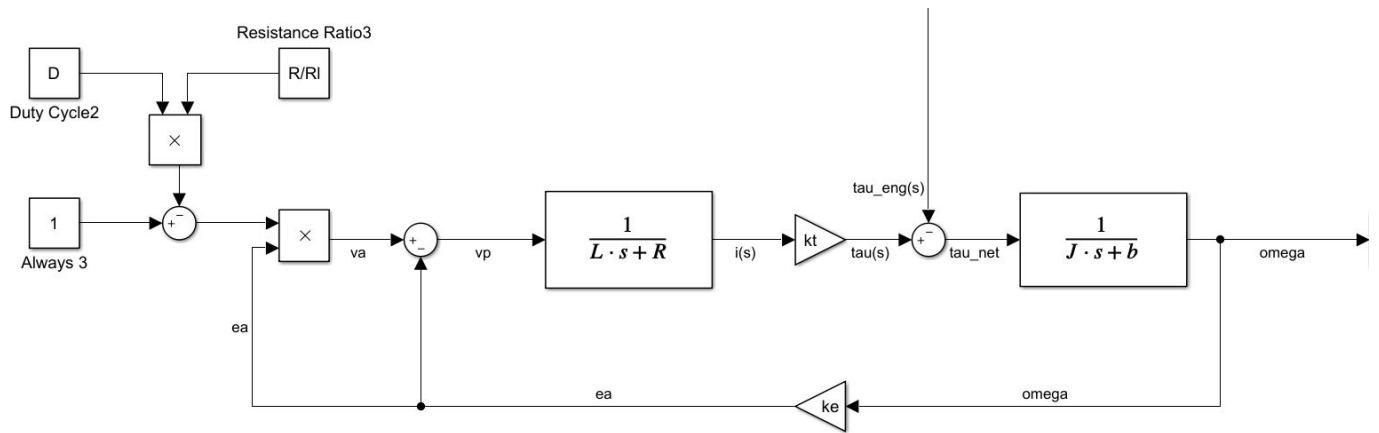


Figure 5.11: Functional block diagram for the PMSM operating as a motor/generator and regulated by the load PWM duty cycle with the T2 term omitted. Note that the current feedback loop present in Fig. 5.10 is gone.

running but producing no useful power. This idle speed is

$$idle\ speed \equiv \omega_0 \tag{5.28}$$

Such that the maximum output power P is

$$P(\omega_0) = 0 \tag{5.29}$$

Since this system must always have angular velocity $\omega > \omega_0$, we will assume that the engine is running at $t = 0$. Therefore, the initial angular velocity of the system $\omega(t = 0) \neq 0$. This means we cannot model the system using its transfer function directly, as use of the Laplace Transform requires zero initial conditions. Rather, we need to represent the system such that non-zero initial conditions can be defined.

Recall that Newton's Second Law for this system is

$$J\ddot{\theta} + b\dot{\theta} = \tau_{net} \tag{5.30}$$

Which can be solved for $\ddot{\theta}$

$$\ddot{\theta} = \frac{1}{J}(\tau_{net} - b\dot{\theta}) \tag{5.31}$$

The block diagram for this equation is shown in Fig. 5.12.

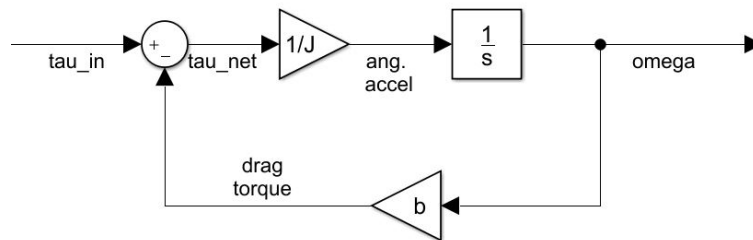


Figure 5.12: Functional block diagram for the mechanical PMSM components based on Eq. 5.31

Similarly, Kirchoff's Voltage Law for this system can be solved for $\frac{di_a}{dt}$.

$$\frac{di_a}{dt} = \frac{1}{L}(v_a - e_a - Ri_a) \quad (5.32)$$

Much like the mechanical system, the block diagram for this is shown in Fig. 5.13.

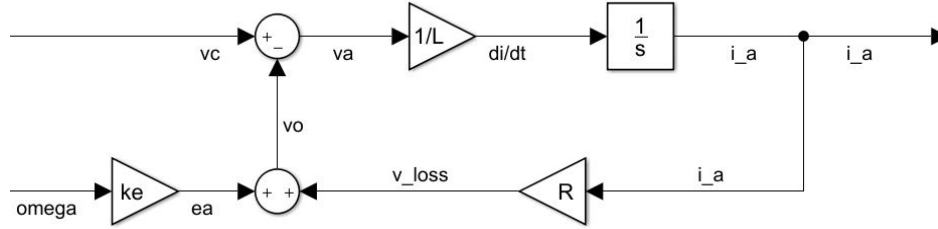


Figure 5.13: Functional block diagram for the mechanical PMSM components based on Eq. 5.32

Combining these system, we can construct a complete block diagram of the system, Fig. 5.14, that is functionally identical to that shown in Fig. 5.12, but where non-zero initial conditions can be specified.

The behavior of the plant system is now defined and therefore this complex block diagram can be replaced in the simulation with a multi-input multi-output (MIMO) sub-system defined by inputs, duty cycle D and engine torque τ_{eng} , and outputs angular velocity ω and back emf e_a , as shown in Fig. 5.15.

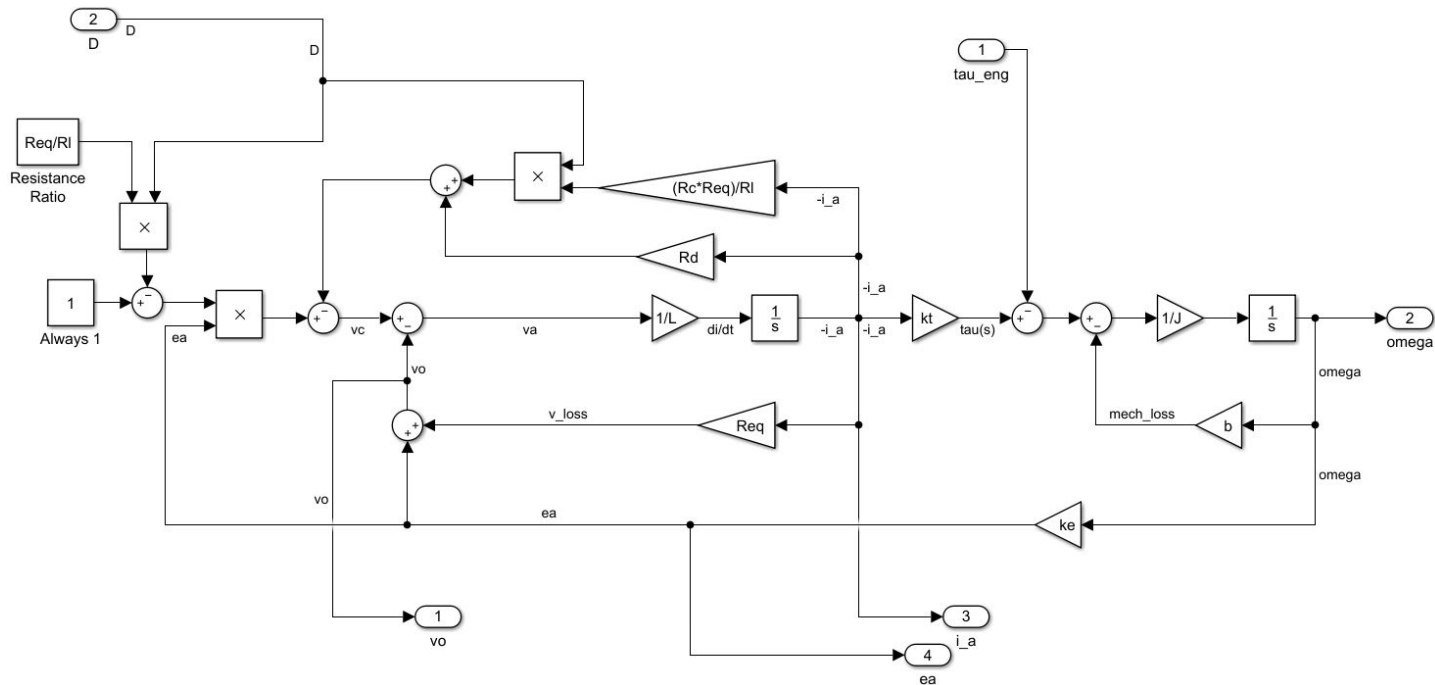


Figure 5.14: Functional block diagram for the mechanical PMSM components based on Eq. 5.32. The T_2 current loop is included here for completeness.

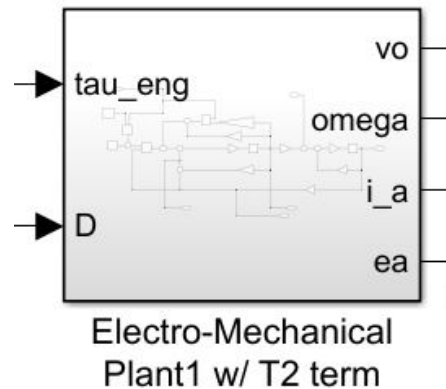


Figure 5.15: Plant MIMO subsystem representation, only critical inputs and output are visible here, though others can be used to monitor the model.

5.2.2 Controller

The experimental hybrid power system used in this research was designed to use only a feedback control loop over the voltage output of the generator. The transfer function of this system, Eq. 5.33, relates the angular velocity of the system, to the input voltage.

$$G_p(s) = \frac{\dot{\Theta}(s)}{V(s)} = \frac{k_T}{(Js + b)(Ls + R) + k_T k_E} \quad (5.33)$$

By inspection, it is clear that this system has two poles. Therefore, we should design a controller to cancel this two pole system.

PID Controller Design

A PID controller is designed for this system. The PID controller is of the form

$$u = k_p e + k_i \int e dt + k_d \frac{de}{dt} \quad (5.34)$$

Where u is the output and e is the error signal.

$$e = \textit{setpoint} - \textit{measurement} \quad (5.35)$$

Taking the Laplace Transform of this equation gives

$$U(s) = k_p E(s) + \frac{k_i}{s} + k_d s E(s) \quad (5.36)$$

Solving for the ratio $\frac{U(s)}{E(s)}$ gives the transfer function of the system which has two zeros and a pole at the origin.

$$G_c(s) = \frac{U(s)}{E(s)} = \frac{k_d s^2 + k_p s + k_i}{s} = \frac{k_d \left(s^2 + \frac{k_p}{k_d} s + \frac{k_i}{k_d} \right)}{s} \quad (5.37)$$

In the experiment, the operating voltage of the system is controlled by a servo connected to the engine's throttle. This servo has an internal controller that, for the purposes of this initial analysis, we will assume is well designed with all unstable poles mitigated, and therefore does not significantly alter the transfer function of the generator system. The transfer function of the closed loop system is

$$G_{CL}(s) = G_c(s)G_p(s) \quad (5.38)$$

$$G_{CL}(s) = \frac{k_d s^2 + k_p s + k_i}{s} \frac{k_T}{(Js + b)(Ls + R) + k_T k_E} \quad (5.39)$$

$$G_{CL}(s) = \frac{k_T(k_d s^2 + k_p s + k_i)}{s[JLs^2 + (RJ + bL)s + bR + k_E k_T]} \quad (5.40)$$

$$H_{CL}(s) = \frac{G_{CL}(s)}{1 + G_{CL}(s)} \quad (5.41)$$

For this experiment the following values are initially assumed for the parameters defining the system, as refined by comparing the simulation outputs with experimental data, as shown in Table 5.1. In particular, the viscous damping coefficient b is difficult to measure or estimate with any accuracy before comparing with the experimental data, as fluid shear is the primary contributor to this parameter.

Experimental Apparatus Parameters		
Parameter	Value	Units
J	0.0015	$kg * m^2$
b	0.0005	$(N * s/m)$
R_{ph}	0.0328	Ω
R_r	0.009	Ω
R_d	0.0094	Ω
R_l	0.768	Ω
L	0.0295	H
k_E	0.0455	$V/(rad/s)$
k_T	0.0455	$(N * m)/A$

Table 5.1: Experimental Apparatus Parameters

Now, we can evaluate the effect of the PID controller on the phase margin of the open loop and closed loop system. The phase margin is defined as

$$\text{Phase Margin, } PM = \phi_{f_c} + 180^\circ \quad (5.42)$$

Where ϕ_{f_c} is the phase angle at the crossover frequency, with f_c , the crossover frequency defined as

$$f_c \equiv \text{the frequency where } G(s) = 0dB \quad (5.43)$$

First, we will examine the open loop response of the system. The transfer function for this system is given by Eq. 5.33.

$$\phi_{OL_{f_c}} = -178^\circ PM_{OL} = \phi_{f_c} + 180^\circ = 2^\circ \quad (5.44)$$

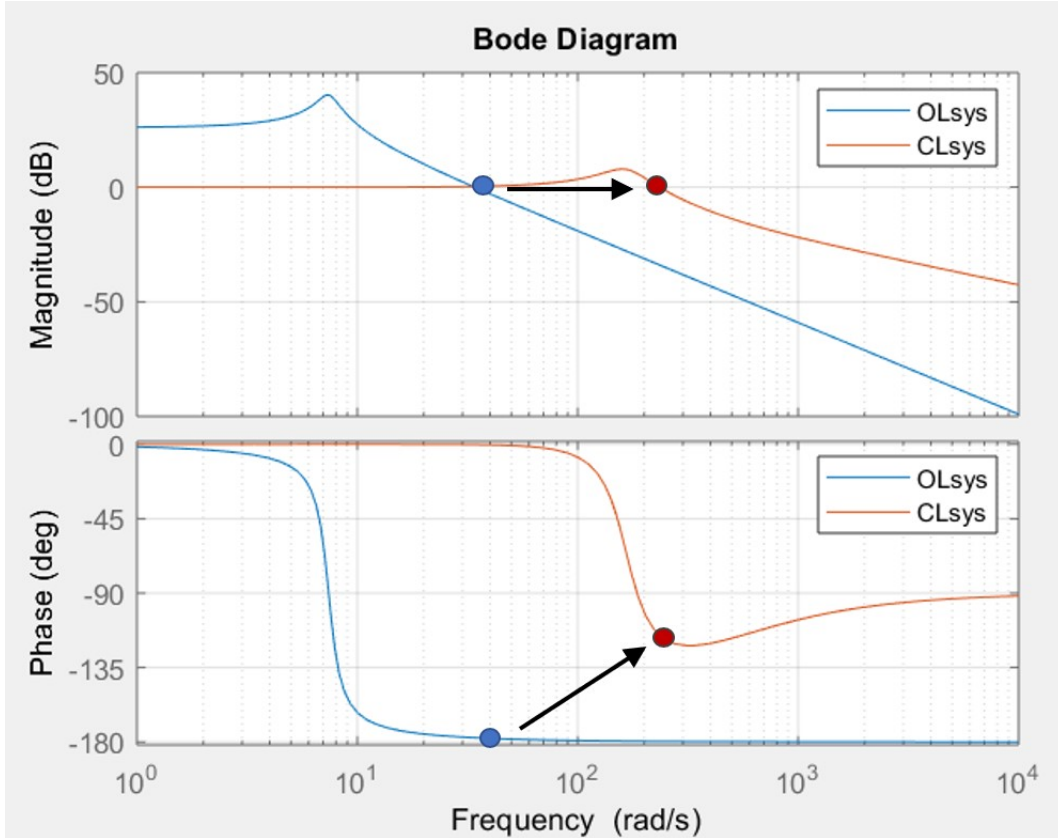


Figure 5.16: Bode Diagram of the open loop and closed loop system with the parameter values defined for the experimental apparatus.

For a robust system response without oscillations, the system should have a phase margin greater than 45°, and preferably close to 60° in many cases.

The gains presented in the table above were shown to produce the desired response in the experiment. The effect of the PID controller on the system can be seen by examining the phase margin of the closed loop system, as shown in Fig. 5.16.

$$\phi_{CL_{f_c}} = -125^\circ PM_{CL} = \phi_{f_c} + 180^\circ = 55^\circ \quad (5.45)$$

Phase Margin Improvement with PID Control			
System	f_c (rad/s)	ϕ_{f_c} (deg)	PM (deg)
$G_{OL}(s)$	35.4	-178	2
$G_{CL}(s)$	533	-125	55

Table 5.2: Phase Margin Improvement with PID Control

This represents a significant improvement relative to the phase margin of the open loop system. While not optimized, the controller used in the experiment will be initially implement in the model as a baseline case. The controller used to achieve this in the experiment is as follows:

$$k_p = 3.0, \text{ proportional gain}$$

$$k_i = 4.0, \text{ integral gain}$$

$$k_d = 0.008, \text{ derivative gain}$$

Model Implementation

A PID controller is implemented in a simple feedback control loop with the Electro-Mechanical Plant defined earlier in this chapter. This system is desined to maintain a constant voltage setpoint and is implemented in the model as shown in Fig. 5.17.

This simplified system is subject to a step input in duty cycle D . Here the duty cycle is stepped from $D = 0.2$ to $D = 0.9$ at $t = 3sec$.

This step change in the duty cycle is applied to two versions of this system, one including the $T2$ term discussed above, and one where it is omitted from the model, see Fig. 5.10 and Fig. 5.11 respectively for reference. The influence of the $T2$ is observed by directly comparing these responses. This comparison is shown in Fig. 5.18.

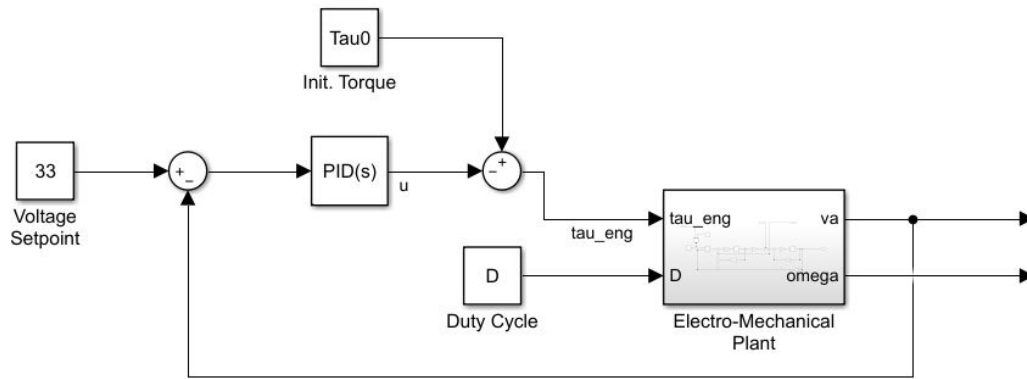


Figure 5.17: The PID controller is implemented in the model of the power system with the ability to specify the initial torque, load duty cycle, and voltage setpoint.

From this comparison, the V_o response of each system is essentially identical, with a very small $\Delta V_o = 0.006V$ maximum difference induced between them when the step function is applied. However, because the $T2$ more accurately represents the resistance losses in the system beyond the PMSM motor/generator equivalent circuit, the current i_a and angular velocity ω_m responses are notably different.

Due to the omission of the power diode in model 1, this voltage loss is not included. As a result, the load current $i_l = -i_a$ is greater than in model 2, where these losses are considered. Consequently, this higher current increases the losses in the generator armature, causing the controller to drive the system to a higher angular velocity. The steady state angular velocity difference is $\Delta\omega_m = 6.0rad/s$, while the steady state current difference $\Delta i = 5.8A$.

Since torque required is directly proportional to current by the torque constant k_T , the torque response follows the current response, as shown in Fig. 5.19.

Since omitting the $T2$ term has negligible influence on the controlled variable v_o , the voltage output from the system, and also because including $T2$ has a significant effect on the

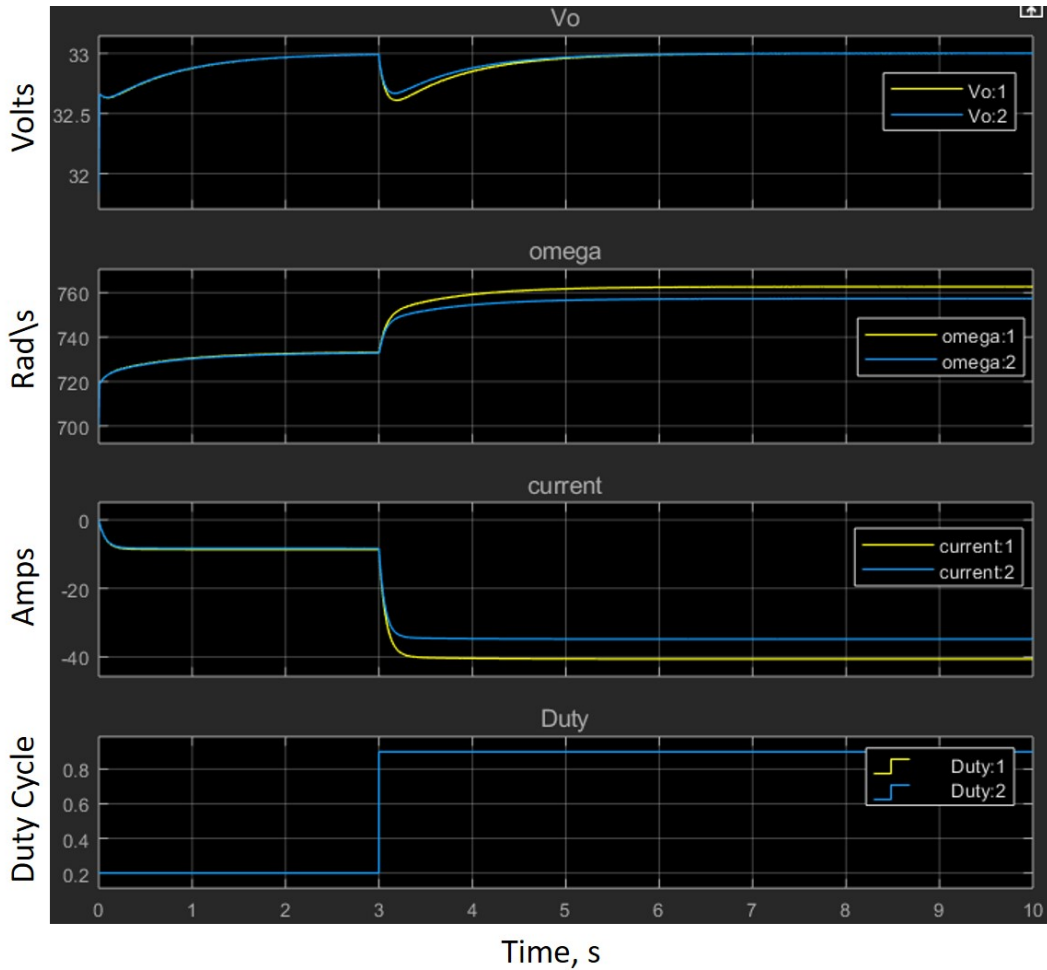


Figure 5.18: Comparison between a model where $T2$ is omitted, and a model where $T2$ is included. These are models 1 and 2 respectively in the plot legends.

current response, the effects of $T2$ will be included in this model. This indicates that more robust nonlinear control schemes will likely be required to manage this system and improve its overall performance.

5.2.3 Throttle Response Model

Up to this point, we have not considered the effects of operating this system using a real engine to power the system. Unlike PMSMs, the power and torque available from an internal

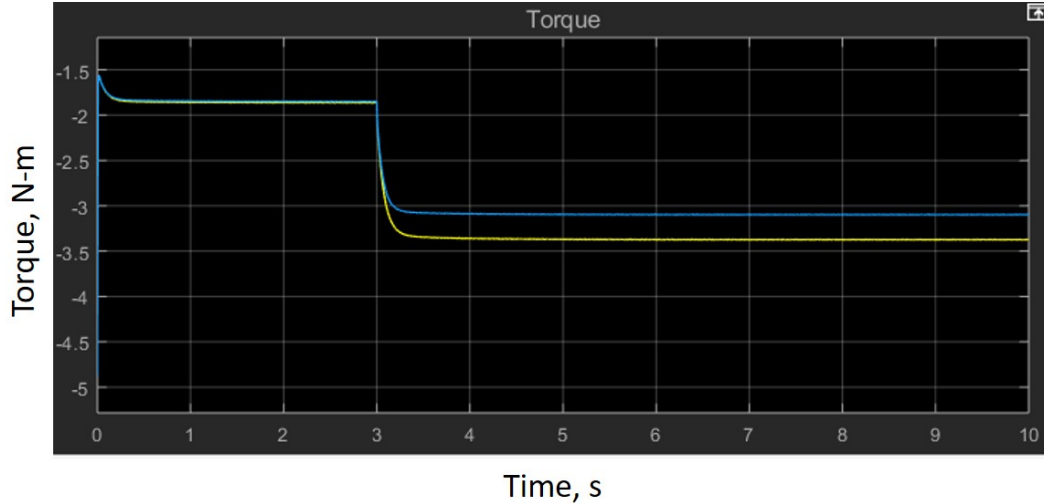


Figure 5.19: The model torque response predictably follows the current response.

combustion engine is strongly dependent on the engine's angular velocity ω_m and throttle setting T_r .

$$\text{Power Available: } P(\omega_m, T) = \tau(\omega_m, T_r)\omega_m \quad (5.46)$$

$$\text{Torque Available: } \tau(\omega_m, T) = \frac{P(\omega_m, T_r)}{\omega_m} \quad (5.47)$$

This is true for all engine types, including naturally aspirated and forced induction two-stroke and four-stroke engines, regardless of carburetor or fuel injection configuration. While it is true that the thermodynamic cycle, fuel injection type, and air induction system all influence the shape of the power and torque curves, they remain nonetheless dependent on angular velocity and throttle setting.

From Eq. 5.46, we have one equation with three unknown variables. This means that we need to specify either power or torque as a function of angular velocity ω_m as well as throttle setting T . This section will develop a generalized approach used for creating a parametric

model of any particular engine for use in the vehicle-level dynamic simulations. This model will be developed in the form

$$\tau(\omega, T|a, \hat{\omega}_0, \tilde{P}_0, P_{max}, \omega_{max}, \mathbf{P}) \quad (5.48)$$

Each of the parameters in this model will be discussed in detail throughout this section.

Normalized Power Curve

In order to develop a general engine model, we must first examine how engine data is typically presented. An example of this data is shown for the Rotax 582 two-stroke aircraft engine in Fig. 5.20. These plots show the peak power and torque available for this engine. This presentation method is commonly used for most engine types.

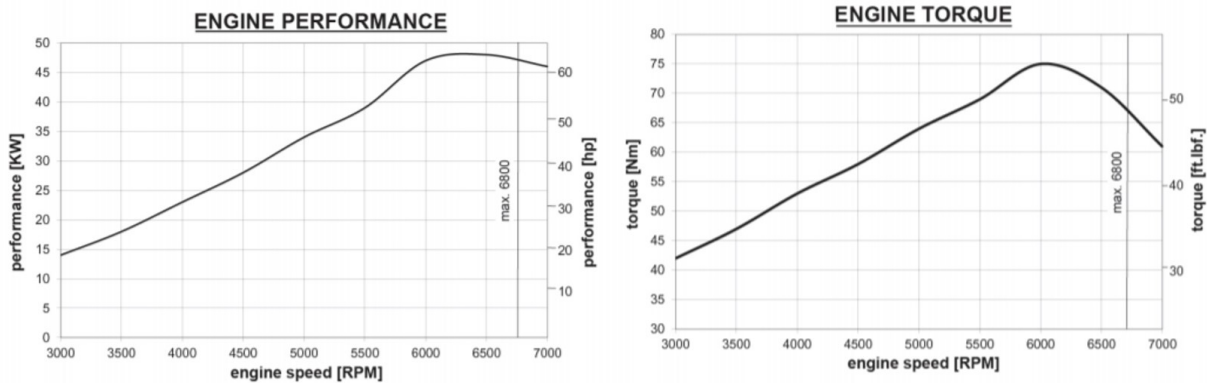


Figure 5.20: Example of power and torque curves for a two stroke engine, taken from the commonly used Rotax 582 [13].

The challenge with this presentation is that only the power and torque capability at maximum throttle are shown. While manufacturers of large automotive and aircraft engines have data fully characterizing these engines throughout their throttle range at all operating speeds, this data is not typically publicly available and only pertains to a specific engine

under well-defined conditions. Additionally, this data is not typically collected for the small engines used in this experiment or similar applications. As such we need to develop a generic model that can be scaled to suit a variety of applications and tuned to represent a variety of engine types, particularly for experimental or preliminary system design efforts, such as this research.

We begin by developing a parametric representation of the power curve for a generic internal combustion engine. Ideally, this function would be continuous and differentiable over an arbitrarily specified range. Also, the capability to fully define the function using a small number of parameters is preferable. To accomplish this, the shape of the power profile is defined using a Bezier Polynomial. These parametric curves are defined as

$$\mathbf{B}(t) = \sum_{i=0}^n \binom{n}{i} t^i (1-t)^{n-i} \mathbf{P}_i, \text{ where } 0 \leq t \leq 1 \quad (5.49)$$

$$\binom{n}{i} = \frac{n!}{i!(n-i)!} \quad (5.50)$$

Where \mathbf{P} is an $n \times 2$ matrix containing the control points for the curve $\mathbf{B}(t)$. So for a two-dimensional curve in x and y , we have expressions for $B_x(t)$ and $B_y(t)$

$$B_x(t) = \sum_{i=0}^n \binom{n}{i} t^i (1-t)^{n-i} P_{(i,1)} \quad (5.51)$$

$$B_y(t) = \sum_{i=0}^n \binom{n}{i} t^i (1-t)^{n-i} P_{(i,2)} \quad (5.52)$$

These curves have the additional convenience of having their end points defined by the first and last control points, \mathbf{P}_1 and \mathbf{P}_n respectively.

For modeling the general power curve of an engine, it is convenient to define the curve on $0 < x \leq 1$ and $0 < y \leq 1$. The reason we exclude zero in both dimension is because, if the engine is running, it must be able to produce some power and therefore torque at idle, otherwise it could not accelerate under any load.

This is accomplished by requiring that

$$\mathbf{P}_1 = (\hat{\omega}_0, \tilde{P}_0) \quad (5.53)$$

and,

$$\mathbf{P}_n = (1, \tilde{P}_\omega) \quad (5.54)$$

where, ω_0 is the idle speed, and $\hat{\omega}_0$ is the normalized idle speed

$$\hat{\omega}_0 = \frac{\omega_0}{|\omega_{max}|} \quad (5.55)$$

and \tilde{P}_0 is the minimum power parameter. If $\max(B_y(t)) \approx 1$, then given the maximum power, P_{max}

$$\tilde{P}_0 \approx \hat{P}_0 = \frac{P_0}{P_{max}} \quad (5.56)$$

Where P_0 is the idle power, and

$$\tilde{P}_\omega \approx \hat{P}_\omega = \frac{P_\omega}{P_{max}} \quad (5.57)$$

Where P_ω is the power at maximum speed. Typically,

$$P_\omega \leq P_{max} \quad (5.58)$$

The initial Bezier curve is shown in Fig. 5.21

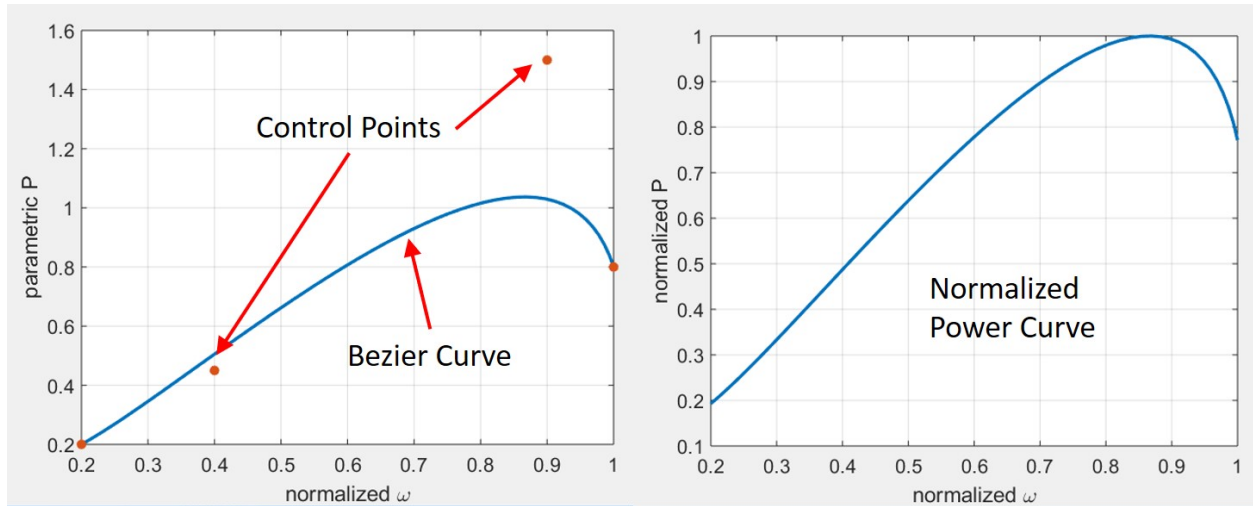


Figure 5.21: Parametric Bezier power curve and conversion to normalized power curve. Note that the control points do not necessarily fall on the generated curve.

This normalized power model \hat{P} is now a function of $\hat{\omega}$.

$$\hat{P}(\hat{\omega}) = \text{Normalized Power Model} \quad (5.59)$$

Now, we can scale this curve to an arbitrary power output and angular velocity range. This is achieved by multiplying the normalized power curve by the maximum desired output power of the engine to be modeled.

$$P = P_{max} \hat{P} \quad (5.60)$$

And,

$$\omega = \omega_{max} \hat{\omega} \quad (5.61)$$

Now, the full power model $P(\omega)$ is defined for the engine operating at full throttle.

$$P(\omega) = \text{Scaled Power Model} \quad (5.62)$$

The scaled torque output of the system can now be calculated.

$$\tau(\omega) = \frac{P(\omega)}{\omega} \quad (5.63)$$

For the Zenoah G320PUM engine use in this experiment, the following engine parameters are given.

$$P_{max} = 3.21kW$$

$$\omega_{max} = 16000rpm = 1676 \frac{rad}{s}$$

Using these parameters, a scaled engine model is developed at maximum throttle.

The initial Bezier curve is shown in Fig. 5.22.

Up to this point, the engine power and torque response have been treated as curves, defined in two dimensions. As discussed previously, the assumption made to enable this has been that the engine is operating with the throttle valve fully opened. While a thorough treatment of the fluid mechanics and thermodynamics of a throttle body is beyond the scope of this research, the torque output from the engine is a strong function of T , the throttle position.

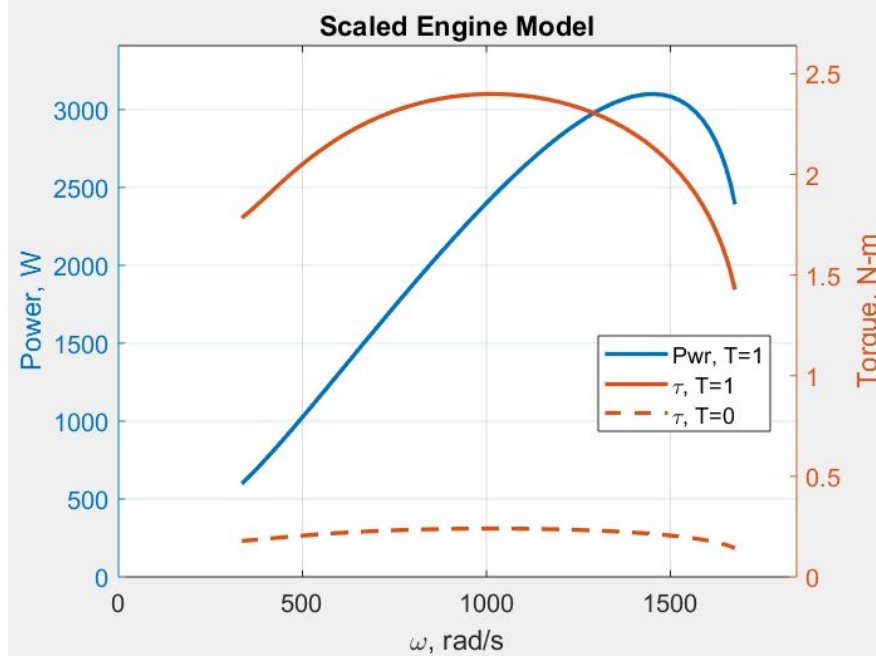


Figure 5.22: Scaled engine model developed from the Zenoah G320PUM two-stroke used in this experiment

We can estimate the inlet mass flow rate given the angular position of the throttle body and pressure ratio across the valve, as shown in the work of [Bordjane and Chalet], see Fig. 5.23. However, without explicit information regarding the design of the carburetor or the fuel map in the case of a fuel-injected engine, it is impossible to reliably estimate the equivalence ratio ϕ of the air-fuel charge entering the cylinder.

$$\phi = \frac{\text{actual - fuel - to - oxidizer - ratio}}{\text{stoichiometric - fuel - to - oxidizer - ratio}} = \frac{m_{fuel}/m_{ox}}{(m_{fuel}/m_{ox})_{st}}$$

Further complicating this, two-stroke engine air-fuel induction is particularly sensitive to the design of the exhaust system, with this response varying throughout the engines operating range. These uncertainties combined render any attempt to accurately model

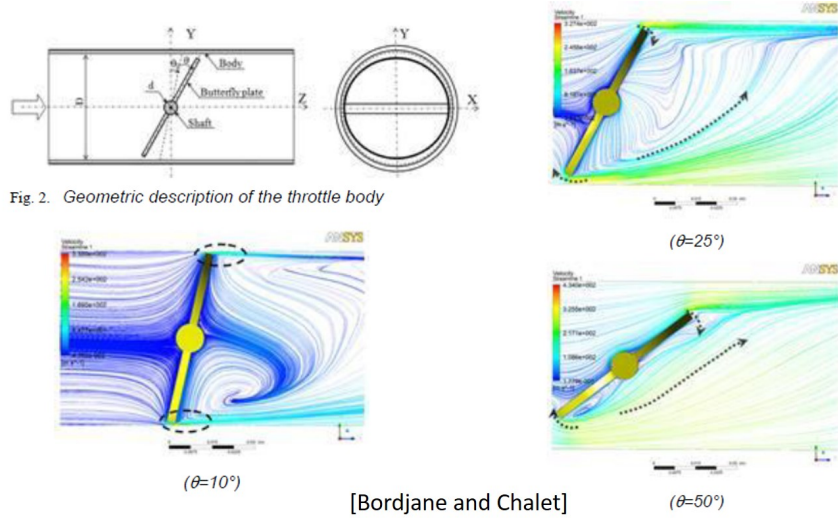


Figure 5.23: Schematic representation and CFD results for the flow through a throttle body [Bordjane and Chalet].

the behavior of the air-fuel induction without explicit knowledge of the system design and settings as futile.

However, we do know that, regardless of the precise throttle response characteristics, all torques between the minimum and maximum torque for a given operating speed are achievable. Therefore, to construct a functional model of engine response, we need only to specify the minimum torque available as a function of angular velocity.

$$\tau(T|\omega) = f(T|\tau(\omega)_{T=0}, \tau(\omega)_{T=1}) , \text{ where } 0 \leq T \leq 1 \quad (5.64)$$

We therefore need to construct a path between $\tau(\omega)_{T=0}$ and $\tau(\omega)_{T=1}$ as a function of the throttle input T . For simplicity, we will define this as

$$\tau(T|\omega) = \tau_{min} + (\tau_{max} - \tau_{min})T^a \quad (5.65)$$

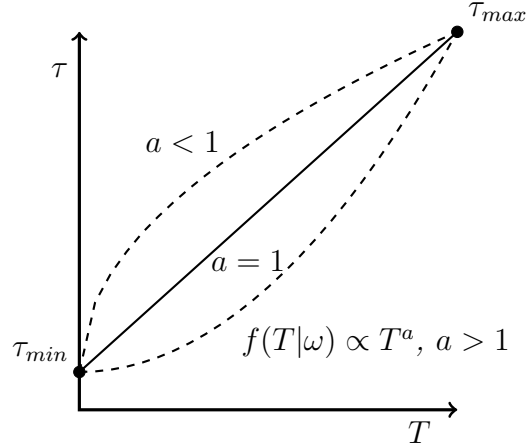


Figure 5.24: The path between the minimum and maximum torque is defined by shape parameter a , to create a concave, linear, or convex path for any angular velocity.

Where the exponent $\{a \in \mathfrak{R}\}$ is used as a shape parameter, $\{0 \leq T \leq 1\}$ and $\{\omega_0 \leq \omega \leq \omega_{max}\}$, as illustrated in Fig. 5.24.

We will assume that the torque curve at minimum throttle, since it cannot be zero, will have the same shape as the torque curve at maximum throttle, but with proportionally lower magnitudes.

$$\tau(\omega)_{T=0} = C\tau(\omega)_{T=1} \quad (5.66)$$

Where C is the proportionality constant, and can be specified as needed on the range $\{0 > C \leq 1\}$. Typically, for this experiment $C \approx 0.1$. This minimum torque curve is shown in Fig. 5.22.

Now, having defined the required model parameters, we can construct a response surface model for the engine output torque as a function of both throttle and angular velocity.

$$\tau(\omega, T|a, \hat{\omega}_0, \tilde{P}_0, P_{max}, \omega_{max}, \mathbf{P}) \quad (5.67)$$

The response surface model for the engine used in this experiment is shown in Fig. 5.25.

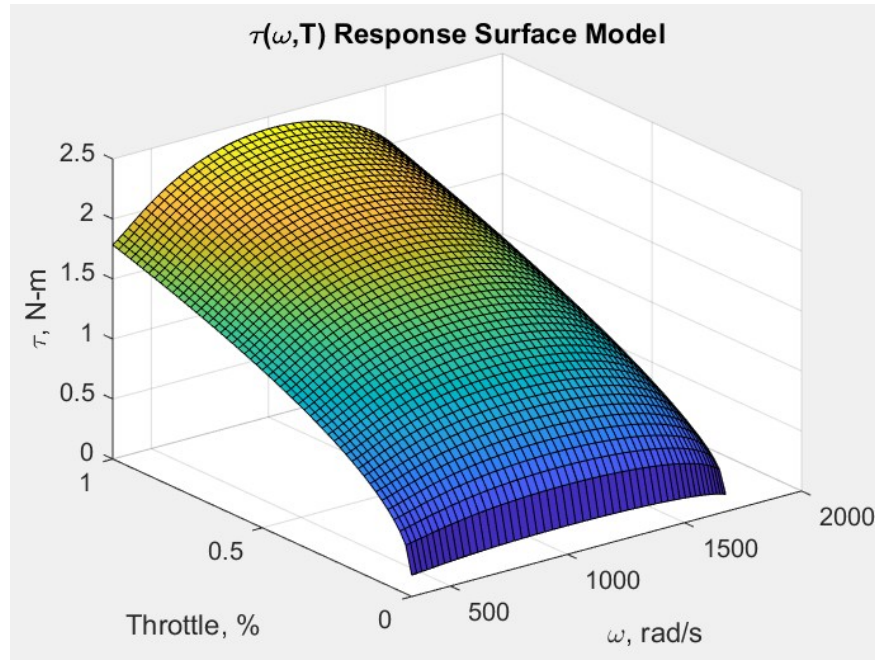


Figure 5.25: Torque response surface model for the Zenoah G320PUM engine used in this experiment where $a = 0.5$

Model Implementation

Recall that the SISO transfer function of the plant is

$$G_p(s) = \frac{\dot{\Theta}(s)}{V(s)} \quad (5.68)$$

While the torque response is an integral characteristic of the true plant system. For the purpose of this analysis, it is treated as a separate system with the MISO transfer function defined by the response surface model $\tau(\omega, T)$.

This is implemented as a interpolated lookup table in the Simulink dynamical model of the system. For the purpose of this analysis, we will assume that $a = 0.5$. This results in the response manifold metamodel shown in Fig. 5.26.

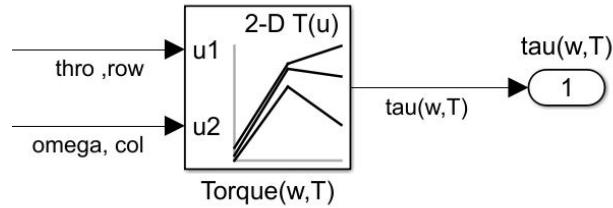


Figure 5.26: Torque response surface model implemented in Simulink

With the model of the engine’s torque response complete, this can now be combined with the model of the controller and the previously constructed electro-mechanical plant model, as shown in Fig. 5.27. Notice that an additional feedback loop over ω is required to implement the engine torque model. Additionally, a saturation limit is added along the control signal path to limit the controller output to $\{0 \leq T \leq 1\}$.

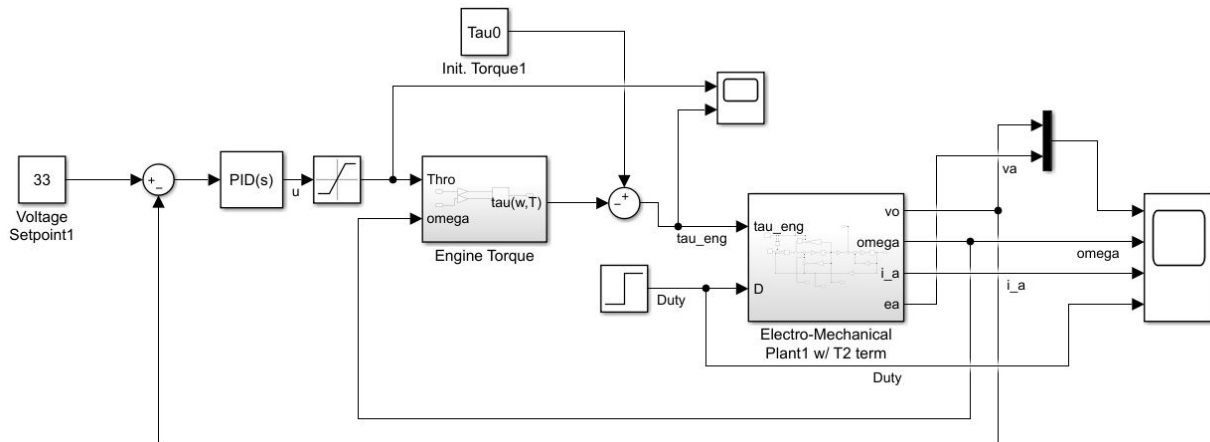


Figure 5.27: Torque response surface model implemented in the complete power system model.

This model can be further simplified by combining the constituent blocks into controller and plant subsystems, as shown in Fig. 5.28.

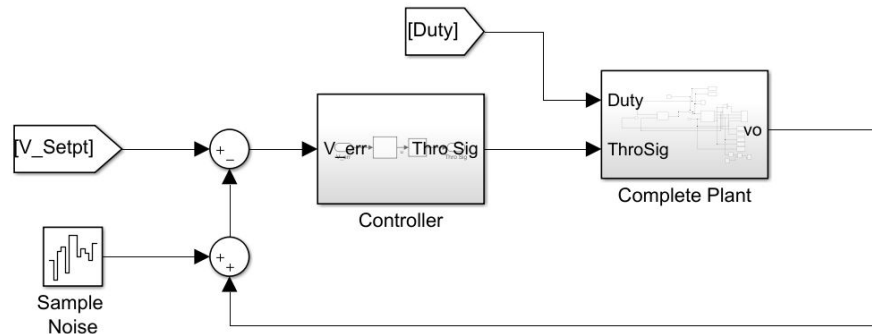


Figure 5.28: Simplified block diagram for the engine-driven hybrid power system.

5.3 Model Tuning and Comparison With Experimental Data

In order to more easily compare the simulation results with the experimental data, the simulation solver is converted from variable time-step to fixed time-step. Here, we will solve the simulation using a fixed-time step of $\Delta t = 0.0025\text{sec}$ or $\Delta t = 1/f_s$ the sampling frequency of the data acquisition system used in the experiment. Though the fourth, fifth, and eighth order continuous time solvers were tested explicitly, each gave identical results, so the `ode4` Runge-Kutta solver is used for this analysis.

In order to ensure that this model is functioning properly and accurately represents the experimental apparatus it will be subjected to three duty-cycle input profiles: a single step response profile; the multi-step duty-cycle profile; and the fast ramp-rate profile used in the

experiment. Note that for this analysis, since the HEPS is generating power to be consumed by a load, the current presented in this is negative, thus representing the flow of current from the PMSM generator.

5.3.1 Single-Step Response Characteristics

The model system is first subjected to a single step change in duty cycle. This function is described by

$$D(t) = \begin{cases} 0.2 & \text{if } 0 \leq t \leq 6\text{sec} \\ 0.6 & \text{otherwise} \end{cases} \quad (5.69)$$

The response to this input is shown in Fig. 5.29.

The voltage output from the generator system is observed to initially drop after the step change in the duty cycle, then recover to the controlled target value of 33V. The maximum voltage drop is $\Delta V_{max} = 1.98V$ in this case. Additionally, this is accompanied by a momentary drop in ω and a significant increase in output current, as expected.

The throttle trajectory is plotted along the response surface model as shown in Fig. 5.30. This shows that the system maintains a significant distance from the boundary of the its operating range under these input conditions.

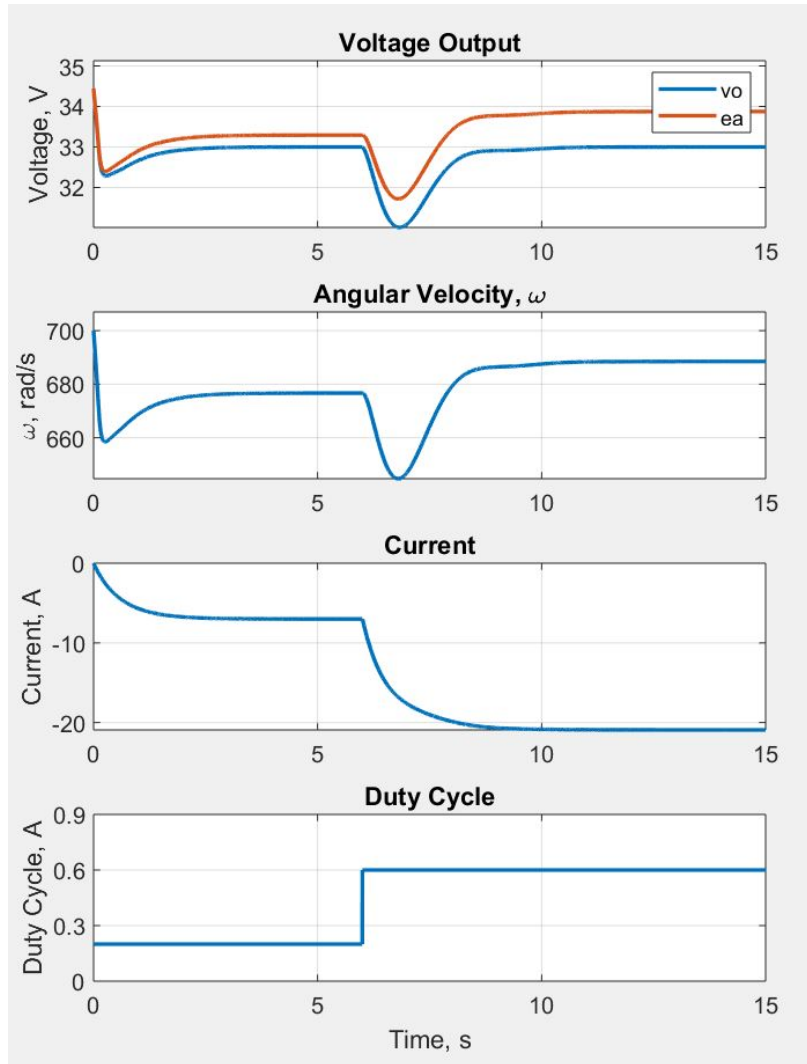


Figure 5.29: System model results for single step up.

The system is then subjected to a falling step change of the same magnitude, as shown in Fig. 5.31, where

$$D(t) = \begin{cases} 0.6 & \text{if } 0 \leq t \leq 6\text{sec} \\ 0.2 & \text{otherwise} \end{cases} \quad (5.70)$$

Here, the system reaches steady state with $D = 0.6$ at approximately $t = 4\text{sec}$. With the step reduction in the duty cycle, the output voltage is observed to jump before returning

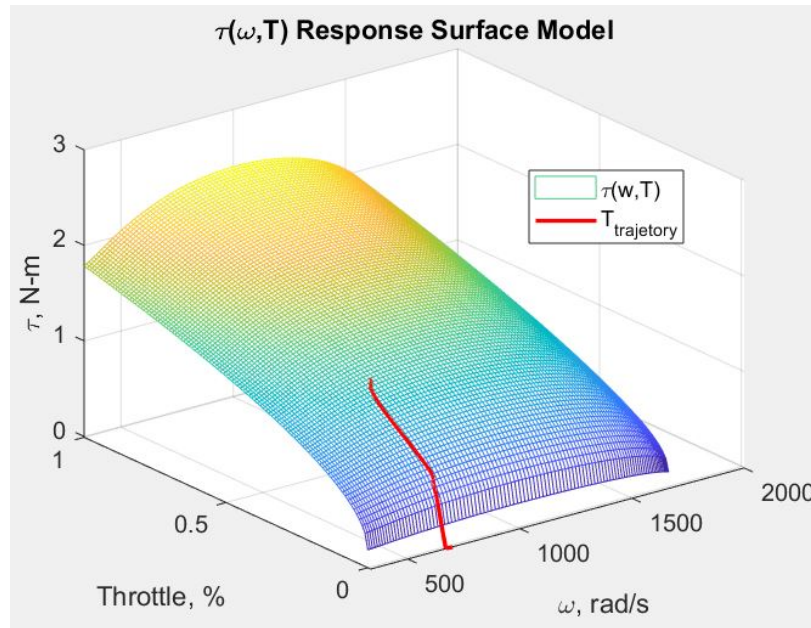


Figure 5.30: Throttle trajectory results for single step up.

to the controlled setpoint, $\Delta V_{max} = 2.87V$. This is accompanied by a concurrent increase in angular velocity and a decrease in output current, again as expected and as shown in Fig. 5.32.

The throttle trajectory is again far from the operating boundaries of the system.

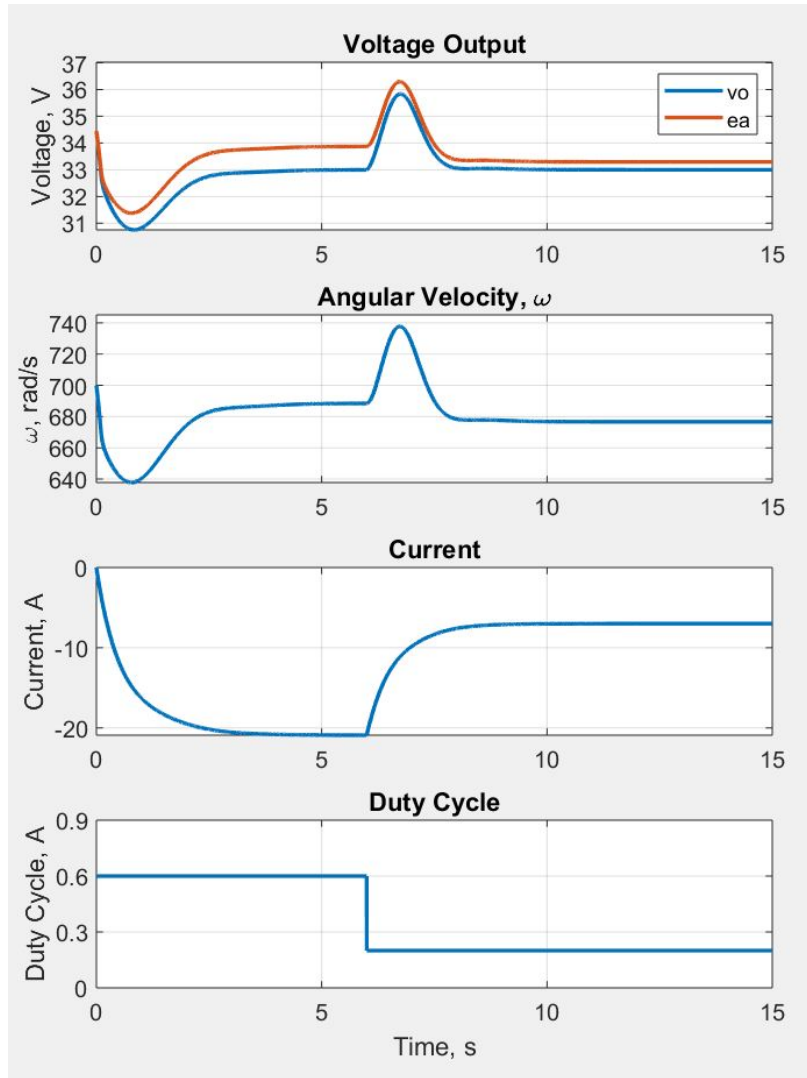


Figure 5.31: System model results for single step down.

5.3.2 Multi-Step Response

The multi-step duty-cycle profile applied to the system is described by

$$D(t) = \begin{cases} 0.0 & \text{if } 0 \leq t \leq 10\text{sec} \text{ or } 80 < t \leq 90\text{sec} \\ 0.225 & \text{if } 10 < t \leq 20\text{sec} \text{ or } 70 < t \leq 80\text{sec} \\ 0.45 & \text{if } 20 < t \leq 30\text{sec} \text{ or } 60 < t \leq 70\text{sec} \\ 0.675 & \text{if } 30 < t \leq 40\text{sec} \text{ or } 50 < t \leq 60\text{sec} \\ 0.9 & \text{if } 40 < t \leq 50\text{sec} \end{cases} \quad (5.71)$$

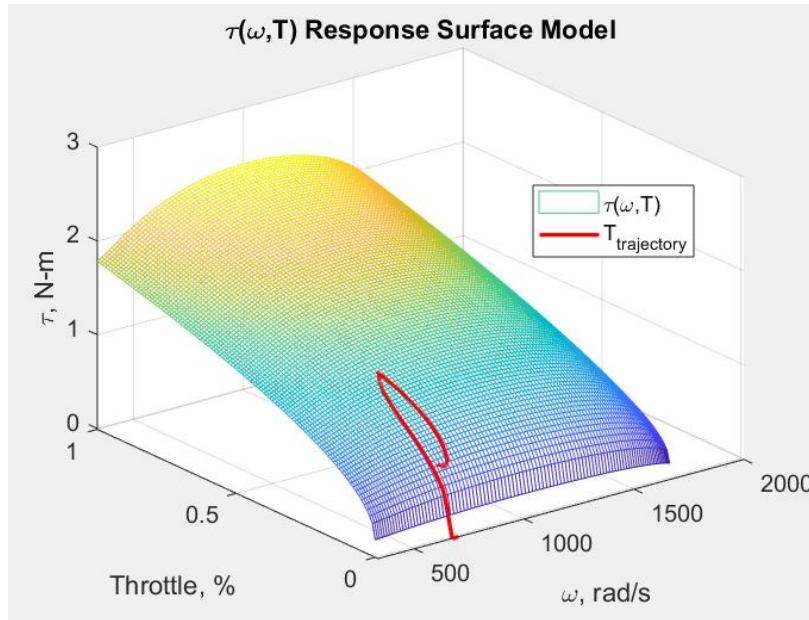


Figure 5.32: Throttle trajectory results for single step down.

In this case, the model exhibits the same dynamic attributes as the experimental apparatus with comparable magnitudes, as can be seen in Figs. 5.33 and 5.34 respectively. For example, both the model and the experimental system exhibit voltage perturbations corresponding with step changes in the load duty cycle throughout the operating range of the system. In both cases these perturbations are typically in the range $2V \leq \Delta V \leq 4V$. Additionally, both the voltage and current signals exhibit an asymptotic recovery to the setpoint or new operating point respectively. With recovery time constants typically less than 1sec.

The trajectory response of the system is shown on the torque and power manifolds respectively in Figs. 5.35 and 5.36.

Notably, power inversions were not observed in the simulation, and could not be produced by tuning the model parameters. Therefore, the underlying dynamics of these power inversions is not captured by this simulation. This is likely due to nonlinear and potentially

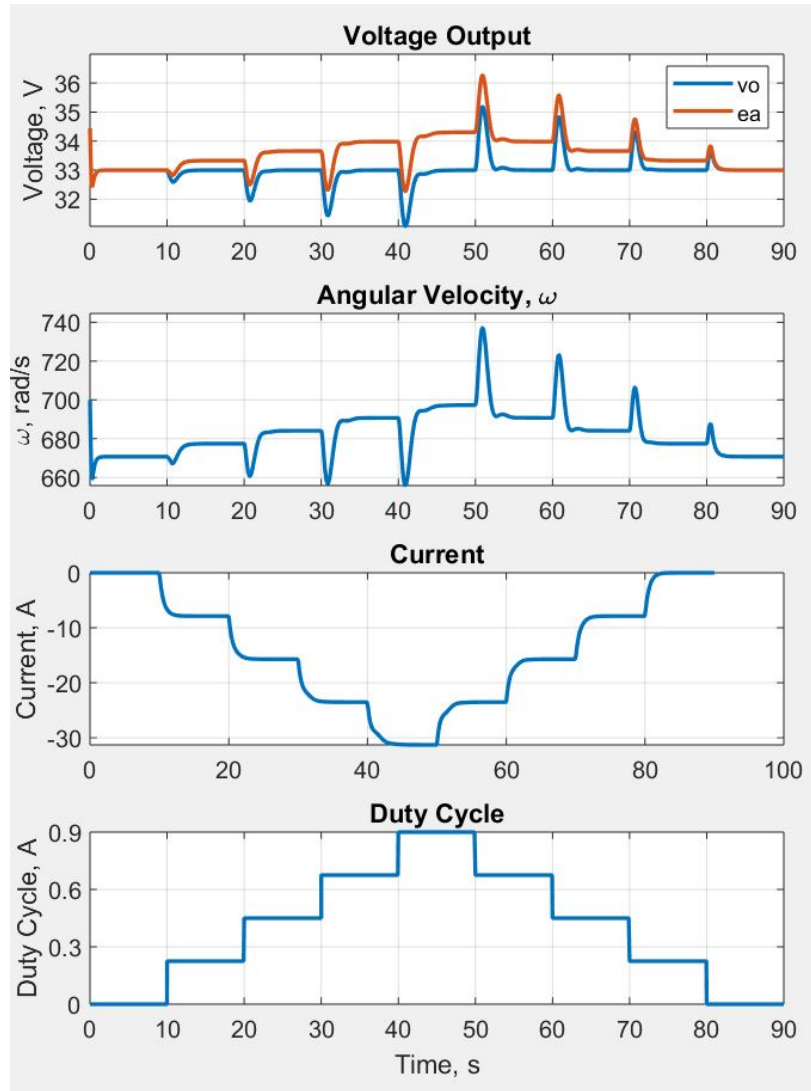


Figure 5.33: System model results for the multi-step duty-cycle profile.

aberrant behavior in the carburetor not captured in the simulation, since these inversions did not occur in the same manner throughout the operating range of the experiment. These inversions can likely be mitigated through the use of a well-designed fuel injection system, though such a system is beyond the scope of this research.

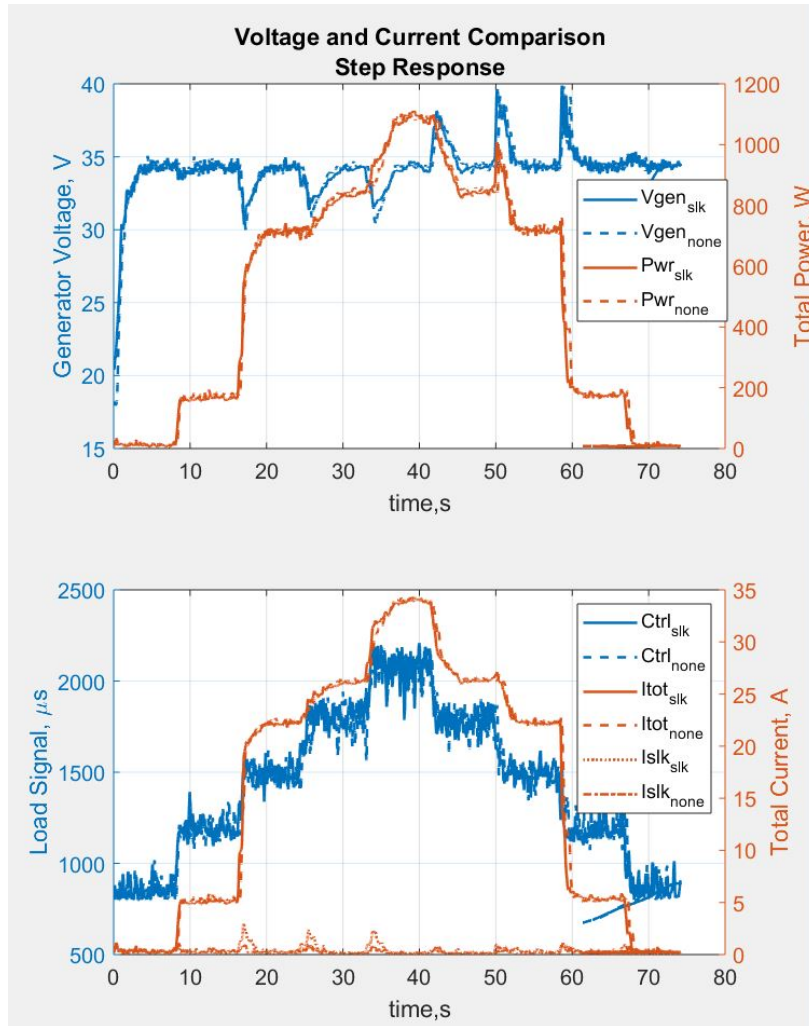


Figure 5.34: Experiment results for multi-step duty-cycle profile for comparison.

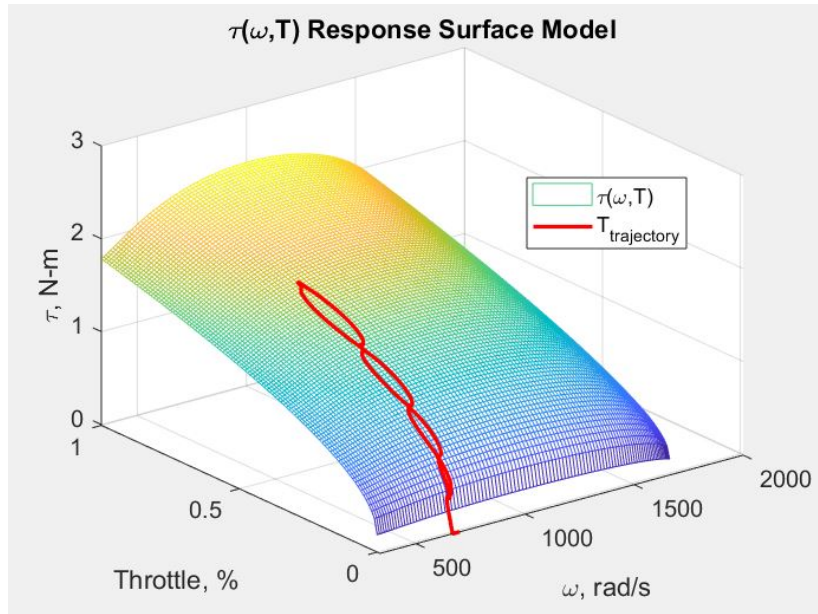


Figure 5.35: Throttle trajectory results for multi-step duty-cycle profile.

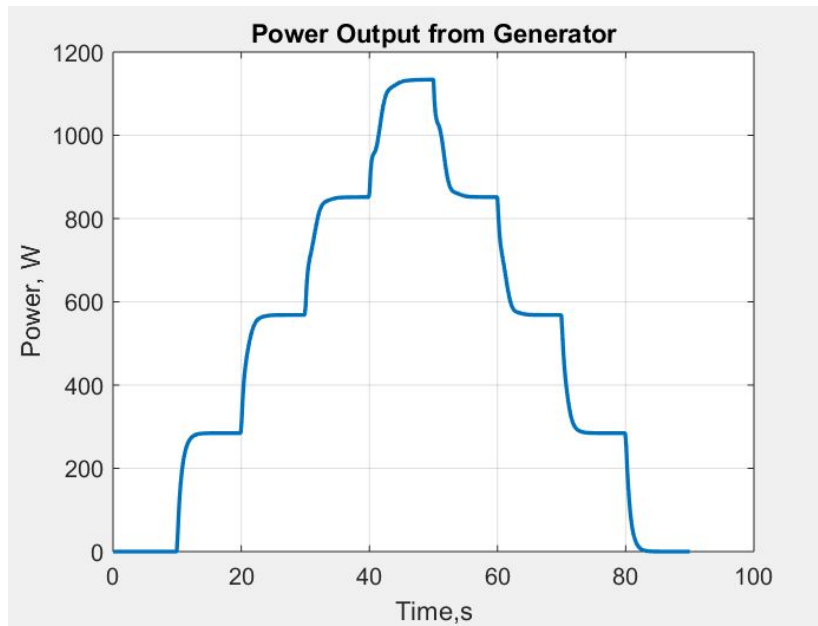


Figure 5.36: Power results for multi-step duty-cycle profile.

5.3.3 Fast Ramp Response

The ramp profile used in this simulation is designed to be identical to that used in the experiment, as shown in Fig. 5.37. In the simulation, this is described by

$$\frac{dD(t)}{dt} = \begin{cases} 0.0/sec & \text{if } 0 \leq t \leq 10sec \\ 0.138/sec & \text{if } 10sec > t \leq 16.5sec \\ 0.0/sec & \text{if } 16.5sec > t \leq 36.5sec \\ -0.138 & \text{if } 43.0sec > t \leq 53.0sec \end{cases} \quad (5.72)$$

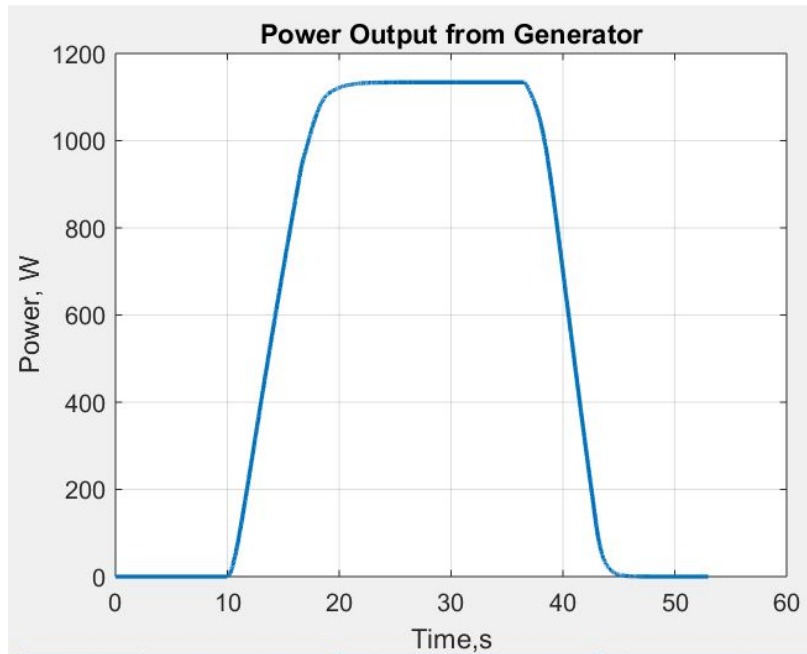


Figure 5.37: Model power output results for the fast-ramp duty-cycle profile.

Again, the simulation and experimental data show similar dynamic response characteristics under the fast-ramp load profile. The ramp-up is characterized by a voltage drop

where $2.0V > \Delta V \leq 3.0V$ in both cases. The voltage jump corresponding to the ramp-down is significantly smaller in the simulation than in the experiment. In the simulation $\Delta V_{max} = 2.0V$, whereas in the experiment $\Delta V_{max} = 6.8V$. Further, in the simulation, under an anti-symmetric ramp-up/ramp-down profile, the associated voltage excursions are approximately symmetric about the control voltage and essentially anti-symmetric. In the experimental results, these voltage excursions do not exhibit this symmetry, but rather provide further indication that certain aberrant behaviors associated with the carburetor, such as fluctuations in equivalence ratio and harmonic interactions with the exhaust system, while not modeled here, are nonetheless present in the system, as shown in Figs 5.38, 5.39, and 5.40.

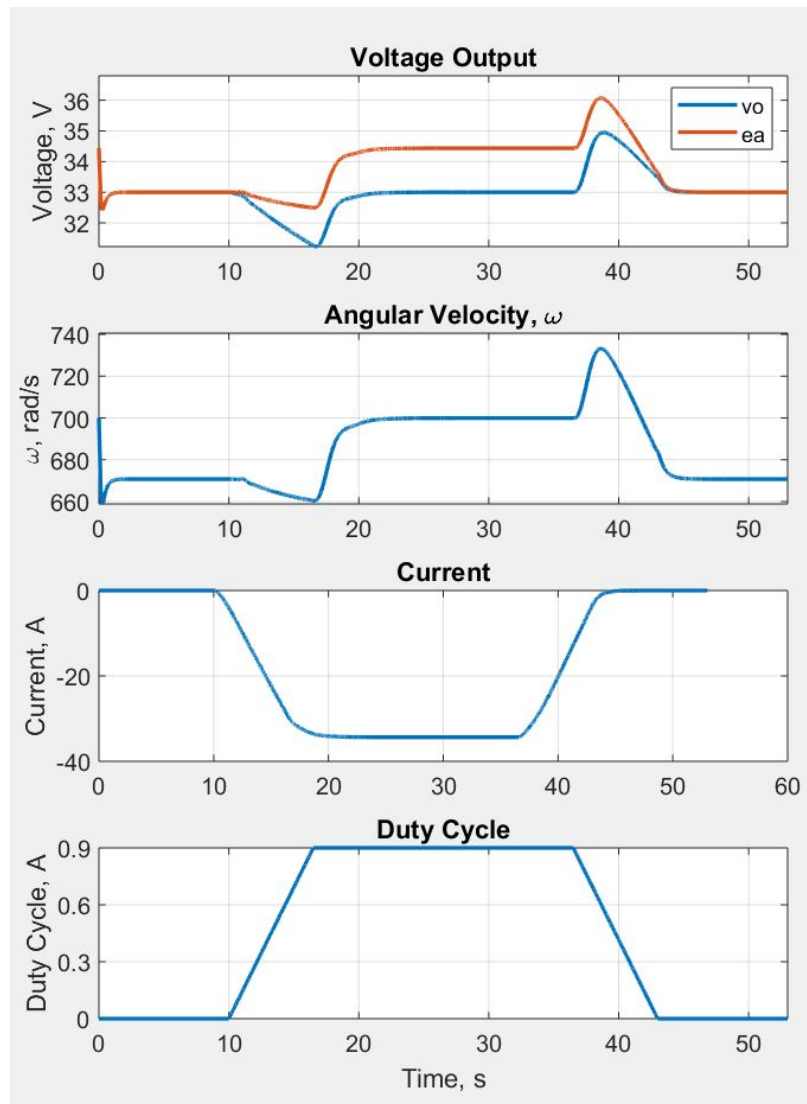


Figure 5.38: System model results for the fast-ramp duty-cycle profile.

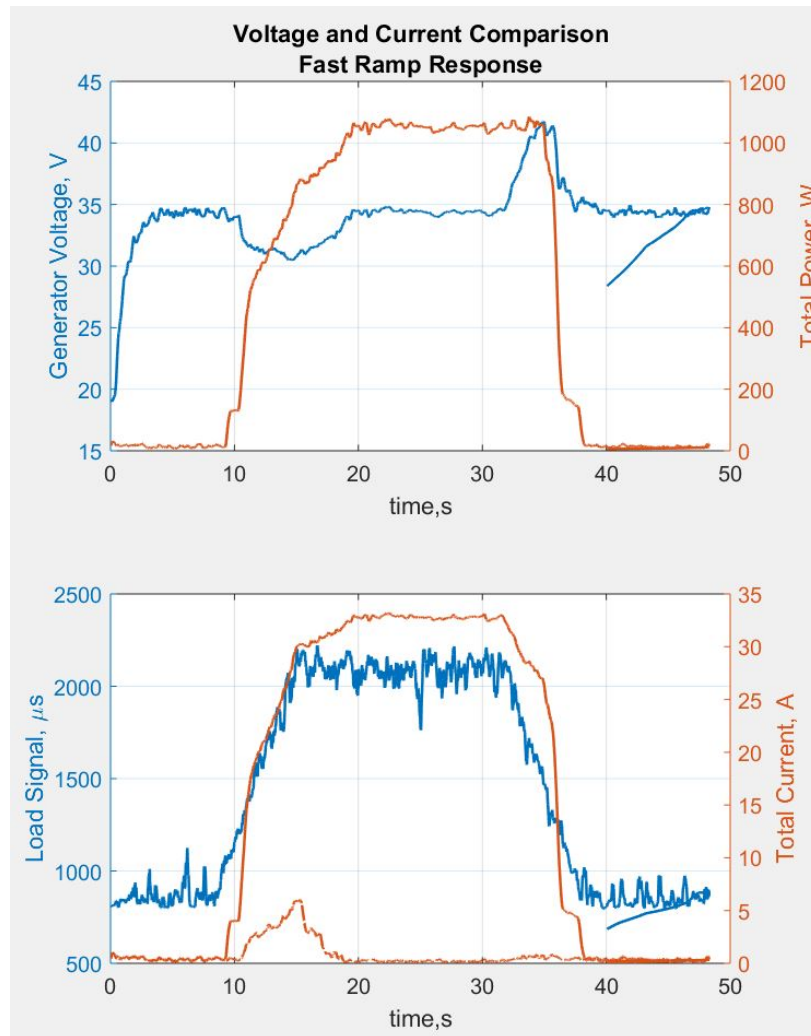


Figure 5.39: Experimental results for the fast-ramp duty-cycle profile. *Note that the data 'tails' in this figure are due to the manual shutoff of an experimental protocol, as well as data processing, and are not physically significant.*

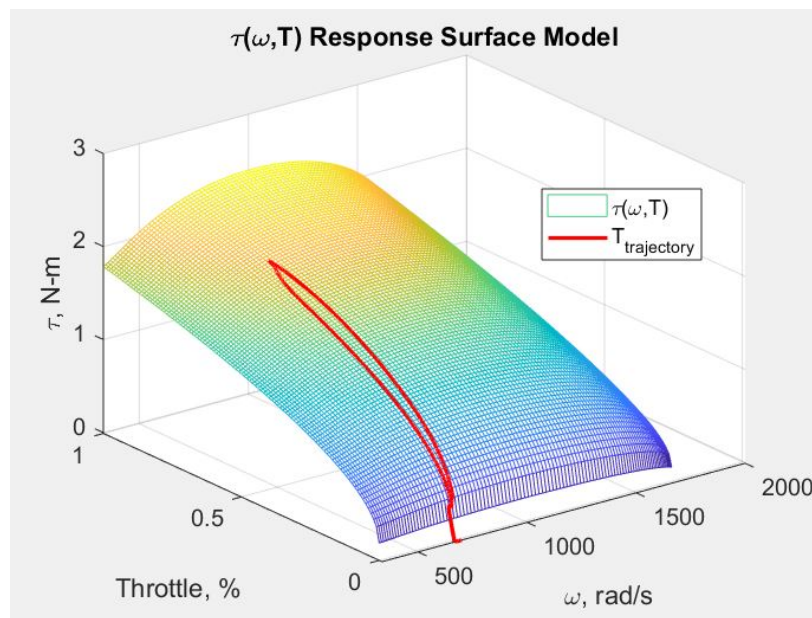


Figure 5.40: Model throttle trajectory results for the fast-ramp duty-cycle profile.

5.4 Conclusions

In this chapter, the experimental data gathered from a two-stroke powered hybrid power system is used to develop a dynamical model of the system using a baseline PID controller. The output from this system is regulated by a PWM-switching PPU that behaves as a type of DC-DC transformer. The governing equations for this system are developed from the equivalent circuit for the engine-generator system.

The development of the plant model, controller, and engine torque response surface model are shown in detail. Since the generator system is shown to be a two-pole system, the use of a single PID controller to regulate the output voltage from the system is sufficient for this baseline model. The power and torque characteristics of the internal combustion engine are captured using a response surface model for the torque as a function of the angular velocity and throttle setting, $\tau(\omega, T)$.

When compared to the experimental data, this baseline model shows excellent agreement regarding the characteristics and magnitudes of the dynamic response. Specifically, the model is tuned to reflect the voltage departures from the setpoint such that they are comparable in magnitude and duration to those observed in the experiment. However, The power inversion behaviors observed in some instances in the experiment were not observed in the simulation. As this does not occur with any regularity in the experimental data collected, we must assume that the associated nonlinear or aberrant behaviors of the engine system, most likely the carburetor, are not well captured in the simulation. These behaviors can be likely be mitigated in future experimental systems through the use of fuel injection coupled with a forced air induction system to deliver a well-controlled fuel-air mixture to the engine.

Generally, this baseline model provides an excellent representation of the experimental hybrid power system and therefore can be used for the remaining analysis in this research with confidence that the results will be physically meaningful.

Chapter 6

Combined ADP VTOL and HEPS

Simulation

6.1 Introduction

This chapter is presented in three parts. In part one, the finite wing performance is developed for a given aircraft approximation based on the ADP experimental results. In part two, the aircraft control objectives are established and the performance of the HEPS control system is extended through the use of nonlinear robust control, power tracking, and dynamically adaptive voltage modulation. Finally, in part three, the aircraft-derived transition power loading developed in part one is applied to the improved HEPS design developed in part two.

6.2 Part One - Developing the Aircraft Models

6.2.1 Developing 3-D Wing Estimates for C_L , C_D and C_M

In order to investigate the performance of the ADP propulsion system in an aircraft configuration, finite wing estimates of C_L , C_D and C_M must be developed from the 2-D wing section data gathered in the wind tunnel experiments discussed previously. For a typical wing, this transition is well described by Prandtl's Lifting line theory, where the circulation distribution in the wake of the finite wing induces downwash, which alters the effective angle of attack of the wing in the spanwise direction, and thereby changes the spanwise lift distribution. Effectively, this downwash unloads the wing by accounting for the effects of highly three-dimensional flows at the wing tips, driving the lift at the wing tips to zero. The manner in which this occurs is a function of the wing planform geometry and wing aspect ratio.

$$AR = \frac{b^2}{S} \quad (6.1)$$

Where b is the wingspan, and S is the wing area. For this analysis we will consider only wings with a rectangular planform, e.g. straight, un-tapered, and un-swept wing. The evolution of the circulation distribution is dependent upon aspect ratio, as shown in Fig. 6.1.

This analysis will leverage a numerical approximation of Prandtl's Classical Lifting Line Theory to estimate the finite wing C_L , C_D , and C_M from the wind tunnel data. The numerical solution approach used in this analysis was originally developed by John D. Anderson in his *Aerodynamics, 5th edition* textbook [6] as well as his *Introduction to Flight* [7]. The

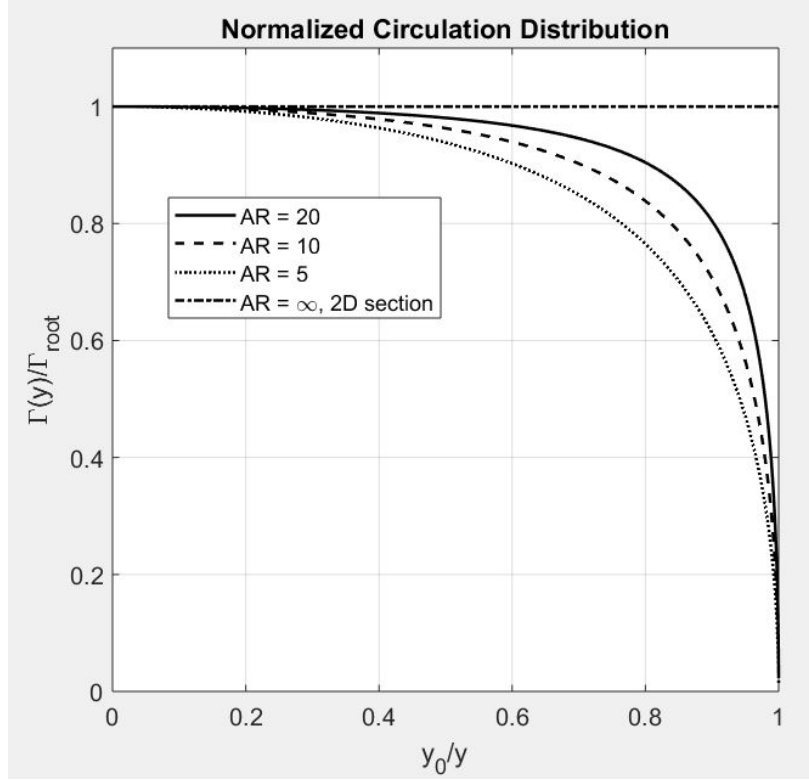


Figure 6.1: Normalized circulation distribution for rectangular planform wings for different aspect ratios. For $AR = \infty$, the result is the circulation induced by the 2D airfoil section.

numerical scheme used in this approximation was developed by J.F. Dannenhoffer, following Anderson's approach [18].

Brief Summary of Classical Lifting Line Theory

Prandtl's Lifting Line Theory proceeds from the Kutta-Joukowski Theorem $L = \rho V_\infty \Gamma$, where the lift force on a vortex filament depends on circulation Γ , as well as the velocity field in the vicinity of a three-dimensional vortex filament as described by the Biot-Savart Law.

$$\vec{V}(x, y, z) = \frac{\Gamma}{4\pi} \int_{-\infty}^{+\infty} \frac{d\vec{l} \times \vec{r}}{|\vec{r}|^3} \quad (6.2)$$

Prandtl reasoned that if a vortex filament with circulation Γ , were somehow bound to a specific region in a flow, there must exist trailing vortices extending to infinity each with circulation Γ , since circulation must be constant along a vortex filament, and a vortex filament cannot end in a fluid [39], as shown in Fig. 6.2.

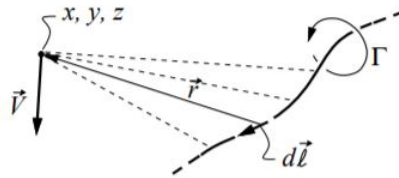


Figure 6.2: Three-dimensional vortex filament, [39]

Prandtl's classical approach, proposed a model whereby a lifting wing is represented by the superposition of an infinite number of horseshoe vortices bound to a lifting line at the wing's quarter chord position. These trailing vortices induce a downward velocity at the lifting line. For an infinite number of vortices, each with circulation $d\Gamma$, the downwash velocity at a specific location y_0 along the span is given by

$$w(y_0) = \frac{1}{4\pi} \int_{-b/2}^{b/2} \frac{(d\Gamma/dy)dy}{y_0 - y} \quad (6.3)$$

Here, the downwash velocity w at the spanwise position y_0 is determined by the circulation distribution of all trailing vortices, that is the entire trailing vortex sheet.

Therefore, the angle of attack induced by this downwash at a particular point, is also determined by the circulation distribution in the entire trailing vortex sheet, as shown in Fig. 6.3.

$$\alpha_i(y_0) = \tan^{-1} \left(\frac{-w(y_0)}{V_\infty} \right) \quad (6.4)$$

Typical aerodynamic systems allow the use of the small angle approximation here, $\tan^{-1}(\alpha_i) \approx \alpha_i$.

$$\alpha_i(y_0) = \left(\frac{1}{4\pi V_\infty} \int_{-b/2}^{b/2} \frac{(d\Gamma/dy)dy}{y_0 - y} \right) \quad (6.5)$$

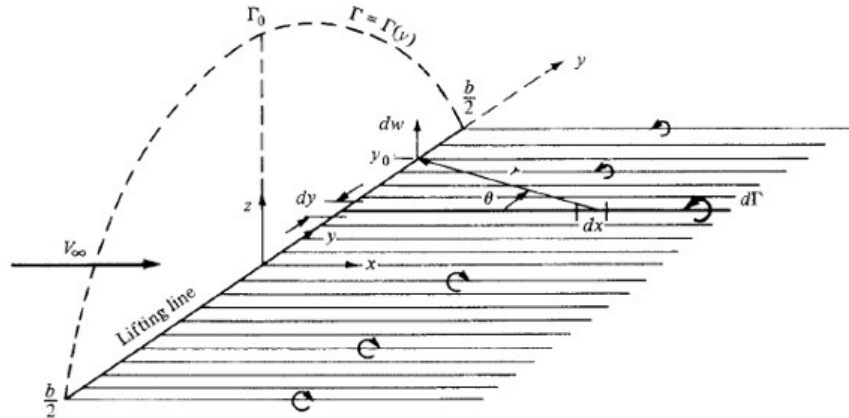


Figure 6.3: A finite wing modeled as a superposition of an infinite number of horseshoe vortex elements, [creditAnderson].]

Application to ADP

While the underlying physical model of lifting line theory holds true for the ADP system, in that the trailing vortex sheet still influences the downwash distribution and thereby the effective angle of attack, the complexity of a distributed propulsion system coupled with the broad operating regime of ADP from $\alpha = 0$ deg to $\alpha = 90$, introduces additional, complex three-dimensional effects that impact this distribution and are not well represented by the analytical models used in lifting line theory. Here, operation at extreme angles of attack generate highly three dimensional flows, particularly near the wing tips. These flows will interact with the embedded fans in the propulsion system, further compounding these effects on the trailing vortex system. At this point, detailed experimental and computational

studies of these wing-tip effects are not feasible given the laboratory and computing resources available to the research team.

For example, fully capturing the unsteady wing-tip effects and their interactions with the embedded fans would require a high-fidelity, fully-unsteady CFD model, where the wing and each embedded fan is modeled in detail, such a calculation is estimated to require a computational mesh in excess of 100 Million cells, a time step of approximately $5\mu s$, and a total flow time in excess of 1 second, to capture one operating condition in detail. The present experimental effort evaluated more than 500 different operation conditions to develop the relatively coarse dataset used in this analysis, rendering the use of hi-fidelity CFD to be unfeasible.

An alternate approach would be to apply particle image velocimetry (PIV) measurement techniques to characterize the flow at an ADP wing tip experimentally. While this is more feasible than the CFD approach, the facility and equipment required to accomplish this still exceeds the resources available for the present effort. Therefore, the detailed investigation of the three-dimensional flows at the wing-tips of the ADP system will be left for future research.

Since the objective of the present research is to evaluate the impact of the ADP propulsion system coupled to a hybrid power system, given the challenge associated with fully characterizing the three-dimensionality of the ADP wing tip flows, and fully acknowledging the shortcomings of a simplified analytical approach, lifting line theory will be used to approximate finite wing aerodynamic coefficients for the ADP system. While these coefficients will not be accurate, they will represent a reasonable, though qualitative approximation of the finite wing performance of the ADP system given the data available at this time.

In order to evaluate this, a lifting approximation is applied numerically according to the following algorithm, using the 2-D profile data collected during the wind tunnel experiments.

Algorithm 1: Numerical Lifting Line Algorithm

Result: Finite Wing Result: C_L, C_D, C_M

- 1 Initialize model by guessing a $\Gamma(y)$ distribution;
 - 2 **while** $C_{L_{old}} - C_{L_{new}} > threshold$ **do**
 - 3 Compute $\alpha_i(y|\Gamma(y))$;
 - 4 Compute effective angle of attack, α_{eff} ;
 - 5 Interpolate new section coefficients, c_l, c_d , and c_m given α_{eff} ;
 - 6 Compute a new circulation, $\Gamma_{new}(y|cl(y))$;
 - 7 Compute finite wing coefficient estimates C_L, C_D, C_M ;
 - 8 Update $\Gamma(y)$ using relaxation;
 - 9 **end**
-

The wing lift coefficient C_L and induced drag coefficient $C_{D,i}$ are integral functions of the spanwise circulation distribution $\Gamma(y)$,

$$C_L = \frac{2}{V_\infty S} \int_{-b/2}^{b/2} \Gamma(y) dy \quad (6.6)$$

$$C_{D,i} = \frac{2}{V_\infty S} \int_{-b/2}^{b/2} \Gamma(y) \alpha_i(y) dy \quad (6.7)$$

while the wing moment coefficient C_M is a an integral function of the section moment coefficients evaluated at the effective angle of attack.

$$C_M = \frac{1}{V_\infty} \int_{-b/2}^{b/2} c_m(\alpha_{eff}(y)) dy \quad (6.8)$$

Once the circulation distribution $\Gamma(y)$ is defined for a given iteration, these integrals are easily evaluated numerically, using simple techniques such as trapezoidal integration. The solution is considered to be converged when the difference in C_L for successive iterations is less than 10^{-4} .

Wing Planform Definition and Results

For this analysis, the aspect ratio of the wing is assumed to be $AR = 8$, with a rectangular planform. When finite wing effects are considered, C_L , C_D , and C_M can be approximated from the section profile data. This is shown in Figs. 6.4, 6.5, and 6.6 respectively.

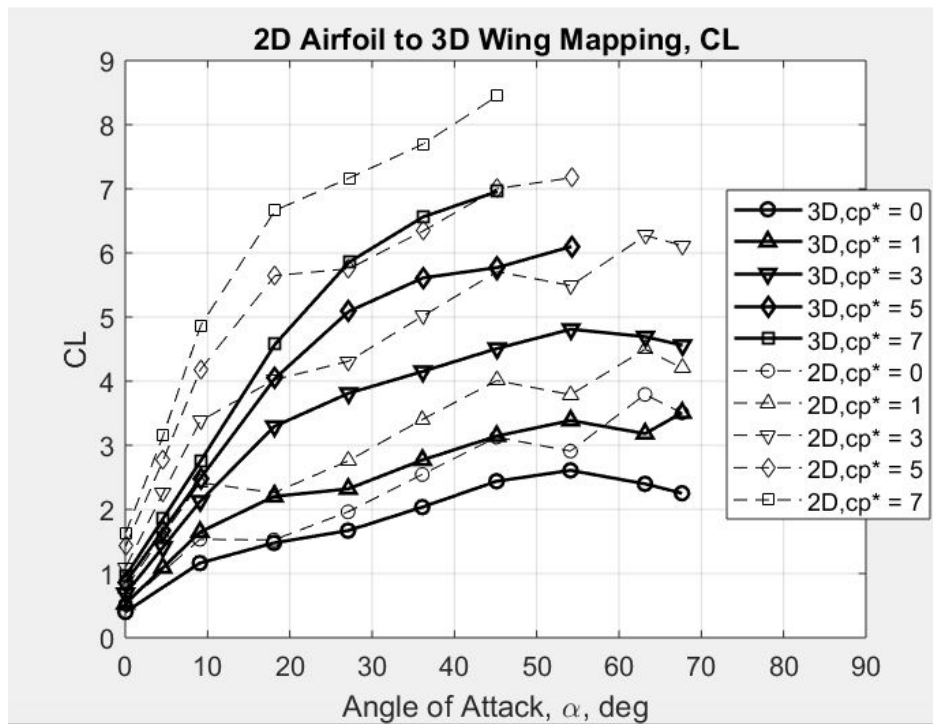


Figure 6.4: Comparison between c_l and C_L for the ADP propulsion system, $AR = 8$]

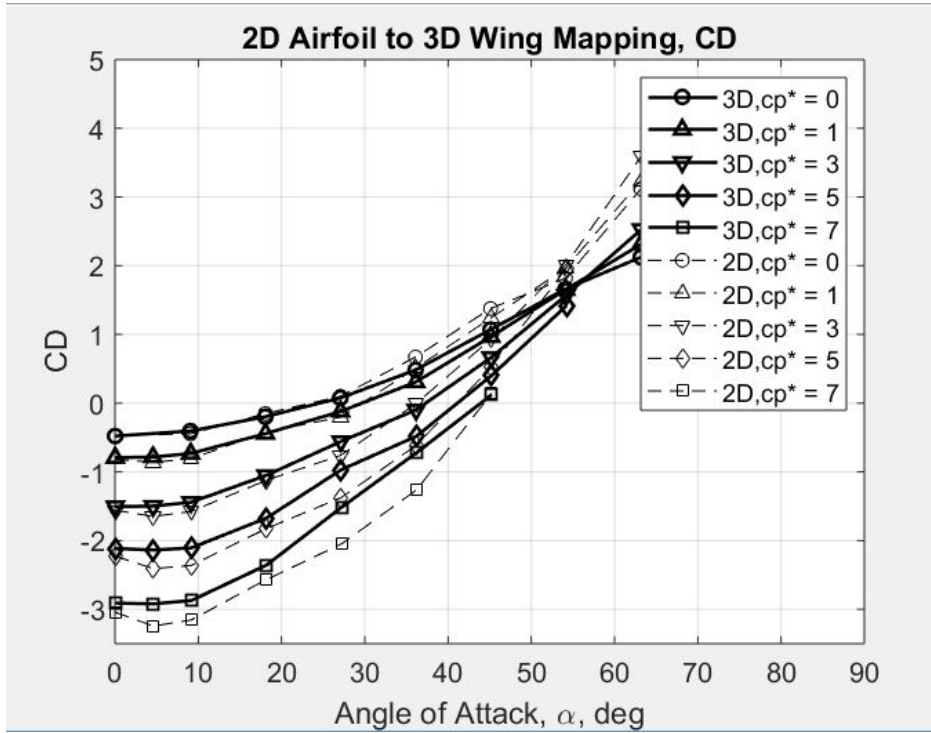


Figure 6.5: Comparison between c_d and C_{Di} the induced drag coefficient, for the ADP propulsion system, AR = 8]

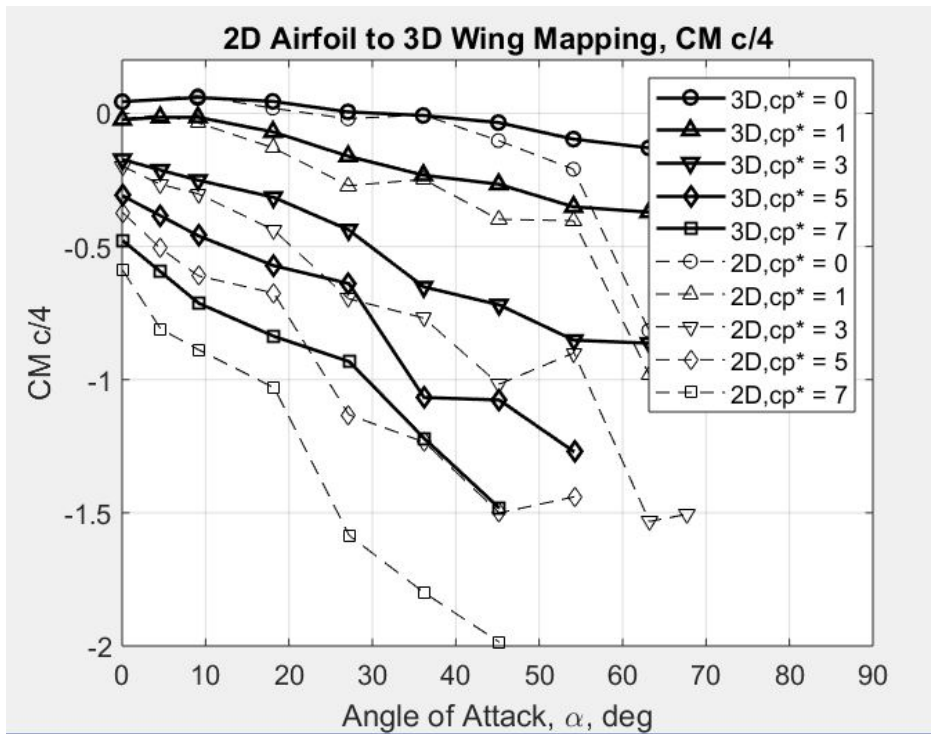


Figure 6.6: Comparison between c_m and C_M for the ADP propulsion system, AR = 8]

6.3 Aircraft Design Parameters

In order to explore the design space for aircraft using the ADP system, it is more convenient and informative to develop scaling parameters that describe aircraft design attributes rather than present results in the context of one specific design. Here we will introduce two parameters that can be used to effectively describe an ADP aircraft configuration at the highest level for the purposes of exploring the feasibility and performance limits of the hybrid propulsion system.

6.3.1 Wing Loading, W_L

Wing loading is a commonly used aircraft design parameter. Significant aircraft performance estimates can be developed in terms of wing loading. Here, wing loading is defined as

$$W_L \equiv \frac{\textit{Weight}}{\textit{Wing - Area}} = \frac{W}{S} \quad (6.9)$$

with units $[N/m^2]$. Just as aerodynamic lift is typically expressed as a function of wing area, this force can be expressed in terms of wing loading, W_L . Consider the typical lift force expression

$$L = \frac{1}{2}\rho V_\infty^2 C_L S \quad (6.10)$$

This can be expressed in terms of wing area

$$\frac{L}{S} = nW_L = \frac{1}{2}\rho V_\infty^2 C_L \quad (6.11)$$

Where n in this case is the current load factor. For straight and level flight, load factor $n = 1$. For maneuvers such as pull-ups and turns, $n > 1$ while for push-downs $n < 1$. Additionally, the required lift coefficient at a specific velocity as well as the stall speed can be expressed in terms of W_L .

$$C_{L_{req}} = \frac{2W_L}{\rho V_\infty^2} \quad (6.12)$$

$$V_{stall} = \sqrt{\frac{2W_L}{\rho C_{L_{max}}}} \quad (6.13)$$

6.3.2 Power Loading, P_L

The next parameter, power loading P_L is unique to this distributed propulsion system. This is an expression of the ideal jet power per unit span for a given operating condition. This is defined as

$$\text{Power Loading, } P_L(c_p^*, V_\infty | c, \alpha) \equiv \frac{P_{jet_{ideal}}(c_p^*, V_\infty)}{b} \quad (6.14)$$

Where b is the wing span.

Here the wing chord c and geometric angle of attack α must be defined for the operating condition. The control volume used to estimate the conditions around each of the embedded fans in the propulsion system is shown in Fig. 6.7.

In order to develop the power loading parameter P_L , size scaling must be addressed first, such that dynamic similarity with the wind tunnel test apparatus is maintained. The chord of the ADP wing c_w is the characteristic length scale in this system, since, for the ADP design studied here, all other length scales in the system can be described relative to c_w . Additionally, for this analysis, the flow around the ADP wind tunnel system is assumed to

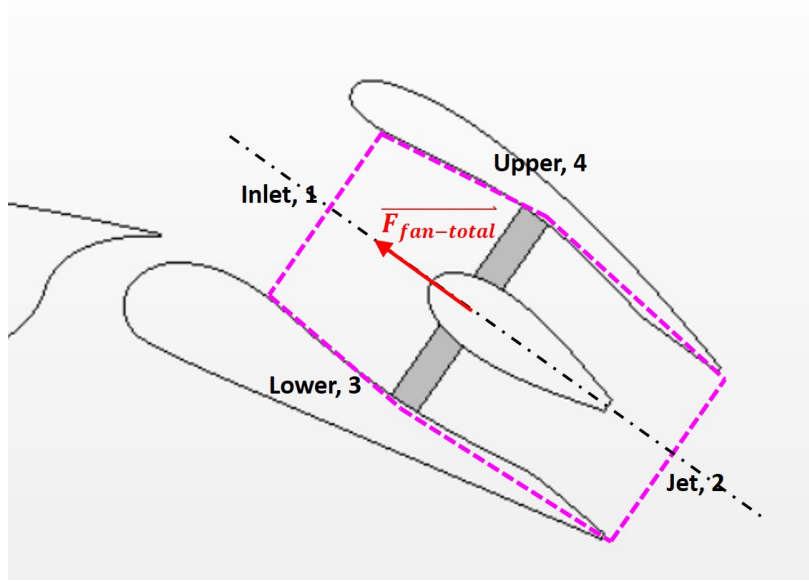


Figure 6.7: Control volume drawn around each embedded fan in the ADP system.]

be fully turbulent and and therefore the effects associated with increasing Reynolds Number R_e can be neglected for increasing wing chord, however, these Reynolds number effects will become significant when decreasing the chord should this decrease result in transitional flow.

Recall the definition of the dimensionless parameter c_p^* , used throughout this research to describe aerodynamic forces in terms of applied power.

$$c_p^* = \frac{\Delta p_{fan}}{q_\infty} \quad (6.15)$$

Since c_p^* can be used to compare the operating condition of the ADP system across a broad range of α , we can evaluate the size scaling of the ADP system in terms of constant c_p^* at a fixed freestream velocity V_∞ .

However, c_p^* , as it is currently defined, can be a negative number. In this context, we would like to define a dimensionless parameter based on c_p^* , but that is strictly positive.

Ideally, this new parameter would be equal to zero when the ideal jet power is zero. To accomplish this, the minimum $c_p^*|_{\alpha=\alpha_0, P=0}$ for a given angle of attack is subtracted from all other $c_p^*|_{\alpha=\alpha_0, P>0}$.

$$c_p^{*'} \equiv c_p^*|_{\alpha=\alpha_0, P>0} - \min(c_p^*)|_{\alpha=\alpha_0, P=0} \quad (6.16)$$

Let ① represent the reference case of the wind tunnel model, and let ② represent the scaled case. For constant V_∞ , and assuming constant fluid density ρ ,

$$V_{\infty_1} = V_{\infty_2} \rightarrow q_{\infty_1} = q_{\infty_2} = q_\infty \quad (6.17)$$

Expanding the c_p^* variable in terms of the total pressure of the flow at the inlet and outlet of the fan duct, Eq. 6.16 becomes

$$c_p^{*'} = \frac{p_2 - p_1}{q_\infty} - \frac{\min(p_2) - p_1}{q_\infty} \quad (6.18)$$

Since p_1 is the stagnation pressure of the freestream flow for the same V_∞ in both cases, this expression simplifies to

$$c_p^{*'} = \frac{p_2 - \min(p_2)}{q_\infty} \Big|_{\alpha=\alpha_0, P \geq 0} \quad (6.19)$$

This new parameter is still dimensionless and with a similar numerator and identical denominator to c_p^* , however it is strictly positive, and must be defined for each operating angle of attack $\alpha = \alpha_0$

If two ADP systems are operating with the same c_p^* or $c_p^*|_{\alpha=\alpha_0}$, then we have

$$\frac{c_{p2}^*}{c_{p1}^*} = \frac{c_{p2}^*}{c_{p1}^*} = \frac{\frac{\Delta p_{fan2}}{q_{\infty 2}}}{\frac{\Delta p_{fan1}}{q_{\infty 1}}} = \frac{\Delta p_{fan2}}{\Delta p_{fan1}} = 1 \quad (6.20)$$

Invoking the fan affinity law for pressure, and assuming constant density ρ

$$\frac{\Delta p_{fan2}}{\Delta p_{fan1}} = \frac{p_2}{p_1} = \frac{\rho_2}{\rho_1} \left(\frac{\omega_2}{\omega_1} \right)^2 \left(\frac{d_2}{d_1} \right)^2 = 1 \quad (6.21)$$

Since the fan diameter d is proportional to the chord c , where for this design

$$d = 0.43c \quad (6.22)$$

Therefore,

$$\frac{\omega_2}{\omega_1} = \frac{c_1}{c_2} \quad (6.23)$$

Now, invoking the fan affinity law for power, again assuming constant density ρ

$$\frac{Pwr_2}{Pwr_1} = \frac{\rho_2}{\rho_1} \left(\frac{\omega_2}{\omega_1} \right)^3 \left(\frac{d_2}{d_1} \right)^5 \quad (6.24)$$

Substituting, Eq. 6.23 and Eq. 6.22 into Eq. 6.24, the power scaling from ① to ② becomes

$$\frac{Pwr_2}{Pwr_1} = \left(\frac{c_1}{c_2} \right)^3 \left(\frac{c_2}{c_1} \right)^5 = \left(\frac{c_2}{c_1} \right)^2 \quad (6.25)$$

Therefore the power scaling relationship for the ADP system can be expressed as a function of the chord ratio only for constant c_p^* and V_∞ .

$$\boxed{\frac{Pwr_2}{Pwr_1} = \left(\frac{c_2}{c_1}\right)^2} \quad (6.26)$$

Now that the geometric power scaling relationship has been established based on the wing chord c , the power loading parameter can be developed for a given value of c .

Recall that the ideal power of the fan jet for a single fan in the propulsion system is a function of the total pressure difference across the fan as well as the rate of production of kinetic energy. Now let ① and ② denote the inlet and outlet of the fan duct, as shown in Fig. 6.7.

$$\dot{W}_s = \dot{m} \left[\left(\frac{p_2 - p_1}{\rho} \right) + \frac{1}{2} (V_2^2 - V_1^2) \right] \quad (6.27)$$

It has been established that in the aerodynamic cruise regime (ACR) and powered lift regime (PLR) the pressure and momentum contributions to power are well resolved by the experimental data. As such, this estimate can only be applied in these regimes. For clarity each term in Eq. 6.27 will be treated separately.

$$T1 = \dot{m} \frac{\Delta p_{fan}}{\rho}$$

$$T2 = \frac{\dot{m}}{2} (V_2^2 - V_1^2)$$

Beginning with $T1$ and then by the definition of c_p^*

$$T1 = \rho A_f V_f \frac{c_p^* q_\infty}{\rho} \quad (6.28)$$

Additionally, from the definition of c_p^{*l} , and assuming that the total pressure change across the fan will result in a change in dynamic pressure, the velocity at the fan V_f is

$$V_f = \sqrt{c_p^{*l} V_\infty^2} = c_p^{*l/2} V_\infty \quad (6.29)$$

Substituting this in to Eq. 6.28 and expanding q_∞ in terms of V_∞ , $T1$ becomes

$$T1 = \frac{1}{2} \rho A_f c_p^{*l/2} V_\infty^3 \quad (6.30)$$

Now addressing $T2$ where,

$$T2 = \frac{\dot{m}}{2} (V_2^2 - V_1^2) \quad (6.31)$$

Since the inlet and outlet areas of the fan housing are functions of the geometry of the system, when the flow is reasonably attached to the duct surfaces, which is the case for ACR and PLR operations, then by continuity and with constant density ρ ,

$$\dot{m}_1 = \dot{m}_2 = \dot{m}_f = \dot{m} \quad (6.32)$$

$$\rho V_1 A_1 = \rho V_2 A_2 = \rho V_f A_f \quad (6.33)$$

$$V_1 \beta_1 A_f = V_2 \beta_2 A_f = V_f A_f \quad (6.34)$$

$$V_1 \beta_1 = V_2 \beta_2 = V_f \quad (6.35)$$

Where the inlet and outlet areas are expressed in proportion to the fan area as $\beta_1 = A_1/A_f$ and $\beta_2 = A_2/A_f$.

Therefore, the inlet and outlet velocities can be expressed in proportion to the velocity through the fan.

$$V_1 = \frac{V_f}{\beta_1} \text{ and } V_2 = \frac{V_f}{\beta_2} \quad (6.36)$$

Here we will again assume that the total pressure change across the fan will result in a dynamic pressure change in the fluid from inlet to outlet. V_1 and V_2 can now be expressed in terms of c_p^* and V_∞ .

$$V_1 = \frac{c_p^{*1/2} V_\infty}{\beta_1} \text{ and } V_2 = \frac{c_p^{*1/2} V_\infty}{\beta_2} \quad (6.37)$$

Substituting these expressions into Eq. 6.31, $T2$ for V_1 and V_2 , and expanding \dot{m} , $T2$ can be expressed in terms of only $c_p^{*1/2}$ and V_∞ .

$$T2 = \frac{1}{2} \rho A_f c_p^{*3/2} V_\infty^3 (\beta_2^{-2} - \beta_1^{-2}) \quad (6.38)$$

Combining terms $T1$ and $T2$, the ideal power input for a single fan becomes

$$\dot{W}_s = \frac{1}{2} \rho A_f c_p^{*3/2} V_\infty^3 [1 + (\beta_2^{-2} - \beta_1^{-2})] \quad (6.39)$$

In order to develop the desired power loading P_L from Eq. 6.39, the area of a single fan A_f must be substituted for the fan area per unit span, given the wing chord c . Since the fan area can be expressed in terms of chord

$$A_f = \frac{\pi}{4} D_f^2 = \frac{\pi}{4} (\gamma_1 c)^2 \quad (6.40)$$

where γ_1 is the proportionality constant relating the fan diameter to the wing chord. This must be multiplied by the number of fans per unit span n_b in order to give the flow area per unit span A_b .

$$A_b = A_f n_b = A_f \frac{1}{\gamma_1 c} = \frac{\pi}{4} \gamma_1 c \quad (6.41)$$

Therefore, the power loading P_L is defined in terms of the system geometry, c_p^* , and V_∞ .

$$P_L = \frac{\pi}{8} \rho (\gamma_1 c) c_p^{*3/2} V_\infty^3 [1 + (\beta_2^{-2} - \beta_1^{-2})] \quad (6.42)$$

Finally, since the jet ideal power cannot be a complex number, and because the c_p^* at a particular $\alpha = \alpha_0$ can be negative for positive input power, the value for c_p^{*f} is used in the power loading estimate.

$$\boxed{P_L = \frac{\pi}{8} \rho (\gamma_1 c) c_p^{*3/2} V_\infty^3 [1 + (\beta_2^{-2} - \beta_1^{-2})]} \quad (6.43)$$

For this ADP system design,

$$\beta_1 = 1.079$$

$$\beta_2 = 1.0$$

$$\gamma_1 = 0.432$$

6.4 Evaluating the Power Demands for Straight, Level, Unaccelerated Flight, (SLUF)

Straight, Level, and Unaccelerated Flight provides the simplest starting point for evaluating the power demands of the ADP system. In this case, all forces are in equilibrium. Simply put, thrust is equal to drag and lift is equal to weight.

$$T = D \quad (6.44)$$

$$L = W \quad (6.45)$$

The lift force was previously defined in terms of wing loading in Eq. 6.11. The drag force is defined as

$$D = q_\infty C_D S \text{ or normalized by area as } \frac{D}{S} = q_\infty C_D \quad (6.46)$$

Where the total drag coefficient C_D is defined for all finite wings as

$$C_D = c_{d0} + C_{Di} \quad (6.47)$$

However, in this case the induced drag coefficient C_{Di} can be both positive and negative, as shown in Fig. 6.5. The requirement of zero net force in the flight direction implies that

$$C_D = 0 = c_{d0} + C_{Di} \quad (6.48)$$

Therefore, SLUF operation is possible only when

$$C_{Di} = -c_{d0} \tag{6.49}$$

Since lift and thrust are coupled for the ADP system, a SLUF trim condition may not be possible for all angles of attack α . In this case, SLUF operations are not possible where the condition stated in Eq. 6.49 cannot be met. For example, SLUF operations are not possible where C_{Di} is strictly positive, due to the integrated propulsion and lifting system. Therefore, in order to find the trim condition, an iterative search procedure is required.

This procedure is defined by the following algorithm.

Algorithm 2: SLUF Condition Calculation Algorithm

Result: SLUF Trim Condition

```
10 Initialize by guessing  $c_p^* = 0$ ;  
11 for  $\alpha = 0 : \alpha_{max}$  do  
12   while  $Err = C_{Di} + c_{d0} > threshold$  do  
13     Interpolate  $C_{Di}|c_p^*, \alpha$ ;  
14     Compute  $Err$ ;  
15     Update  $c_p^*$ ;  
16   end  
17   Compute  $C_L|c_p^*, \alpha$ ;  
18   Compute  $V_{\infty req}|C_L$ ;  
19   Compute  $c_p^{*'}|\alpha$ ;  
20   Compute Power Loading  $P_L$ ;  
21 end
```

The trim velocity V_{trim} and power loading P_L for an ADP aircraft are strong functions of both wing loading W_L and the relative scale. Since this design has been defined in proportion to the wing chord c , the relative scale parameter is

$$Relative\ Scale = \frac{c}{c_{ref}} \quad (6.50)$$

where c_{ref} is the chord of the wind tunnel model.

Increasing wing loading has a dramatic effect on both power loading and trim velocity, as seen in Fig. 6.9 and Fig. 6.8 respectively. Here, increasing the wing loading from $W_L = 50$

to $W_L = 500$ increased the power loading significantly. It is worth noting, that with the exception of operation in high-speed cruise $\alpha \leq \sim 6$ deg, the power loading for these systems does not exceed that required to hover.

A similar increase in power loading is observed when the wing loading is held constant and the chord is increased. However, in this case the increase is linearly proportional to the scaling parameter $\frac{c}{c_{ref}}$, as can be seen in Eq. 6.43.

$$P_L \propto c \propto \frac{c}{c_{ref}} \quad (6.51)$$

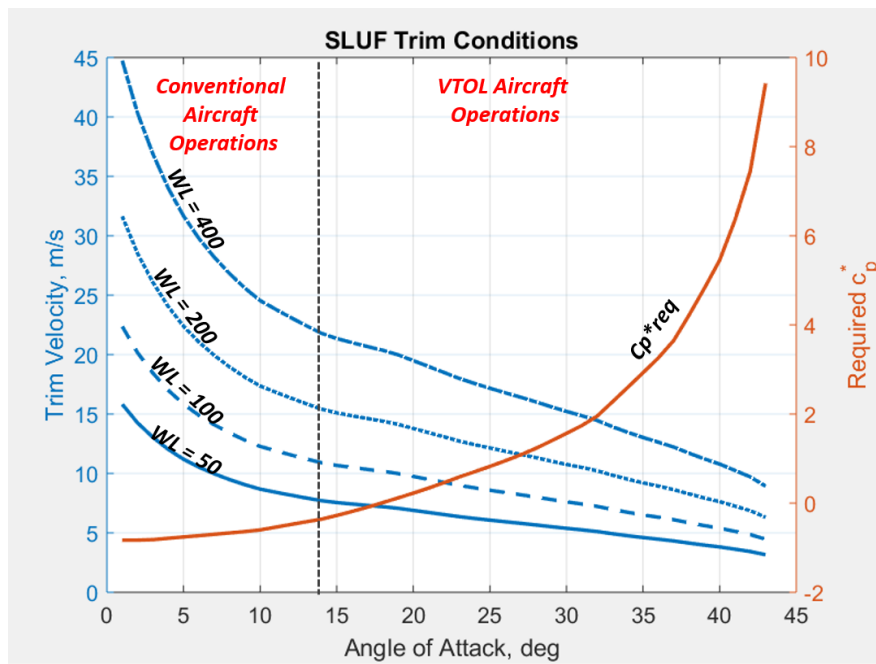


Figure 6.8: SLUF operating conditions for the ADP system with increasing wing loading.

Additionally, the ideal power loading as a function of wing chord are presented in Fig. 6.10.

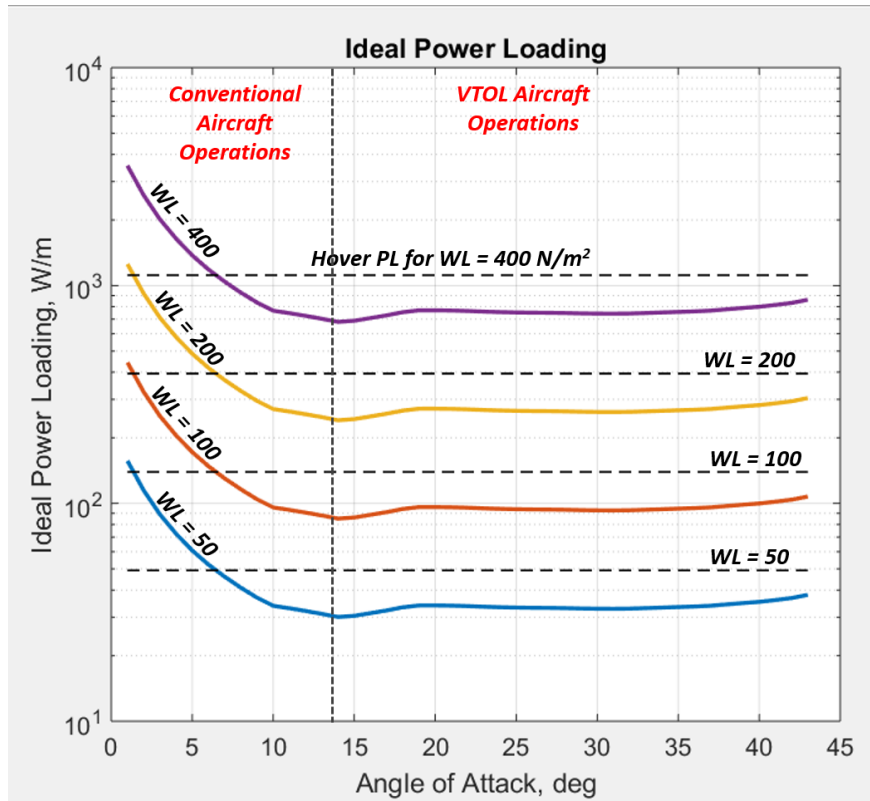


Figure 6.9: Power loading for SLUF operating conditions with increasing wing loading.

The force coefficient trajectories on the CL and CD_i response manifolds are shown in Figs. 6.11 and 6.12 respectively.

For the purposes of this discussion, the boundary between ADP VTOL operations and conventional aircraft operations will be where $\alpha = 12$ deg. Here a conventional aircraft wing begins to stall, preventing safe operations beyond this point, particularly near the ground on approach or departure. Remarkably, the behavior of the ADP system permits SLUF operation well beyond the limits of conventional aircraft without a dramatic increase in ideal power consumption. While the influence of fan efficiency will be dealt with later in this chapter, in this ideal case, the power required to maintain safe operations in this regime does not exceed the power required for hovering operations.

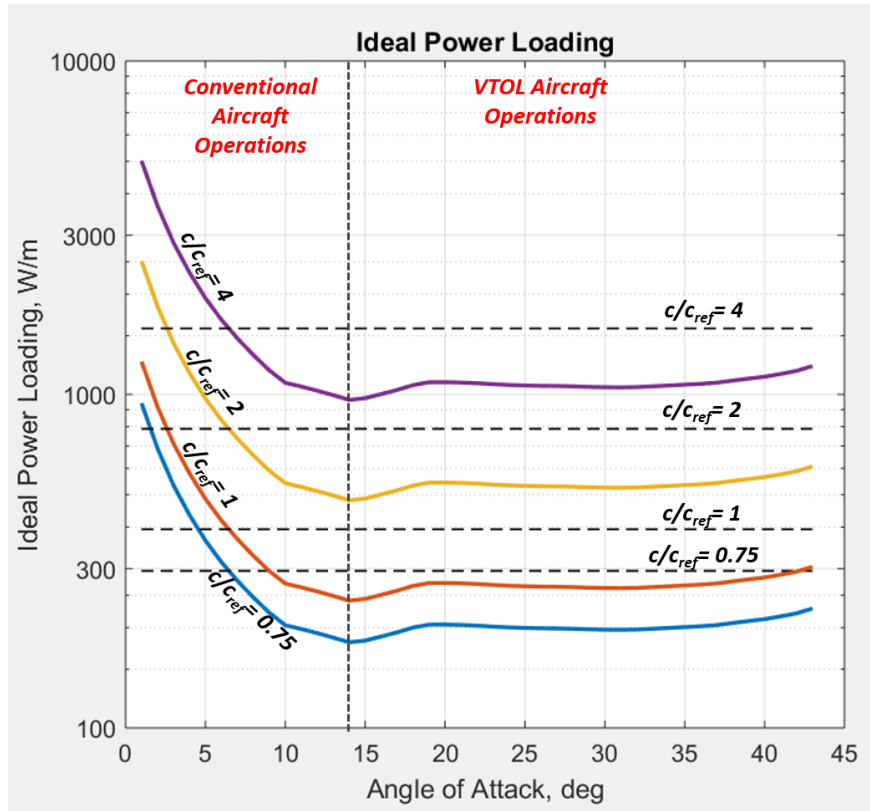


Figure 6.10: Power loading for SLUF operating conditions with increasing wing chord.

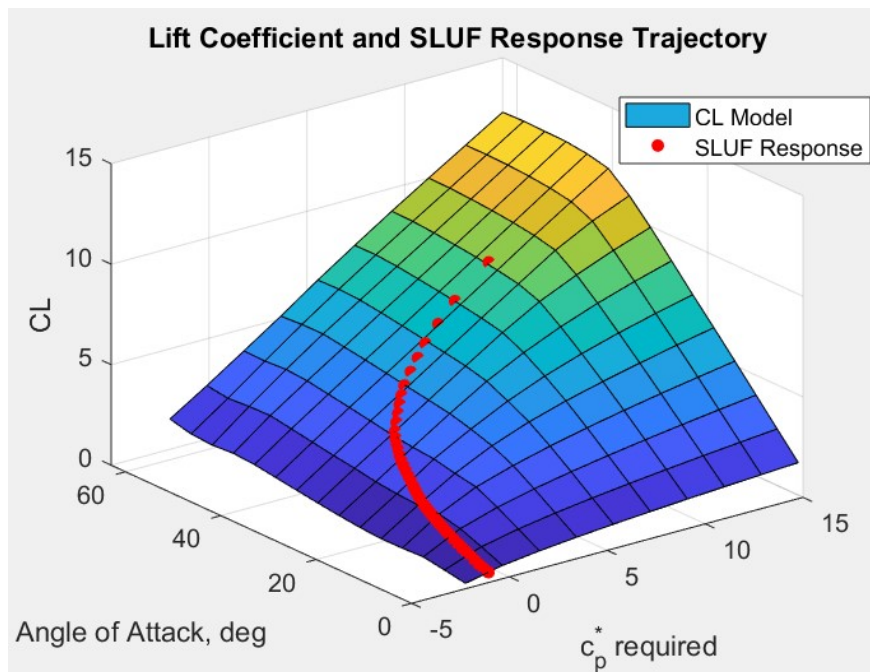


Figure 6.11: CL model and SLUF response trajectory.

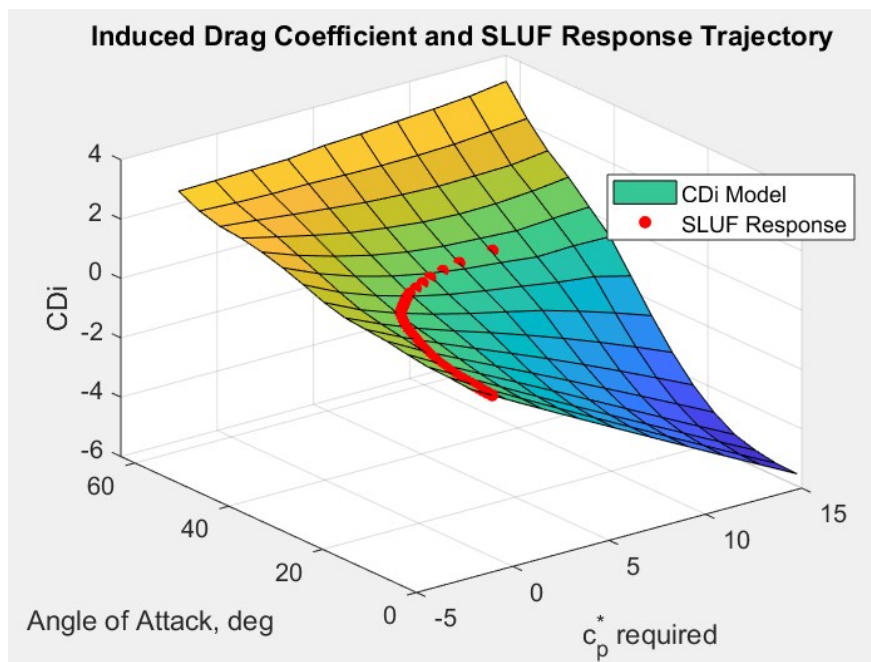


Figure 6.12: CDi model and SLUF response trajectory. Note that SLUF conditions cannot be achieved with this system for $C_{Di} \geq -c_{d0}$.

6.5 Developing Transition Profiles

6.5.1 Hypothetical Aircraft Configuration and Assumptions

In order to develop power demand profiles for a prospective aircraft using the ADP system, a general configuration must be proposed. In this case, the assumed aircraft to be considered will be a bi-wing configuration employing the ADP system on the entirety of each wing. These wings are neither twisted nor tapered, each with an aspect ratio $AR = 8$, representative of many small UAS as well as civilian aircraft, as shown in Fig. 6.14. The transition power model is further predicated on the following simplifying assumptions.

- 1 The forward and aft wings are spaced sufficiently far apart that they can be considered independently.
- 2 The wing tilts relative to the aircraft during transition.
- 3 The orientation of the fuselage remains fixed relative to the inertial reference frame.
- 4 The model is limited to two-degrees of freedom. Vertical and longitudinal motions, u and v , are permitted, lateral motion and rotations are constrained.
- 5 The power required to maintain aircraft attitude and orientation is negligible compared to the power required to accelerate the aircraft and maintain altitude.
- 6 All maneuvers are conducted out of ground effect.

As a result of assumptions **1** and **2**, the following relationship can be defined for the angle of attack and tilt angle.

$$\alpha = \alpha_t - \alpha_f \tag{6.52}$$

Where the flight path angle is α_f

$$\alpha_f = \text{atan}\left(\frac{V_y}{V_x}\right) \quad (6.53)$$

6.5.2 Hover Performance and System Efficiency

The hover regime for this aircraft will be defined as any operating condition for which the angle of attack of the system cannot sustain SLUF. Generally, these are α operating conditions where

$$C_{Di}(\alpha, c_p^*) > -c_{d0} \quad (6.54)$$

For the aircraft configuration considered here, this is approximately $\alpha \gtrsim 43$ deg.

Additionally, for the calculation of the power loading associated with inbound and outbound transition profiles, the efficiency of the system must be included in the power calculations. During the ADP experiments, the net system efficiency was measured. This is defined as

$$\eta_{net} = \eta = \frac{P_{jet-ideal}}{P_{elec-input}} \quad (6.55)$$

The measured efficiency response surface $\eta(\alpha, c_p^*)$ is shown in Fig. 6.13.

Beyond the range of SLUF operation, the power loading is assumed to be the power loading required to maintain hover given the wing tilt angle α_t .

$$P_{L,hover|\alpha_t} = \frac{P_{L,hover-ideal}/FOM_{hover}}{\sin(\alpha_t)} \quad (6.56)$$

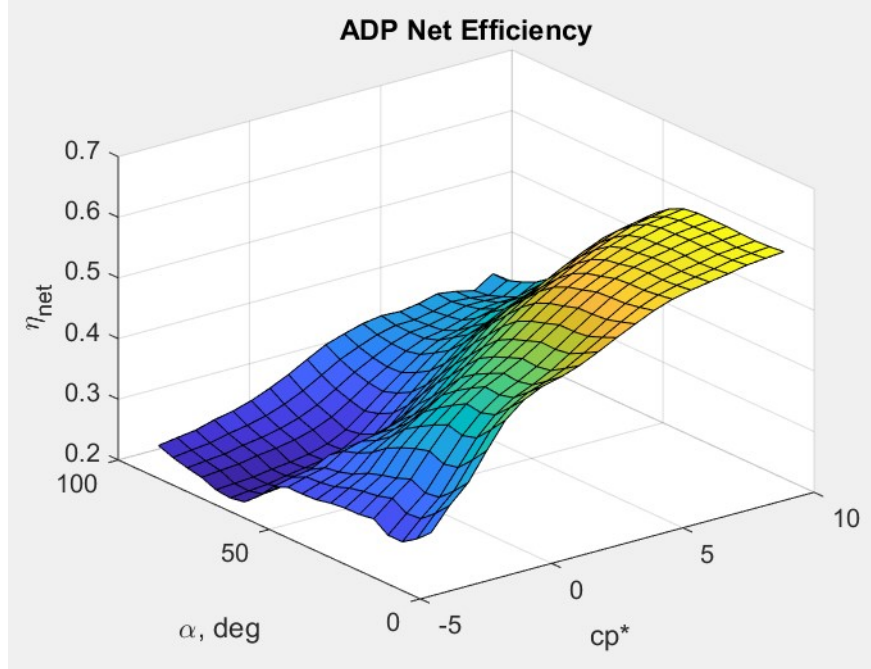


Figure 6.13: ADP system efficiency as a function of α and c_p^* .

Where FOM_{hover} is assumed to be the mean system efficiency over all measured operating conditions.

$$FOM_{hover} = \text{mean}(\eta(\alpha, c_p^*)) \quad (6.57)$$

In order to estimate the transition power loading, an aircraft configuration is assumed. This configuration is a variation of the Lightning Strike concept aircraft developed by Aurora Flight Sciences around the ADP system, as shown in Fig. 6.14.

6.5.3 Inbound Transition

For small aircraft, both fixed wing and rotor craft, the approach to landing is typically made by establishing an approximately constant descent velocity, and maintaining this velocity until flare for touchdown for fixed-wing aircraft or entry into hover-taxi for rotor-craft. A similar model will be followed when designing the inbound transition model.

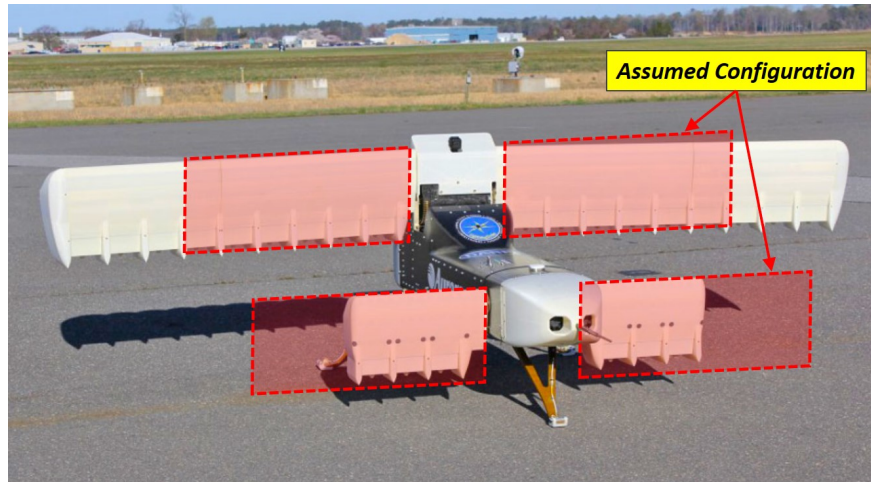


Figure 6.14: Assumed bi-Wing ADP aircraft configuration, relative to the DARPA Lightning Strike sub-scale prototype.

Because an analytical trim condition is not necessarily possible for all combinations of wing tilt angle α_t , aircraft velocity, V_∞ and c_p^* required to execute the inbound transition. A linear *PI* controller is applied to the motion of the aircraft system to initiate and sustain the descent velocity by controlling the aircraft load factor, as shown in Fig. 6.15.

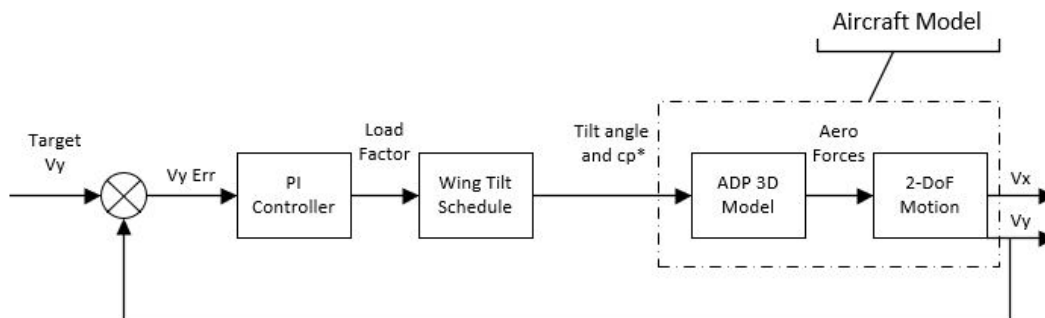


Figure 6.15: The vertical velocities for both the inbound and outbound transition require closed loop control.

Because the aircraft body coordinates are assumed to be locked to the inertial frame, and only 2-DoF motion in the horizontal and vertical directions is considered. The motion of

the system can be solved entirely in the inertial frame. The equations of motion are simply

$$m\ddot{x} + b_x\dot{x} = F_L - mg = f_y \quad (6.58)$$

$$m\ddot{y} + b_x\dot{y} = f_x \quad (6.59)$$

Where F_L is the total lifting force and F_x is the net horizontal force.

Here, there are only two states

$$q_1 = \dot{x} = u \quad (6.60)$$

$$q_2 = \dot{y} = v \quad (6.61)$$

Leading to two state equations

$$\dot{q}_1 = \frac{1}{m}(-b_x q_1 + f_y) \quad (6.62)$$

$$\dot{q}_2 = \frac{1}{m}(-b_y q_2 + f_x) \quad (6.63)$$

Initially, this problem appears to be quite simple, however, the input forces F_L and F_x are each functions of α and c_p^* .

$$F_L(\alpha, c_p^*) = nWL = 1/2\rho V_\infty^2 C_L(\alpha, c_p^*) \quad (6.64)$$

For any operating condition where circulatory lift is utilized, the required lift coefficient is

$$C_{L,req}(\alpha, c_p^*) = \frac{nWL}{\rho V_\infty^2} \quad (6.65)$$

The wing loading WL is considered to be constant, however the load factor parameter can be used to tune the lift requirement at each time step, as shown in the block diagram in Fig. 6.16.

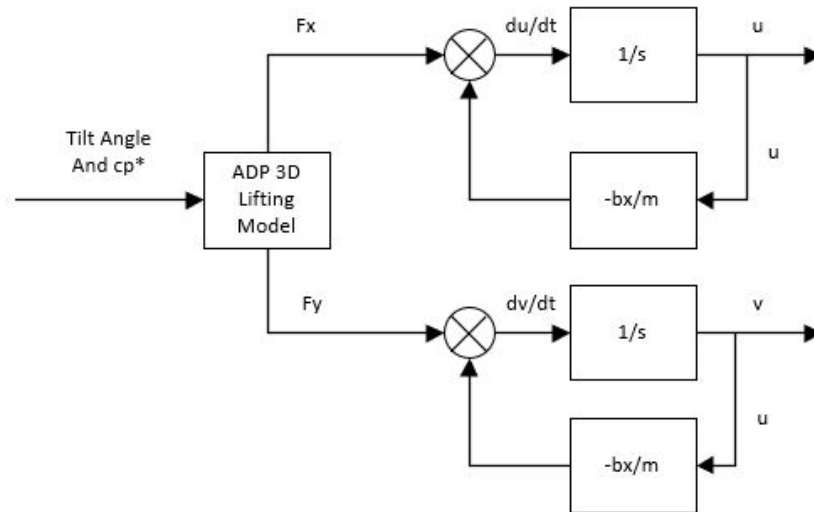


Figure 6.16: Both the horizontal and vertical forces are functions of only α and C_p^* .

The transfer function describing the relationship between the vertical force and vertical velocity is

$$G_o(s) = \frac{V(s)}{F_y(s)} = \frac{1}{ms + b_y} \quad (6.66)$$

which has a single stable pole at $s = -b_y/m$ for $b > 0$, or at $s = 0$ for $b = 0$.

PI controllers are commonly used in autopilot systems to control rate of climb and descent, and gave acceptable performance when developing the inbound transition profile:

To accomplish this, the aircraft initiates an abrupt descent and transition from a maximum power cruise condition. Power is rapidly reduced and the descent is initiated over approximately four seconds, with the wing tilt beginning at $t = 0sec$. The wing tilt proceeds at a constant rate of $\frac{d\alpha}{dt} = 2.95 \text{ deg/s}$, from $4 \text{ deg} \leq \alpha \leq 43 \text{ deg}$. Note that the simulation

ends at $\alpha = 43$ deg, as this is the threshold angle beyond with SLUF operation is no longer possible, as shown in Figs. 6.17 and 6.18.

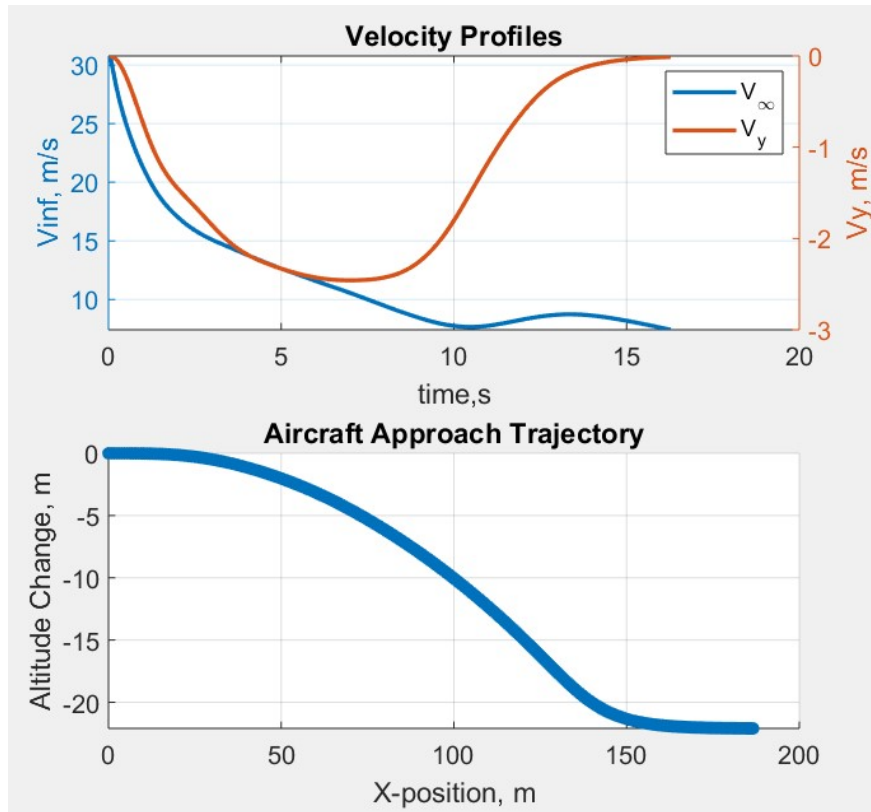


Figure 6.17: The inbound transition velocity profile

The tilt schedule and range were specified approximately based on publicly available flight test video of the DARPA Lightning Strike sub-scale demonstration aircraft, though at the data of this research, no publications have been made explicitly detailing the Lightning Strike X-Plane program.

The power loading excursions observed in the first few seconds of Fig. 6.18 are due to the rapid deceleration of the aircraft with the abrupt change in power at the beginning of the simulated descent. These will be included in the power profile applied to the HEPS to evaluate the robustness of the generator control system.

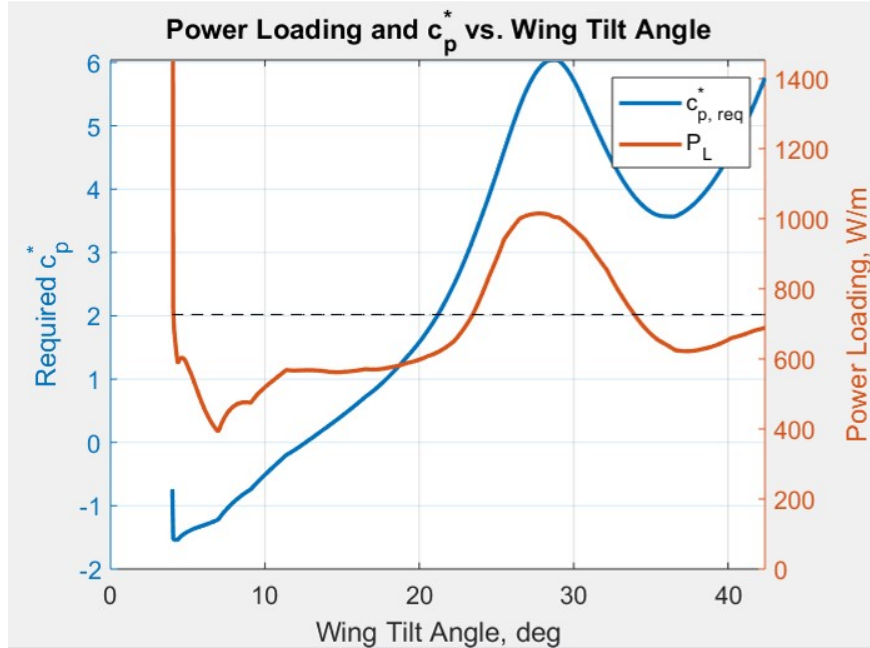


Figure 6.18: The inbound transition power loading P_L and c_p^* profiles.

6.5.4 Outbound Transition Profile

The aircraft departure transition was developed in a manner similar to the approach transition. The initial conditions of the model were specified, as were the tilt rate, wing tilt range, and outbound rate of climb. The model was then executed to maintain a constant rate of climb.

In this case, the initial conditions were specified to be $\alpha = 40$ deg and $V_{init} = V_{SLUF}|_{\alpha=40 \text{ deg}}$. These initial conditions were selected because, based on the finite wing approximation of the ADP system, the maximum wing tilt angle where SLUF can be maintained is $\alpha = 40$ deg. This margin prevents the model from collapsing for the departure conditions this simulation is designed to capture.

Since the tilt schedule proceeds at a constant rate throughout this simulation, the thrust from the system given c_p^* will increase over time. Since the horizontal velocity is not explicitly

controlled, in this model the horizontal motion is subject only to the condition that the net horizontal force per unit span must be greater than or equal to zero, only allowing the velocity of the aircraft to increase or remain steady for a given time step.

$$F_x = D_{net} = g_\infty C_D c \geq 0 \quad (6.67)$$

This results in the condition

$$C_{Di}(\alpha, c_p^*) \leq -c_{d0} \quad (6.68)$$

Here there are two options for c_p^* given a specific tilt angle α , the first is the $c_p^*|_{C_L}$ required to satisfy Eq. 6.65, and the second is $c_p^*|_{C_D}$ required to satisfy Eq. 6.68. For the outbound transition, the larger of these will be used for the given time step.

$$c_p^*|_{\alpha_0} = \begin{cases} c_p^*|_{C_D} , & \text{if } c_p^*|_{C_D} \geq c_p^*|_{C_L} \\ c_p^*|_{C_L} , & \text{otherwise} \end{cases} \quad (6.69)$$

The aircraft departure trajectory and power loading is shown in Fig. 6.19 and Fig. 6.20 respectively.

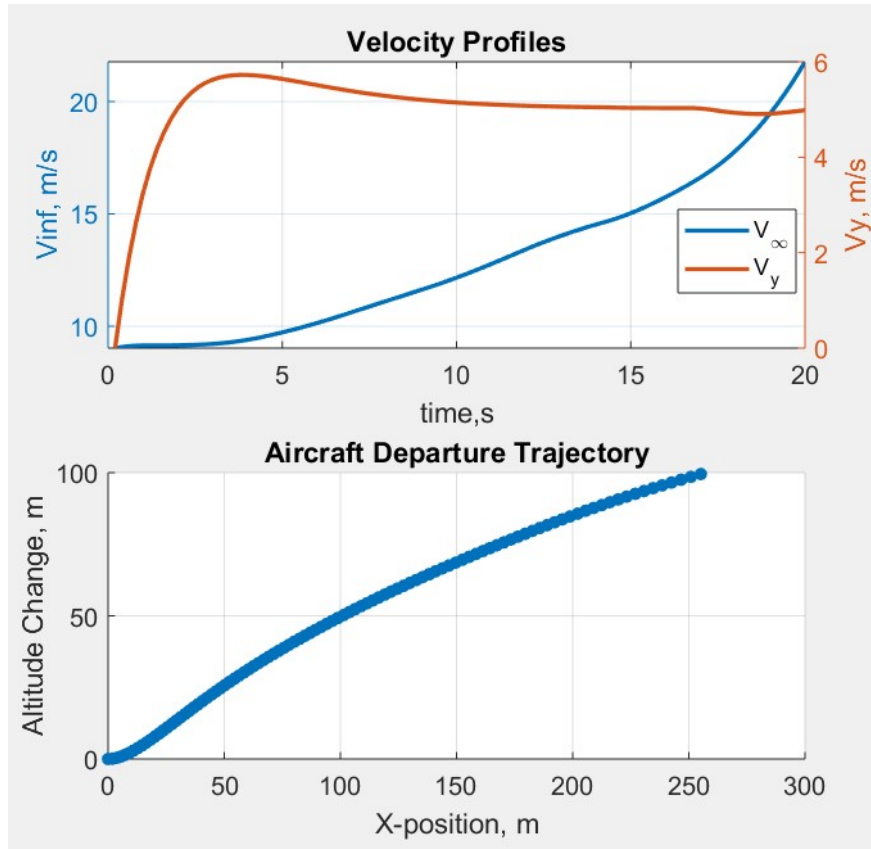


Figure 6.19: The outbound transition velocity profile

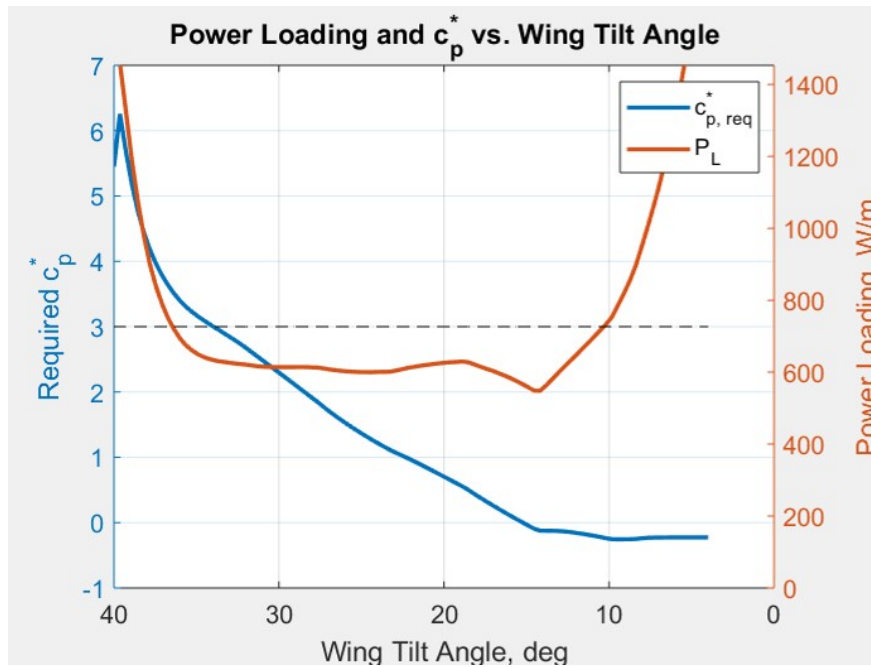


Figure 6.20: The outbound transition power loading P_L and c_p^* profiles.

6.6 Aborted Landing Profile

An aborted landing, or a "go-around" is a common maneuver executed whenever a landing cannot be performed safely. This occurs for a variety of reasons for both UAS and general aviation aircraft and rotor craft. These reasons range from simple practice to emergency situation such as debris in the landing area, wind gusts or weather disrupting the approach, pilot error, and any combination of other factors. It is essential that any aircraft be able to safely perform aborted landing procedures. Therefore, a 'go-around' profile will be developed to test the robustness of the ADP-hybrid aircraft system based on the data collected in these experiment.

The maneuver is assumed to be conducted on the center-line of the runway, with the aircraft body coordinate system again constrained to the inertial system as before, with only 2-Dof motion permitted. The aircraft flies a normal approach, transitions to hover, then immediately transitions out of hover and departs, without touching down or entering ground effect. The 'go-around' maneuver is comprised of both an approach and a departure, as well as time in hover.

To develop this profile, the approach and departure trajectories and power loading profiles will be combined with estimates for hovering conditions, to develop a complete power loading profile representing the effects of a "go-around" maneuver on the power system., .

A baseline power profile is constructed from the approach and departure trajectories developed previously in this chapter, as shown in Fig. 6.21. Critical parameters associated with each phase this profile are given in the following table, Tab. 6.1. Additionally, note that there are discontinuities in this baseline power loading profile where the different flight

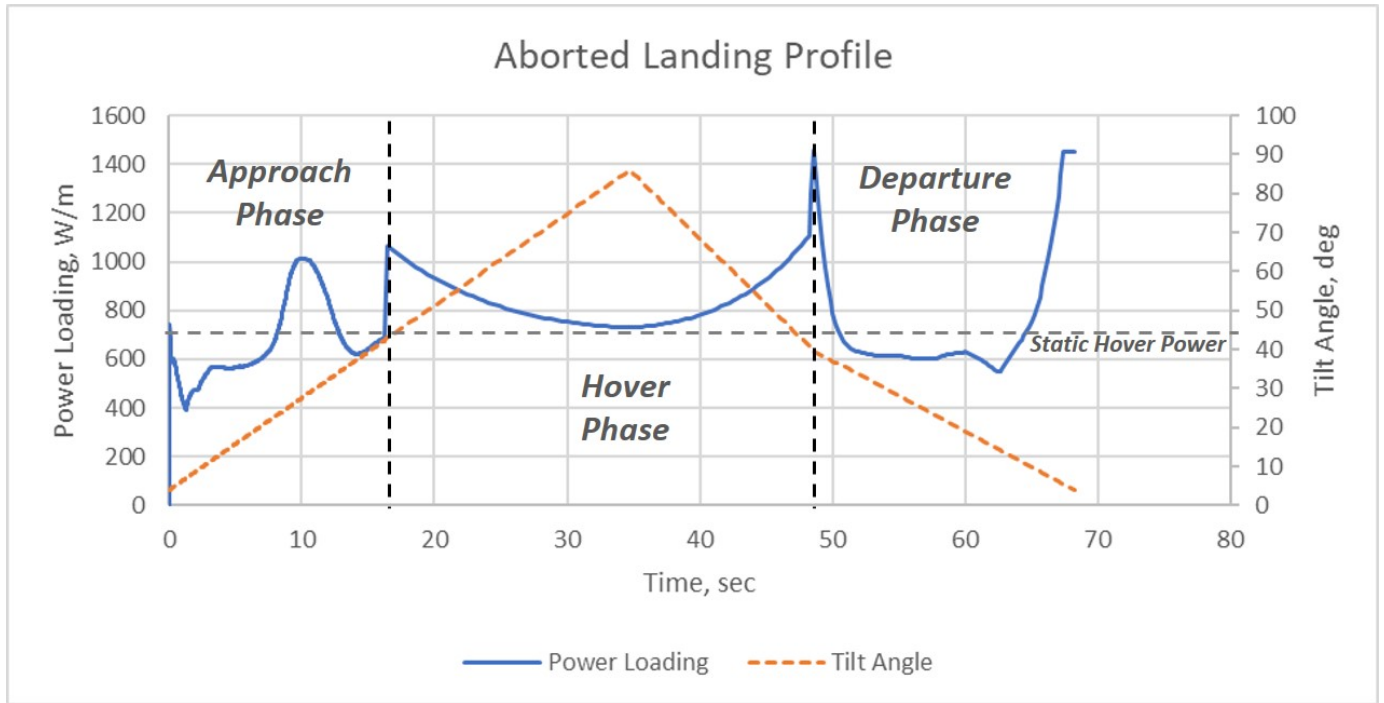


Figure 6.21: The baseline aborted landing maneuver power loading profile.

regimes are appended to each other. These would be unlikely in practice, however they will be retained in this model to evaluate the robustness of the power system to abrupt changes in power demand.

Aborted Landing Maneuver Phases				
Phase	Tilt Angle Range (deg)	Tilt Rate(s) (deg/s)	Target Rate of Climb (m/s)	
Approach Phase	$0 \text{ deg} \leq \alpha \leq 43 \text{ deg}$	2.36	-2.5	
Hover Phase	$44 \text{ deg} \leq \alpha \leq 86 \text{ deg}$	+2.36, -3.33	0.0	
Departure Phase	$0 \text{ deg} \leq \alpha \leq 43 \text{ deg}$	-1.85	-2.5	

Table 6.1: Aborted Landing Maneuver Parameters

6.7 Part Two - Aircraft Control Objectives

The objective of this chapter is to present an improved control architecture suitable for use in airborne hybrid-electric power systems (HEPS) in small UAS. The linear PID controller applied to the hybrid system in the previous simulations was developed only to facilitate the characterization of the dynamic response inherent in the experimental system. This enabled a direct comparison between the experimental system and the dynamical model developed previously. Moreover, this prior validation enables confident development of more sophisticated non-linear controllers and system architectures through dynamic simulation.

6.8 Identifying Non-linear Plant Elements

The engine control system can be represented using the simplified block diagram shown in Fig. 6.22. Additionally, the equivalent circuit for the system is shown in Fig. 6.23.

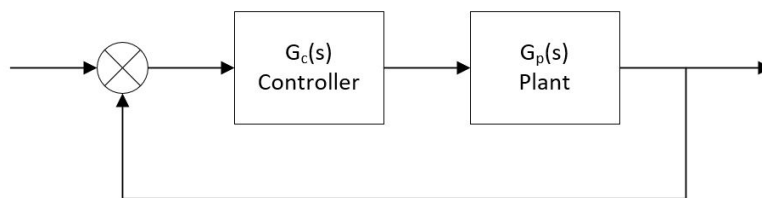


Figure 6.22: Simplified block diagram representation of the HEPS voltage control system.

Expanding these systems, reveals their constituent components. The controller system consists of the voltage controller and a servo actuator. While the dynamics of the servo are very fast relative to the the dynamics of the HEPS mechanical plant, they will be used

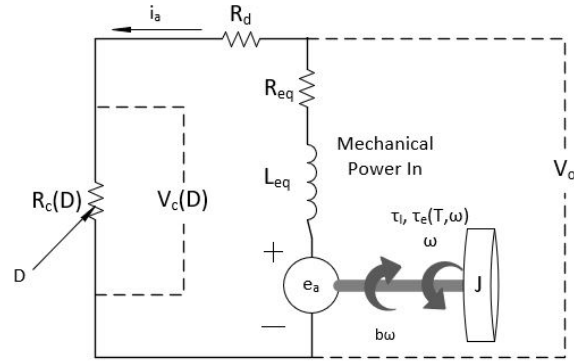


Figure 6.23: Equivalent circuit representation of the HEPS voltage control system.

later in this analysis to evaluate the feasibility of the response of the controller designed in this chapter. The electro-mechanical plant consists of the engine components, generator and power electronics components for the purposes of this discussion, as shown in Fig. 6.24.

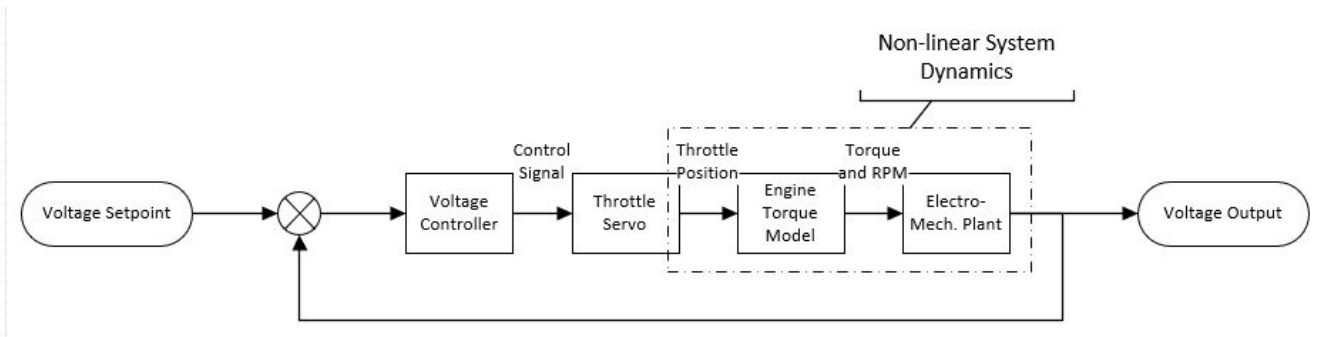


Figure 6.24: Expanded simplified block diagram representation of the HEPS voltage control system.

In this design, the system voltage is required to track a voltage setpoint while the system undergoes loading perturbations. The torque response of the engine is a function of both the throttle setting T and of angular velocity ω .

$$\tau_{eng} = \tau(T, \omega) \quad (6.70)$$

This response is a non-linear function of both angular velocity as well as throttle input. For the purposes of this model, these functions are specified, however they are not generally well characterized for many of the candidate small engines used in small UAS.

The dynamics of the electro-mechanical plant are given by the set of differential equations,

$$J\ddot{\theta} - b\dot{\theta} = \tau_{engine} - \tau_{load} \quad (6.71)$$

$$V_c(D) + R_d i_a = e_a - R_{eq} i_a - L_{eq} \frac{di_a}{dt} \quad (6.72)$$

where the load torque $\tau_{load} = k_T i_a$ the generator torque constant multiplied by the armature current. There are two energy storage elements in the system, the flywheel system comprised of the rotating engine and generator components, and the generator armature coils. Therefore, the system has only two states given by

$$q_1 = \dot{\theta}$$

$$q_2 = i_a$$

With derivatives

$$\dot{q}_1 = \dot{\omega} = \ddot{\theta} \quad (6.73)$$

$$\dot{q}_2 = \frac{di_a}{dt} \quad (6.74)$$

Resulting in the state equations

$$\dot{q}_1 = \frac{1}{J}(\tau_{eng}(T, q_1) - k_T q_2 + b q_1) \quad (6.75)$$

$$\dot{q}_2 = \frac{1}{L_{eq}}(k_E q_1 - (R_d + R_e q + R_c(D))q_2) \quad (6.76)$$

6.9 Sliding Mode Controller Design

A sliding mode controller is a type of nonlinear robust controller capable of rejecting bounded unknown disturbances. These are particularly well suited for motion control systems similar to the present HEPS control problem. [56],[38], [16].

Since the objective of this design effort is to control the output voltage of the generator system by manipulating the engine's throttle to affect the rotational speed, we will consider only the rotational dynamics of the system in this control design, given by Eq. 6.71, which can be reframed in terms of an unknown disturbance $f(x_2, t)$ and a feedback control law u .

With $x_1 = \theta$,

$$\dot{x}_1 = \dot{\theta} = x_2 \quad (6.77)$$

$$\dot{x}_2 = u + f(x_2, t) \quad (6.78)$$

with the initial condition $x_2(0) = x_{2,0}$. Note that the unknown disturbance is only a function of x_2 and that inertial effects and viscous damping have been included in the disturbance term $f(x_2, t)$.

The objective of a sliding mode controller is to introduce a sliding variable σ such that the controller u will drive σ to zero asymptotically and in finite time. According to [56],[50] the sliding variable is typically some function of the tracking error and its derivatives, depending upon the compensated dynamics desired for the controlled system. The tracking error is the difference between output y and its desired value y_{DES} .

$$e \equiv y - y_{DES} \quad (6.79)$$

The recommended form [DIEE] of the sliding variable is given in general by

$$\sigma = e \left(\frac{d}{dt} + p \right)^{r-1} \quad (6.80)$$

where r is the the relative degree between the output y and the controller u . In this case, y , the angular velocity output of the system, and is defined by a first order system, and controller u , is the scalar throttle position

$$r = \mathbf{O}(y) - \mathbf{O}(u) = 1 - 0 = 1 \quad (6.81)$$

Therefore for this system the sliding variable has only one dimension and is equal to the system tracking error.

$$\sigma = e \quad (6.82)$$

6.9.1 Generator Voltage as the $q1$ State Observer

In this system, the angular velocity is not measured accurately. Generally, for small engines the angular velocities are quite high, up to 14,000 rpm in many cases, therefore accurate measurement of angular velocity is not typically feasible using high-accuracy optical encoders. Further, for airborne systems, the additional weight of an encoder system will penalize the overall aircraft performance. It is therefore desirable to estimate the angular velocity of the system by constructing an observer from easily measured quantities.

The electrical dynamics of the generator are given by the following equation with the generator output voltage of principle concern when controlling this system,

$$v_o = e_a - R_{eq}i_a - L_{eq}\frac{di_a}{dt} \quad (6.83)$$

where the back electromotive force (back emf) $e_a = k_e\dot{\theta}$ is equal to the generator voltage constant multiplied by the system angular velocity. At steady state and with low resistance the back emf becomes linearly proportional to the angular velocity.

$$v_o \approx k_E\dot{\theta} \quad (6.84)$$

The angular velocity x_2 is therefore estimated from voltage as

$$\hat{x}_2 = \frac{v_o}{k_E} \quad (6.85)$$

This is particularly convenient because although the system output voltage is not explicitly a system state, it is the output we seek to manage by controlling state q_1 , the angular velocity.

The suggested observation algorithm is

$$\dot{\hat{x}}_1 = \hat{x}_2 = v \quad (6.86)$$

where v is the observer injection term which satisfies the conditions laid out in [Shtessel, et. al].

Additionally, when the system load is changing rapidly, the generator output voltage will respond instantaneously to changes in current via the $\frac{di_a}{dt}$ term.

6.9.2 2nd Order Sliding Mode Control (2-SMC)

While sliding mode control is well known for its robustness and fast tracking properties, true first order sliding mode controller rely on high frequency switching in the controller to affect control of the system. In a first order sliding mode controller 1-SMC, controller design is typically of the form

$$u = -U^* \text{sign}|\sigma| \quad (6.87)$$

where U is a sufficiently large positive constant and the control u is discontinuous across the manifold σ , due to $\text{sign}|\sigma| \equiv \sigma/\text{abs}(\sigma) = 1 \text{ or } -1$, as shown in the example case presented in Fig. 6.25.

A simple motion tracking simulation shown in Fig. 6.25, illustrates that while the overall system behavior is well controlled, the chattering behavior of the controller u switching be-

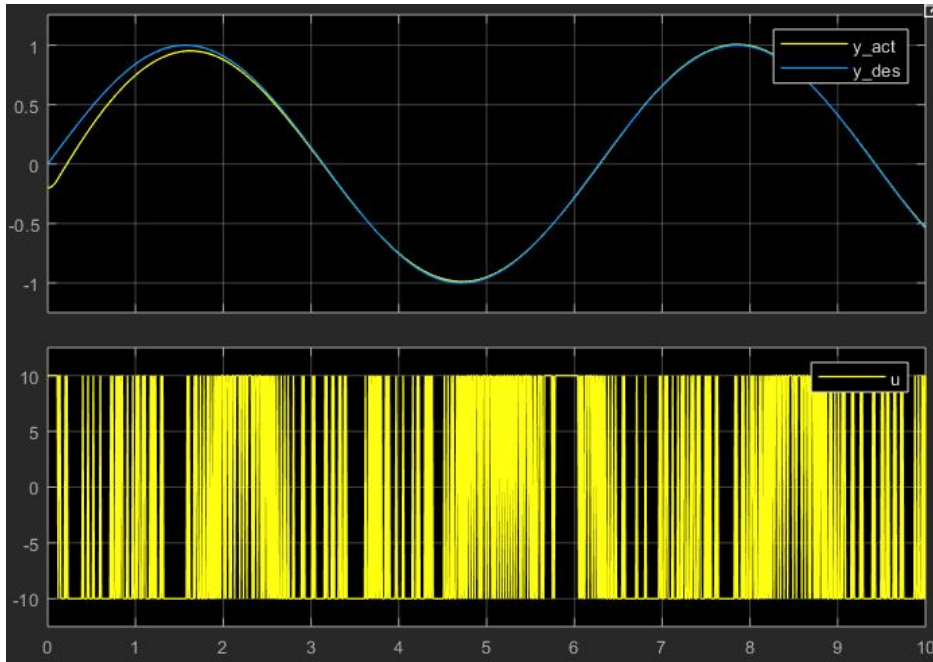


Figure 6.25: First order sliding mode control example (1-SMC). Note that the control u 'chatters' about the σ manifold.

tween $+U$ and $-U$ is not feasible for implementation in continuous time mechanical systems, as the high frequency is assumed to be infinitely fast, or in practice equal to the simulation frequency.

Smoothing the switching function using a continuous function, such as a 'sigmoid' or $\tanh(\sigma)$ results in a continuous control response, eliminating the control chatter as well as chatter in the system output.

$$\text{sign}|\sigma| \approx \frac{\sigma}{|\sigma| + \epsilon} \approx \tanh(\sigma/\epsilon) \quad (6.88)$$

However, these quasi-sliding mode controllers cannot provide finite time convergence of the sliding variable to zero. Moreover, the sliding variable and state variables converge only

to domains in the vicinity of the origin. The result is a loss of robustness and a loss of accuracy.[50].

Instead, a second order sliding mode controller (2-SMC) will be used which addresses many of the challenges associated with 1-SMC and quasi-1-SMC. The algorithm utilized here is the well established 'super-twisting' 2-SMC controller.

$$u = -\lambda\sqrt{|\sigma|}sign(\sigma) + w \quad (6.89)$$

$$w = -Wsign(\sigma) \quad (6.90)$$

With the proposed parametric relationships [16]

$$\lambda = \sqrt{U^*} \quad (6.91)$$

$$W = 1.1U^* \quad (6.92)$$

The response of this controller is presented for an example case in Fig. 6.26.

Here, the control u is not longer switching between $+U$ and $-U$, though the high speed switching characteristics are still somewhat apparent.

6.9.3 Implementation in the HEPS Model

The 2-SMC controller is used as a direct replacement for the PID controller designed and evaluated previously, as shown in Fig. 6.27. Since the throttle is limited to the range $0 \leq T \leq 1$, the controller output to the engine torque model is limited to this range as well.

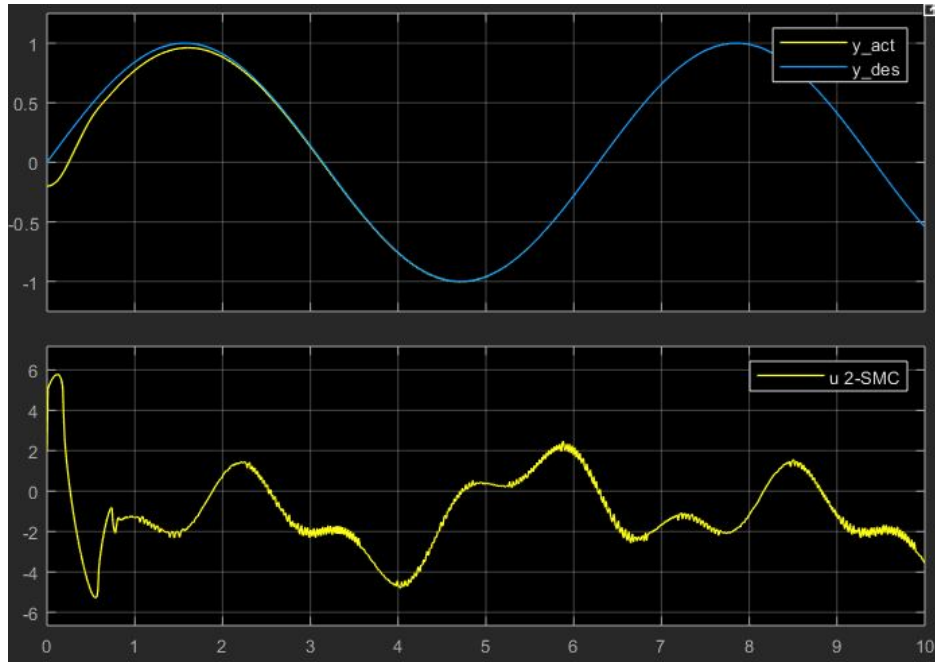


Figure 6.26: Second order sliding mode control example (2-SMC). Note that the control u chattering is reduced.

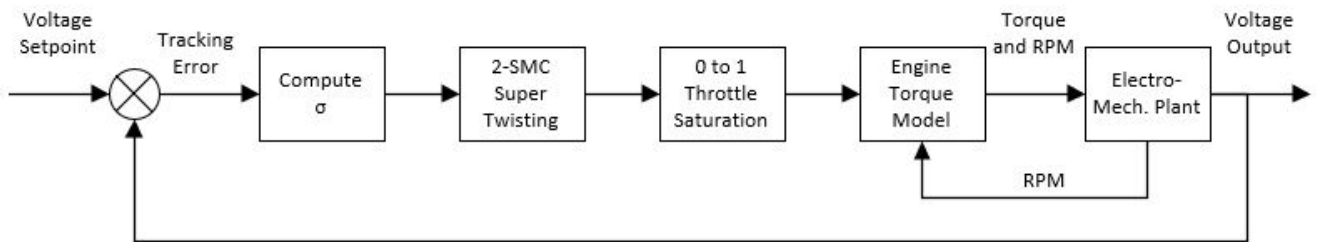


Figure 6.27: 2-SMC controller implemented in the HEPS voltage control system.

2-SMC vs. PID Multi-Step Response

The response of the system using the original PID controller is compared to response when using the 2-SMC compared under the multi-step loading profile used to characterize both the experimental apparatus and the dynamical model. The results are summarized in the following figures. Fig. 6.28 shows the overall response characteristics of each system, while Fig. 6.29 shows the voltage tracking error for each system, with a model time-step of

$\Delta t = 0.0025s$. The PID tuning used for this simulation is implemented in continuous time as follows:

$$k_p = 0.0119, \text{ proportional gain}$$

$$k_i = 0.0556, \text{ integral gain}$$

$$k_d = 0.0003, \text{ derivative gain}$$

$$N = 42.99, \text{ filter coefficient}$$

In the 2-SMC case, the simulation parameters remain the same, and the controller tuning used is as follows:

$$\sigma = v_o - v_{des}, \text{ the tracking error}$$

$$\lambda = \sqrt{U^*}$$

$$w = -W \text{sign}(\sigma)$$

$$W = 1.1U^*$$

$$U^* = 0.350, \text{ scalar constant}$$

Relative to the PID controlled system the 2-SMC controlled system does not exhibit any of the identified aberrant dynamic characteristics. The voltage response exhibits excellent setpoint tracking and the controller rejects the disturbances caused by the step changes in the load duty cycle. This is further illustrated by examining the voltage tracking errors of the system response for each controller, Fig. 6.29. Here, the PID controlled system exhibits tracking error up to $\pm \sim 4V$ or $\sim \pm 12\%$ of the voltage setpoint. In contrast, once the

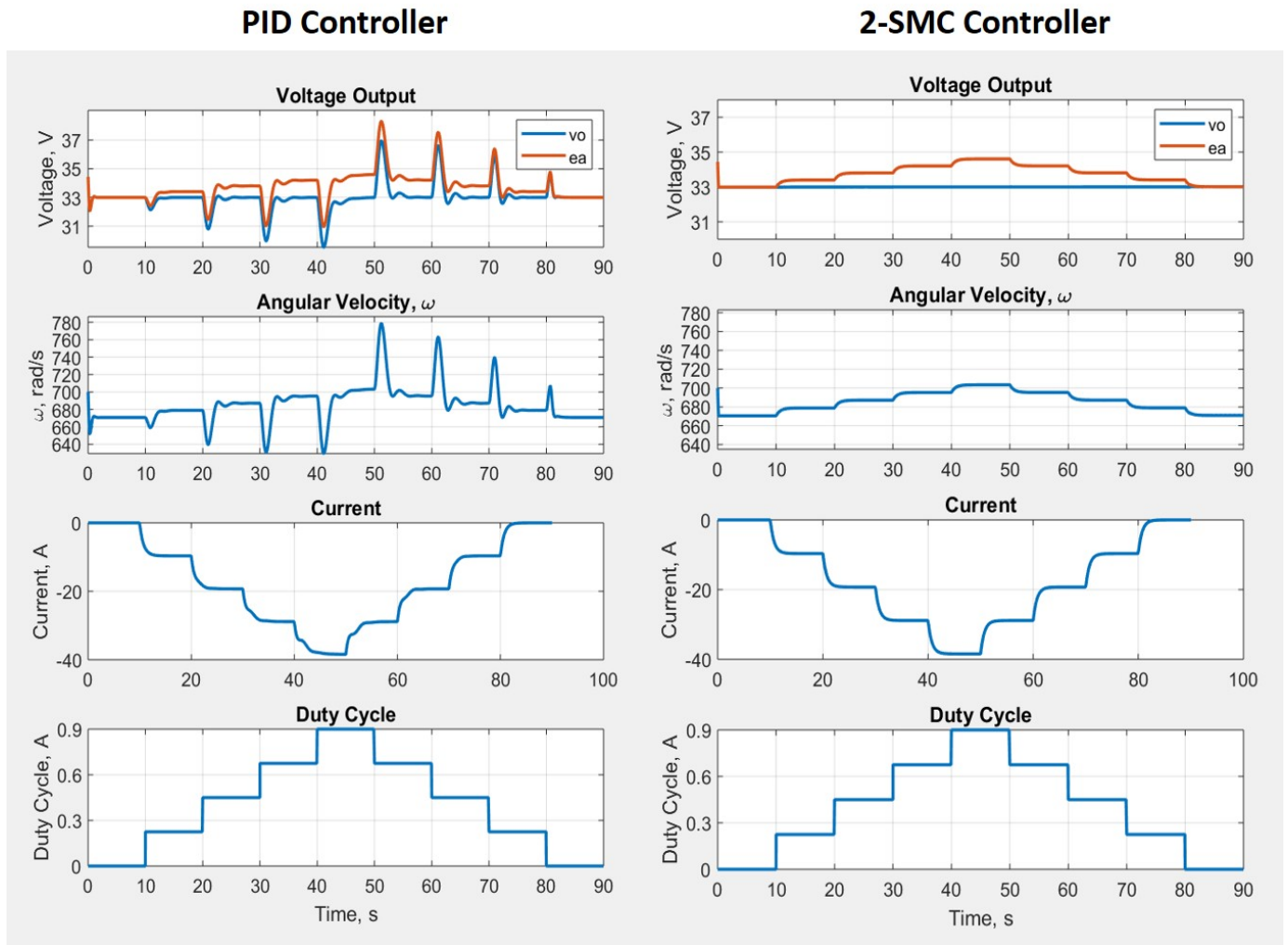


Figure 6.28: PID vs. 2-SMC controller system response implemented in the HEPS voltage control system and subjected to the multi-step load profile for a constant voltage setpoint.

2-SMC sliding variable has converged, at $t = 0.21\text{sec}$, the voltage tracking error is typically $\pm 0.007\text{V}$ only $\pm 0.02\%$ of the setpoint.

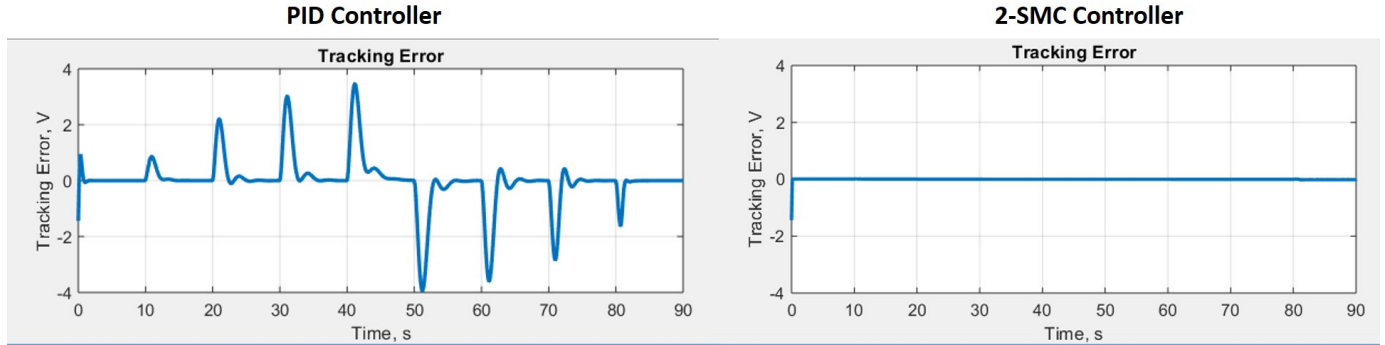


Figure 6.29: PID vs. 2-SMC controller tracking error implemented in the HEPS voltage control system and subjected to the multi-step load profile for a constant voltage setpoint.

Comments on Servo Actuator Implementation Feasibility

In order to evaluate the feasibility of implementing a 2-SMC design in the HEPS considered in this research, the throttle rate of change was considered, as the high-frequency switching properties of the 2-SMC design will likely drive the servo actuator design requirements.

The simulation time step $\Delta t = 0.0025\text{sec}$ is sufficiently small as to provide excellent controller convergence. The first derivative of the resulting throttle response $\frac{dT}{dt}$ is assumed to be the rate response requirement of the servo actuator through which the control is implemented.

In order to establish a rate feasibility limit, several high-speed commercially available servo actuators were surveyed. Typically, these actuators can traverse their full range in $\Delta t_{fr} = 0.04\text{s}$ leading to a rate threshold of $r_T = 1/\Delta t_{fr} = 25\text{Hz}$. As can be seen in Fig. 6.30, the throttle signal does not saturate and the throttle response rate does not exceed the feasibility threshold for modern high speed servos.

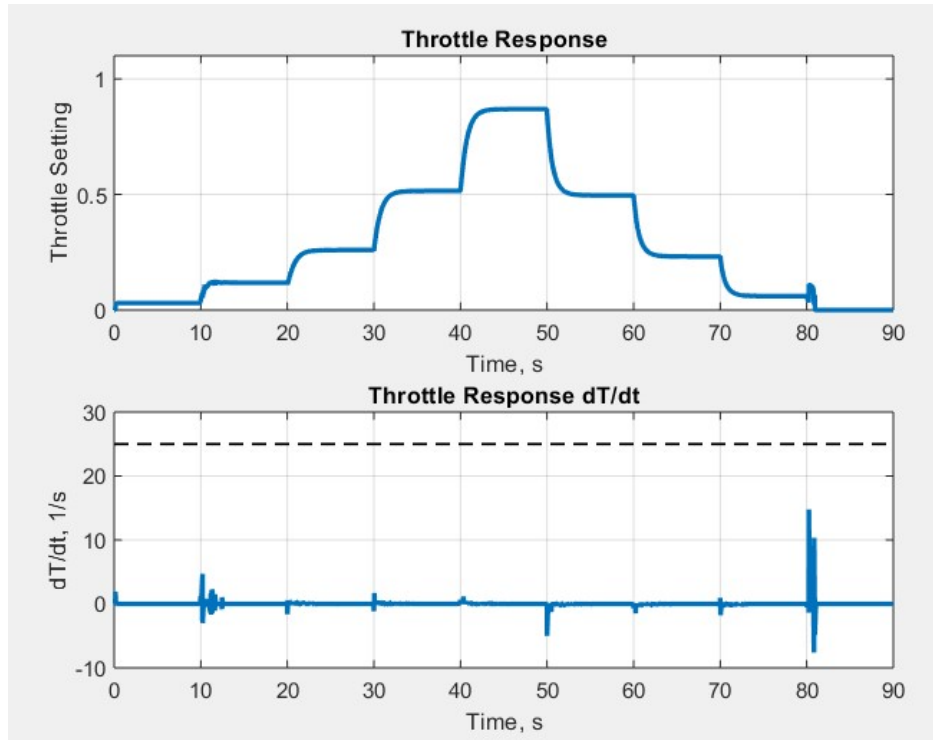


Figure 6.30: Servo rate response requirements based on 2-SMC controller with a timestep of $\Delta t = 0.0025sec$

6.10 Power Output Control

In order to accommodate large changes in power demand, the ability to control the power output of the system is desirable. This is particularly true in the present case for airborne HEPS, where the power demand can be calculated from known flight conditions, see Part 1 of this chapter.

So far, the duty cycle of the power regulator has been used to impose different loads on the engine generator system. However, when used in tandem with the 2-SMC design developed in the previous section, this duty cycle can be used to directly control the output of the generator system to a desired setpoint. The reasoning for this is as follows.

The power output from the generator is

$$P_o = v_o i_a \quad (6.93)$$

As given by Eq. 6.72 and Eq. 6.76, the armature current i_a is a function of the load duty cycle D . Also, since the output voltage v_o is well controlled by the 2-SMC design, we can assume that v_o is approximately known.

$$v_o \approx v_{des} \quad (6.94)$$

This implies that the power output of the generator is simply

$$P_o = v_o i_a(D) = v_o \frac{v_c(D)}{R_c} \quad (6.95)$$

Obviously, we can therefore control the power output of the system by varying the duty cycle of the load power regulator.

For a constant output voltage, the power system dynamics are well approximated by the transfer function for the current output of the generator.

$$G_P(s) \approx V(s)G_I(s) = V(s)\frac{I(s)}{\dot{\Theta}(s)} = V(s)\frac{k_T}{L_{eq}s + R_{eq}} \quad (6.96)$$

So the use of a *PI* controller is appropriate in this case [58]. The implementation of this controller is shown in Fig. 6.31.

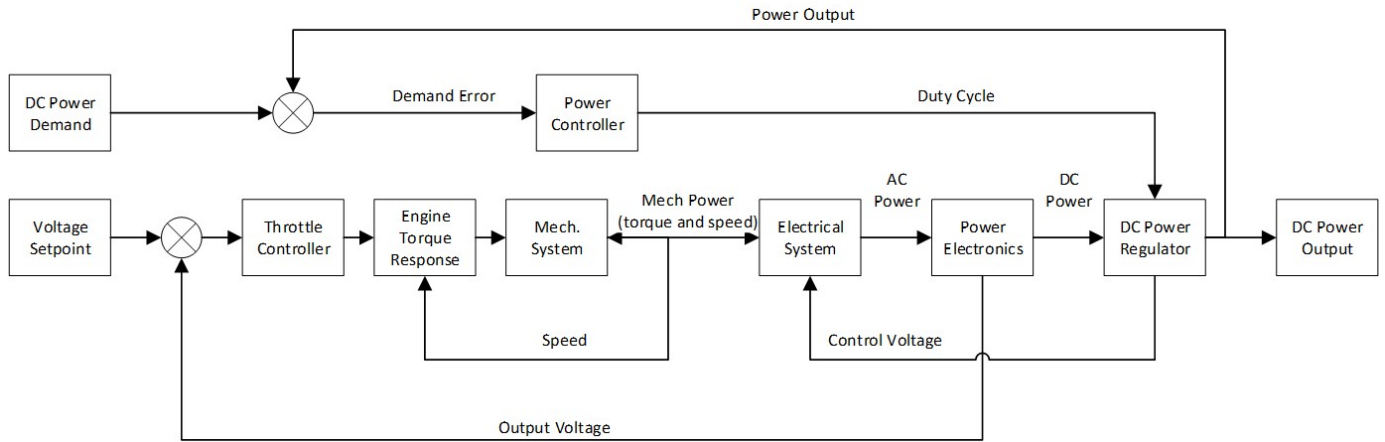


Figure 6.31: Simplified MIMO block diagram including the power PI controller.

When applied to the HEPS considered in this model, as shown in Fig. 6.31, the system power output tracks the desired power output very closely. The power tracking results are shown in Fig. 6.32.

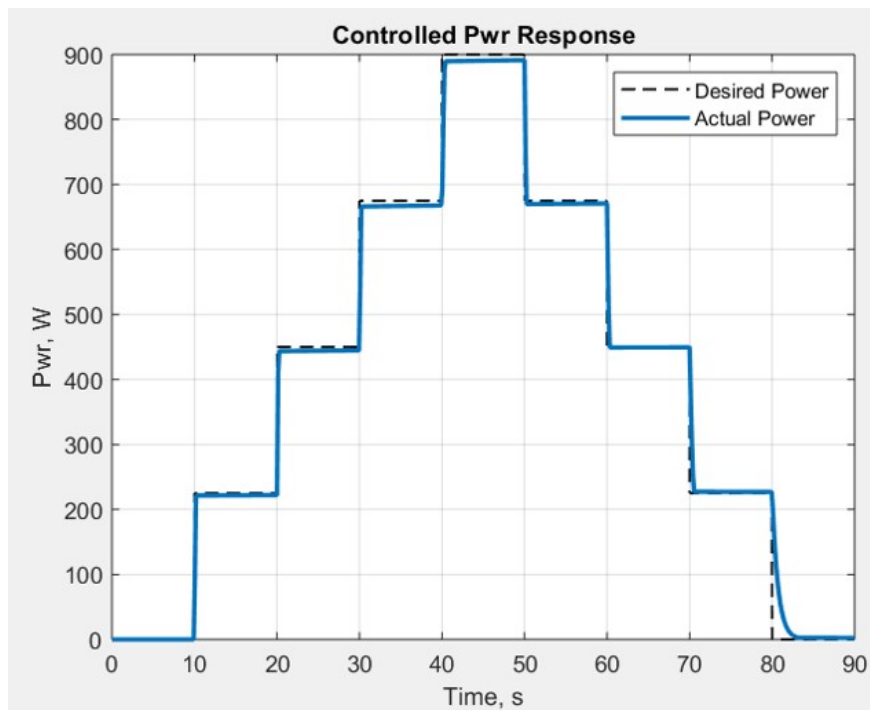


Figure 6.32: Power tracking behavior using a PI controller to update the load regulator duty cycle D .

Because changes to the load regulator duty cycle do not require mechanical input, the rate of change of the duty is unlimited. As such, the controller can change the duty cycle arbitrarily from one simulation time step to the next. The only requirement is that the duty cycle falls in the range $0.0 \leq D \leq 0.9$. As such, the duty cycle controller is defined to saturate on this range. This behavior, as well as the summary response of the system is shown in Fig. 6.33.

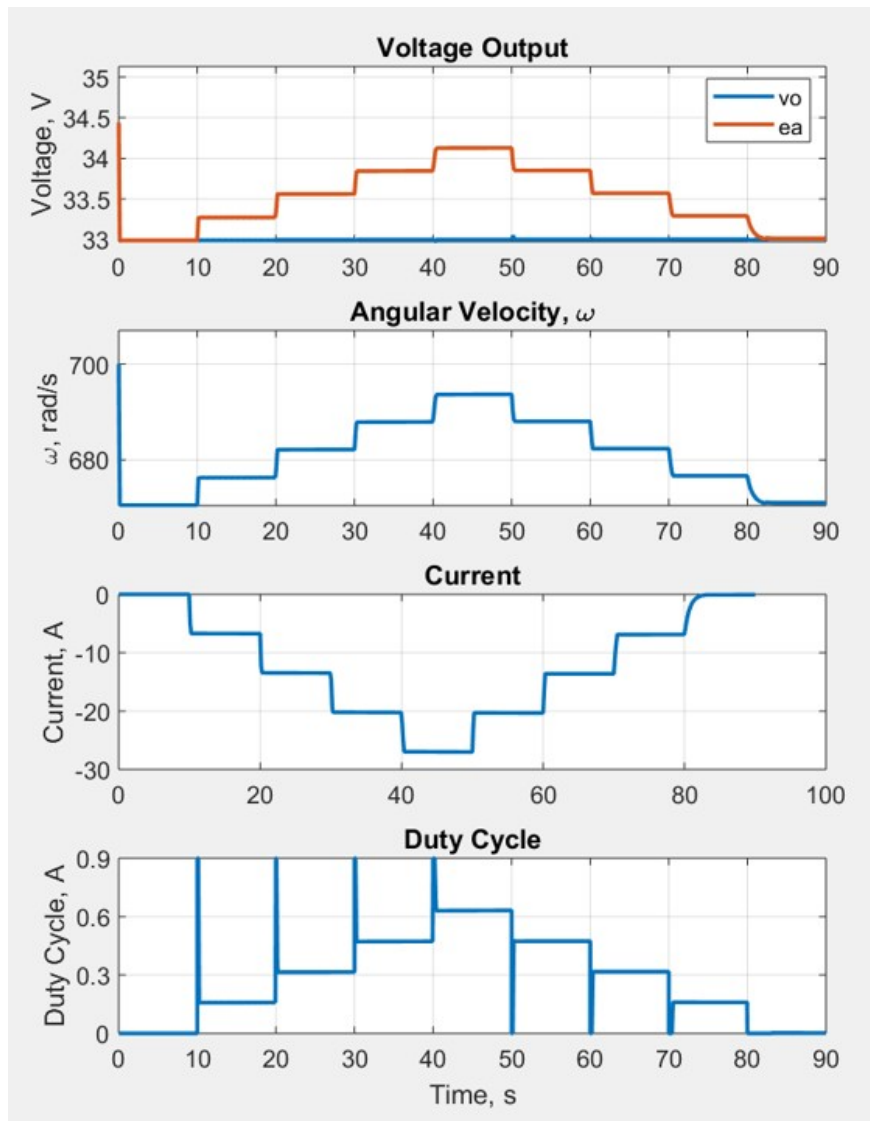


Figure 6.33: System summary behavior using a PI controller to update the load regulator duty cycle D .

6.11 Voltage Setpoint Modulation

Up to this point, the system has been required to maintain a constant voltage setpoint. With a PID controller, this requirement was challenging, given the poor tracking performance of PID in this situation. However, with the introduction of a 2-SMC design to manage the non-linear behaviors of the engine-generator system, and the subsequent introduction of a power controller to manage the duty-cycle of the power regulator, attention can now be directed to enabling the system to operate throughout the engine's entire power range.

Since the output voltage of the generator is directly related to the angular velocity of the engine generator system, by restricting the voltage to a constant value, the angular velocity is restricted to a narrow range of values, as can be seen by examining the power trajectory of the previous test case, shown in Fig. 6.34.

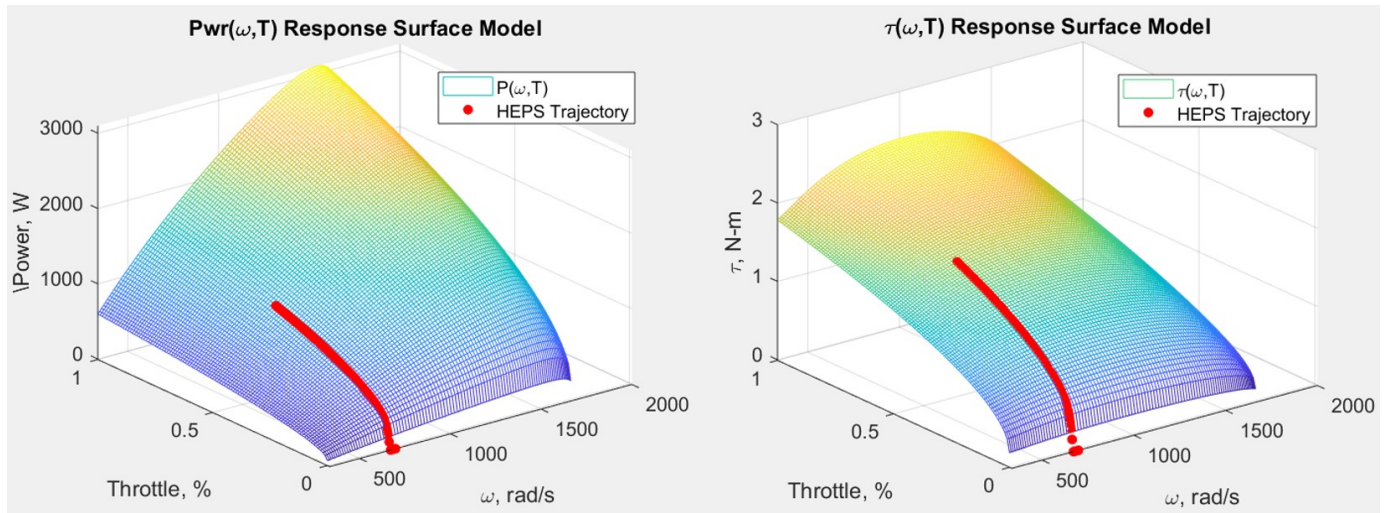


Figure 6.34: HEPS engine power and torque trajectories under the power-tracking multi-step load profile, for a constant voltage setpoint, $V_{setpt} = 33V$.

When the operating range of the system is restricted, the engine is only able to develop its maximum power given that operating range. Eventually, the throttle will saturate and the system will fail to deliver the required power, as shown in Fig. 6.35.

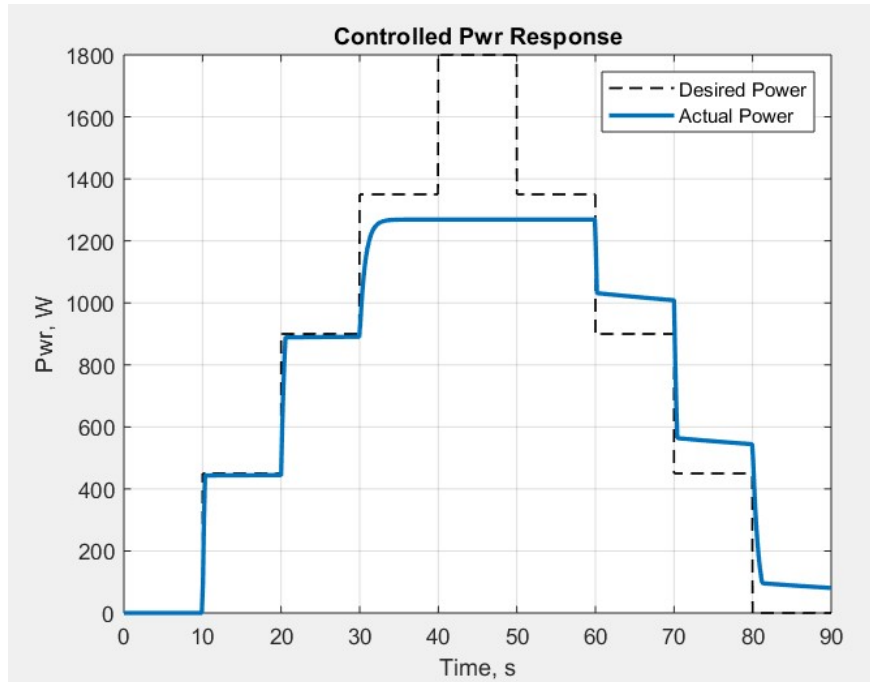


Figure 6.35: HEPS engine power and torque trajectories under the power-tracking multi-step load profile, for a constant voltage setpoint, $V_{setpt} = 33V$. Note that when the voltage is restricted to a constant value, the system will be unable to deliver the required power beyond a certain point.

As shown in Fig. 6.35, as the power demand increases, the system is initially able to track the power requirement. However, as the throttle begins to saturate, near $T = 1$, there is no longer any excess torque available to sustain the increasing current required to meet the power demand at constant voltage. In this case, the maximum mechanical power that can be developed by the engine at the constant voltage specified is approximately half of the maximum mechanical power available, as shown in Fig. 6.36.

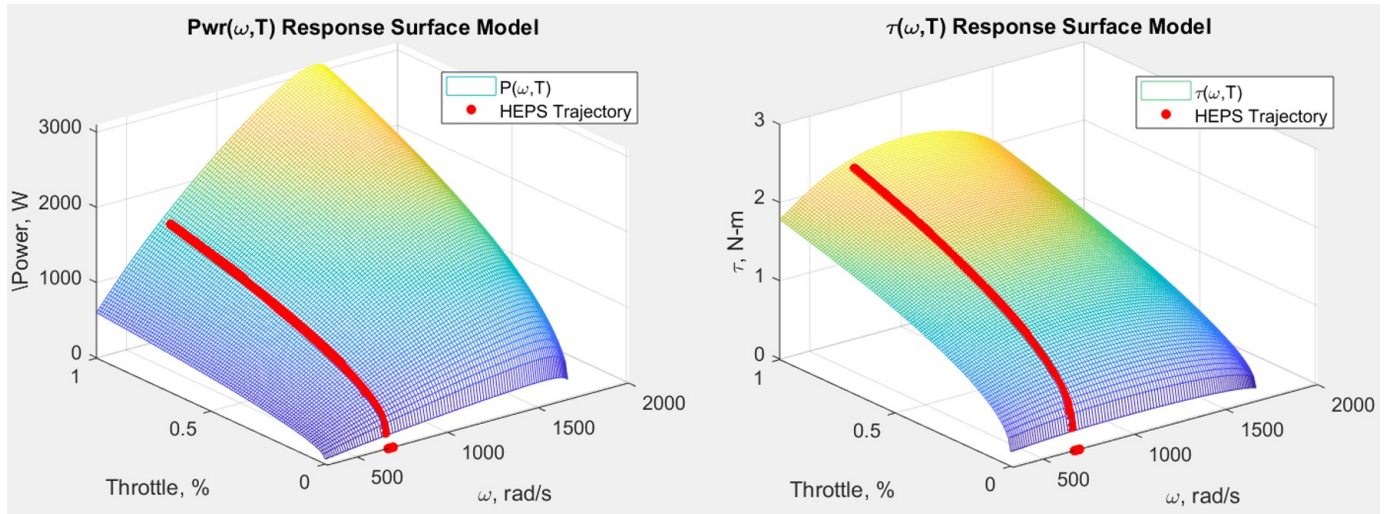


Figure 6.36: HEPS engine power and torque trajectories under the power-tracking multi-step load profile, for a constant voltage setpoint, $V_{setpt} = 33V$. The power target cannot be satisfied as the HEPS trajectory approaches the maximum throttle boundary.

Practical Design Considerations

Operating in this manner represents extremely poor asset utilization thus requiring the engine system to be excessively over-sized for a given application. The argument can be made that the operating voltage could simply be increased to better align the operating angular velocity with the engine's peak power condition. However, due to the shape of the engine's torque profile, doing this would degrade the torque response of the system. Operating continuously at this condition will typically damage most existing candidate engines for this type of application. Further compounding this, operating at this condition would lead to higher fuels consumption, increased heat dissipation requirements and other unnecessary challenges.

Therefore, it is desirable to develop an algorithm whereby the operating voltage of the generator system can float according to a prescribed set of rules that reflect the practical operating considerations and requirements.

In order to accomplish this we can develop a pilot function in terms of the operating voltage v_o and throttle setting T that can be defined in terms of allowable voltage operating range desired. Consider the candidate pilot function

$$v_o = v_{min} + (v_{max} - v_{min})T^{1/2} \quad (6.97)$$

The function having $T^{1/2}$ chosen in this case to match the approximate behavior of the torque response to throttle setting $\tau(\omega, T)$. This implementation is shown in Fig. 6.37.

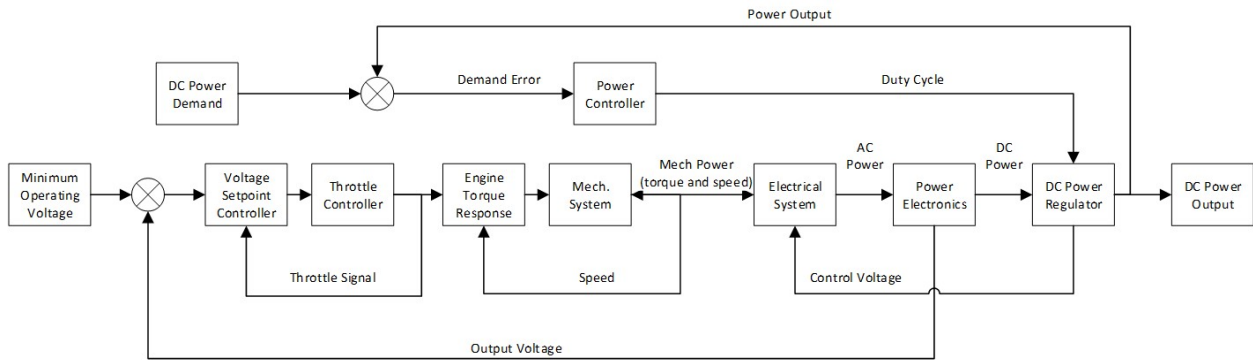


Figure 6.37: Simplified block diagram including the voltage setpoint controller.

Overall, the response of the system can be tailored by specifying the operation voltage parameters v_{max} , v_{min} , and the power of T used in the pilot function. The results for this example under the same power demand as the previous case are shown in Figs. 6.38, 6.39, and 6.40. Generally, the robustness of the system response is extended to much broader range of operating conditions, thereby improving the utilization of the mechanical shaft power available from the engine. This becomes increasingly clear by examining the power manifold trajectory shown in Fig. 6.39.

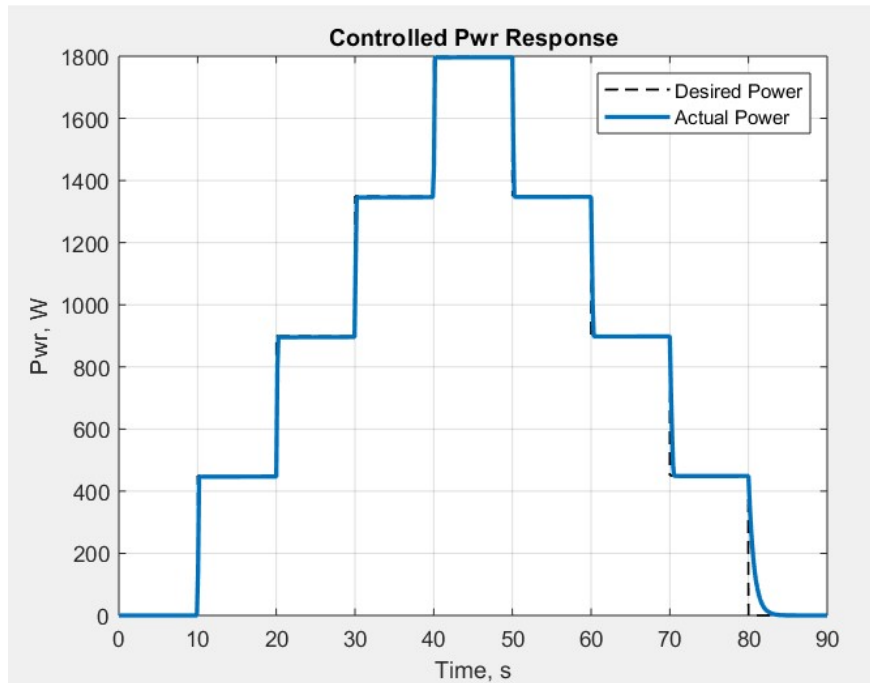


Figure 6.38: When the operating voltage is permitted to float, the response to high power demands is much more robust.

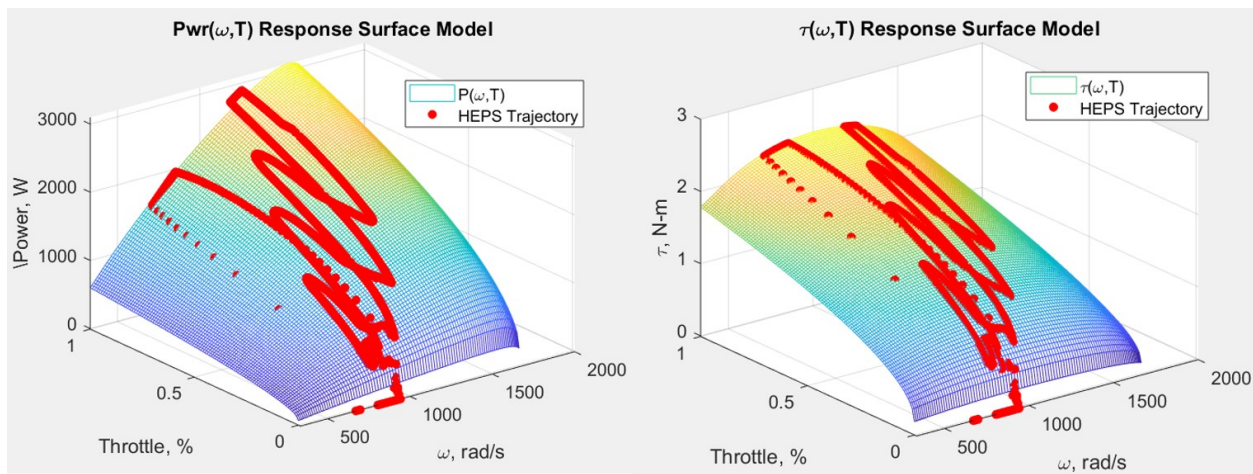


Figure 6.39: The HEPS trajectory is capable of more fully utilizing the power and torque available in the engine.

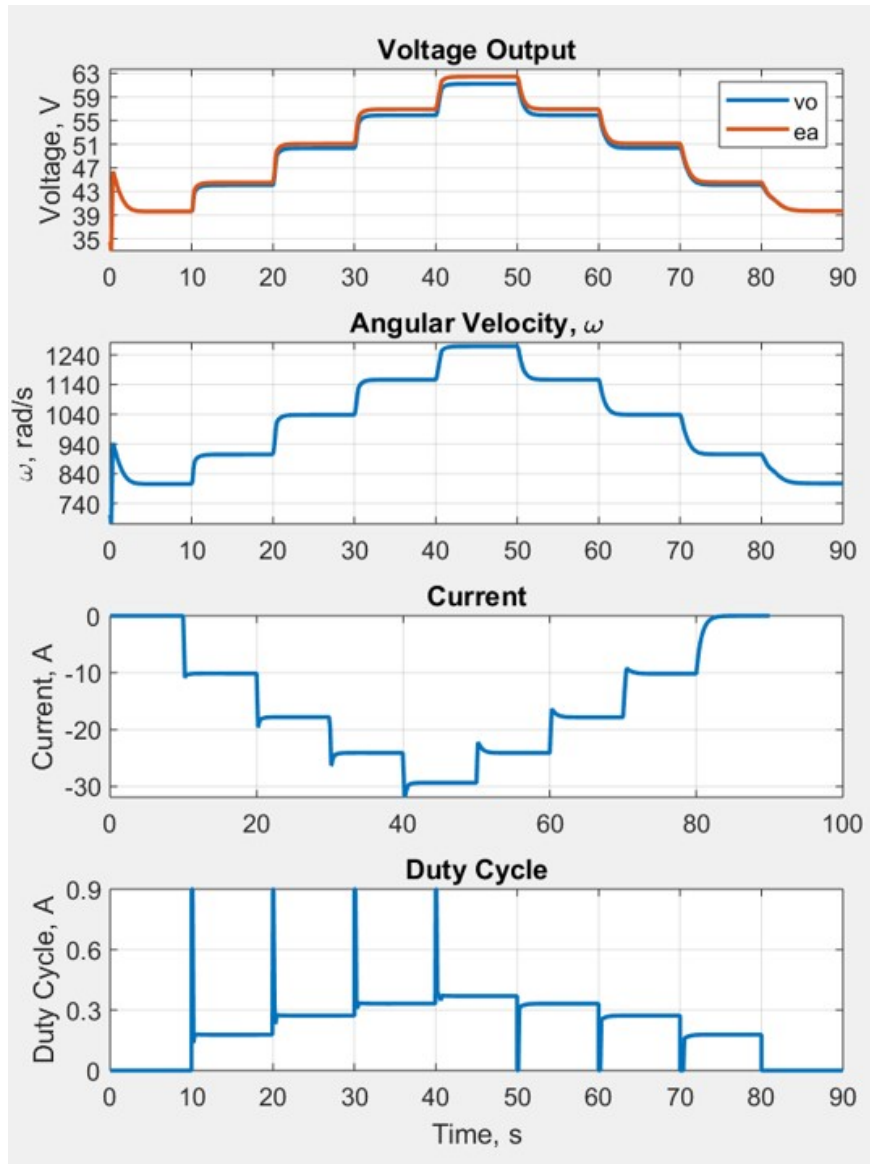


Figure 6.40: The voltage setpoint response increases with power demand, then decreases as power is reduced.

6.12 HEPS Extension Using a Slack Bus

The performance of the HEPS under consideration in this analysis can be further extended through the use of a slack bus to supplement the power output of the system during periods of high demand or rapid transient demand. Typically, any airborne HEPS will need to be coupled with a battery bank to provide constant voltage DC power to the flight control electrics and payload onboard the aircraft, as well as to handle a potential engine-out emergency situation. These batteries will need to provide full flight power for a short duration, on the order of three to five minutes, in order to execute a safe landing. As such, these onboard batteries will be capable of supplying supplemental power while the engine is running as well, though managing the state of charge is beyond the scope of the present research.

For the purposes of this analysis, the battery bank will be paired with a buck converter with the nominal battery voltage V_b being greater than the maximum output voltage $v_{o,max}$ of HEPS, as shown in Fig. 6.41.

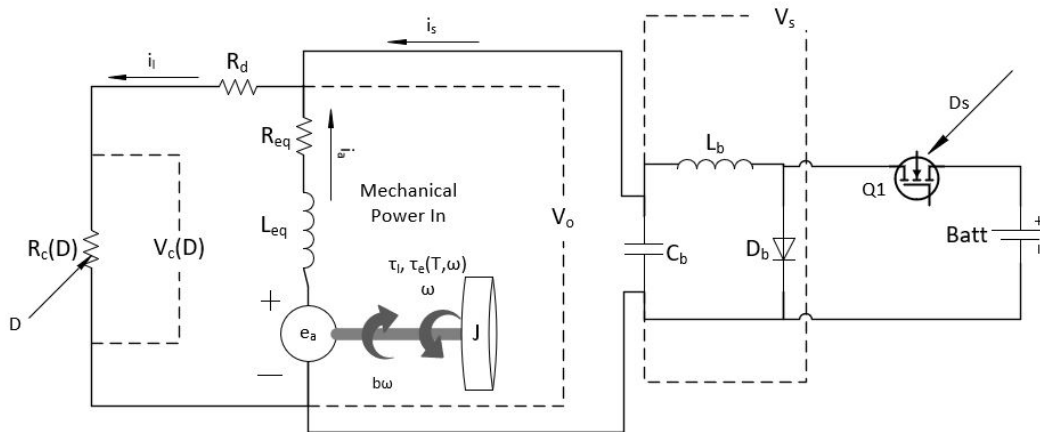


Figure 6.41: HEPS equivalent circuit with Buck converter battery attached.

The dynamics of the buck converter can be ignored in this case as the switching element in the circuit will be either an IGBT or a MOSFET, which have typical switching frequencies of $f_{sw_{IGBT}} \approx 20kHz$ and $f_{sw_{MOSFET}} \approx 50kHz$ respectively. With a model update frequency $f_{model} = 1/\Delta t = 400Hz$, this yields a minimum frequency ratio of

$$f_r = \frac{f_{sw_{IGBT}}}{f_{model}} = 50 \quad (6.98)$$

Which implies that the dynamics of the buck converter cannot be resolved in the present model. As a result, the circuit in Fig. 6.41 will be simplified as shown Fig. 6.42.

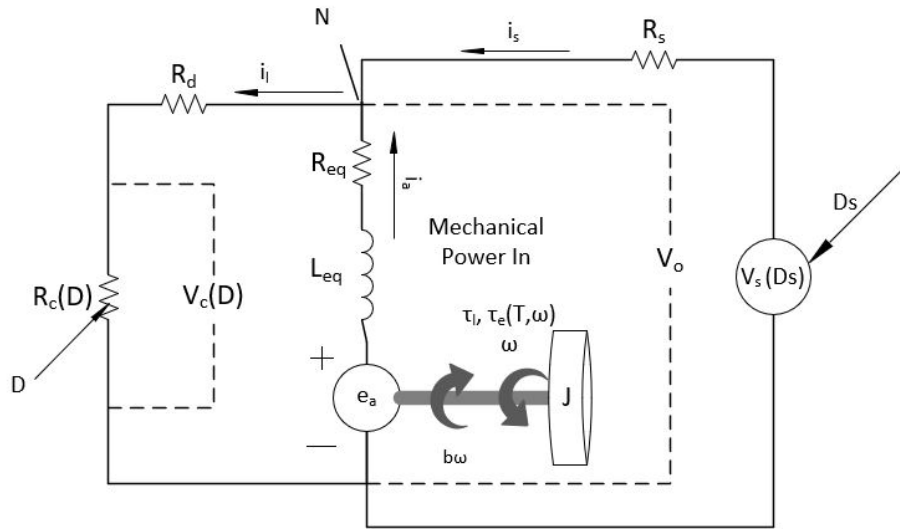


Figure 6.42: HEPS equivalent circuit with Buck converter represented as a controlled voltage source.

In this case, the buck converter is represented as a controlled voltage source $V_s(D_s)$. The buck converter output voltage is adjusted such that supplemental current i_s is induced in the system.

Since the objective of this design is to augment the power produced by the engine-generator system such that the power demand is always satisfied, the supplemental current is provided accordingly. If the power demand is satisfied, then

$$P_d = i_l v_o \quad (6.99)$$

Summing the currents at node N

$$i_l = i_a + i_s \quad (6.100)$$

Then we solve for the supplemental current requirement

$$i_s = \frac{P_d - i_a v_o}{v_o} \quad (6.101)$$

and also for the slack bus voltage,

$$v_s(D_s) = R_s \left(\frac{P_d - i_a v_o}{v_o} \right) \quad (6.102)$$

Essentially, this means that if the power demand is not met by the output of the engine-generator for a given timestep, the slack bus controller will adjust $v_s(D_s)$ to satisfy the power demand.

Additionally, as the throttle begins to saturate, the excess torque capacity of the system diminishes. When designing the output of the slack-bus, this challenge can be addressed as well. We will therefore design a parametric function to augment supplemental current defined in Eq. 6.101. and limit the throttle saturation.

To accomplish this, let T_l be the threshold throttle setting, below which no current augmentation is required, such that,

$$i_s(T, v_o, i_a) = \begin{cases} 0 & \text{if } T < T_l \\ \frac{P_d - i_a v_o}{v_o} \left(\frac{1 - T_l}{1 - T + b} - \frac{1 - T_l}{1 - T_l + b} \right) + k_s i_a \left(\frac{1 - T_l}{1 - T + b} \right) & \text{otherwise} \end{cases} \quad (6.103)$$

Utilizing the multi-step power demand profile, the need for this slack-bus augmentation becomes clear. Here the maximum power demand is increased to 75% beyond the output that the un-augmented HEPS can sustain. As shown in the left-hand plot in Fig. 6.43, the un-augmented HEPS system can deliver only a short burst of power above the sustained power threshold, before collapsing to a lower power output steady state with $T = 1$.

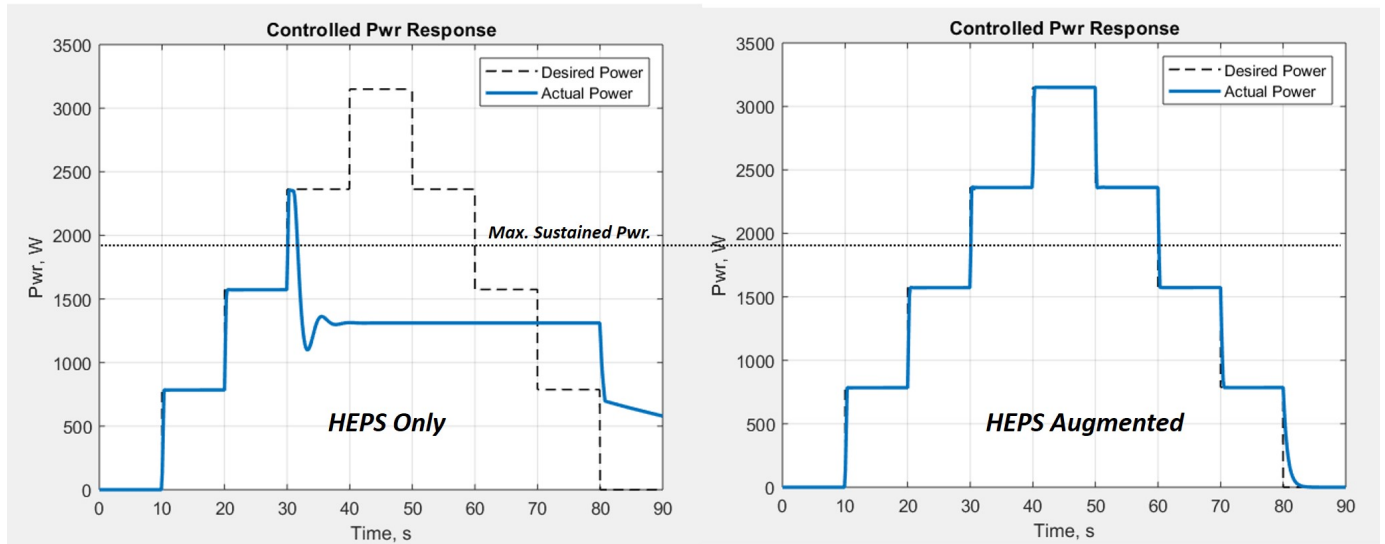


Figure 6.43: HEPS only collapse under large transient power demand.

In contrast, when supplemental current is provided by the slack bus according to Eq. 6.103, the system is able to sustain the high power demand, as shown in the right-hand plot

in Fig. 6.43. A comparison between the currents flowing through node N is given in Fig. 6.44

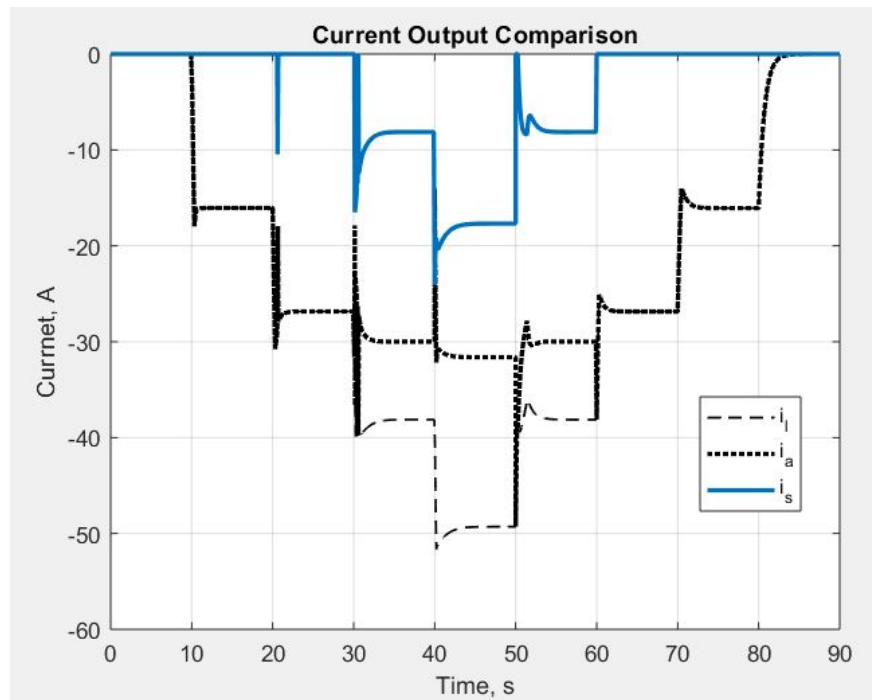


Figure 6.44: Current output comparison between the slack bus supplemental current, the armature current, and the load current.

6.13 Comments on Practical Implementation and Future Improvements

6.13.1 Aircraft state estimation for computing power demand.

In the examples presented in this discussion, we have assumed that the power demand is reasonably known at start of each model time-step. This is a reasonable assumption for an aircraft system, either manned or unmanned as state estimation for autopilot design is a mature though very active area of research for all types of aircraft. This is particularly

true if this system is employed onboard an autonomous or semi-autonomous UAS, where the autopilot system controls all vehicle motion states, so the input variables required by this methodology are well estimated.

Additionally, note that this power system control methodology is not predicated on forecasting the power demand, only that the current power demand is known. The power tracking performance of this system could be further improved by introducing such a power forecast and optimizing the operating conditions (T, ω) of the HEPS to accommodate these demand changes in advance.

6.13.2 Slack bus DC-DC converter type

In this chapter, the use of a buck converter for conditioning the voltage output of the slack bus is briefly discussed. The choice of a buck converter or boost converter to accomplish the DC-DC converter requirements is inconsequential in the context of the present model as the dynamics of the converter are ultimately neglected. However, in practice this distinction is critical for several reasons, making the buck converter a more practical choice.

- The characteristic behaviors of DC-DC converters are quite different as a function of duty cycle.

$$\text{Buck Converter: } V_{out} = V_{in}D \quad (6.104)$$

$$\text{Boost Converter: } V_{out} = \frac{V_{in}}{1 - D} \quad (6.105)$$

Clearly, the boost converter has pole at $D = 1$, which requires that the duty cycle is limited to the range $0 \leq D \leq 0.9$. Additionally, in the event of a control system

failure, this introduces the potential for the output of the boost converter to damage other components in the system.

- Use of a buck converter requires that the batteries used in the slack bus have a combined voltage greater than the maximum output of the HEPS. This is advantageous because via the buck converter DC-DC transformer-like behavior, the current drawn from the batteries will always be less than or equal to that supplied to the propulsion system, whereas the inverse is true for a boost converter, given the batter characteristics shown in Fig. 6.45. Since the location of batteries are typically decentralized, i.e. along the wings, in aircraft for structural reasons, this also reduces the weight of the conductors required to transmit the power from the battery to the converter and central power system.

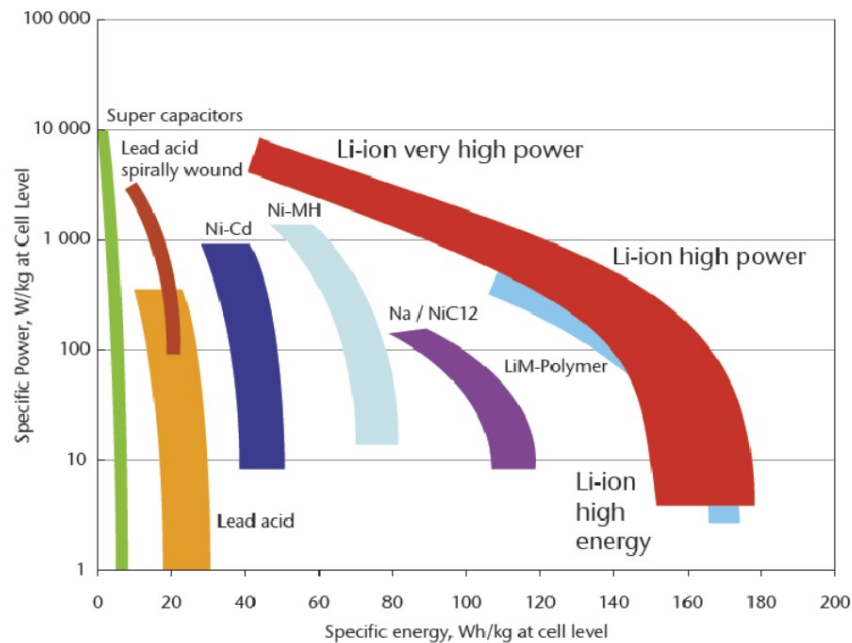


Figure 6.45: Battery comparison, Specific Power vs. Specific Energy [41]

- In battery selection, there is always a trade-off between specific power and specific energy of the cell type, as shown in Fig. 6.45. A simplified view of this is that for a constant cell voltage, the specific power equates to a measure of the maximum currently delivery capacity of that cell, the 'C Rating'. For a given total power requirement, a higher battery voltage reduces the current output requirement per cell and allows the use of cells with higher energy density, therefore increasing the total energy density of the battery system.

6.14 Part Three - Aircraft/HEPS Transition Response Behavior Analysis

The objective of the final part of this chapter is to present the response of the hybrid electric power system (HEPS) to the transition power loading profile developed in part 1 of this chapter. The combination of the 2-SMC design, power tracking controller, floating voltage setpoint and slack bus compensation are required to extend the performance of the HEPS to manage a complex loading profile of this nature. The transition power loading profile (xPLP) response will be examined at three different power levels. First, the xPLP will be scaled such that the peak power demand is equal to the maximum sustained power threshold (MSPT) of the un-augmented HEPS. Next, the xPLP will be scaled such that the maximum sustained power loading is equal to the MSPT. Finally, the xPLP will

be scaled such that the hover power loading is equal to the MSPT. Additionally, these results will be discussed in the context of aircraft power system design.

6.15 Defining the Power Loading Conditions

The xPLP will be scaled to three different conditions relative to the MSPT of the HEPS.

$$\text{Case 1: } P_{L_{pk,xPLP}} = MSPT \quad (6.106)$$

$$\text{Case 2: } P_{L_{sus,xPLP}} = MSPT \quad (6.107)$$

$$\text{Case 3: } P_{L_{hover,xPLP}} = MSPT \quad (6.108)$$

Let us begin by defining the MSPT of the system. In this context the MSPT is defined as the maximum continuous power the un-augmented HEPS can sustain where the following condition for operating torque τ_{op} is met.

$$\tau_{op}(\omega, T) = 0.9 * \tau_{max}(\omega_0) \quad (6.109)$$

Given that $\tau \propto T^{1/2}$, this occurs where $T \approx 0.8$ for all ω . This can be extracted easily from the simulation, by subjecting it to a slow ramping increase in power demand, and restricting the throttle input to the range $0 \leq T \leq 0.8$. Here a power ramp rate $\frac{dP}{dt} = 35W/s$ is used. The power tracking response to this input is shown in Fig. 6.46.

Without the augmented power provided by the slack bus, the HEPS is able to track the power demand requirement up to the MSPT, where it ultimately collapses to a lower power

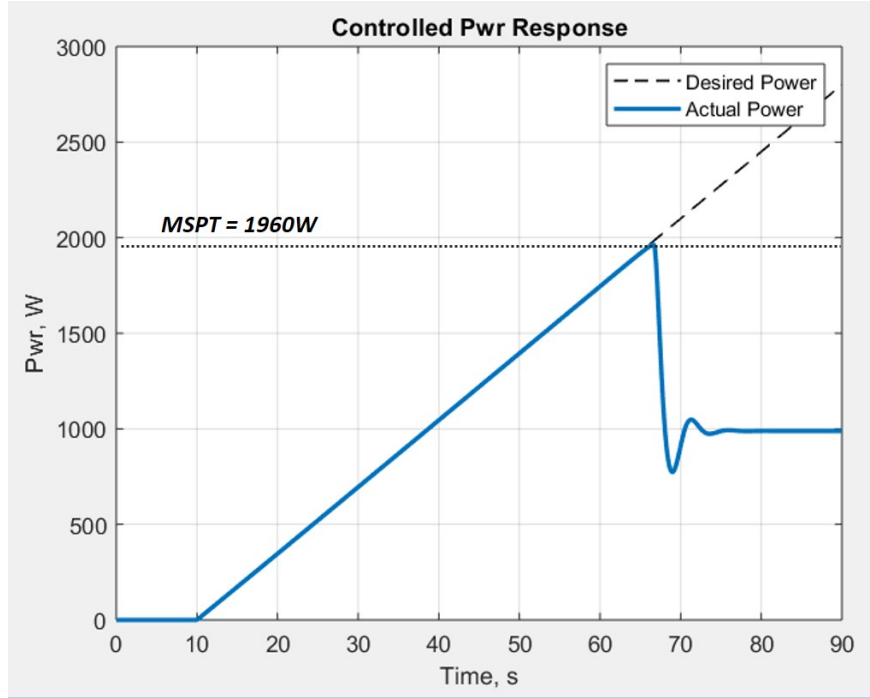


Figure 6.46: Maximum sustained power threshold (MSPT) for the un-augmented HEPS.

steady state, as shown in Figs. 6.47 and 6.48. This collapse is due to the shape of the engine torque output as a function of angular velocity ω . In this case,

$$MSPT = 1960W \tag{6.110}$$

The summary of the system response is shown in Fig. 6.48. The current and angular velocity plots illustrate the nature of the system collapse. Since the load torque on the engine from the generator is given by $\tau = i_a k_T$, the system has two possible steady state conditions depending on the current value. Saturation of the throttle at the higher power condition, ω_1 , will cause the system to collapse to a lower power condition at ω_2 if the system is perturbed with τ^+ , as shown in Fig. 6.47.

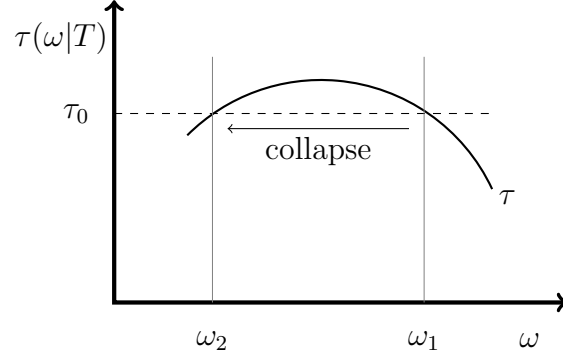


Figure 6.47: System collapse for constant torque.

Now with MSPT defined and the potential collapsed operating modes understood, the power scaling factors can be defined.

Recall that the power loading is defined as the power requirement per unit span given a specific wing chord.

$$\text{Power Loading, } P_L(\alpha, c_p^*|c, W_L) = \frac{P_{req}}{\text{unit span}} \quad (6.111)$$

This has dimension $[W/m]$, so the scaling factors to be developed are effectively the total span of ADP wing in the hypothetical aircraft design.

Examining the power loading profile for the aborted landing maneuver developed in part 1 of this chapter, the three loading cases can be developed, as shown in Fig. 6.49.

The reference power loading for each case is summarized as follows.

$$\text{Case 1: } P_{L1} = 1458W \rightarrow b_1 = MSPT/P_{L1} = 1.35m \quad (6.112)$$

$$\text{Case 2: } P_{L2} = 1000W \rightarrow b_2 = MSPT/P_{L2} = 1.97m \quad (6.113)$$

$$\text{Case 3: } P_{L3} = 726W \rightarrow b_3 = MSPT/P_{L3} = 2.70m \quad (6.114)$$

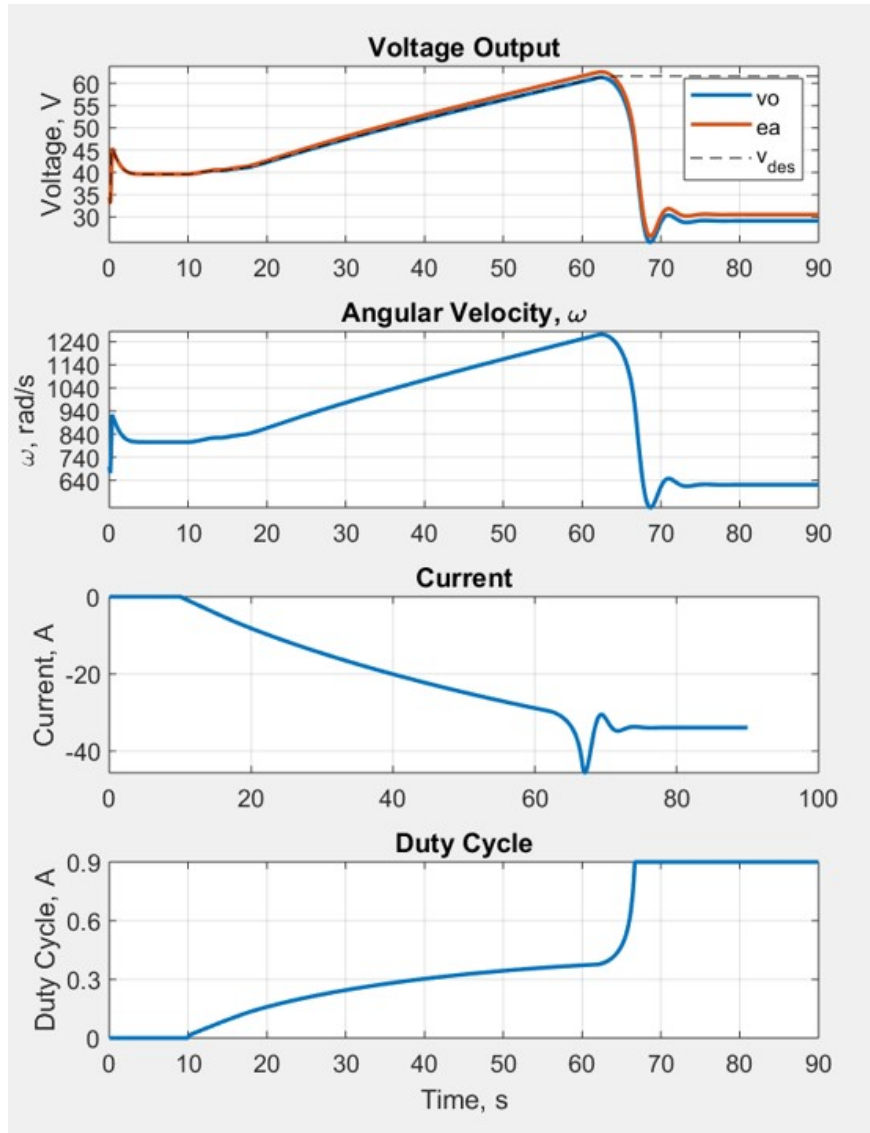


Figure 6.48: Maximum sustained power threshold (MSPT) system response summary for the un-augmented HEPS.

Because the power loading profile was developed for an aircraft with a known wing loading, in this case $W_L = 200N/m^2$ and a known wing chord $c = 0.167m$, the gross weight of the aircraft is given by

$$GW_n \approx W_L c b_n \quad (6.115)$$

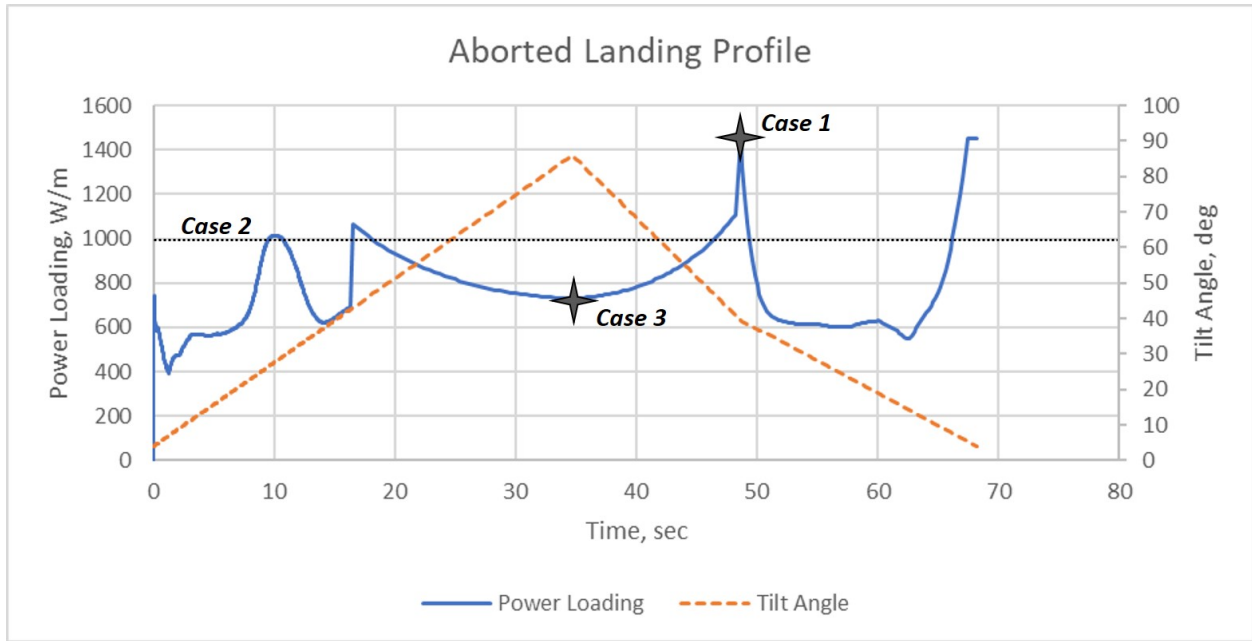


Figure 6.49: Power loading cases taken from the aborted landing maneuver profiles

This is an approximation because, while the relationships between each of the variables are consistent, the span estimates b_n are variable with fixed chord c .

6.16 Loading Case 1 Results, $b_1 = 1.35m$

The simulation results will be presented in two sections for clarity. The discussion subsection will be presented first, followed by a subsection containing the corresponding figures.

6.16.1 Results Discussion, $b_1 = 1.35m$

The load profile in this case is defined such that the peak load required is equal to the MSPT of the un-augmented HEPS system, without the supplemental support of the slack bus. As seen in the voltage output and voltage tracking error plots in Fig. 6.50, the 2-SMC controller is able to maintain the floating voltage output once the sliding variable σ has converged.

The tracking error is only non-zero when σ is in sliding. This occurs in three instances. First, the largest errors are present at $t = 0s$ due to a mismatch in the initial state of the system and the first operation condition at $t = 0s$. Here σ is in sliding and all other controllers are moving the system toward the required operating condition. The second and third instances occur at $t \sim 17s$ and $t \sim 49s$ where the power requirement is discontinuous between timesteps due to the manner in which the transition between slow wing-borne flight and hovering flight was handled when developing the aborted landing transition profile. This discontinuity was intentionally left in the power loading profile to evaluate the robustness of the system to step changes and cusps while tracking a complex and rapidly changing loading profile. In each case, the sliding variable is pushed away from zero by the discontinuity, however, the maximum voltage tracking errors are $\sim 0.5V$ and $\sim 0.3V$ respectively.

These discontinuities impact the power demand tracking error of the system as well. Here the maximum tracking errors are each $\sim 10W$ or $> 1.0\%$ of the target power value.

Though the throttle signal briefly saturates, this does not cause the system to collapse. When the throttle saturates briefly at $t = 48s$, the slack bus delivers a small amount of current to compensate. This is the only instance of non-zero supplemental current i_s in this simulation.

The output of the slack bus can be described by the amount of energy it provides under a specific loading condition.

$$\text{Slack Bus Energy Output} \equiv \int_0^t v_o(t)i_s(t)dt \quad (6.116)$$

evaluated numerically here as

$$SBO = \frac{\Delta t}{3600} \sum_{j=1}^N i_{s_j} v_{o_j} \quad (6.117)$$

where N is the number of time steps in the model, giving a result in Wh if using the dimension $[s, A, V]$.

For comparison, we can evaluate the total energy output of the system during the loading simulation as

$$\text{Total Energy Output} \equiv \int_0^t v_o(t)i_l(t)dt \quad (6.118)$$

evaluated similarly as

$$TEO = \frac{\Delta t}{3600} \sum_{j=1}^N i_{l_j} v_{o_j} \quad (6.119)$$

Therefore the impact of the slack bus on the output of the system can be expressed by the ratio

$$\Psi = \frac{SBO}{TEO - SBO} \quad (6.120)$$

If the slack bus has a negligible energy contribution to system output, $\Psi \approx 0$, whereas if the energy from the engine-generator is equal to that provide by the slack bus, $\Psi \approx 1$.

For this loading example

$$SBO = -0.0161Wh$$

$$TEO = -19.08Wh$$

$$\Psi = 8.45 \times 10^{-4} \approx 0$$

For, $b_1 = 1.35$ the slack bus makes a negligible energy contribution to the HEPS output.

6.16.2 Results Figures, $b_1 = 1.35m$

A summary of the response characteristics for this condition are shown in Fig. 6.50 and the trajectory of the system on the torque and power manifolds are shown in Fig. 6.51.

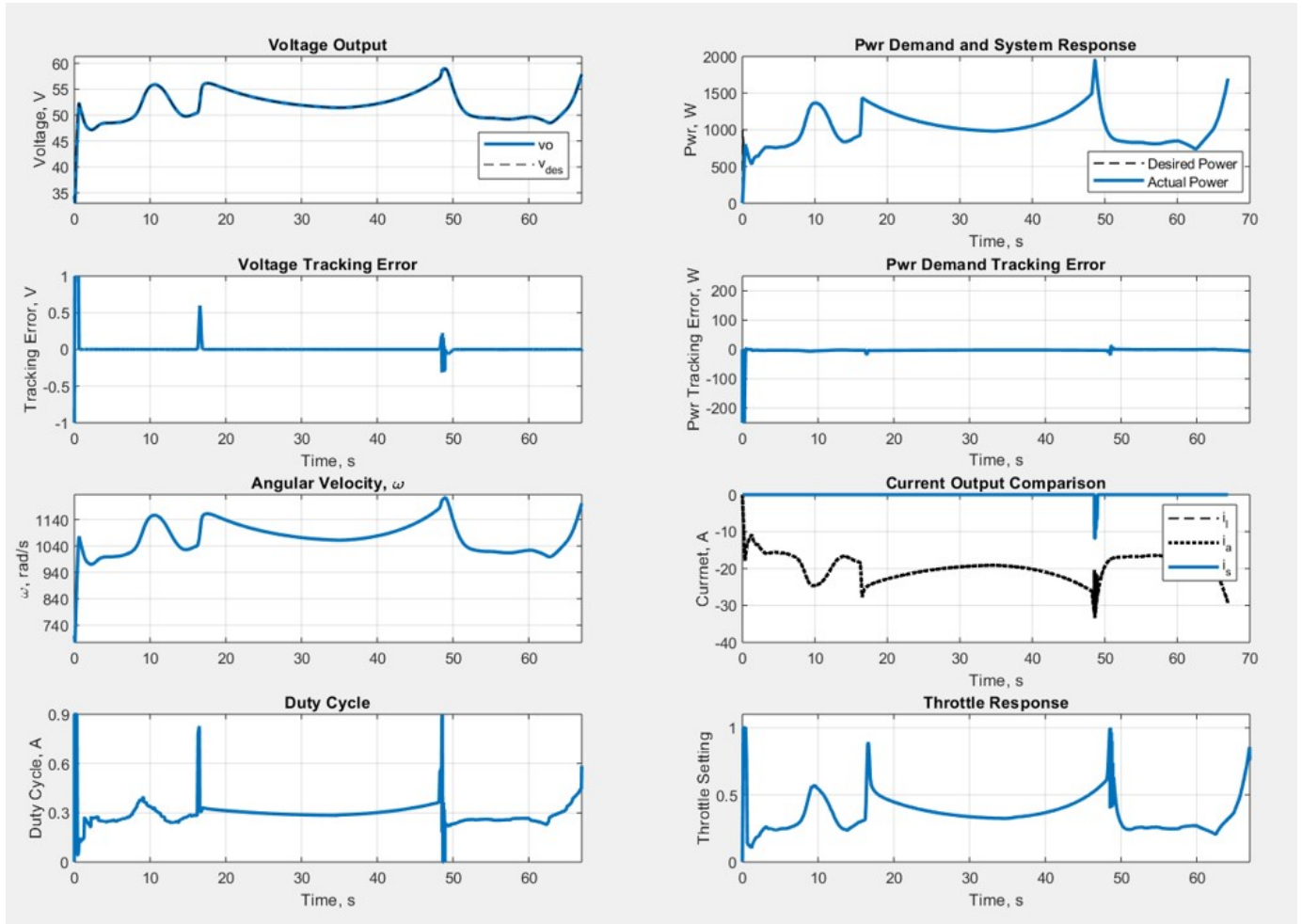


Figure 6.50: Summary data from the transition profile simulation where $b_1 = 1.35$

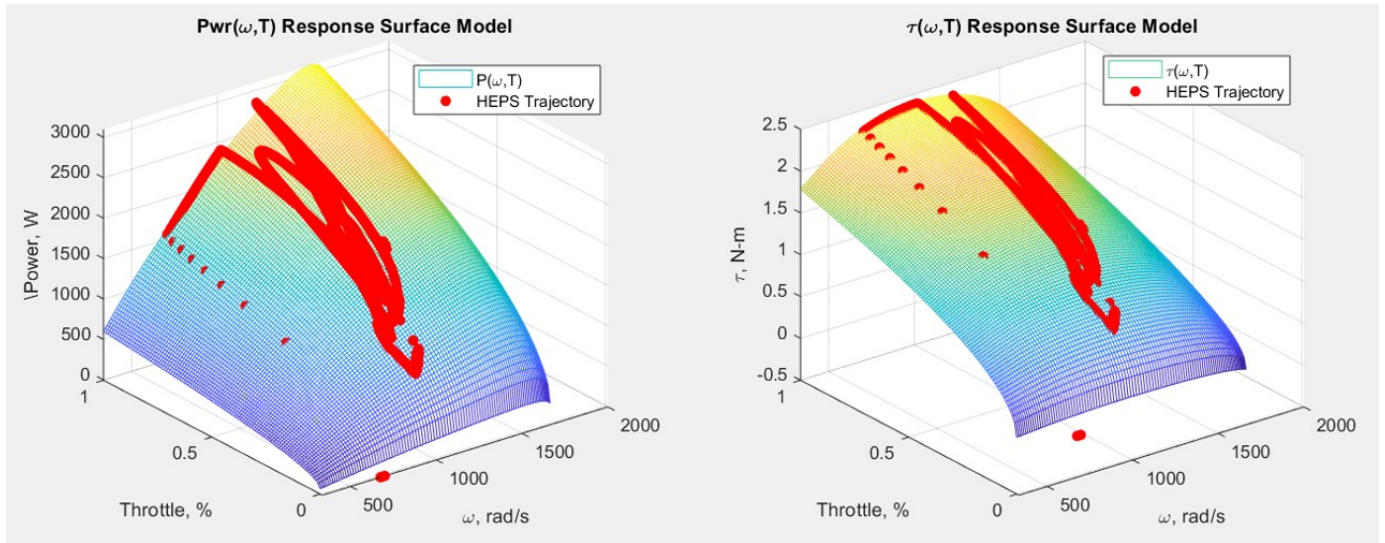


Figure 6.51: HEP trajectory results from the transition profile simulation where $b_1 = 1.35$

6.17 Loading Case 2 Results, $b_2 = 1.97m$

Again, the simulation results for this case will be presented in two sections for clarity. The discussion subsection will be presented first, followed by a subsection containing the corresponding figures.

6.17.1 Results Discussion, $b_2 = 1.97m$

For this loading example the HEPS again exhibits excellent floating voltage and power demand tracking characteristics, though the increased reliance on the contribution of the slack bus introduced larger voltage and power tracking errors. As developed for the purposes of this analysis, the dynamics of the buck converter and load duty cycle control are assumed to be arbitrarily fast, able to commute their full range between model time-steps, Fig. 6.52. This is a reasonable assumption for these parameters given that they are associated with systems whose internal dynamics occur at a frequency on the order of $50\times$ greater than that of the simulation. However, while the throttle response is not rate limited in this model, mechanical throttle servos and the fluid dynamic response of the engine's fuel-air induction system may limit the actual response of the system. Therefore, in practice it may be necessary to design the interaction between the slack-bus and the engine-generator system in such a way as to prevent this high-frequency oscillation. The power and torque response trajectories are presented in Fig. 6.53.

With this in mind, the HEPS again demonstrates a robust response to the complex power loading profile imposed by the aborted landing transitional flight regime of the ADP

system.

$$SBO = -1.539Wh$$

$$TEO = -27.86Wh$$

$$\Psi = 0.058$$

For, $b_2 = 1.97$ the slack bus makes a $\sim 6\%$ energy contribution to the HEPS output.

6.17.2 Results Figures, $b_2 = 1.97m$

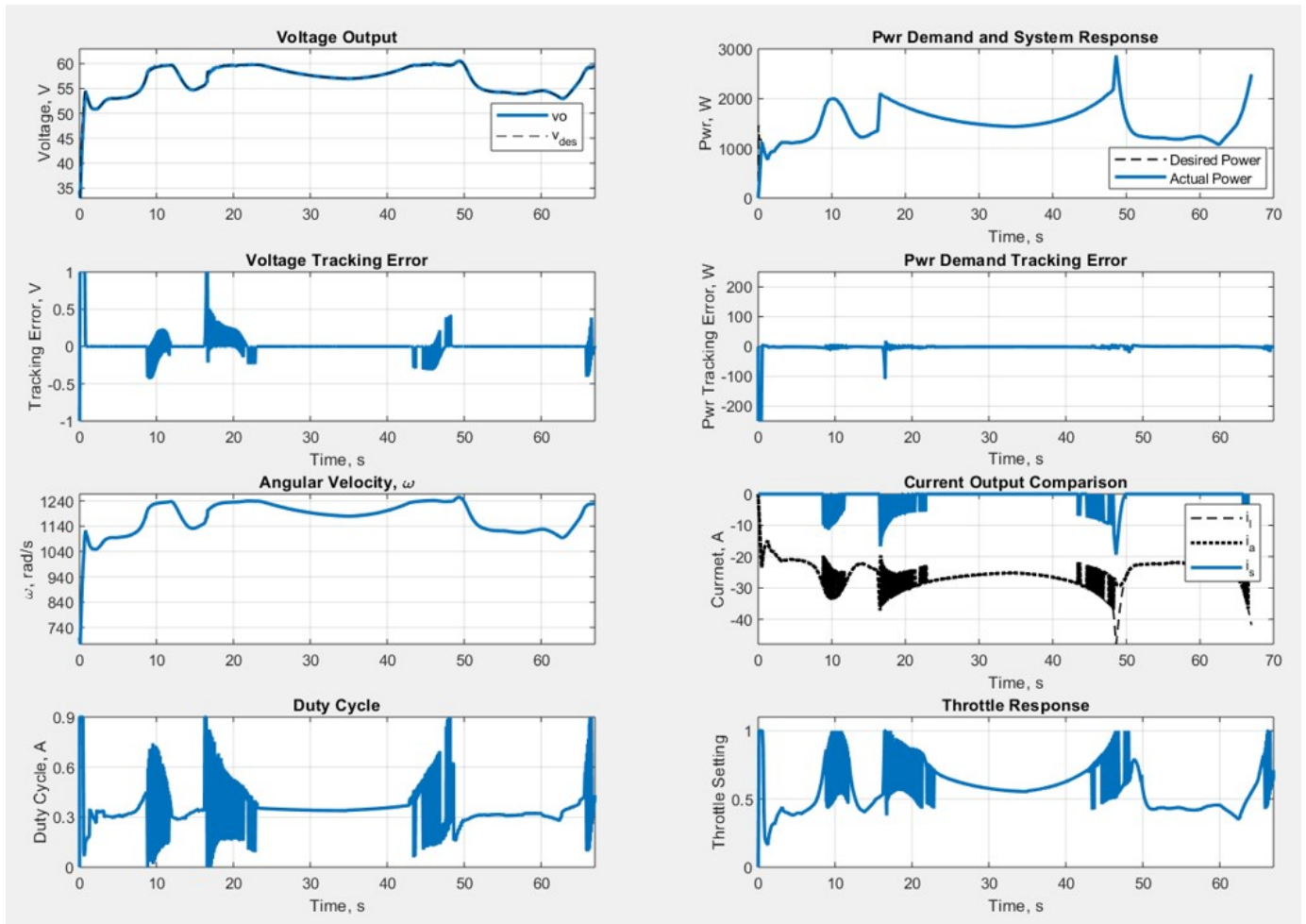


Figure 6.52: Summary data from the transition profile simulation where $b_2 = 1.97$

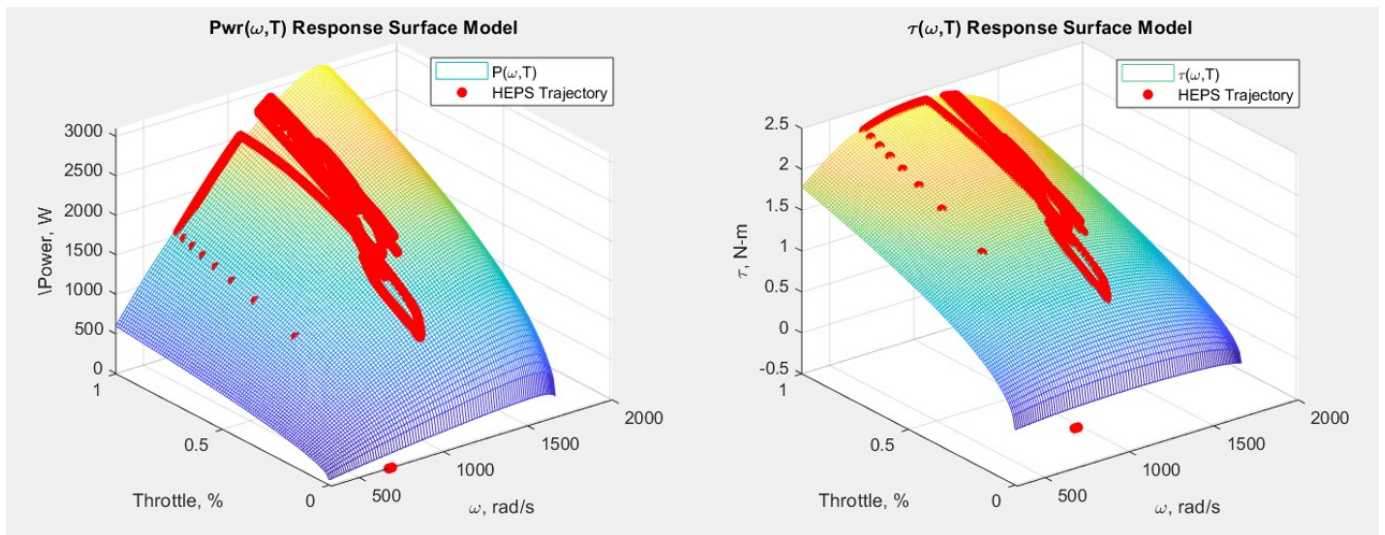


Figure 6.53: HEP trajectory results from the transition profile simulation where $b_2 = 1.97$

6.18 Loading Case 3 Results, $b_3 = 2.70m$

Again, the simulation results for this case will be presented in two sections for clarity. The discussion subsection will be presented first, followed by a subsection containing the corresponding figures.

6.18.1 Results Discussion, $b_3 = 2.70m$

As in the previous two cases, where $b_1 = 1.35m$ and $b_2 = 1.97m$, this case shows excellent tracking of the floating voltage and power demand. As in case 2, the increased reliance on the slack bus supplemental current i_s introduces high frequency oscillation of the power regulator duty cycle, and the buck converter output current. This again leads to increased tracking errors for both voltage and power relative to case 1. However, with the exception of the start-up error near $t = 0s$, the voltage tracking errors are $> 0.5V$. The 2-SMC voltage controller quickly drives the sliding variable σ back to zero after each excursion.

With the exception of the response to the step change in power demand at $t \sim 17s$, the power tracking errors remain less than $\pm 10W$. At the step change however, the power tracking error is approximately $220W$ due to the combined effects of a saturating throttle input as well as a saturating power regulator duty cycle.

Examining the current plot in Fig. 6.54 reveals that a significant portion of the total load current is supplied by the slack bus. This contribution is characterized by

$$SBO = -7.358Wh$$

$$TEO = -38.20Wh$$

$$\Psi = 0.239$$

For, $b_3 = 2.70$ the slack bus makes a $\sim 24\%$ energy contribution to the HEPS output. The power and torque trajectories are presented again for this case in Fig. 6.55, with the system spending a majority of the time at or near the peak power condition of the engine-generator system.

6.18.2 Results Figures, $b_3 = 2.70m$

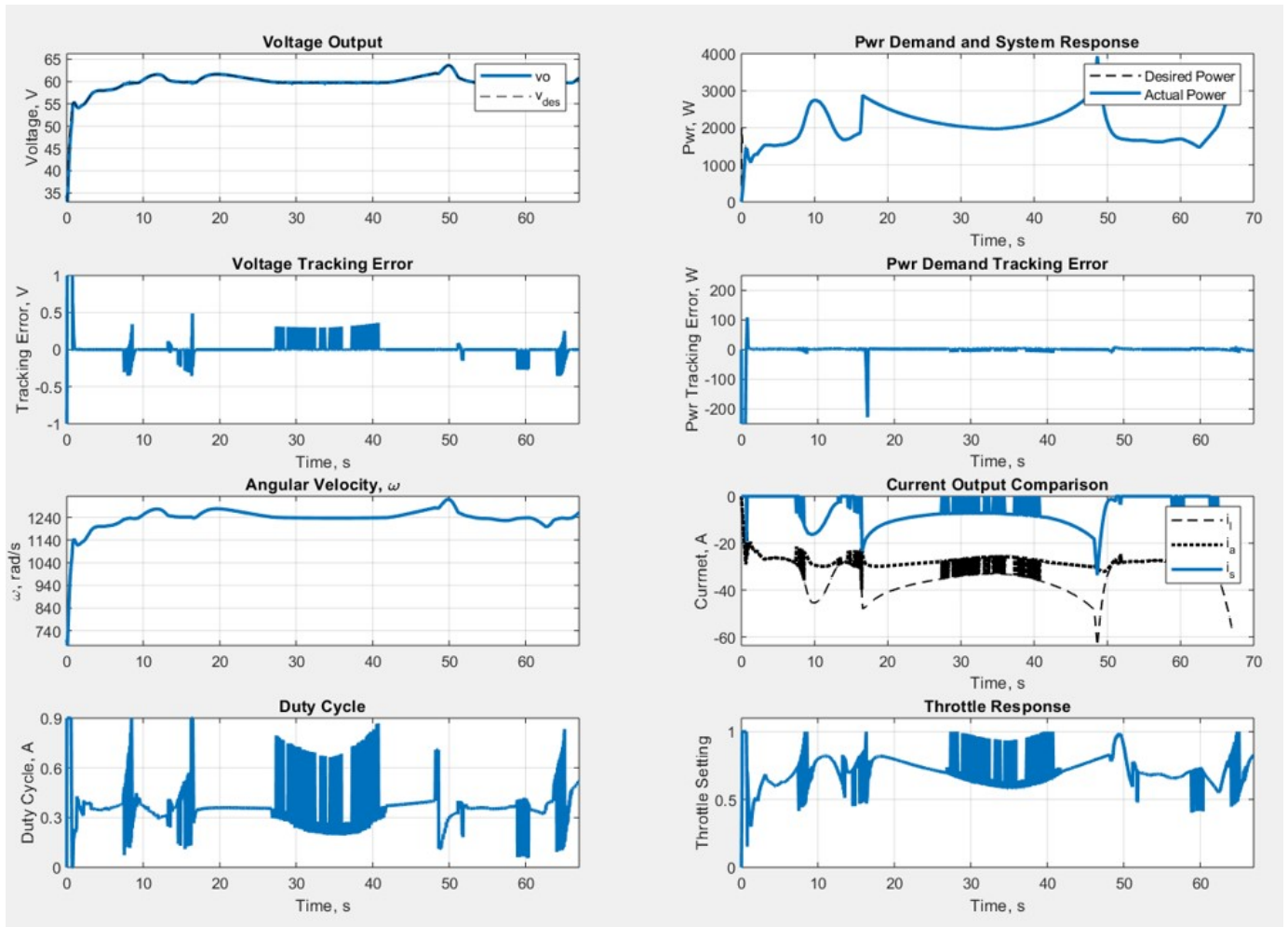


Figure 6.54: Summary data from the transition profile simulation where $b_3 = 2.70$

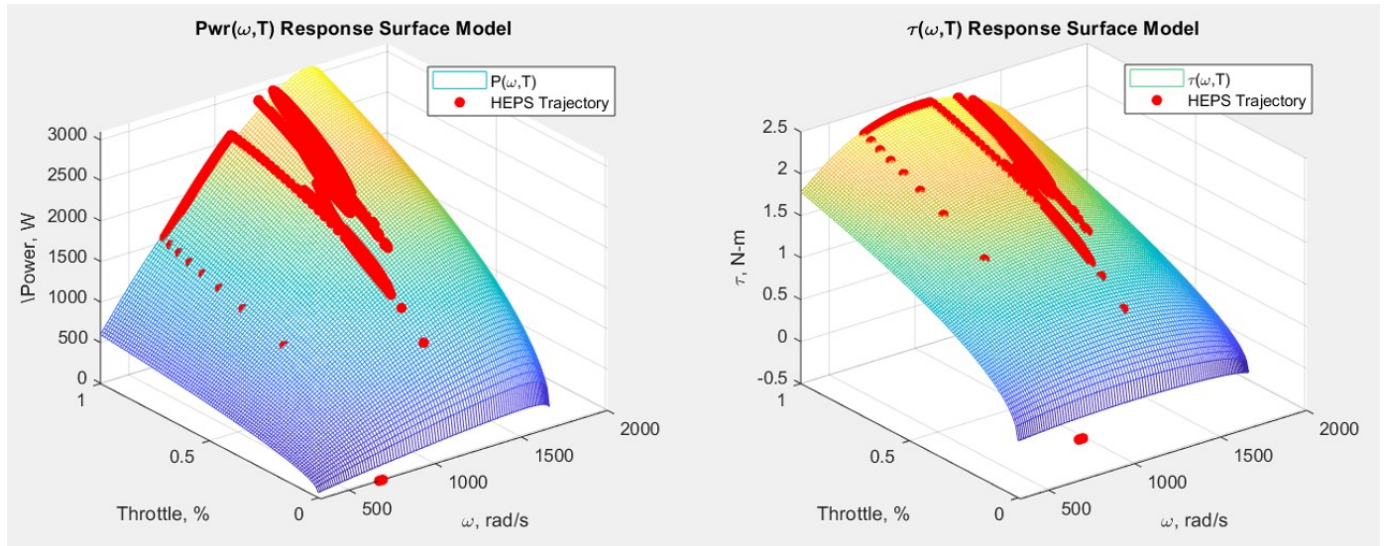


Figure 6.55: HEP trajectory results from the transition profile simulation where $b_3 = 2.70$

6.19 Conclusions

6.19.1 Part 1

Part 1 of this chapter presented the development of a parametric power loading profile derived from the flight performance and corresponding aerodynamic loads for an aircraft using the ADP system. This profile combined the wing-borne and hovering flight performance of inbound and outbound VTOL transitional flight regimes to be applied as an unknown disturbance load to the HEPs dynamical model in Simulink. This loading profile was developed in terms of wing loading W_L and power loading P_L to facilitate convenient scaling to applications of varying power demand.

6.19.2 Part 2

Part 2 of this chapter considered the extension of the HEPS controller required to accommodate the broad and rapidly varying power demands of the hypothesized ADP aircraft developed in Part 1. A robust 2-SMC design is used to control the operating voltage of the system. This enabled a combined cascade and interleaved controller design where the operating voltage is allowed to float according to the instantaneous power demand and operation conditions of the system, to more fully utilize the power output capacity of the two-stroke engine driving the HEPS.

The operating regime and robustness of the system was further improved by introducing a buck-controlled slack bus to augment the engine-generator when the instantaneous power demands could not be met.

6.19.3 Part 3

Finally, Part 3 of this chapter addressed the application of the aerodynamically derived power loading profile developed in Part 1 to the improved HEPS design developed in Part 2. Three cases for comparison are presented here where the power loading profile was extended to a specific aircraft design with constant wing loading $W_L = 200N/m^2$ and a constant chord, allowing the scaling factors to be computed as a reference 'span' for each case. This approximation, though not strictly rigorous, provides a uniform basis for comparing the HEPS response to each loading condition. It is demonstrated that the experimentally validated dynamical model of the HEPS can, with proper control, sustain the demanding and variable power demands of transitional VTOL operation.

Chapter 7

Conclusions and Next Steps

7.1 Concluding Remarks

In conclusion, the ADP and CDP propulsion systems are evaluated both experimentally and computationally throughout this research effort, representing the first time the performance of either of these systems is evaluated in academic literature. The ADP system is found to provide the most robust aerodynamic basis for developing a VTOL aircraft, as the dynamic response of the system to changing angle of attack and power input follows predictable trends that closely mirror the expected analytical behaviors. Additionally, the response of the ADP system can be easily segmented using these characteristics into three operating regimes, the Aerodynamic Cruise Regime (ACR), the Powered Lift Regime (PLR), and the Hover Breakdown Regime (HBR). The CDP system is observed to exhibit a bi-modal response to power input at many operating conditions and is consequently eliminated from further analysis.

In order to properly characterize the results of the experiments, the conventional methods for evaluating aircraft performance are extended to include systems where circulatory lift is considerably enhanced by applied power, as is the case with embedded propulsion systems. The parameter c_p^* is a direct result of this analysis. Once this methodology is established, the evaluation of the ADP and CDP systems is greatly simplified.

For ADP, in the ACR and the PLR the horizontal and vertical force coefficients c_u and c_v , are each linearly proportional to the dimensionless pressure parameter c_p^* in each domain respectively. That is, in the ACR, $c_u \propto c_p^*$ and in the PLR, $c_v \propto c_p^*$. In both of these operating regimes, the jet ideal power is observed to maintain a power-law proportionality with c_p^* , as $P_{jet} \propto c_p^{*3/2}$. These relationships are observed to breakdown in the HBR.

These two-dimensional wing section results are used to estimate finite, three-dimensional wing performance. Here a lifting line approximation is made using a wing-element model numerical estimate. From these estimates, the straight, level, and unaccelerated flight (SLUF) envelope of an ADP-VTOL is established. As the propulsion system and aerodynamic forces are interdependent, SLUF operation is only possible up to a wing tilt angle of approximately 43 degrees. Ultimately, a scalable transition power loading profile (xPLP) is developed based on these finite wing performance estimates. This profile is given in terms of wing loading $W_L[N/m^2]$, a force per unit area, and power loading $P_L[W/m]$, the power per unit span, for a given ADP configuration. In these terms, the xPLP can be scaled different size aircraft relative to the maximum sustained power threshold (MSPT) of the power system.

Regarding the hybrid power systems, in order to investigate the transient behavior of small hybrid-electric power systems (HEPS), a two-stroke powered HEPS experiment is constructed and evaluated. This platform is subjected to a battery of tests consisting of

multi-step load profiles as well as ramp-response load profiles. These tests are conducted at a fixed operating voltage using a linear PID controller to facilitate extracting the dynamic characteristics of the HEPS from experimental data.

These results are then used to tune and validate a dynamical model of the electro-mechanical HEPS system constructed in Matlab and Simulink. This model employs a novel means of modeling the transient engine response to changes in load. A multi-variate manifold regression meta-model is used to represent the engine's dynamic torque output as a function of angular velocity and throttle command. The tuning and validation of this model based on experimental data is further facilitated by the used of the linear PID controller, as this controller, while sub-optimal is easily implemented experimentally, and easily represented numerically in the simulation environment.

Once the simulation is validated and tuned, additional development is undertaken to improve the control design. A second-order sliding mode controller is implemented using a variation of the super-twisting algorithm. This controller gives a smooth control input that yields finite-time convergence. As a result, the voltage of the system is well controlled and exhibits a robust response and is shown to reject the bounded input disturbances to the engine-generator system.

The system architecture is further improved by adding an additional controller for instantaneous power. Here, the generator and load are actively controlled in tandem to meet the instantaneous power demand without the need for sophisticated demand forecasting algorithms. Additionally, an adaptive voltage controller is introduced to enable more complete and efficient utilization of the mechanical power available from the engine.

A buck-converter controlled slack-bus is then used to augment the HEPS system. This enables the HEPS to share the power demand at peak load allowing for a more efficient propulsion system design. The engine-generator system can be sized for a nominal load, yielding a smaller and lighter design, while the slack-bus can supplement the load when the power demand exceeds the MSPT of the HEPS alone.

Ultimately, the xPLP developed from the ADP experimental data is applied to the augmented HEPS model at different power levels relative to the MSPT, with a robust response to this demand demonstrated in each case. **Considering these results, hybrid-electric distributed power is a viable option for VTOL aircraft.**

7.2 Next Steps and Future Work

Perhaps the most obvious area for improvement of this work is to further investigate the bi-modal response of the CDP system with the intention of mitigating this behavior. The CDP system has the potential for very efficient cruise performance as well as increased operational safety relative to ADP, given that a portion of the CDP wing remains fixed, therefore allowing the aircraft to glide in an emergency. This additional work should be undertaken both experimentally and computationally, with an emphasis on flow visualization during periods of transient power in both cases. This would reveal truly bi-modal, hysteric behaviors and the energy-state of each case. Further, the design of the CDP might be improved to limit these characteristics to operating regimes that can be avoided during all phases of flight.

Next, in order to more accurately extend wing section results to finite wing performance estimate, it is necessary to characterize the wake structure of the ADP and CDP systems

and therefore the effect on the downwash distribution. Since there are axial fans distributed along the span of these systems, it may be possible to manipulate the wake vorticity distribution using these fans, thereby influencing the downwash distribution and controlling the three-dimensional flow around the wing. Additionally, further study of the wing-tip flows is necessary as well, as it is unclear how this three-dimensionality should be considered when designing the wing tip axial fans.

There are significant shortcomings of small two-stroke engines regarding fuel efficiency and emissions, owing primarily to intrinsic features of two-stroke engine design, such as the required fuel/oil mixtures, and aspiration of the fuel/air charge into the cylinder through the crankcase and cylinder wall. These characteristics result in a significant quantity of un-burned hydrocarbons in the exhaust stream which represent both energy loss and environmental pollution. This HEPS architecture could be further extended by combining this research with the work of (Welles, T. and Ahn, 2018) [57]. Integrating a high temperature solid oxide fuel cell into this system would simultaneously improve the efficiency of the system, increase the power output, and reduce the environmental impact of this system.

Additionally, other power sources and engine types should be considered for this HEPS system as well. The torque characteristics of the prime mover of the system, while essentially transparent to the 2-SMC voltage controller, may require changes to the overall system architecture and adaptive voltage functions. For example, the two-stroke engine upon which the present model is based has a very rapid throttle response, high mechanical losses, minimal stored energy and low system inertia. In contrast, a micro gas turbine has slow throttle response, but low mechanical losses, very high stored rotational energy, and similar inertia. Developing a generalized system architecture for small HEPS with an arbitrary prime mover

is a natural extension of this work, including the scalability and applicability of this approach to other weight-sensitive power systems and vehicles, such as portable power units for remote personnel, manned and unmanned marine power systems, as well as range extending systems for electric ground vehicles and transportation.

Appendix A

Wind Tunnel Data Acquisition

A.1 Pressure Data Acquisition

A.1.1 Introduction

The purpose of this chapter is to discuss the data collection methods used during the wind tunnel experiments. This includes considerations for manometer panel imaging and calibration as well the design of the electric power data acquisition system. Uncertainty and confidence interval analyses are included as well.

The wind tunnel model constructed for evaluation of both the CDP and ADP configurations is fitted with an array of static pressure ports about the center line of the model and along the interior of fan duct no. 4. The forward wing has 20 ports, the lower fan flap has 14 ports, and the upper fan flap has 12 ports. In total, 46 static pressure taps are used to capture the pressure distribution around the CDP and ADP experiments. Additionally, there are 8 total pressure taps installed in the outlet duct of fan # 3.

Each of the pressure taps is connected to a fluid manometer. The height of the fluid in the manometer reflects the pressure condition experienced by the individual pressure tap, shown in Fig. A.2. Ultimately, this pressure data is integrated around each of the aerodynamic surfaces to yield the net force due to the static pressure distribution on the bodies. The total pressure ports in the fan duct are used to characterize the operation of the fan at each operating condition, as are the digital signals that reflect the fan power consumption at a particular operating condition. The process by which this data acquired is shown in Fig. A.22.

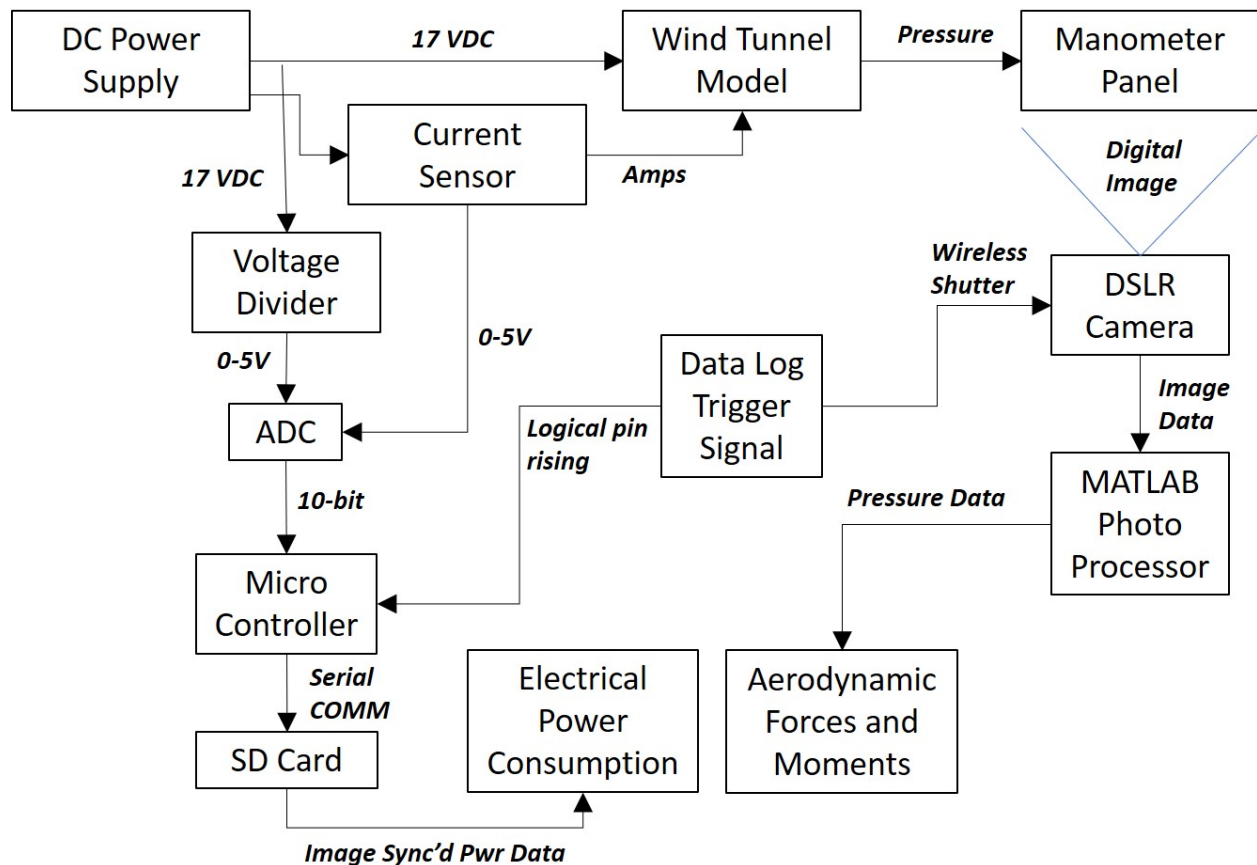


Figure A.1: Functional block diagram of the wind tunnel data acquisition system.

A.1.2 Imaging Considerations

In order to ensure consistency within the data set, all 58 pressure measurements must be captured simultaneously. To achieve this, a digital single-lens reflex (DSLR) camera is used to photograph the manometer bank and capture each operating condition. For this research, an 18 megapixel Canon Rebel T3i was used. From each digital image, the height of each fluid column can be precisely measured and compared to the atmospheric pressure baseline to obtain Δh for each manometer column.

The angle of the field of view (FOV) was minimized to the greatest extent practical to reduce the effect of image warping on the data. This measurement method requires that the zoom and focal length of the lens, distance from the camera to manometer bank, and lighting parameters remain constant throughout any particular test. In order to achieve this, the camera is positioned on a tripod at a fixed distance from the manometer bank, the lens is zoomed to its minimum field of view, the camera is manually focused, all automatic focus capabilities are deactivated, and the camera shutter is triggered using a wireless shutter release.

Particular care was taken when lighting the manometer panel during data collection, as the image processing algorithms developed for this research rely primarily on the contrast between the dark colored manometer fluid and the white background to produce accurate pressure measurements. The meniscus of the fluid in each manometer tube is typically distinct and therefore provides a strong visual signal from which to obtain a pressure measurement.

A.1.3 Image Processing

All images for each operating configuration for both the ADP and CDP systems are processed according to the following algorithm. The details of algorithm 3 are discussed in this subsection as well as subsection A.1.4.

Algorithm 3: Photo processing and raw column height data extraction

Result: Manometer Fluid Column Height Measurement

```
22 Initialization;
23 Scale column centers to current image set; figure A.4 ;
24 Obtain vertical pixels/inch scaling;
25 for  $k$ , Each image in the series do
26     Crop image to the index points;
27     rgb2grey(Image); Convert to grey scale;
28     im2double(Image); Convert grey scale image to double;
29     for Each Fluid Column, i do
30         for Each pixel on the column,  $j = n - k : 1 : n + k$  do
31             grad = gradient(Image(:,j)), compute the column gradient vector;
32             [minVal(j), minIdx(j)] = min(grad); find the index of the minimum
                 from the top of the image;
33             colHt(j) = imageHt - minIdx(j); height of column from the bottom of
                 the cropped image;
34         end
35         colReading(i) = median(colHt); find the median height measurement;
36     end
37     allColHts(k,:) = colReading; concatenate the reading for each image
38 end
39 outputFile = csvwrite(fileName, allColHts); Write the output file;
```

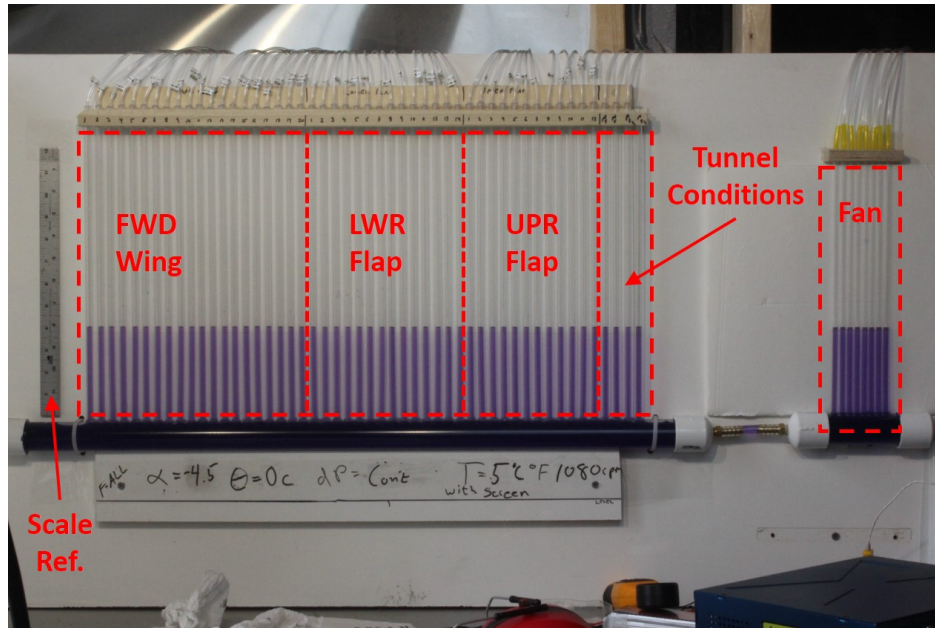


Figure A.2: Layout of the manometer panel, showing the primary panel, tunnel conditions, fan outlet subpanel, and vertical length scale.

The manometer images include data from the primary and sub-panel manometers that reflect a certain operating condition, as shown in Fig. A.7.

The original image is cropped at specific locations to simplify data extraction and processing as shown in Fig. A.4.

The images are converted to grey-scale and the contrast is adjusted to accentuate the fluid columns for both the main panel and the sub panel, as shown in Figs. A.5 and A.6 respectively.

A.1.4 Extracting the Fluid-Column Height Data

Once the images are cropped and converted to double values, the pressure measurement can be extracted. At this point the image is a simple $m \times n$ weights matrix of the form:



Figure A.3: The raw manometer panel images are scaled to include both the main panel and sub panel, the scale reference, and notes regarding the current model configuration and operating condition.

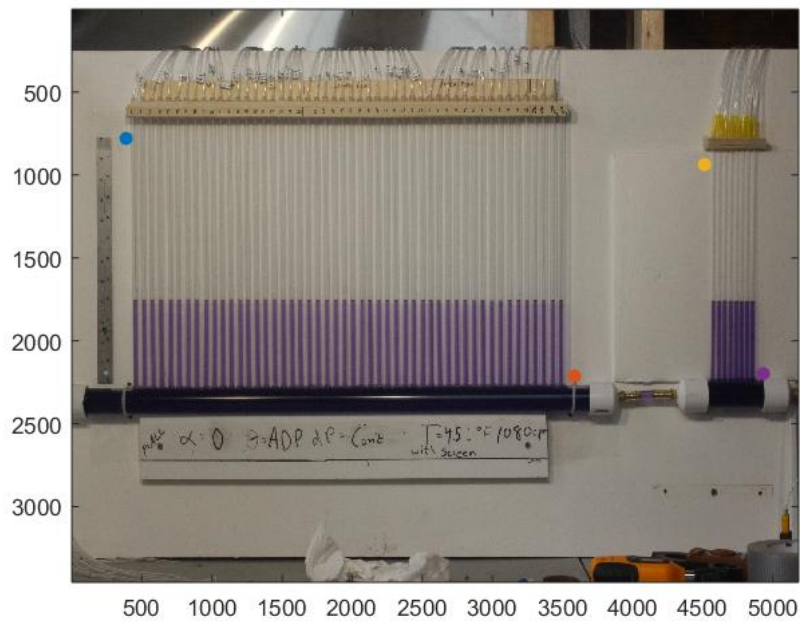


Figure A.4: Original image showing the pixel index locations used for cropping this and all subsequent images during data processing

$$\begin{bmatrix}
 wt_{1,1} & wt_{1,2} & \dots & wt_{1,n} \\
 wt_{2,1} & wt_{2,2} & \dots & wt_{1,n} \\
 \vdots & \vdots & 287 & \vdots \\
 wt_{m,1} & wt_{m,2} & \dots & wt_{m,n}
 \end{bmatrix}$$

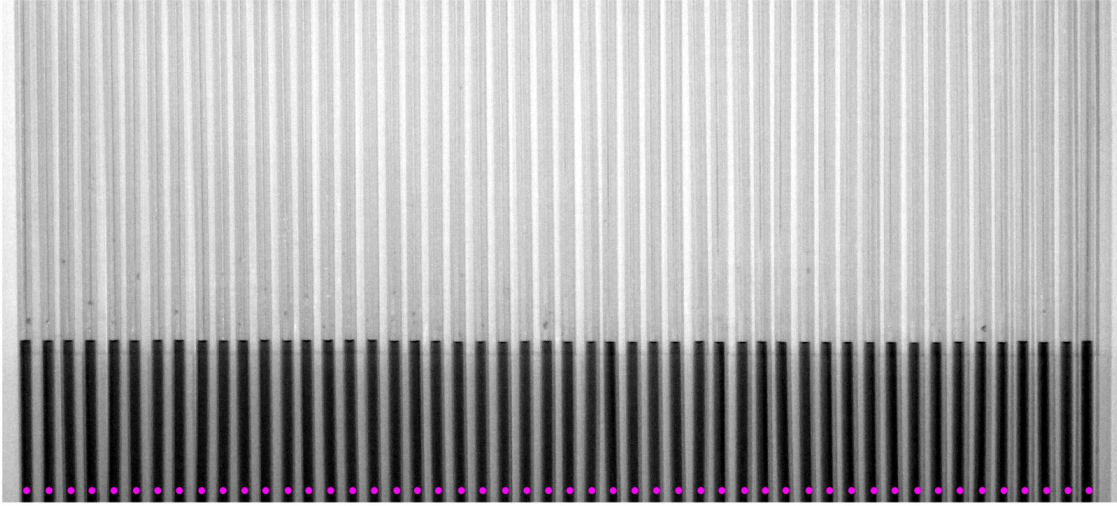


Figure A.5: Primary manometer panel imaged cropped to reference locations, converted to grey-scale with contrast adjusted to improve pressure data extraction from the image. The approximate center of each fluid column is marked as well. Image aspect ratio is true to scale.

Where the weights, $wt_{i,j} \in [0, 1, 2, \dots, 250]$ correspond to the grey-scale value of each pixel, from dark to light, and the (m, n) position of each entry corresponds to that pixels' position in the image. Therefore, identifying the row-index where pixel weight changes from light to dark, provides a measurement of the height of the fluid column. These pixel positions can then be converted to Δh and ultimately to ΔP_{gauge} relative to a calibrated zero-pressure baseline according to the hydro-static relation $\Delta P_{gauge} = \rho g \Delta h$.

The center of each fluid column is identified during pre-processing for each batch of images representing a specific case or operating condition. The row-index position of this transition is easily identified when scanning each of the center-line column vectors from top to bottom. The measurement is the index of the entry that satisfies the following condition:

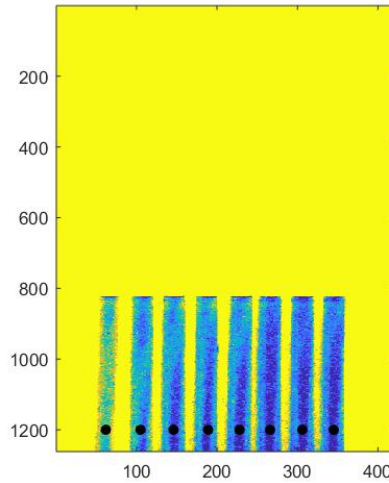


Figure A.6: Manometer sub-panel imaged cropped to reference locations, converted to grey-scale, though displayed using RGB wights, with contrast adjusted to improve pressure data extraction from the image. *Note that when displayed in this manner, the meniscus of the fluid column is clearly visible as the darkest patch at the top of each column.* The approximate center of each fluid column is marked as well. Image aspect ratio has been adjusted to display within this document.

$$m_i = \text{median}(\text{index}[\min\{\frac{\partial}{\partial m} C_j\}]) \quad (\text{A.1})$$

Where, C_j is the column vector containing the pixel weights associated with each fluid column center and adjacent points.

And, $n - k \leq j \leq n + k$ are the n column index locations of the $i = [1, 2, \dots, 58]$ center-line reference points and the k adjacent pixels. The finite width of the fluid columns is leveraged to improve the fidelity of the measurement. The median, as opposed to the mean, of these height estimates is used because this has the effect of removing outliers from the data-set and provides cleaner, more accurate measurement estimates, as shown in Fig. A.7.

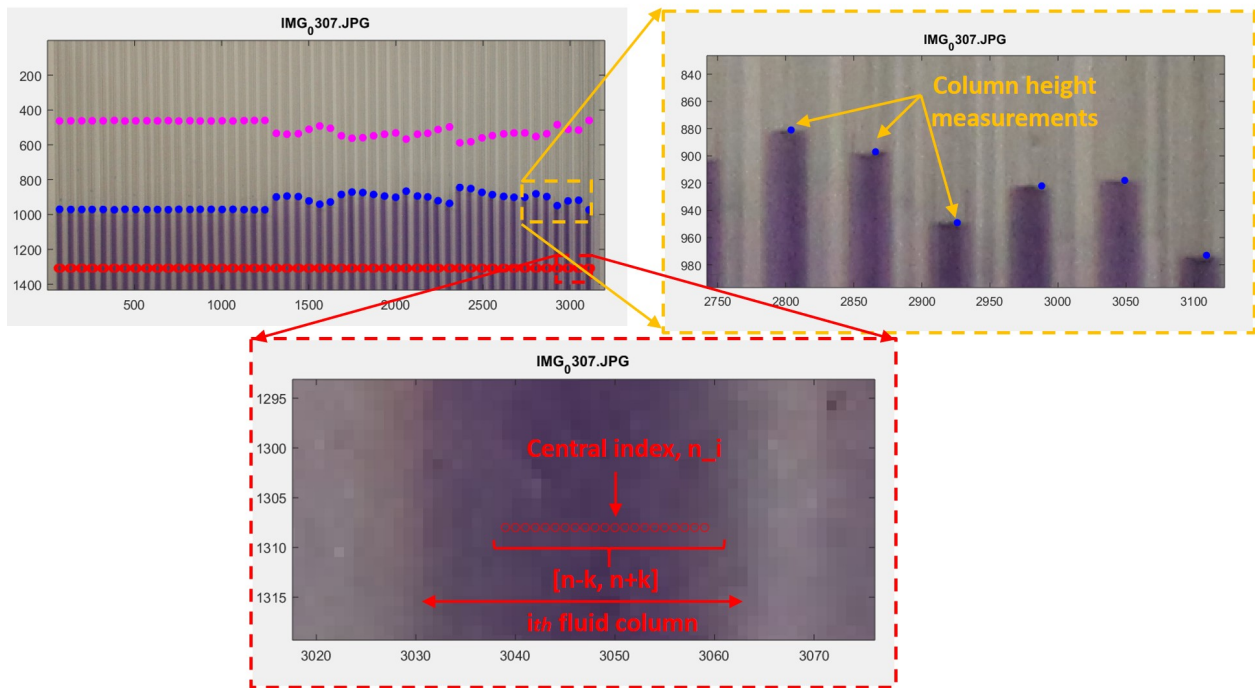


Figure A.7: Taken from ADP test data, the first 20 pressure taps are not used, as can be clearly seen. The identified column center indexes are augmented by taking measurements along adjacent additional pixels. The resulting measurement is the median of the row indexes identified by the algorithm.

The height of the column is determined for each pixel column by examining the derivative of the pixel weight along the column, as shown in Fig. A.8.

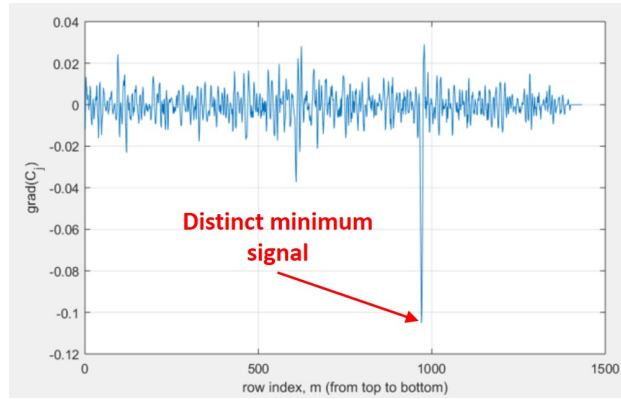


Figure A.8: Examining $\frac{\partial}{\partial m}C_j$ shows a distinct minimum value. This is interpreted as the transition between the light and dark regions of the fluid column, i.e. the height of the fluid in the column.

Collating these results for each manometer fluid column represents the pressure distribution around the experiment, as shown in Fig. A.9.

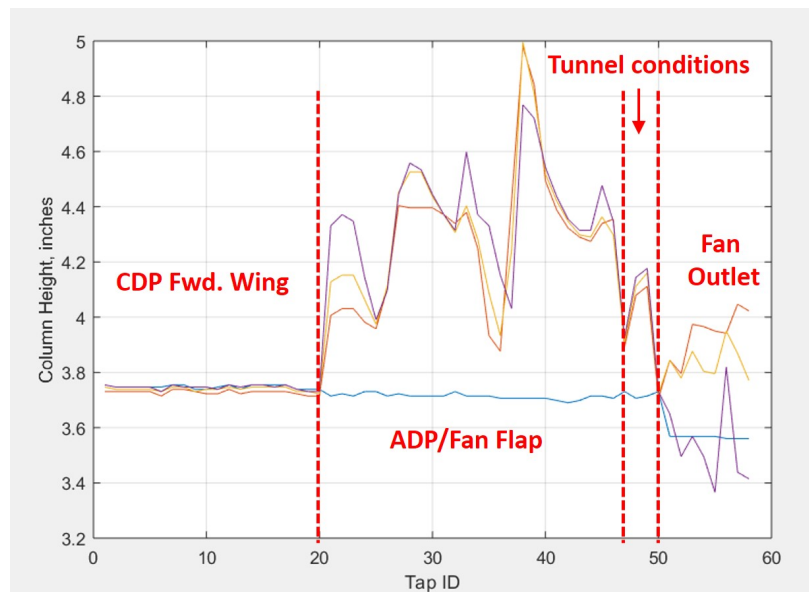


Figure A.9: Collating the column height estimates from each fluid column produces a complete data set comprised of all 58 individual pressure taps. This sparse data set is shown for clarity, only the data from a few images included.

A given test run includes between 70 and 100 operating conditions as shown in Fig.

A.10.

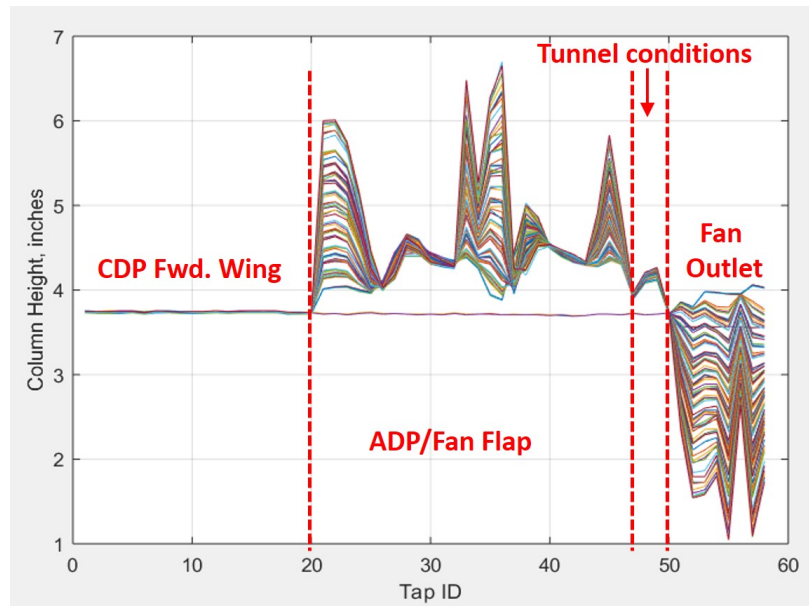


Figure A.10: Typically, data is extracted from between 70 and 100 photos in order to characterize the performance for a given configuration.

A.1.5 Processing the Fluid-Column Height Data

Once the column height data has been extracted from the image, these measurements can be converted into pressure using the length scale references provided in the image as well as the density of the manometer fluid.

Manometer Fluid

Accurate measurement of the density of the manometer fluid is critical for the accuracy of the pressure measurement in this experiment. The manometer fluid is simply a 34.2% aqueous solution of methanol, mixed with water-soluble dye for increased contrast. The density of

the solution was measured to be:

$$\rho_{mf} = \frac{92.886g}{100mL} = 928.86 \frac{kg}{m^3}$$

The low density of this solution, compared to water alone, helps to slightly improve the resolution of the pressure measurements, as the maximum precision of the measurement is ± 1 pixel.

Vertical Scale Reference

A vertical scale reference is included in each of the images. A standard 12 inch scale is attached to the manometer panel as shown in figure A.2. Since neither the camera nor the manometer panel are moved during the experiments and all other image parameters remain constant, the length-scale corresponding to 1 pixel remains constant for that camera-manometer condition. As such, the vertical scale can be used to determine the number of pixels per unit length in the vertical direction, which is used to scale from pixel location indexes to column height measurements, as shown in Fig. A.11.

The scale reference and the manometer tubes lay on vertical planes parallel to, but slightly offset from each other. This offset causes the manometer fluid column to appear to be slightly taller in the image than its true height. This is a systematic error that is directly proportional to the ratio of the distances from each to the focal point of the camera lens. Fortunately, this error can be compensated for by adjusting the scaling factor used to convert pixel position to geometric height. The scaling factor is defined as follows:

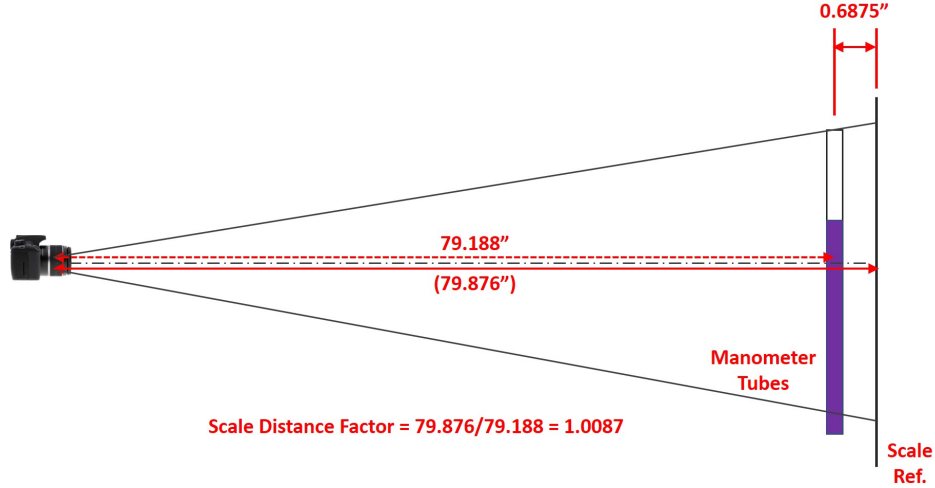


Figure A.11: The scaling factor used to compensate for the planar offset between the scale-reference and the manometer tubes is the ratio between the total distance of each to the camera lens focal point.

$$SDF = \frac{D_{lens-scale}}{D_{lens-tubes}} = \frac{79.876in}{79.188in} = 1.0087 \quad (A.2)$$

This scale factor defined in equation A.2, is used for all experiments. Once the camera was set up, the distances were held constant and remained fixed throughout the experiment.

Zero-Pressure Reference Images

In order to extract pressure measurements from fluid column height data, a set of reference conditions is required. To achieve this, a set of reference photos was taken at static atmospheric conditions. This photo set creates a gauge-reference pressure condition for each tube in the manometer. These photo sets consist of four unique images. These images are processed according to algorithm 3 like all other photos in the series. The zero pressure reference vector is assembled by selecting the median value taken from each fluid column in the series, as shown in Fig. A.12.

IDs	Description
Main Panel	
1-20	FWD Wing Static Pressure Taps
21-34	LWR Flap Static Pressure Taps
35-47	UPR Flap Static Pressure Taps
47	Tunnel Far Field Pitot Tube – Total Pressure
48	Tunnel Far Field Pitot Tube – Static Pressure
49	Tunnel Near Field Pitot Tube – Static Pressure
50	Ambient Pressure Reference – Outside Tunnel
Fan Sub-Panel	
51,53,55,57	Fan Outlet - Outer Radius Total Pressure
52,54,56,58	Fan Outlet – Inner Radius Total Pressure

Figure A.12: Tap ID Reference

$$P_{ref0_i} = median[P_{ref0_{k_0}}] \quad (A.3)$$

Where column index, $i = [1, 2, \dots, 58]$ and $k = all\ zero\ conditions$

The following calculation is performed for all i fluid columns in all k images for a given configuration.

$$P_{k,i} = P_{raw_{k,i}} - P_{ref0_i}, \text{ gauge pressure with ambient reference} \quad (A.4)$$

$$\Delta P_{scr_k} = P_{k,47} - P_{k,50}, \text{ pressure drop across the inlet screen} \quad (A.5)$$

$$P_{gk,i} = -[P_{k,i} - \Delta P_{scr_k} - P_{k,50}], \text{ corrected gauge pressure, far-field tunnel reference} \quad (A.6)$$

This produces a gauge pressure measurement vector for each image in the series relative to the instantaneous total pressure in the tunnel far field. The subtraction of $P_{k,50}$ in the

final gauge pressure calculation corrects the pressure measurements for changes in the height of the fluid reservoir as the test conditions change.

Other Critical Assumptions

Several critical assumptions are required to perform data extraction from manometer images in the manner described in the preceding sections. Some are stated explicitly, while others are implied. This section seeks to clarify these assumptions before proceeding with the evaluation of the uncertainties associated with this method.

- The total pressure in the wind tunnel test section is constant in the stream-wise direction.
- The upstream velocity measurement is sufficiently far upstream to be corrected by the methods discussed later in this work.
- The displacement thickness of the boundary layer at the experimental model is neglected in this experiment.
- Turbulent flow is assumed in all test conditions.
- The relative positions of the camera and manometer are constant during an experimental session, or until the camera is disturbed to remove the SD memory card - upon which the calibration is repeated.
- The lens optics remain at a constant focal length until the camera is manually re-focused - at which time the calibration is repeated.

- Since the tunnel facility used during this experiment was exposed to the outdoors, and since these test were conducted over a period of several months during all weather conditions between during the winter and spring of 2018, air density is computed relative to international standard atmosphere conditions at an altitude of 0m mean sea level (MSL) on a standard day (SSL).

$$P_{atm_{SSL}} = 101,325Pa$$

This assumption will yield a consistent estimate of all velocities and force coefficients c_l , c_d and c_m as the true altitude of the test facility is known and the ambient temperature was recorded during each test condition.

- The density of the manometer fluid is assumed to be independent of temperature and remains constant during the experiment.
- All flows are incompressible, including those inside the manometer panel and connective tubing.

A.1.6 Measurement Uncertainty Analysis

This novel approach to wind tunnel data acquisition has several inherent benefits. First, once the density of the manometer fluid is known, minimal additional calibration is required during usage. The capture of the zero pressure conditions serves to tare the system prior to data acquisition, with the majority of the system variables remaining constant throughout a broad range of operating conditions. Next, a change in height of any fluid column requires

a change in the volume of air and manometer fluid inside the fluid column. The viscous damping associated with these flows serves as a low-pass filter, inherently time-averaging the pressure measurement and reducing signal noise significantly. Lastly, the changes in height of the fluid-columns serves as visual confirmation of changes in operating conditions in real-time providing direct affirmation of the progress of the experiment.

While this is a very visual, inherently time-averaged, and primarily analog process, it is subject to quantization error through the DSLR camera, which functions as an analog to digital converter (ADC), as well as other uncertainties associated with the camera optics and processing algorithms, as shown in Fig. A.13.

Image Warping

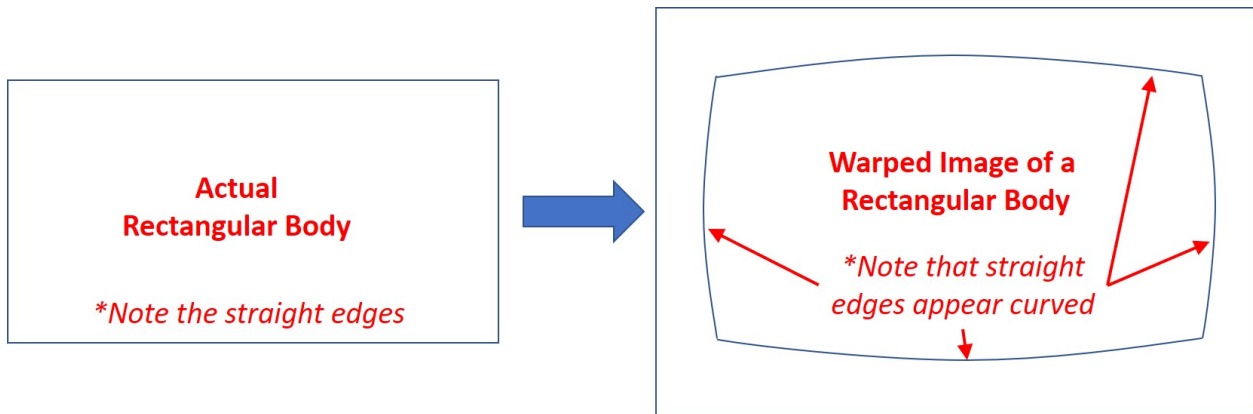


Figure A.13: Depending on the lens optics and the overall FOV of the lens, straight features in an image can appear to be curved or warped, particularly near the edges of the frame.

The warping of an image is essentially the result of rectangular geometries reflected onto the camera sensor through the curved surfaces of the lens optical elements. Though modern lenses compensate for this to varying degrees, depending upon lens design and intended use. (This "fish-eye" is used for artistic effect or very wide FOV). This effect may be present to

some degree in any digital image, and therefore the uncertainty associated with it must be estimated in this experiment.

To determine the degree to which this is present, a long feature that is known to be straight must be present near the edge of the frame. Two control points are taken near the extreme edges of the feature and a line is constructed between them. Then a third point on the image feature is selected, approximately equidistant to the control points. The distance of this third point is calculated to the reference line between the control points to determine the degree of warping in that image, Fig. A.14.

For the purpose of this analysis, the upper edge of the manometer panel is used, as this feature is known to be straight to within 0.010” as it was cut using a CNC router.

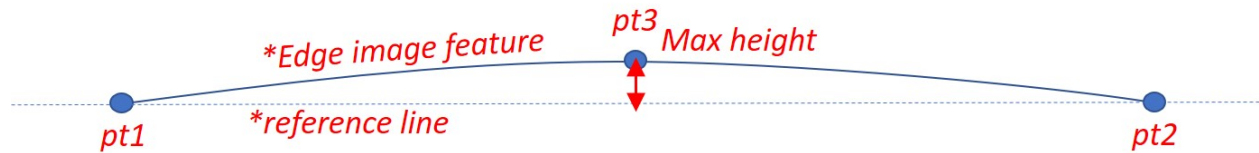


Figure A.14: Method for estimating the uncertainty due to optical image warping

Applying this method to the actual manometer photos yields a maximum optical warp estimate of 1.5 pixels or 0.012” at a distance 12in from the centerline of the frame. For conservatism and given the narrow FOV, this error can be assumed to increase linearly from the center of the frame. Since this is approximately equal to the expected straightness tolerance of the upper edge of the manometer panel, +/-0.001 in/in ” will be used as the uncertainty due to possible image warping.

$$u_w(h) = \pm 0.001 \text{ in/in} \tag{A.7}$$

Though this warping is a systematic error that increases to a maximum of u_w with distance from the optical center of the image, it is accounted for as a symmetric random error affecting the direct measurement of the fluid column height, as shown in Fig. A.15.

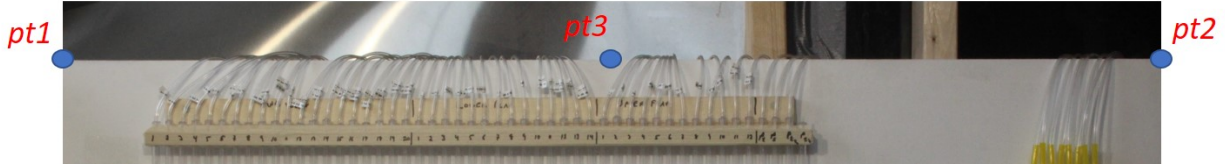


Figure A.15: Method for estimating the uncertainty due to optical image warping applied to actual manometer panel images.

Manometer Fluid Density

Computing the combined standard uncertainty of the measurement of the manometer fluid density provides a simple illustrative example of the process used throughout this section. The general form of the combined uncertainty of a calculated property, density in this case, is given by:

$$u_c(y(x_1, x_2, \dots, x_n)) = \sqrt{\left[\frac{\partial y}{\partial x_1} u_1(x_1)\right]^2 + \left[\frac{\partial y}{\partial x_2} u_2(x_2)\right]^2 + \dots + \left[\frac{\partial y}{\partial x_n} u_n(x_n)\right]^2} \quad (\text{A.8})$$

Where $[x_1, x_2, \dots, x_n]$ are the various measurements required to calculate the desired quantity.

In the simple case of the manometer fluid density,

$$\rho_{mf} = \frac{\text{mass}(g)}{\text{volume}(mL)} \quad (\text{A.9})$$

Therefore,

$$u_{\rho c}(\rho(m, V)) = \sqrt{\left[\frac{\partial \rho_{mf}}{\partial m} u_m\right]^2 + \left[\frac{\partial \rho_{mf}}{\partial V} u_V\right]^2} \quad (\text{A.10})$$

$$\frac{\partial \rho_{mf}}{\partial m} = \frac{1}{V} = \frac{1}{100mL} \quad (\text{A.11})$$

$$\frac{\partial \rho_{mf}}{\partial V} = \frac{m}{V^2} = \frac{92.886g}{(100mL)^2} \quad (\text{A.12})$$

$$u_m = \pm 0.1g, \text{ uncertainty of the mass measurement} \quad (\text{A.13})$$

$$u_V = \pm -0.5mL, \text{ uncertainty of the volume measurement} \quad (\text{A.14})$$

Note that the resulting uncertainty in each case has the consistent units g/mL , which is a unit of density. The resulting combined uncertainty of the fluid density measurement is determined to be

$$u_{\rho c}(\rho(m, V)) = \pm 0.0046 \frac{g}{mL} = \pm 0.495\% \quad (\text{A.15})$$

Pressure Calculation

The calculation of pressure is central to this experimental effort. The uncertainties of all the measurements discussed so far contribute to the total combined standard uncertainty of the pressure measurement taken from each fluid column.

In order to proceed with this analysis, some nominal parameters must be specified to use as a basis for comparison. Based on a review of the data, the following values are

representative of 'typical' cases. At the distances specified, the spatial resolution of the camera is

$$\bar{s} = 125.0 \frac{\text{pixels}}{\text{in}} \quad (\text{A.16})$$

And the reference change in column height is

$$\bar{h} = 2.0 \text{in} = 0.0508 \text{m} \quad (\text{A.17})$$

Now,

$$u_w = 0.001\bar{h} = 0.002 \text{in} \quad (\text{A.18})$$

The maximum image resolution is $\pm 1 \text{ pixel}$. Given the assumed value of $\bar{s} = 125 \text{ppi}$ this gives

$$u_{pix} = \pm 0.008 \text{in} \quad (\text{A.19})$$

The combined uncertainty of the column height measurement is

$$u_h = \sqrt{u_w^2 + u_{pix}^2} = \pm 0.0082 \text{in} \quad (\text{A.20})$$

Then, the total uncertainty of the pressure measurement can be estimated as

$$u_{P_{\rho,h}} = \sqrt{[\bar{h}g u_{\rho c}]^2 + [\rho g u_h]^2} = \pm 2.97 \text{Pa} \quad (\text{A.21})$$

The uncertainty of the measurement of the distance between the manometer panel and the camera is $\pm 0.0625 \text{in}$. Since two measurements were conducted, i.e. from the camera to

the manometer panel and from the camera to the scale-plane

$$u_s = \pm 0.125 \text{ in} \quad (\text{A.22})$$

This results in a scale factor uncertainty, (from Eq. A.2)

$$u_{SDF} = 0.079\% \quad (\text{A.23})$$

This makes another small contribution to the total pressure measurement uncertainty, estimated as

$$P(\bar{h}) \approx 462.89 \pm 0.079\%, \text{ due to the uncertainty in SDF} \quad (\text{A.24})$$

This results in

$$u_{P_{SDF}} = \pm 0.3657 \text{ Pa} \quad (\text{A.25})$$

Therefore the total combined uncertainty in the pressure measurement is

$$u_{P_T} = \sqrt{u_{P_{\rho,h}}^2 + u_{P_{SDF}}^2} = \pm 2.99 \text{ Pa} \quad (\text{A.26})$$

Finally, a coverage factor $k = 2$ is applied to give the expanded uncertainty

$$\boxed{u_{P_{exp}} = \pm 5.99 \text{ Pa}} \quad (\text{A.27})$$

A.2 Power System and Control Data Acquisition

A.2.1 Introduction

This experiment requires that power consumption data is logged concurrently with the pressure data images discussed in section A.1. This is accomplished using a micro-controller based data logging system developed specifically for this experiment. This system is based on the commercially available Arduino Pro-Micro and micro-SD card breakout board, shown in Fig. A.16.

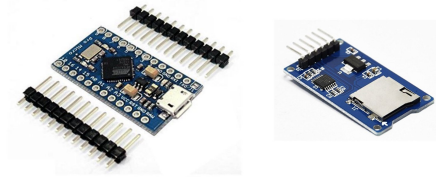


Figure A.16: The Arduino Pro-Micro features both analog and digital I/O pins, as well as USB communication. The micro-SD card breakout board enables direct data logging.

Additionally, the ASC712ELC-30A current sensing module, Fig. A.17, is used for measuring the DC current delivered to one of the motors in the system. This module operates using a 5V VCC input and a 0-5V signal output. The output signal response is $66 \frac{mV}{A}$, with the zero current response equal to $VCC/2$.

These hardware components can be easily integrated with the power supply system for the experiment, and provide a method for concurrently logging the power consumption data for one of the motors in the experiment.

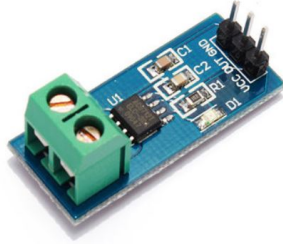


Figure A.17: This module can measure $\pm 30A$ when placed in series with the DC power supply circuit.

A.2.2 Data Logger Design and Integration

The primary objective of the data logging system is to record the electrical power required to operate one of the seven fans in the distributed propulsion system. The underlying assumption here being that since all fans are mechanically and electrically identical, and calibrated to the same input signal, the power demand of a single fan will represent the power demands of each of the fans. This data logger is integrated with the wind tunnel experimental apparatus. Both the electrical and mechanical elements are coupled such that neither system will operate without the other functioning properly.

This system uses the ATmega32u4 5V 16MHz microprocessor. This processor has several convenient features for use in this type of application. First, the 5V operating voltage is common to a large number of peripheral sensors and breakout boards, eliminating the need for logic level voltage converters. Next, the Arduino integrated development environment (IDE) uses primarily standard C++ and JavaScript syntax and program structures with a large number of libraries developed for robotics, communication, and controls tasks. Modification of source code is straightforward, and new libraries are easily constructed. The small form factor allows this processor to be integrated easily into the system using only a solder-less breadboard. Finally, the available analog and digital I/O enable event triggering,

sensor monitoring and data recording without extensive hardware development. The use of a 10-bit analog to digital converter (ADC) provides excellent resolution for voltage measurements on the analog input pins. The 16MHz processor is fast enough for reading and writing high speed digital pulse-width-modulated (PWM) control signals with microsecond resolution. Figure A.18 shows a schematic of this system.

The trigger for the camera shutter release was mechanically combined with the trigger for microprocessor to begin logging data concurrently. The operator triggers both systems simultaneously. The log file is triggered by the rising edge of the digital signal and begins storing a fixed number of data samples over a constant time interval.

Algorithm 4: Simultaneously take a photo and store 50 data samples.

Result: Concurrent Digital Images and Power Log Files

```

40 Initialization, Create a new LOGGER.csv file and prepare SD card for write;
41 index = 0;
42 if statePin == RISING, trigger signal received then
43     Take photo;
44     index++;
45     while  $i \leq 50$  do
46         get all sensor data;
47         dataString = [millis(),volts, amps, PWM, index];
48         logfile.println(dataString);
49         i++
50     end
51 end

```

A.2.3 Power Data Cleanup

The DC power used by the experiment is converted back to variable frequency AC power immediately prior to use in the motor driving each fan. This is accomplished using a series of MOSFET-based micro-inverters which construct an AC trapezoidal wave, varying the

frequency and amplitude of this wave to regulate the speed of the motor. This is accomplished by rapidly switching the MOSFETs from conducting to non-conducting states. This generates high frequency harmonic distortion in the power system which is captured as noise in the power signal measurement. Therefore, the nominal steady state power, for a given condition is given by the mean of the data entries with a particular index, corresponding to the same photo/pressure condition.

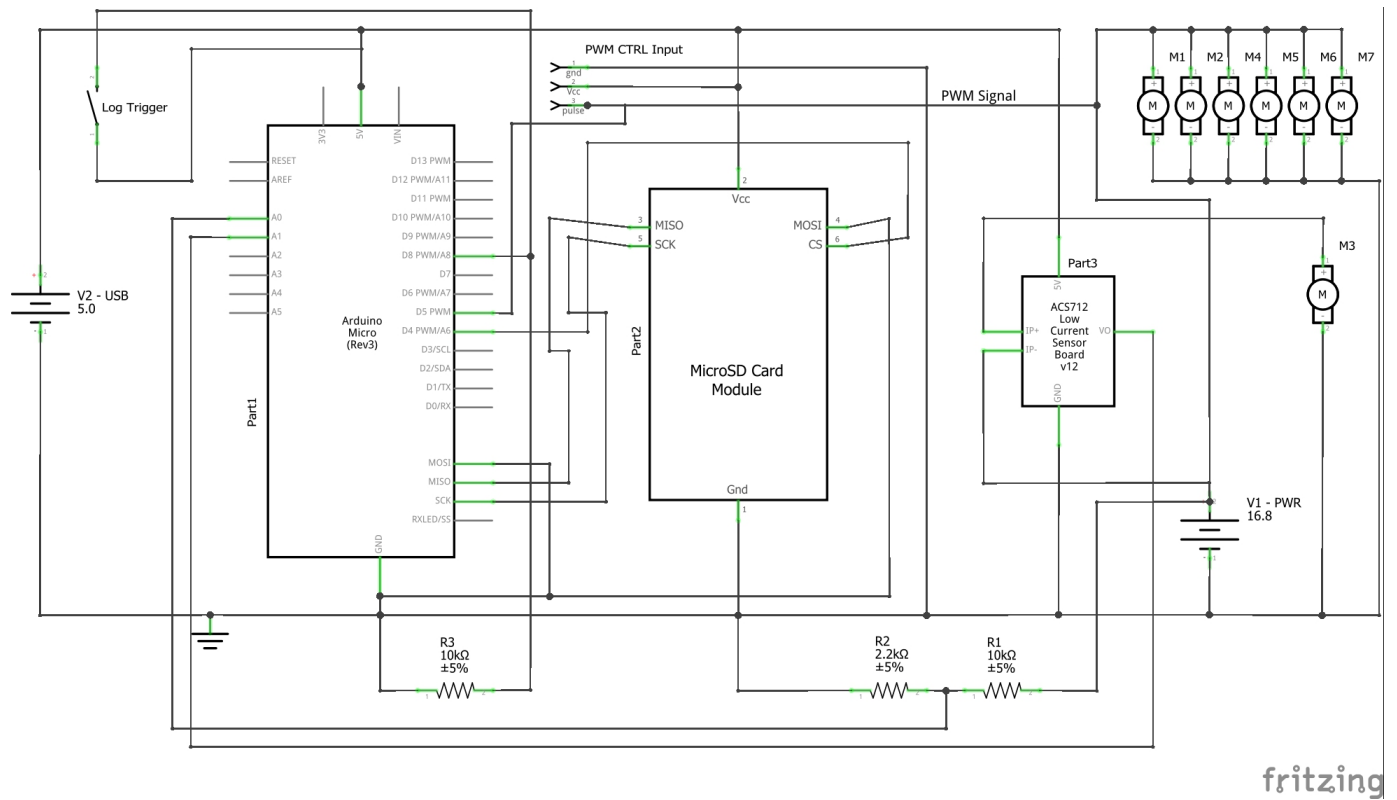


Figure A.18: Schematic representation of the data logging system developed for the wind tunnel experiments.

Given the noise in the power data, shown in Fig A.19, and since the assumption is that the mean of this data is an estimate of the time-averaged power consumption for a given operating condition, a $\gamma = 0.99$ or 99% observed confidence interval is calculated for each of

these conditions. The computed means and associated confidence intervals (CI) are plotted in Fig. A.20.

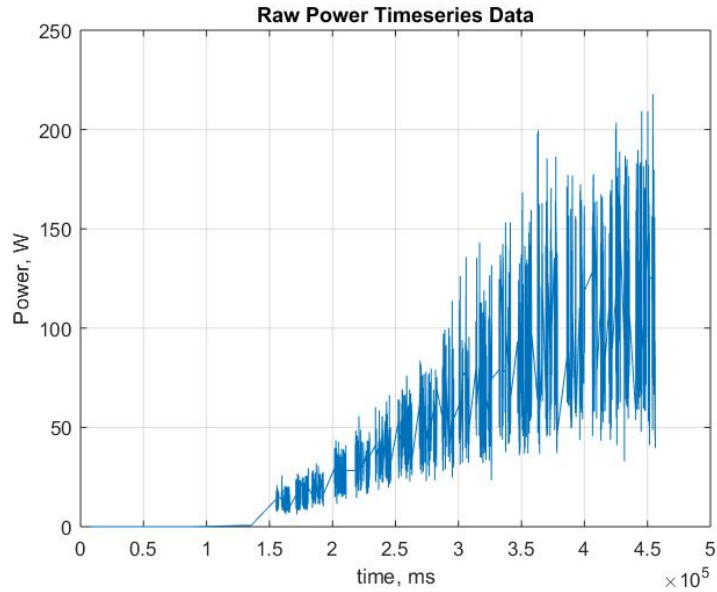


Figure A.19: Considerable signal noise is evident in the unfiltered power signal data.

The following is assumed for power-data samples associated with each j operating conditions for each experimental configuration. Assuming that μ is a random variable sampled from a normal distribution with mean μ , and standard deviation σ .

$$\bar{X}_n = E(\mu) \tag{A.28}$$

Making use of the random variable

$$U = \frac{n^{\frac{1}{2}}(\bar{X}_n - \mu)}{\sigma'} \tag{A.29}$$

We can compute the probability

$$Pr(-c < U < c) \tag{A.30}$$

Which can be expressed involving μ for each j

$$Pr_j(\bar{X}_{n_j} - \frac{c_j \sigma'_j}{n_j^{1/2}} < \mu < \bar{X}_{n_j} + \frac{c_j \sigma'_j}{n_j^{1/2}}) = \gamma = 0.99 \tag{A.31}$$

The semi-span of the 99% CI for these measurements was normalized by the resulting mean power estimate for each j condition recorded. In the case shown here for reference, the boundaries of the interval were $\pm 2.84\%$.

$$\bar{c} = \frac{1}{n} \sum_{j=1}^n \frac{(\frac{c_j \sigma'_j}{n_j^{1/2}})}{Pwr_j} = \pm 2.84\% \tag{A.32}$$

The mean power and 99% CI boundaries are shown in Fig. A.20. These statistics are computed for each of the configurations discussed throughout this research.

A.2.4 Voltage and Current Measurement Uncertainty Analysis

Voltage Measurement

Both the voltage and current measurements in this experiment are relayed to the microprocessor using standard unipolar 0-5V analog signals. This means that the uncertainties of these measurements are due to the finite bit-depth of the ADC as well as the characteristics of the sensors used.

The ATmega32u4 processor uses a 10-bit, 0-5V unipolar analog to digital converter. The resolution of the measurement is the least significant bit (LSB). With a 5V analog reference

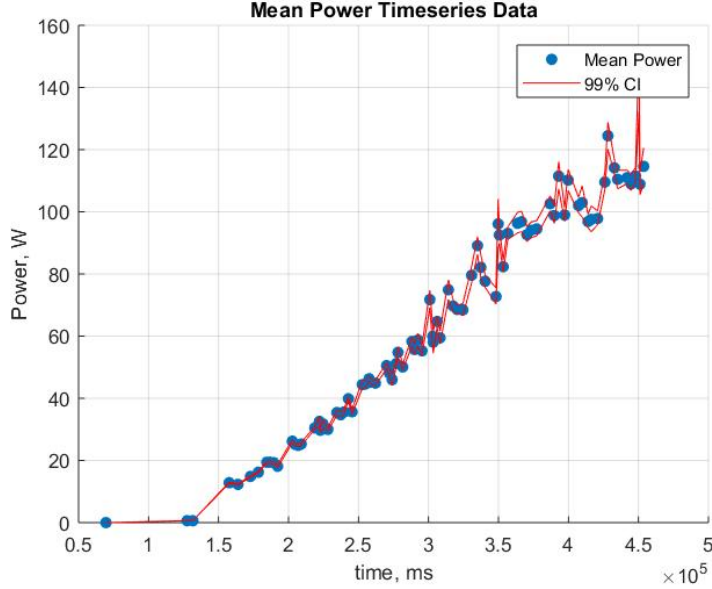


Figure A.20: Signal noise is significantly reduced by simply taking the mean of all samples with a specific record index.

voltage, e.g. $V_{AREF} = 5V$ and a ground reference voltage $V_{SSA} = 0V$, the resolution of the voltage measurement is

$$1LSB = \frac{V_{AREF} - V_{SSA}}{2^n - 1} = \frac{5}{1023} = 4.89mV \approx 0.1\% \text{ of full range} \quad (\text{A.33})$$

The $\sigma = 1$ boundary for this resolution is

$$u_{ADC:\sigma=1} = \frac{4.89mV}{2\sqrt{3}} = \pm 1.41mV \quad (\text{A.34})$$

Here, we will use the $\sigma = 2$ boundary which represents a confidence interval of $\sim 95\%$.

$$u_{ADC:\sigma=2} = \pm 2.82mV = 0.0577\% \text{ of the full } 0\text{-}5V \text{ range} \quad (\text{A.35})$$

A functional block diagram for the ASC712 sensor is provided in Fig. A.21.

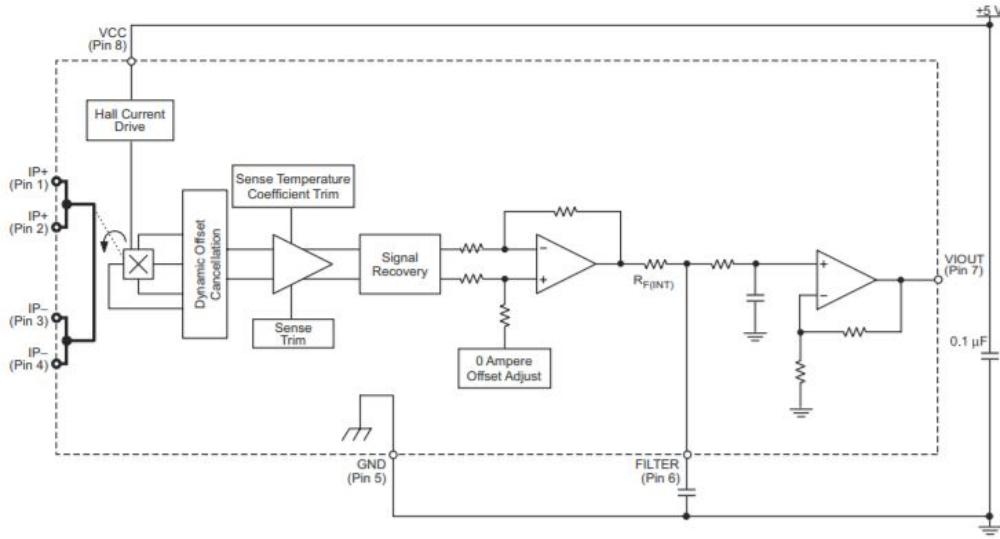


Figure A.21: Functional block diagram of the ASC712-30A sensor chip, [5].

The high voltage powering the experiment must be reduced to a 0-5V analog logic signal in order to be read by the ADC. This accomplished using the simple voltage divider circuit shown in figure A.18. Although the resistors used in this circuit have resistance uncertainties of $\pm 5\%$, the circuit was calibrated using a TekPower 3005T DC power supply. This power supply has a combined voltage output and read-back uncertainty of

$$u_{VD} = u_{PS} \approx \pm 0.1\% \quad (\text{A.36})$$

This calibration uncertainty will be used for the uncertainty of the voltage divider output, since the resistance of this circuit remains constant throughout the experiment.

Current Measurement

Per the manufacturer, the ASC712-30A has maximum total measurement error @25C.

$$u_{cs@25C} = \pm 1.5\% \quad (\text{A.37})$$

Additionally, since the experiments were exposed to changes in ambient temperature, and the temperature of the chip was not explicitly monitored, an additional uncertainty due to the thermal condition of the sensor is required per the manufacturers guidelines

$$u_{csTemp} = \pm 0.75\% \quad (\text{A.38})$$

Therefore, the uncertainty of the current sensor measurement is

$$u_{ACS712} = \pm 1.67\% \quad (\text{A.39})$$

A block diagram representation of this system is provided in Fig. A.22.

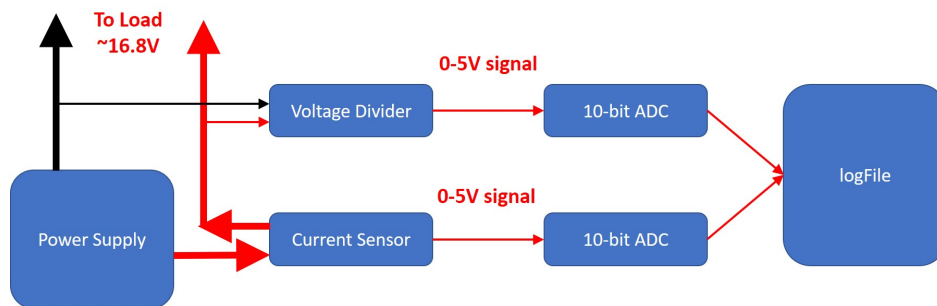


Figure A.22: Flow of information through the power data acquisition system.

Finally, the standard combined uncertainty of the electric power measurements

$$u_{P_{meas}} = \sqrt{u_{VD}^2 + u_{ACS712}^2 + 2u_{ADC:\sigma=1}^2} = \pm 1.67\% \quad (\text{A.40})$$

Given the observed power measurement data and calculated measurement uncertainty, an additional coverage factor $k = 2$ is applied to the power measurement uncertainty calculated in Eq. A.40. The expanded uncertainty then becomes

$$\boxed{u_{P_{wrexp}} = \pm 3.35\%} \quad (\text{A.41})$$

Which contains the 99% CI range \bar{c} described in Eq. A.32.

A.3 Conclusions

The data acquisition system developed for the ADP and CDP wind tunnel experiments is well suited for measuring both the pressure distribution data and electrical power consumption data concurrently. The pressure measurement system is able to precisely measure the time-averaged static pressure distribution around the aerodynamic surfaces of the wind tunnel models. However, it is not capable of resolving time-varying dynamic phenomena due to the viscous damping effects inherent in the design. As a result, each condition measured is considered to be quasi-steady, and therefore sufficient settling time, typically several seconds, must be allowed between each operation condition before measurement begins.

The electrical power data logging system is also well suited for this experiment. This system is capable of storing data at a rate in excess of 400Hz. Given the quasi-steady nature

of the conditions being examined, this system provides an abundance of data from which to compute an estimate of the mean power consumed by the model for a given condition. These statistics are typically computed from approximately 800 samples, or about two seconds of recorded data, taken concurrently with the image of the manometer panel for a given condition.

These systems in tandem, represent precise, accurate, and low cost alternatives to traditional data acquisition systems. This is particularly beneficial for capturing accurate pressure measurements from low-speed aerodynamic models with a highly resolved pressure distribution. Typically, most pressure transducer-based data acquisition systems, such as the system used in the Syracuse University subsonic wind tunnel, have 16 to 32 parallel static pressure channels. With these systems, multiple experimental runs must be completed to record data from all channels in the system. This introduces significant uncertainty in that each condition must be repeated exactly in order capture accurate data in each successive test. In this case, 58 pressure channels were resolved simultaneously, eliminated the need to "change taps" and subsequently collate data from multiple tests, leading to more accurate results.

Appendix B

Wind Tunnel Data Methods of Analysis

B.1 Introduction

The purpose of this chapter is to discuss the methods of analysis used to derive aerodynamic forces and moments from the pressure data collected during the various experiments. Due to the extreme circulation generated about these powered lift systems, the thrust generated, and the size of the models relative to the cross-sectional area of the tunnel, several correction factors are developed and applied. Ultimately, force and moment coefficients are developed from these results for use later in this research effort.

The wind tunnel model used in this experiment spans the entire test section of the wind tunnel in order to eliminate 3-D wingtip effects and promote 2-D aerodynamic behavior to the greatest extent possible. This analysis is predicated on the assumption that the flow

about these models is essentially 2-D, and that 3-D effects - the swirl induced by the fans or jet non-uniformity for example - have negligible contributions to the system behavior, as swirl is typically small for fans with high stagger angle blading.

$$\Delta P = \rho(\Omega R_m)c_\theta \tag{B.1}$$

In these cases, swirl velocity c_θ is small since the tangential blade velocity at the mean radius ΩR_m is large. Additionally, the fans employed in this experiment are fitted with stator vanes having very little curvature.

B.2 System Geometry and Coordinate System Transformations

This analysis pertains to the ADP and CDP propulsion system experiments, as shown in Fig. B.1. These experiments are designed to represent two-dimensional wing sections for each of these systems as they span the entire wind-tunnel test section. Further, these systems are represented by a series of discrete pressure taps and surface elements as shown in Fig. B.2.

There are three distinct reference frames used in this analysis. First there is the inertial reference frame, or the frame of the wind tunnel $[X_{ref}, Y_{ref}]$. It is convenient to transform the model geometry into this frame for computing forces and components.

Next, the forward wing position can vary relative to the wind tunnel $[X_{wing}, Y_{wing}]$ constituting the *wing-frame*. This can rotate relative to the tunnel frame by the angle α . The origin of the wing-frame remains coincident with the origin of the inertial-frame.

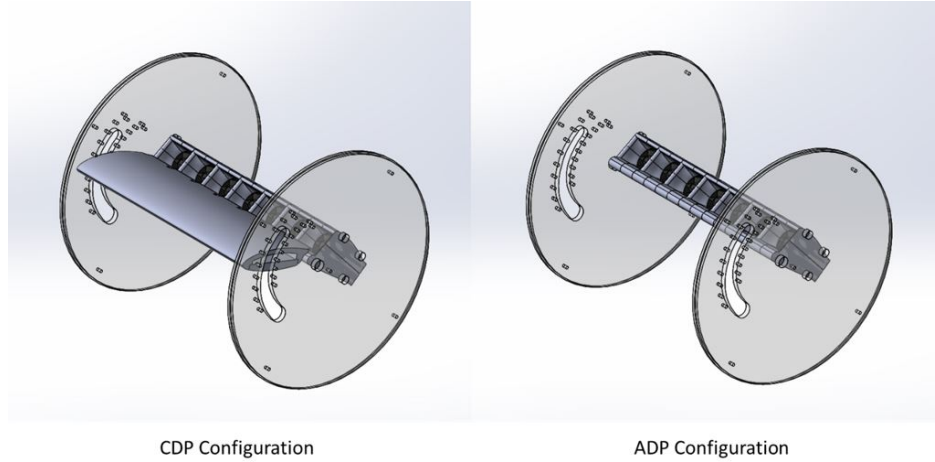


Figure B.1: CDP vs. ADP Experiment Configurations. ADP is a sub assembly of the CDP system.

The third reference frame is the *flap-frame*, $[X_{flap}, Y_{flap}]$. This frame can rotate through angle θ and translate relative to the wing-frame. The flap-frame offsets are specified relative to the origin of the wing-frame. These coordinate systems are summarized in Fig. B.3.

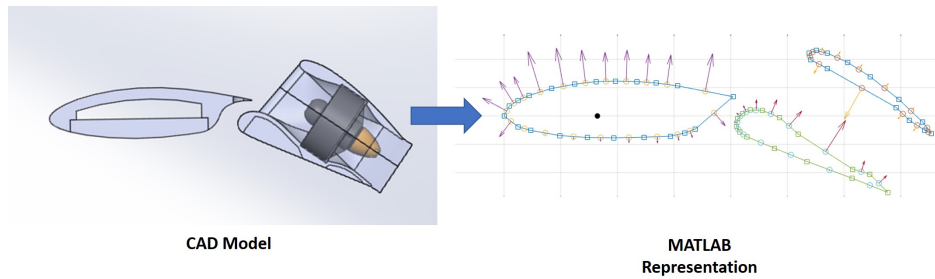


Figure B.2: The wind tunnel models are represented as a series of panels between pressure taps.

$$\begin{aligned}
 \alpha &\equiv \text{rotation angle of the wing-frame} \\
 \theta &\equiv \text{rotation angle of the flap-frame relative to the wing-frame}
 \end{aligned}
 \tag{B.2}$$

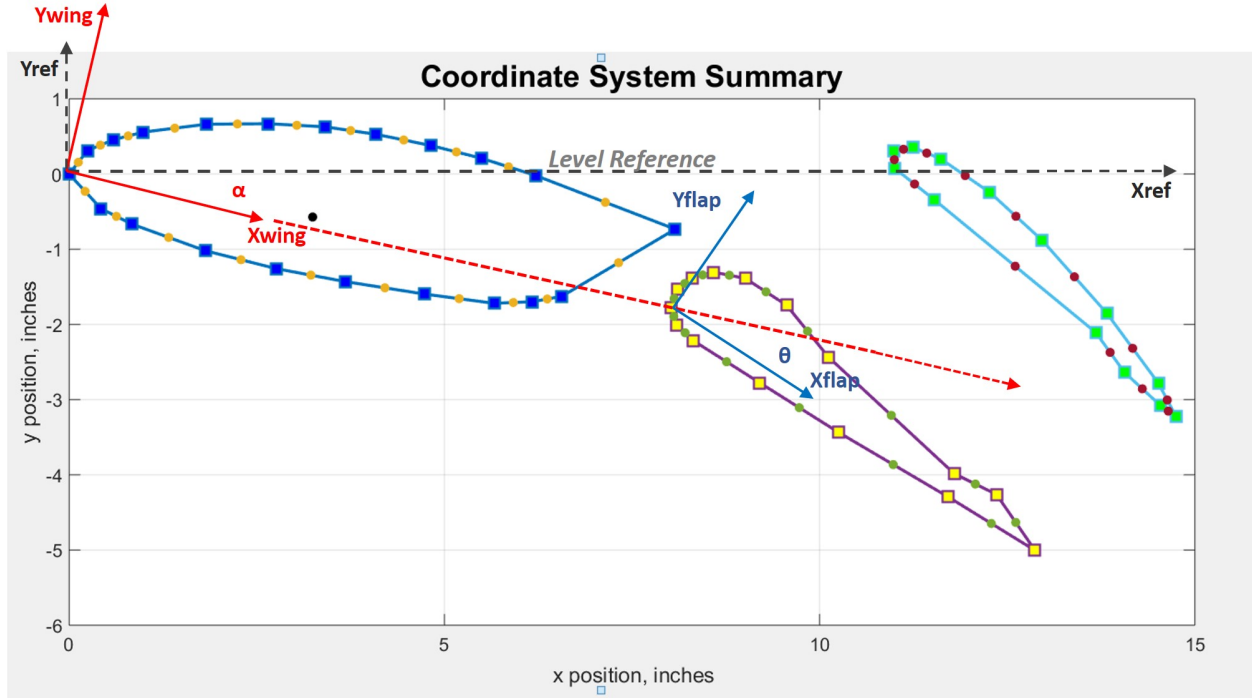


Figure B.3: Coordinate systems for transforming the wing and flap geometries for each model configuration.

$$\mathbf{A} = \begin{bmatrix} \cos(\alpha) & -\sin(\alpha) \\ \sin(\alpha) & \cos(\alpha) \end{bmatrix} \quad (\text{B.3})$$

$$\mathbf{T} = \begin{bmatrix} \cos(\theta) & -\sin(\theta) \\ \sin(\theta) & \cos(\theta) \end{bmatrix} \quad (\text{B.4})$$

In order to construct the numerical representation of the geometry, the flap pressure-tap coordinates, defined relative to the origin of the inertial-frame, are first rotated through angle, θ . Then x and y offsets are applied to position the flap correctly next to the forward wing.

$$\begin{bmatrix} \mathbf{x}_{F_1} \\ \mathbf{y}_{F_1} \end{bmatrix} = \begin{bmatrix} \mathbf{x}_{F_r} \\ \mathbf{y}_{F_r} \end{bmatrix} \mathbf{T} + \begin{bmatrix} \mathbf{x}_{F_{offset}} \\ \mathbf{y}_{F_{offset}} \end{bmatrix} \quad (\text{B.5})$$

Next, the translated flap coordinates $[\mathbf{x}_{F_1}, \mathbf{y}_{F_1}]$, are rotated a second time through angle α to give the final transformed positions of the flap assembly pressure taps in the inertial-frame.

$$\begin{bmatrix} \mathbf{x}_{F_2} \\ \mathbf{y}_{F_2} \end{bmatrix} = \begin{bmatrix} \mathbf{x}_{F_1} \\ \mathbf{y}_{F_1} \end{bmatrix} \mathbf{A} \quad (\text{B.6})$$

The forward wing transformation is a simpler case, as only rotation through angle, α is required.

$$\begin{bmatrix} \mathbf{x}_{W_2} \\ \mathbf{y}_{W_2} \end{bmatrix} = \begin{bmatrix} \mathbf{x}_{W_r} \\ \mathbf{y}_{W_r} \end{bmatrix} \mathbf{A} \quad (\text{B.7})$$

Additionally, in cases involving the ADP configuration, i.e. no forward wing, $[\mathbf{x}_{F_{offset}}, \mathbf{y}_{F_{offset}}] = [0, 0]$ and only rotation through angle α is required.

B.3 Force and Moment Coefficients

Due to the strong coupling between the power input to the embedded propulsion system and the net force on the aerodynamic surfaces for both CDP and ADP configurations, the force coefficients used to typically describe the performance of an aircraft need to be redefined for this effort, in order to place them in the proper context. Typically, lift, drag, thrust, power,

and moment can be effectively decoupled for use in aircraft analysis. Here, that is not the case.

B.3.1 Lift

For conventional aircraft, lift is generated by an airfoil or a finite wing moving through a fluid at some velocity with some angle of attack. Also typically, there is a region where the resulting lift is a linear function of angle of attack. According to thin airfoil theory, for a 2D wing the slope of this linear response, i.e. the lift-curve slope is $\alpha_0 = 2\pi$ *per radian*. Beyond this region, the boundary layer at the surface of the wing can no longer overcome the adverse pressure gradient imposed by the angle of attack along the suction surface, and so the flow separates, causing the wing to stall, as shown in Fig. B.4.

This stall phenomena causes the wing to lose lift beyond a specific range of angle attack. With no camber, this range is typically ± 12 deg. The departure from the linear behavior at low angles attack is due primarily to stall, but can be still be reasonably defined as the force, perpendicular to the free-stream, resulting from the pressure and shear distributions around wing as a function of angle of attack.

Typically, this force is normalized by the dynamic pressure and wing area (or chord length for a 2D wing) to define the lift coefficient. At this point, the lift coefficient is dependent on the angles α and θ , which are considered to be dimensionless.

$$\text{Lift Coefficient, } c_l(\alpha, \theta) \equiv \frac{L(\alpha, \theta)}{1/2\rho V_\infty^2 S} = \frac{L(\alpha, \theta)}{q_\infty S} \quad (\text{B.8})$$

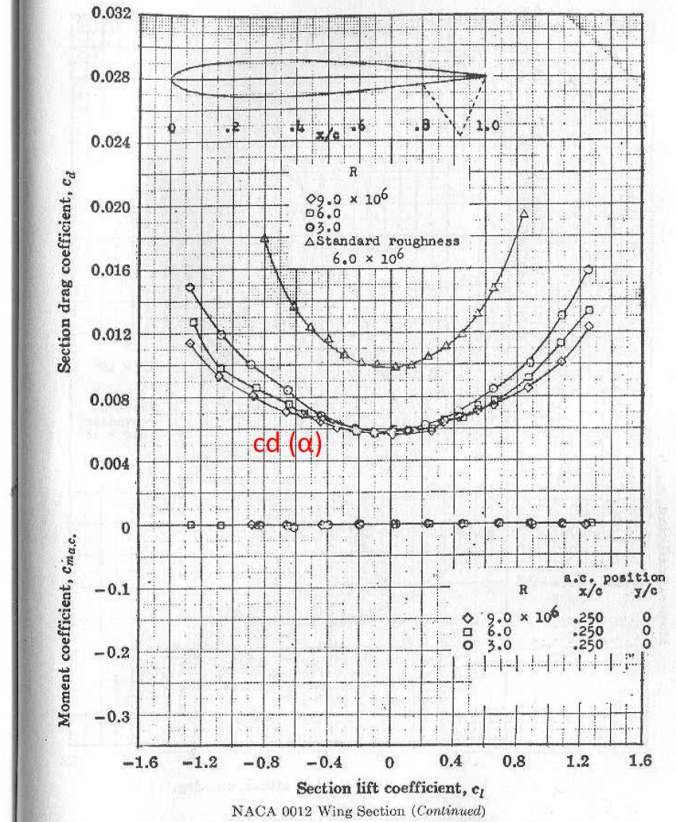
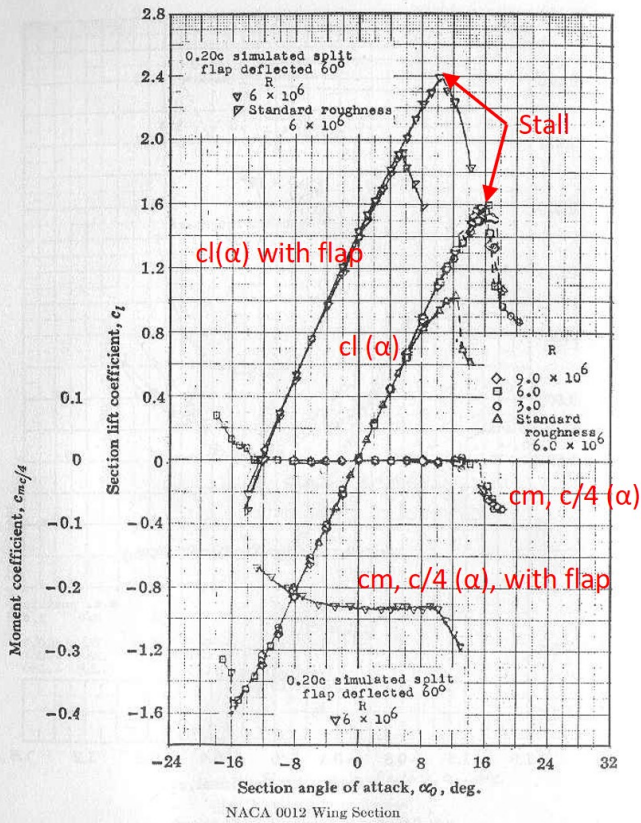


Figure B.4: This figure shows the lift and moment coefficients, c_l and $c_{m_{c/4}}$ as a function of angle of attack, α , as well as the drag coefficient, c_d as a function of c_l . The $c_l(\alpha)$ curves with and without flaps are parallel until very near stall. Note the corresponding change in moment coefficient at stall, both with and without flaps.

The addition of a flap to a conventional wing increased both lift and drag. The maximum lift the wing can produce increases significantly, though effectively, the lift curve slope remains constant in most cases, as the curve is shifted upward for a given angle of attack. Though the useful range of angle of attack may change, the increase in lift is nearly uniform throughout this range.

With the exception of large variations in Reynolds Number, Re , the lift coefficient for a conventional wing with flaps and control surfaces is still predominantly a function of angle of attack alone.

The lift from the CDP and ADP embedded propulsion systems in this research cannot be described in this manner. While there is still clearly a vertical component to the net force on the CDP and ADP systems, it can no longer be thought of as aerodynamic lift as it is typically described. Dimensional analysis of the v-Force component is required to show the correct relationship between the variables in the problem.

$$v\text{-Force}, F_v(\alpha, \theta, c, \rho, V_\infty, \underline{P}) \quad (\text{B.9})$$

In addition to dependence on α and θ , there is also a significant dependence on fan power, \underline{P} , as well as the freestream velocity, V_∞ , density, ρ , and a characteristic length scale, c . Since α and θ are considered to be dimensionless, the dimensional group to be analyzed consists of

$$f(F_v, c, \rho, V_\infty, \underline{P}) \quad (\text{B.10})$$

Choosing $[M]$, $[L]$ and $[T]$ as the fundamental dimensions, two dimensionless quantities are developed. The first of these is

$$\Pi_1 = \frac{F_v}{\rho c^2 V_\infty^2} \quad (\text{B.11})$$

Choosing the characteristic area, c^2 , to be the reference area of the wind tunnel model, which in this 2D case is the model chord, C , multiplied by unit depth, and by introducing

the constant 1/2 in the denominator, this becomes

$$\Pi_1 = \frac{F_v}{1/2\rho V_\infty^2 C} = \frac{F_v}{q_\infty C} \equiv c_v, \text{ } v\text{-Force coefficient} \quad (\text{B.12})$$

The second dimensionless quantity that emerged is

$$\Pi_2 = \frac{P}{\rho V_\infty^3 c^2} \quad (\text{B.13})$$

Then, recasting the power input in terms of pressure rise ΔP_{fan} and volumetric flow rate Q_{fan} by choosing c^2 to be the fan swept area. Assuming that

$$\underline{P} = \underline{P}_{ideal} = \dot{Q}, \text{ the ideal energy flow through the fan} \quad (\text{B.14})$$

The total power input to the system is

$$\underline{P}_{input} = \frac{\dot{Q}}{\eta_{fan-motor}} = \frac{\Delta P_{fan} Q_{fan}}{\eta_{fan-motor}} \quad (\text{B.15})$$

For the purpose of this dimensional analysis, the efficiency of the real fan-motor system will not be considered, rather we will assume that $\eta_{fan-motor} = 1$, as this is dimensionless and will not impact this analysis.

This now becomes

$$\Pi_2 = \frac{\Delta P_{fan} Q_{fan}}{1/2 \rho V_\infty^3 c^2} \quad (\text{B.16})$$

$$= \frac{\Delta P_{fan} Q_{fan}}{1/2 \rho V_\infty^2 c^2 V} \quad (\text{B.17})$$

$$= \frac{\Delta P_{fan} Q_{fan}}{q_\infty Q_{fan}} \quad (\text{B.18})$$

Canceling the volumetric flow rate,

$$\Pi_2 = \frac{P_{totout} - P_{totin}}{q_\infty} \quad (\text{B.19})$$

Using the definition of gauge pressure, $P_{totin} = 0$, and assuming that the fan outlet condition will be reasonably approximated by the arithmetic mean of the stagnation pressure measurements, this becomes

$$\Pi_2 = \frac{\overline{P}_{totout}}{q_\infty} \equiv c_p^* \quad (\text{B.20})$$

Which is the dimensionless parameter presented earlier in Eq. B.83.

Now the vertical force component can be described using α and θ as before, a force coefficient, c_v which is similar to c_l for conventional wings, and the new parameter, c_p^* , which is the dimensionless ratio of the mean stagnation pressure at the fan outlet to the freestream dynamic pressure. This gives the relationship for the more complex CDP system

$$\boxed{c_v(\alpha, \theta, c_p^*)_{CDP}} \quad (\text{B.21})$$

This space, described by three independent dimensionless parameters, shows that CDP system performance must be described in terms of a response volume.

And for the simpler ADP system, the dependence on flap angle, θ , is eliminated.

$$\boxed{c_v(\alpha, c_p^*)_{ADP}} \quad (\text{B.22})$$

A function of two dimensionless parameters, this relationship indicates that the ADP system can be described in terms of a response surface.

B.3.2 Drag

A similar argument can be made for the drag force. For a conventional wing, the force in the streamwise direction is due to both pressure and shear contributions. Again, this can be decoupled from power and thrust for aircraft performance analysis. The conventional u-force is normalized by the freestream dynamic pressure and a reference area, giving the drag coefficient.

$$\text{Drag Coefficient, } c_d \equiv \frac{D}{1/2\rho V_\infty^2 S} = \frac{F_u}{q_\infty S} \quad (\text{B.23})$$

Following the dimensional analysis presented in the previous section, the u-Force component for the present embedded propulsion systems depends again on fan power in addition to the system geometry, fluid density, and free stream velocity.

$$F_u(\alpha, \theta, c, \rho, V_\infty, \underline{P}) \quad (\text{B.24})$$

Again choosing $[M]$, $[L]$ and $[T]$ as the fundamental dimensions, the dimensional analysis yields similar results.

$$\Pi_1 = \frac{F_u}{\rho c^2 V_\infty^2} \quad (\text{B.25})$$

$$\Pi_2 = \frac{P}{\rho V_\infty^3 c^2} \quad (\text{B.26})$$

Similar to the v-Force case,

$$\Pi_1 = \frac{F_u}{1/2\rho V_\infty^2 C} = \frac{F_u}{q_\infty C} \equiv c_u, \text{ v-Force coefficient} \quad (\text{B.27})$$

And,

$$\Pi_2 = \frac{\bar{P}^{totout}}{q_\infty} = c_p^* \quad (\text{B.28})$$

Therefore, the u-force coefficient for the CDP system can be described as a function of α , θ , and c_p^* .

$$\boxed{c_u(\alpha, \theta, c_p^*)_{CDP}} \quad (\text{B.29})$$

And for the ADP system, the dependence on flap angle, θ , is again eliminated.

$$\boxed{c_u(\alpha, c_p^*)_{ADP}} \quad (\text{B.30})$$

B.3.3 Moment

Following this analysis a third time, the moment about a specific pitch axis can be examined. For a conventional wing, the pitching moment is typically described about the quarter-chord position, $c/4$, the location of the aerodynamic center as described by thin airfoil theory. This pitching moment is due to the combined effect of the pressure and shear distribution about the wing for a given operating condition. Typically, this moment is given as a dimensionless moment coefficient

$$c_{m_{c/4}} = \frac{M_z}{q_\infty SC} \quad (\text{B.31})$$

Where C is the mean aerodynamic chord.

For the CDP and ADP embedded propulsion systems, the moment about $c/4$ is due to the combination of pressure, shear and fan thrust contributions. Choosing the same dimensional quantities and fundamental dimensions as in the u-Force, and v-Force cases. Two dimensionless groups are developed.

$$\Pi_1 = \frac{M_z}{\rho c^3 V_\infty^2} = \frac{M_z}{q_\infty C^2} \equiv c_{m_{c/4}} \quad (\text{B.32})$$

$$\Pi_2 = \frac{P}{\rho V_\infty^3 c^2} = c_p^* \quad (\text{B.33})$$

The first of these groups is identical to the conventional moment coefficient by choosing reference area $c^2 = Cx_1$, the model reference area, and the remaining length scale to be the model wing chord. The second, is again equal to the parameter c_p^* .

This again yields the following descriptions of the CDP response volume and ADP response surface respectively.

$$\boxed{c_u(\alpha, \theta, c_p^*)_{CDP}} \quad (\text{B.34})$$

$$\boxed{c_u(\alpha, c_p^*)_{ADP}} \quad (\text{B.35})$$

B.4 Force Calculations

Integrated propulsion systems present considerable challenges for analysis. The net force acting on these systems consist of the contributions from the pressure and shear integrated around the aerodynamic surfaces, as well as surface and fan support force integrated around the control volume drawn around the fan, *see Fig B.9*.

$$F_{total} = F_{aero_{pres}} + \cancel{F_{aero_{shear}}} + \overset{0}{+} F_{fanCV_{Surf}} + F_{fanCV_{Support}} \quad (\text{B.36})$$

Evaluating the first contribution, pressure, is straightforward, as this is well represented in the wind tunnel data. The details of this analysis are developed in the following section, B.4.1. The shear contributions are assumed to be negligible. This assumption is verified by CFD calculations for both ADP and CDP systems across all operating conditions of concern to this effort. Finally, the fan contributions present a particular challenge for analysis given the data available. At best, an estimate of the fan contributions can be developed based on the fan outlet total pressure survey, with nearby static pressure measurements, and checked using the Power Balance Method developed by [cite Sho] as well as CFD analysis. The details of this estimate will be discussed in section B.4.2.

B.4.1 Pressure Force and Moment Contributions

Figures B.5 and B.6 show the static pressure taps distributed along the centerline of the wind tunnel models. Figure B.5 shows the pressure taps on the physical hardware, while figure B.6 shows the locations of each tap on the pressure and suction surfaces of all aerodynamic surfaces.

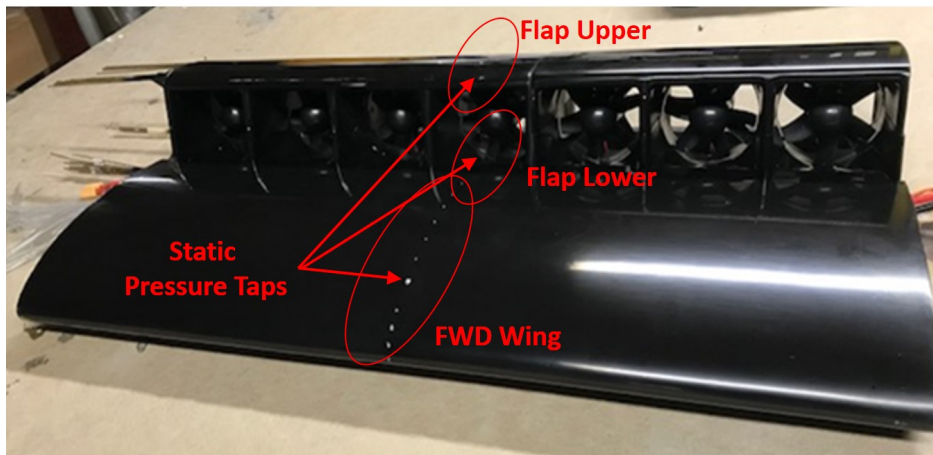


Figure B.5: The wind tunnel model has static pressure taps surrounding nearly the entire perimeter of each aerodynamic surface.

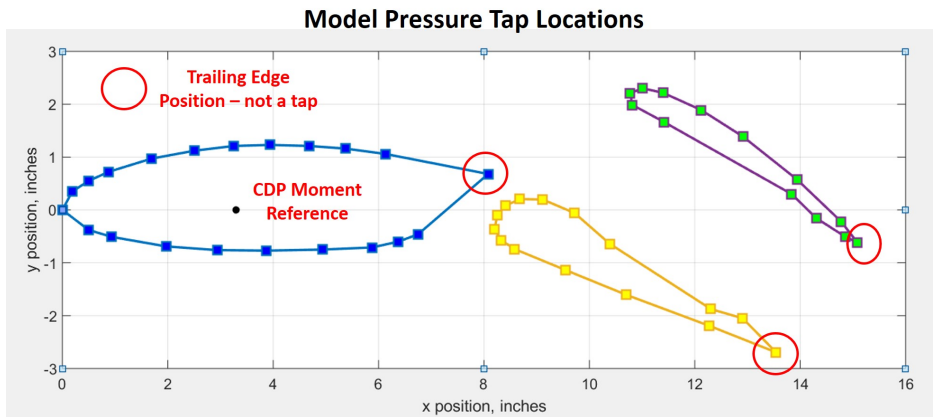


Figure B.6: The wind tunnel models have static pressure taps surrounding nearly the entire perimeter of each aerodynamic surface.

With the addition of the trailing edge coordinates, the pressure distribution about each aerodynamic surface can be estimated. Integrating these pressures around the surface of the model yields the pressure force contribution for each body in the model.

$$\vec{F}_p = L \left\{ - \oint_{wing} P \hat{n} \cdot ds_w - \oint_{lwr} P \hat{n} \cdot ds_l - \oint_{upr} P \hat{n} \cdot ds_u \right\} \quad (\text{B.37})$$

With resulting moments about the inertial Z-axis

$$\vec{M}_{pz} = L \left\{ \oint_{wing} r_w P \hat{n} \cdot ds_w + \oint_{lwr} r_l P \hat{n} \cdot ds_l + \oint_{upr} r_u P \hat{n} \cdot ds_u \right\} \quad (\text{B.38})$$

Where r_w , r_l , and r_u are distances to a moment reference axis. Here, these are distances from the path along each surface to the quarter chord of the assembled wind tunnel model.

The x and y distances between each pressure tap and/or trailing edge is computed for each of the bodies in the system.

$$\Delta x_i = x_{i+1} - x_i \quad (\text{B.39})$$

$$\Delta y_i = y_{i+1} - y_i \quad (\text{B.40})$$

$$\Delta A_i = L \Delta s_i = L \sqrt{\Delta x_i^2 + \Delta y_i^2} \quad (\text{B.41})$$

$$= \sqrt{\Delta x_i^2 + \Delta y_i^2} \quad (\text{B.42})$$

$$\text{for } L = 1; \text{ unit depth} \quad (\text{B.43})$$

Here, the normal vector, \hat{n}_i is computed for the midpoint of the cell formed between adjacent pressure taps, or between the extreme end taps and the trailing edge. Unit depth is assumed for all cases.

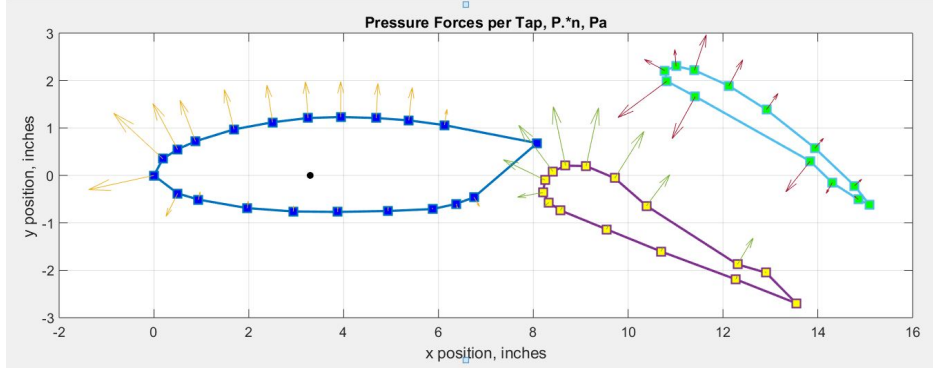


Figure B.7: The static pressure measurements at each tap are shown as an example, arrow length indicates the relative magnitude.

With the approximations given above for a the finite number of taps in the model, the integrals equations B.37 and B.38 above become

$$\vec{F}_p = \vec{F}_{pw} + \vec{F}_{pl} + \vec{F}_{pu} \quad (\text{B.44})$$

$$\vec{F}_p = \sum_{i=1}^{22} P_i \hat{n}_i \Delta A_i + \sum_{j=1}^{16} P_j \hat{n}_j \Delta A_j + \sum_{k=1}^{14} P_k \hat{n}_k \Delta A_k \quad (\text{B.45})$$

$$\vec{M}_{pz} = \vec{M}_{pz_w} + \vec{M}_{pz_l} + \vec{M}_{pz_u} \quad (\text{B.46})$$

$$\vec{M}_{pz} = \sum_{i=1}^{22} r_{w_i} P_i \hat{n}_i \Delta A_i + \sum_{j=1}^{16} r_{l_j} P_j \hat{n}_j \Delta A_j + \sum_{k=1}^{14} r_{u_k} P_k \hat{n}_k \Delta A_k \quad (\text{B.47})$$

These resultant forces are shown in figure B.8 as they are applied to each cell around the perimeter of the wind tunnel models.

For each model configuration, i.e. for all combinations of α and θ , the geometry transformations and normal vector calculations are updated. Therefore, the vertical and horizontal contributions to force in the inertial-frame are estimated directly from the measurement of the pressure distribution around each aerodynamic body.

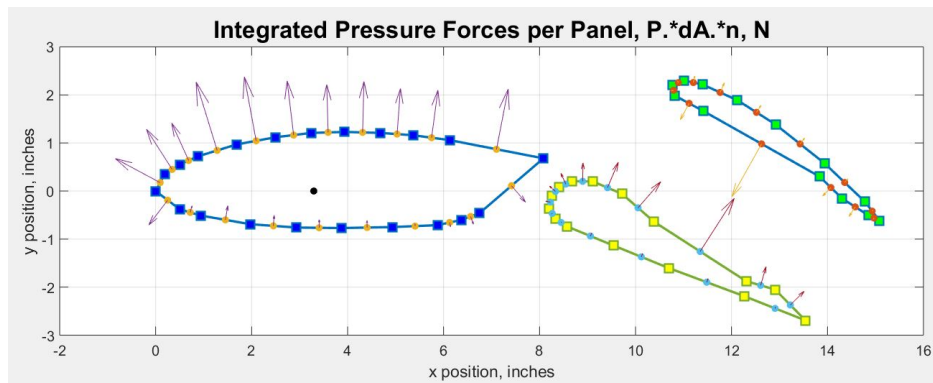


Figure B.8: Resulting forces are applied at the cell-center position, the midpoint between each pressure tap.

The locations of the pressure taps on the surface of the wing intersecting the vertical symmetry plane of the system are given in Tables B.1, B.2, and B.3.

B.4.2 Fan Contributions

The objective of this section is to develop a conservative approximation for the vertical and longitudinal force contributions from the embedded fan. For all cases, it is assumed that the fan force contribution acts along the rotational axis of the fan, though in some cases the fan may be loaded asymmetrically. This asymmetry will not be considered in this analysis as it cannot be reasonably estimated from the experimental data available.

Forward Wing Tap Locations: 1-10		
Tap ID	X(in)	Y(in)
1	6.1250	1.0600
2	5.3750	1.1600
3	4.6875	1.2100
4	3.9375	1.2300
5	3.2500	1.2100
6	2.5000	1.1200
7	1.6875	0.9700
8	0.8750	0.7200
9	0.5000	0.5500
10	0.1875	0.3500

Forward Wing Tap Locations: 11-20		
Tap ID	X(in)	Y(in)
11	0	0
12	0.5000	-0.3800
13	0.9375	-0.5100
14	1.9688	-0.6900
15	2.9375	-0.7600
16	3.8750	-0.7700
17	4.9375	-0.7500
18	5.8750	-0.7100
19	6.3750	-0.6000
20	6.7500	-0.4600

Table B.1: Forward wing pressure tap locations, given in the forward wing reference frame.

Lower Flap Tap Locations: 1-7			Lower Flap Tap Locations: 8-14		
Tap ID	X(in)	Y(in)	Tap ID	X(in)	Y(in)
1	2.1200	0.6000	8	0.3000	-0.3700
2	1.2500	0.7700	9	0.6000	-0.3900
3	0.6000	0.6900	10	1.6400	-0.2500
4	0.2200	0.4800	11	2.8700	-0.0800
5	0.0500	0.2400	12	4.5300	0.2000
6	0	0	13	5.0100	0.6400
7	0.0900	-0.2500	14	4.4000	0.4900

Table B.2: Upper flap pressure tap locations, given in the flap reference frame

Upper Flap Tap Locations: 1-6			Upper Flap Tap Locations: 7-12		
Tap ID	X(in)	Y(in)	Tap ID	X(in)	Y(in)
1	1.8600	3.1100	7	3.3000	3.6200
2	1.1800	3.0900	8	4.5900	3.4300
3	1.0300	3.2600	9	5.7100	3.1600
4	1.1900	3.4600	10	5.9200	2.9500
5	1.5700	3.5800	11	5.2700	2.9800
6	2.3600	3.6600	12	4.6400	3.1400

Table B.3: Lower flap pressure tap locations, given in the flap reference frame

For this estimate to proceed, the force contributions from the surface forces on the control volume must be decoupled from the momentum flux contribution for a given fan operating condition. Conservation of u and $v - momentum$ will be applied to the stream tube passing through fan #3, with the assumption that this is reflective of all embedded fans for a given condition. The resulting forces are reflected in the pressure distribution measured around the fan and estimated for the momentum flux through the control volume. To check this estimate, a power balance estimate is computed for the system based on the measured electrical power consumption and total jet energy flux.

Developing a Thrust Estimate

Accounting for the force contributions from the fan is particularly challenging in this case for two primary reasons: First, while integrating the propulsion system into the lifting surfaces in this configuration provides numerous benefits in cruise, including wake-filling and boundary layer ingestion, decoupling the propulsion system from the airframe for analysis becomes quite problematic using conventional means [47]. This is exaggerated in this case, where the fan aggressively augments circulatory lift while producing significant thrust along its own axis of rotation. Second, with the large circulations present in this system, the flow through

the fans is highly three-dimensional. This requires that the fan outlet is mapped in both radial and circumferential directions, particularly with large flap deflection angles, θ .

The control volume used in this analysis is shown in Fig. B.9.

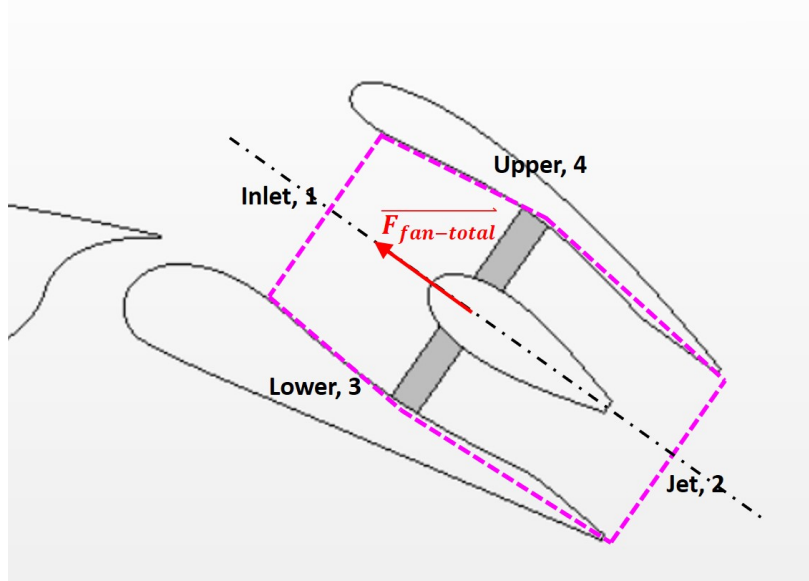


Figure B.9: In order to develop a fan thrust estimate, a control volume is drawn around fan #3, and is assumed to be representative of all fans in the experiment. For all cases, it is assumed that the total fan force contribution acts along the fan’s axis of rotation.

In this experiment, all flows are considered to be incompressible. For this analysis, the fan thrust will have significant components in both the stream-wise, u and perpendicular, v directions. Of primary concern is the contribution of the fan to the net force acting on the ADP and CDP systems. Therefore, both x and y -momentum components must be considered.

First, the continuity equation is applied to the control volume.

$$\frac{dM}{dt} = \frac{\partial}{\partial t} \int_{CV} \rho dV + \int_{CS} \rho \vec{V} \cdot d\vec{A} \quad (\text{B.48})$$

$$\int_{CS} \rho \vec{V} \cdot d\vec{A} = 0 \quad (\text{B.49})$$

The inlet, ①, and jet outlet, ②, are boundaries drawn through the fluid, whereas the upper, ③ and lower, ④ boundaries are drawn along the inner walls of the fan duct. Since the walls are impermeable, there is no mass flux through these boundaries.

$$0 = \rho \vec{V}_2 \cdot \vec{A}_2 - \rho \vec{V}_1 \cdot \vec{A}_1 + \cancel{\rho \vec{V}_4 \cdot \vec{A}_4} - \cancel{\rho \vec{V}_3 \cdot \vec{A}_3} \quad (\text{B.50})$$

$$\rho \vec{V}_2 \cdot \vec{A}_2 = \rho \vec{V}_1 \cdot \vec{A}_1 \quad (\text{B.51})$$

$$\dot{m}_2 = \dot{m}_1 = \dot{m} \quad (\text{B.52})$$

Next, conservation of momentum is applied to this control volume. The net force on this volume is the sum of forces acting on the control volume.

$$\vec{F} = \int_{CV} \vec{V} (\rho \vec{V} \cdot d\vec{A}) \quad (\text{B.53})$$

$$\vec{F} = \vec{F}_S + \vec{F}_{Support} \quad (\text{B.54})$$

Where the surface forces,

$$\vec{F}_S = \int_{CS} -pd\vec{A} \quad (\text{B.55})$$

When applied to this control volume, this gives

$$\sum \vec{F} = (\vec{F}_{S_2} + \vec{F}_{Support_2}) - (\vec{F}_{S_1} + \vec{F}_{Support_1}) + (\vec{F}_{S_4} + \cancel{\vec{F}_{Support_4}}) - (\vec{F}_{S_3} + \cancel{\vec{F}_{Support_3}}) \quad (\text{B.56})$$

Since ③ and ④ are impermeable walls, there can be no momentum flux through these boundaries, and therefore the associated body force terms vanish.

The surface force \vec{F}_S terms at ③ and ④ are the pressure forces on the upper and lower boundaries of the control volume, though these terms nearly cancel each other in most cases, they are included here to ensure a complete representation. Applying the continuity relation developed from Eq. B.49, this is then reduced to

$$\sum \vec{F} = (\vec{F}_{S_2} + \vec{F}_{Support_2}) - (\vec{F}_{S_1} + \vec{F}_{Support_1}) + \vec{F}_{S_4} - \vec{F}_{S_3} \quad (\text{B.57})$$

$$\sum \vec{F} = [p_2 \vec{A}_2 - p_1 \vec{A}_1] + \left[\int_4 p_4 d\vec{A}_4 - \int_3 p_3 d\vec{A}_3 \right] + \int_{CS} \vec{V} \rho \vec{V} \cdot dA \quad (\text{B.58})$$

$$\boxed{\sum \vec{F} = [p_2 \vec{A}_2 - p_1 \vec{A}_1] + \left[\int_4 p_4 d\vec{A}_4 - \int_3 p_3 d\vec{A}_3 \right] + \dot{m}(\vec{V}_2 - \vec{V}_1)} \quad (\text{B.59})$$

Given the definition of the control volume show in figure B.9, both the pressure and momentum contributions to the net force on the fan must be considered.

The stream-tube passing through the fan can be visualized using a CFD case, here CDP at $\alpha = 0$ deg and $\theta = 30$ deg, as shown in Fig. B.10.

As can be seen from figure B.10, the stream-tube is distorted dramatically in the near-field by the embedded propulsion system and forward wing. However, by approximately 8-12 chords upstream the flow conditions are consistent with the far-field assumptions of $u = V_\infty$ and $v = 0$.

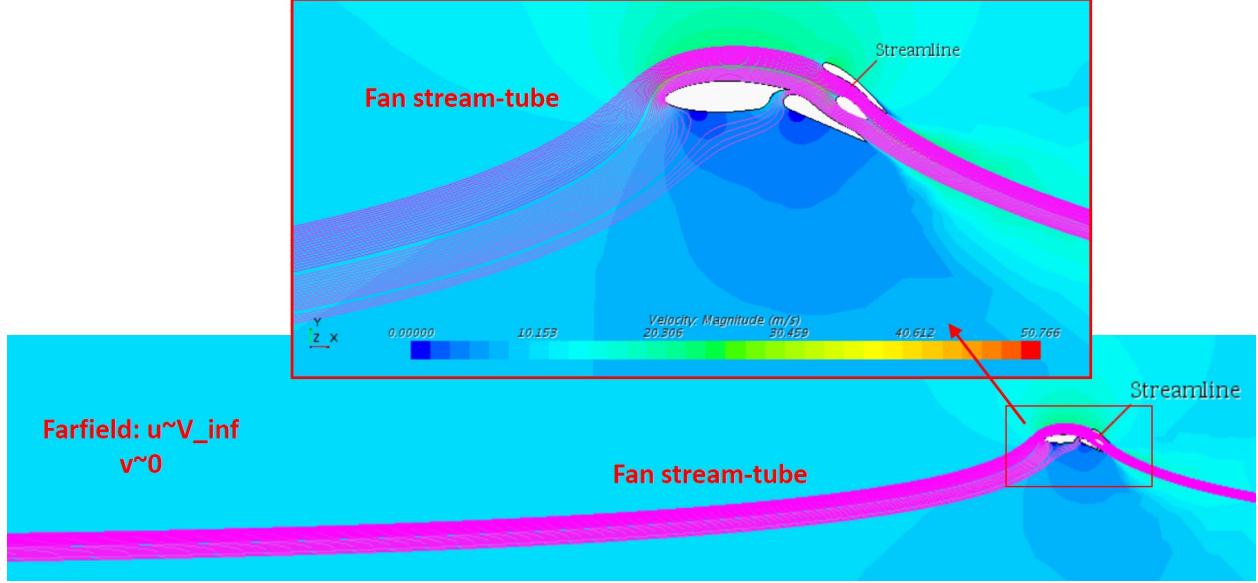


Figure B.10: URANS CDF results, CDP configuration with moderate flap deflection, showing the instantaneous stream-tube passing through the fan.

At the measurement plane, the flow is assumed to be aligned with the duct. In the inertial frame, the fan thrust angle is

$$\Phi_{fan} = \alpha + \theta + \beta \quad (\text{B.60})$$

Where $\beta = 4.85 \text{ deg} = \text{const}$. The resultant force from the fan is assumed to be parallel to the fan axis as shown in figure B.11.

The result given in Eq. B.59 is further decomposed into u and v components in order to calculate the fan contributions to the net forces acting in each direction.

$$F_x = \cos(\Phi) \left[[p_1 \vec{A}_1 - p_2 \vec{A}_2] + \left[\int_4 p_4 d\vec{A}_4 - \int_3 p_3 d\vec{A}_3 \right] + \dot{m}(\vec{V}_2 - \vec{V}_1) \right] \quad (\text{B.61})$$

$$F_y = \sin(\Phi) \left[[p_1 \vec{A}_1 - p_2 \vec{A}_2] + \left[\int_4 p_4 d\vec{A}_4 - \int_3 p_3 d\vec{A}_3 \right] + \dot{m}(\vec{V}_2 - \vec{V}_1) \right] \quad (\text{B.62})$$

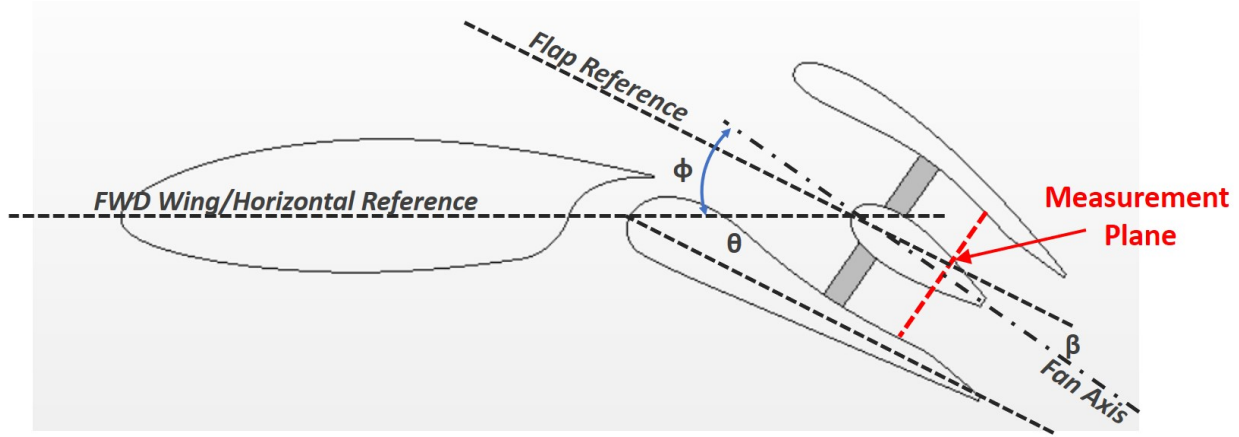


Figure B.11: For both the CDP and ADP configurations, the fan axis is offset from the flap reference by angle $\beta = 4.85$ deg.

Finally, conservation of energy can be applied to this control volume.

$$\dot{Q} - \dot{W}_s - \dot{W}_{shear} - \dot{W}_{other} = \frac{\partial}{\partial t} \int_{CV} e \rho dV + \int_{CS} (e + pv) \rho \vec{V} \cdot d\vec{A} \quad (\text{B.63})$$

Again, assuming steady-flow, and also considering that shear is negligible, and only the fan is operating in the control volume, this becomes.

$$\overset{0}{\cancel{\dot{Q}}} - \dot{W}_s - \overset{0}{\cancel{\dot{W}_{shear}}} - \overset{0}{\cancel{\dot{W}_{other}}} = \frac{\partial}{\partial t} \int_{CV} e \rho dV + \int_{CS} (e + pv) \rho \vec{V} \cdot d\vec{A} \quad (\text{B.64})$$

$$\dot{W}_s = \int_{CS} (e + pv) \rho \vec{V} \cdot d\vec{A} \quad (\text{B.65})$$

where total energy

$$e = u + \frac{V^2}{2} + gz \quad (\text{B.66})$$

is the sum of internal energy, kinetic energy, and potential energy. Then Eq. B.65 becomes

$$\dot{W}_s = \cancel{\dot{m}(u_2 - u_1)} + \dot{m} \left(\frac{p_2 - p_1}{\rho} \right) + \cancel{\dot{m}g(z_2 - z_1)} + \int_{A_2} \frac{\vec{V}_2^2}{2} \rho \vec{V}_2 \cdot d\vec{A}_2 - \int_{A_1} \frac{\vec{V}_1^2}{2} \rho \vec{V}_1 \cdot d\vec{A}_1 \quad (\text{B.67})$$

Since the flow is adiabatic and there is no significant change in gravitational potential energy across the control volume, those terms can be eliminated.

The remaining terms are due to the pressure rise from the inlet ① to outlet ② and the rate of production of kinetic energy within the control volume.

$$\dot{W}_s = \dot{m} \left(\frac{p_2 - p_1}{\rho} \right) + \int_{A_2} \frac{\vec{V}_2^2}{2} \rho \vec{V}_2 \cdot d\vec{A}_2 - \int_{A_1} \frac{\vec{V}_1^2}{2} \rho \vec{V}_1 \cdot d\vec{A}_1 \quad (\text{B.68})$$

$$\dot{W}_s = \dot{m} \left(\frac{p_2 - p_1}{\rho} \right) + \left[\frac{V_2^2}{2} \rho V_2 dA_2 \hat{e}_2 - \frac{V_1^2}{2} \rho V_1 dA_1 \hat{e}_1 \right] \quad (\text{B.69})$$

Where \hat{e}_1 and \hat{e}_2 are the unit vectors normal to ① and ②.

$$\dot{W}_s = \dot{m} \left(\frac{p_2 - p_1}{\rho} \right) + \dot{m} \left[\frac{1}{2} (V_2^2 - V_1^2) \right] \quad (\text{B.70})$$

Since the control volume is drawn such that inlet ① is parallel to outlet ② and the inlet and outlet flows are assumed to be normal to the boundaries, and since $\dot{m}_2 = \dot{m}_1 = \dot{m}$, the ideal fan power consumption is

$$\boxed{\dot{W}_s = \dot{m} \left[\left(\frac{p_2 - p_1}{\rho} \right) + \frac{1}{2} (V_2^2 - V_1^2) \right]} \quad (\text{B.71})$$

B.4.3 Estimating Critical Variables

In order to compute both the surface and body force contributions on the fan control volume, Fig. B.9 and Eqs. B.59 and B.71, estimates must be developed for several critical variables. From Eqs. B.59 and B.71, we can see that V_1, V_2, A_1, A_2, p_1 and p_2 are required in order to calculate the thrust and ideal power consumption for each fan. Some of these quantities can be calculated directly from the experimental data, while others must be estimated indirectly.

We can begin by making the following basic assumptions about the problem

- Steady flow \rightarrow the motor power and manometer levels are allowed to stabilize for each new measurement condition.
- Incompressible flow $\rightarrow V_\infty \approx 10m/s$ and $M_{blade-tip} \leq 0.25$
- Uniform static pressure at the inlet ①
- Gauge pressure reference, $p_{1_{tot}} = 0Pa_{gauge} \rightarrow p_{1_{static}} = -p_{1_{dyn}} = -\frac{\rho V_1^2}{2}$

Estimating V_2

There are eight total pressure probes positioned in the outlet of fan #3. Assuming, that the operation of each fan is well represented by a single fan, the outlet velocity profile, \vec{V}_2 , for each fan can be calculated directly from the experimental data.

Since the fan duct cross-section transitions from rectangular to round and back to rectangular, at the plane of the total pressure probes it is assumed to be nominally round. The annular flow area is divided into eight sub-annular regions with four regions comprising an

inner and outer annulus as shown in figure B.12. The total flow area on the measurement plane is

$$A_{Total} = A_{Outer} + A_{Inner} = A_{Inner} \sum_{i=1}^4 w_{Inner,i} + A_{outer} \sum_{i=1}^4 w_{Outer,i} \quad (\text{B.72})$$

Where weight vectors $\hat{\mathbf{w}}_{Inner,i}$ and $\hat{\mathbf{w}}_{Outer,i}$ contain the proportion of the inner or outer annulus where the mean velocity is determined by the probe measurement in that region.

$$\sum_{i=1}^4 w_{Inner,i} = \sum_{i=1}^4 w_{Outer,i} = 1 \quad (\text{B.73})$$

For each probe location, the calculated velocity is assumed to be the mass-averaged velocity for that region. The mean velocity in each region is determined in a manner similar to a typical pitot-static velocity measurement. The total pressures are measured in each location, the static pressure is estimated using nearby wall-tap measurements, and the dynamic pressure is calculated as

$$P_{dyn} = P_{total} - P_{static} \quad (\text{B.74})$$

The local velocity is computed from the dynamic pressure

$$P_{dyn} = \frac{1}{2} \rho V_{local}^2 \quad (\text{B.75})$$

$$V_{local} = \sqrt{\frac{2P_{dyn}}{\rho}} \quad (\text{B.76})$$

Where this method diverges from the typical measurement and becomes an approximation is the static pressure reference used in this calculation is not measured at each total

pressure location. Rather, a representative static pressure is taken from the maximum of the wall static ports downstream of the fan and adjacent to the total-pressure measurements.

$$P_{static_{est}} \equiv \max[\mathbf{P}_{adj}] \quad (\text{B.77})$$

The locations of these pressure measurements are shown in figure B.13. The justification for why the maximum pressure is selected instead of the mean is two-fold. First, the wall geometry where these taps are located is not flat. The surfaces of both the upper and lower surfaces of the duct interior is curved, alternating from concave to convex in the stream-wise direction. If the flow remains attached to the wall, this curvature will induce a transverse pressure gradient according to Euler's n -component equation.

$$\frac{\partial p}{\partial r} = \frac{\rho V^2}{r} \quad (\text{B.78})$$

Since static pressure increases in the direction of increasing radius of curvature, pressure taps on the concave wall regions will have locally higher static pressure. These higher static pressure estimates will yield comparable lower, i.e. more conservative, velocity estimates than their counterparts on convex surfaces.

Second, the velocity calculation is predicated on the assumption that the flow is attached in the region of the static pressure measurements. From the CFD analysis, this is not always the case, particularly at high angles of attack or large flap deflections. In this case, the assumption needs to be made that the flow is attached to *at least* the upper or lower duct surface, which CFD analysis shows is typically valid. Regions where the flow is separated

will have static pressures that are not representative of the flow in the fan jet. Typically, this will include both taps on either the upper or lower wall, skewing the average of all four taps and any subsequent velocity calculation.

With the static pressure measurements taken at the outlet of a single fan, as shown in Fig. B.12, the velocity and mass flow rate through each area element can be computed.

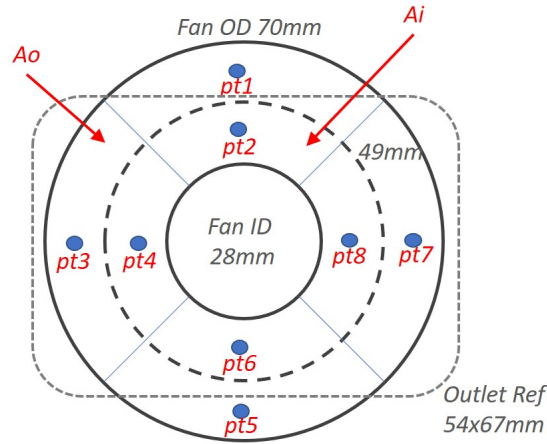


Figure B.12: Fan #3 is instrumented with eight total pressure taps positioned in the fan outlet on the measurement plane.

$$P_{dyn_i} = P_{total_i} - P_{static_{est}} \quad (B.79)$$

where P_{total_i} is the measurement at each tap location.

$$V_i = \sqrt{\frac{2P_{dyn_i}}{\rho}} \quad (B.80)$$

$$\dot{m}_i = \rho A_i V_i \quad (B.81)$$

$$\dot{m}_T = \sum_{i=1}^8 \dot{m}_i \quad (B.82)$$

At this point it is convenient to use the new dimensionless parameter from Eq. B.20, c_p^* .

$$c_p^* \equiv \frac{P_{T_{local}}}{1/2\rho V_\infty^2} \quad (\text{B.83})$$

This parameter is a ratio between the local total pressure and the free-stream dynamic pressure. This parameter is useful primarily because it is always finite for non-zero tunnel velocity and it allows different operating conditions and configurations to be compared by dynamic similarity.

In these experiments, recirculating regions are common inside the fan duct, especially at high angles of attack. As such, a logical test must be developed in order to identify possible recirculating regions and treat them appropriately. There are three cases to consider.

Case 1 Under ideal conditions with the fan running at moderate to high power settings and mid-range angles of attack, each of the eight pressure taps would give a positive dynamic pressure reading and a positive c_p^* when this estimation method is applied. The fan outlet is relatively uniform under these conditions, and no re-circulations are present.

Case 2 With the fans operating at very low power or turned off, many of the pressure taps will have a very small, often irregular dynamic pressure measurement and negative c_p^* for most pressure taps. The logical test used for this case is, if $n_{taps} \geq 4$ where $c_p^* < 0$.

Case 3 When the fan is operating at high power, extreme angles of attack, or both, separated and recirculating regions are regularly seen in the fan duct during CFD analysis. Here,

most of the pressure taps would provide a positive reading for both c_p^* and dynamic pressure, though some are negative. The logical test used for this case is, if $n_{taps} \leq 3$ where $c_p^* < 0$.

An algorithm is required in order to recognize and deal with each of these cases in the data. Where regions of the flow in the fan duct are recirculating, the flow through that area is essentially blocked, and therefore cannot contribute to the net thrust of the system. Instead, these regions restrict the flow, causing the mass flow to move through a smaller area, causing additional losses in the process.

Algorithm 5: Remove recirculating regions from thrust and power estimates

Result: Identify and eliminate recirculating regions from the thrust and power estimates

```

52 Compute  $P_{dyn}$ ;
53 Compute  $c_p^*$ ;
54 testRec = (find( $P_{dyn} < 0$ ));
55 testRec2 = (find( $c_p^* < 0$ ));
56 testRec = union(testRec,testRec2);
57 rec=0;
58 if length(testRec) ≤ 3, identified recirculating region(s) then
59   |  $\dot{m}_i$ (testRec,i)=0;
60   |  $A_i$ (testRec,i)=0;
61   | rec++, track number of rec's;
62 end
63 Compute forces and powers based on the new  $\dot{m}_i$  and  $A_i$ 

```

If three or fewer of the total pressure probes in the fan outlet are showing negative P_{dyn} or c_p^* , there are likely recirculating regions that are blocking the flow through some portion of the fan. However if four, i.e. half or more, of these taps show negative P_{dyn} or c_p^* , then the fan is simply off and "windmilling" or is operating at a very low power setting. This pressure taps associated classification results are shown in Figs. B.13 and B.14 respectively.

An example showing the results of this estimation strategy is shown in Fig. B.15.

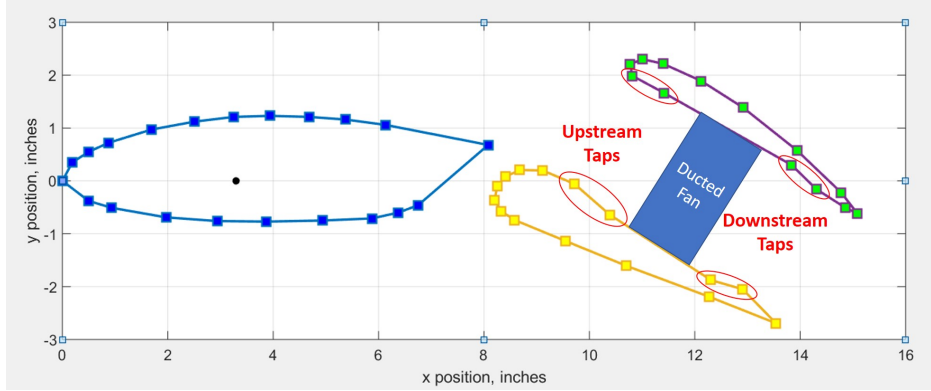


Figure B.13: Wall static pressure taps in the fan #4 duct are used for reference when estimating the velocity at each total pressure probe.

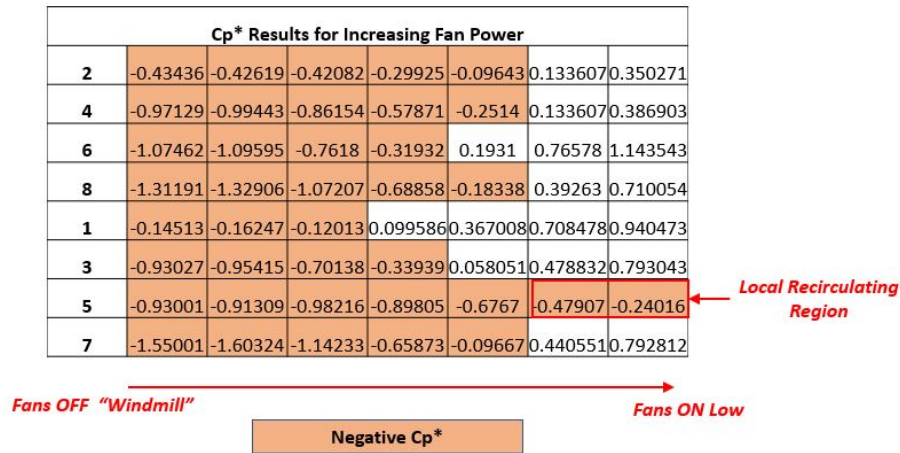


Figure B.14: Example of a case where recirculating region was identified for removal from the thrust estimate.

At this point, an estimate of the jet outlet velocity can be constructed from the mass-averaged velocity at each probe location, since potentially recirculating regions have been removed from the estimate according to the process in Alg. 5. This estimate is

$$E(\vec{V}_2) = \vec{V}_2 \equiv \frac{1}{\dot{m}_T} \sum_{i=1}^8 V_i \dot{m}_i \hat{e}_2 \quad (\text{B.84})$$

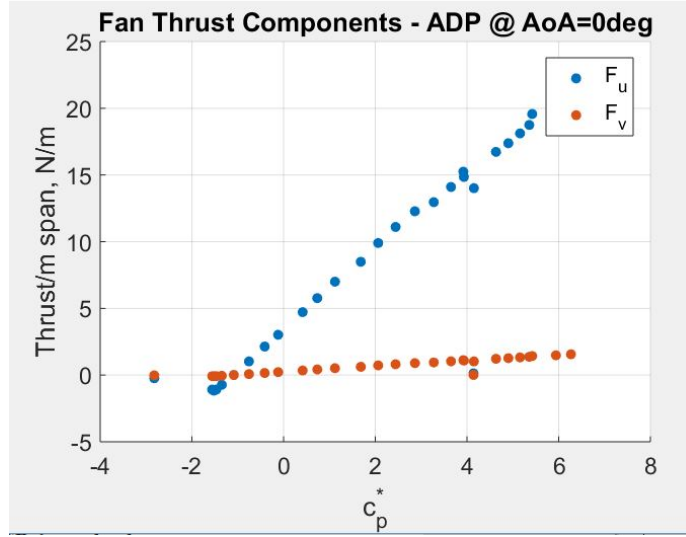


Figure B.15: Example showing the u and v thrust components estimated for an ADP configuration at $\alpha = 0$ deg

Estimating A_2

Though there is a geometric area associated with the fan duct outlet, this will not be used as the effective outlet area of the jet due to the potential for separated regions within the jet as discussed previously. The outlet velocity estimate given in Eq. B.84 requires that a similar approach is used when estimating the outlet area. As shown in Alg. 5, the identified recirculating areas are removed from the estimate by setting the identified $A_i = 0$. Therefore,

$$E(A_2) = \bar{A}_2 \equiv \sum_{i=1}^8 A_i \quad (\text{B.85})$$

There are three implicit assumptions in this formulation for $E(A_2)$.

- 1 The flow is not necessarily attached to both the upper and lower surfaced of the duct.
- 2 The boundaries of the control volume remain fixed relative to the duct, regardless of the presence of separated flow.

- 3 If the inlet boundary crosses a recirculating region, the net flux across that region of the boundary is zero and any pressure contributions from that region are neglected.

Estimating V_1

As shown in Fig. B.13, there are four wall static pressure taps located on the center-line of the duct, upstream of the fan. When α or θ are small, the inlet velocity profile is reasonably uniform. However, when α or θ are increased, there is a significant velocity gradient across the inlet of the fan duct. Therefore, the inlet velocity is estimated by first calculated a velocity based on each of the four static pressure taps, assuming that flow total pressure $P_{Tot1} = 0$.

$$V_{fwd_i} = \sqrt{\frac{2 * p_{fwd_i}}{\rho}} \quad (\text{B.86})$$

Then, since we know nothing about the exact shape of the vertical or lateral velocity profiles, the inlet velocity is estimated as the mean of these V_{fwd_i}

$$E(\vec{V}_1) = \vec{V}_1 \equiv \frac{1}{4} \sum_{i=1}^4 V_{fwd_i} \hat{e}_1 \quad (\text{B.87})$$

Estimating A_1

From continuity, we have $\dot{m}_1 = \dot{m}_2 = \dot{m}$ Therefore, with ① and ② parallel

$$\dot{m}_2 = \dot{m}_1 \quad (\text{B.88})$$

$$\rho \bar{V}_2 \bar{A}_2 = \rho \bar{V}_1 A_1 \quad (\text{B.89})$$

$$\bar{V}_2 \bar{A}_2 = \bar{V}_1 A_1 \quad (\text{B.90})$$

From this we can construct an estimate of the inlet flow area from the estimates of the other variables discussed so far.

$$E(A_1) = \bar{A}_1 \equiv \frac{\bar{V}_2 \bar{A}_2}{\bar{V}_1} \quad (\text{B.91})$$

Like the estimate for $E(A_2)$, there are three implicit assumptions in this formulation for $E(A_1)$.

- 1 The flow is not necessarily attached to both the upper and lower surfaced of the duct.
- 2 The boundaries of the control volume remain fixed relative to the duct, regardless of the presence of separated flow.
- 3 If the inlet boundary crosses a recirculating region, the net flux across that region of the boundary is zero and any pressure contributions from that region are neglected.

Given the control volume shown in Fig. B.9, the inlet area estimate \bar{A}_1 is subject to the following constraint:

$$0 \leq \bar{A}_1 \leq A_{inlet} \quad (\text{B.92})$$

The estimated inlet flow area must be positive and less than the geometric flow area of the inlet, A_{inlet} . However, given that \bar{A}_1 is computed from an estimated inlet velocity \bar{V}_1 , there is opportunity for error due if the static pressure conditions used to construct \bar{V}_1 are not representative of the mean static pressure at the inlet boundary $\textcircled{1}$.

Therefore it is necessary to check that \bar{A}_1 satisfies the required constraints. This process is recursive in that if the constraints are not satisfied, the inlet velocity is recalculated given the measured outlet conditions, and by requiring that $\bar{A}_1 = A_{inlet}$, according to the algorithm, Alg. 6.

Algorithm 6: Compute inlet velocity such that continuity is satisfied over the fan control volume, Fig. B.9

Result: Compute estimate \bar{V}_1

64 Compute \bar{V}_2 ;

65 Compute \bar{A}_2 ;

66 Compute \bar{V}_1 ;

67 Compute $(\bar{A}_1|\bar{V}_2, \bar{A}_2, \bar{V}_1)$;

68 **if** $\bar{A}_1 \leq 0$ || $\bar{A}_1 \geq A_{inlet}$, *outside the required bounds* **then**

69 $\bar{A}_1 = A_{inlet}$;

70 Re-compute $(\bar{V}_1|A_{inlet}, \bar{A}_2, \bar{V}_2)$;

71 Compute $T_{u_{mom}}$, u-momentum thrust contribution;

72 Compute $T_{v_{mom}}$, v-momentum thrust contribution;

73 **else if** $\bar{A}_1 > 0$ *and* $\bar{A}_1 \leq A_{inlet}$ **then**

74 Compute $T_{u_{mom}}$, u-momentum thrust contribution;

75 Compute $T_{v_{mom}}$, v-momentum thrust contribution;

76 **end**

77 **end**

Performing this logical test ensures the calculated moment thrust contribution is a conservative estimate. If this correction is required, the resulting inlet velocity estimate is

$$\bar{V}'_1 \equiv (\bar{V}_1|A_{inlet}, \bar{A}_2, \bar{V}_2) \quad (\text{B.93})$$

Estimating p_1 and p_2

Since this experiment is performed using a draw-down wind tunnel, the free-stream stagnation pressure is taken to be the gauge reference pressure.

$$P_{T_\infty} = 0Pa, \text{ gauge} \quad (\text{B.94})$$

Therefore, assuming that inlet velocity is well represented by \bar{V}_1 , the uniform static pressure at ① is

$$E(p_1) = \bar{p}_1 \equiv -\frac{\rho\bar{V}_1^2}{2} \quad (\text{B.95})$$

The estimated uniform static pressure at ② is equal to the farfield static pressure

$$E(p_2) = p_\infty = \bar{p}_2 \equiv -\frac{\rho V_\infty^2}{2} \quad (\text{B.96})$$

Therefore the change in static pressure from ① to ② is equivalent to the mass-flow-averaged change in total pressure across the fan, as measured.

$$\bar{p}_2 - \bar{p}_1 = \Delta\bar{P}_{T_{fan}} = \frac{1}{\dot{m}} \sum_{i=1}^8 P_{T_i} \dot{m}_i - \bar{p}_2 \quad (\text{B.97})$$

For conservatism, since the majority of the thrust contribution comes from the pressure rise across the fan, as opposed to momentum flux. The estimate \bar{A}_1 will be used only when computing momentum flux contributions. The typically larger geometric inlet area

$$A_{inlet} = 0.0041m^2/fan \quad (\text{B.98})$$

will be used when computing the pressure contributions to thrust. The outlet pressure contributions will be computed using the recirculation-reduced estimator \bar{A}_2 . These results are given in Fig. B.16.

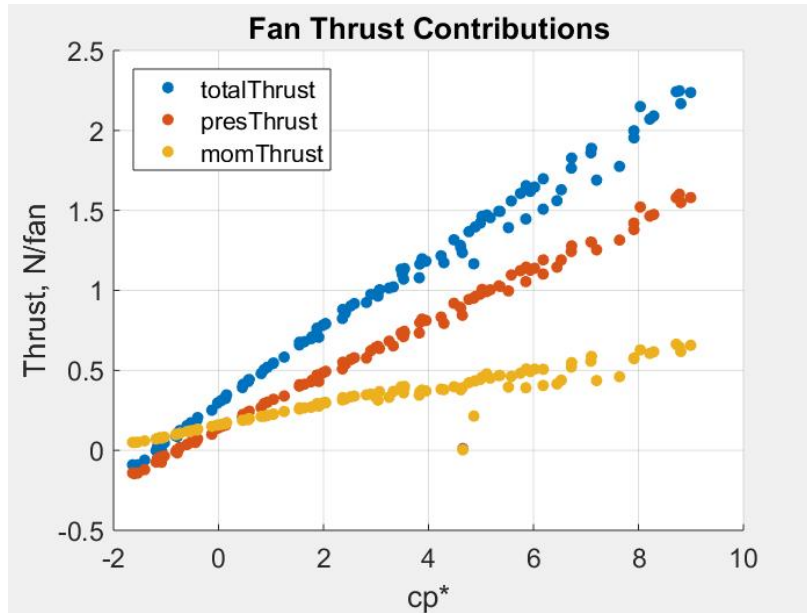


Figure B.16: An example case showing the computed u and v components of thrust - ADP at $\alpha = 0$ deg. Note that the net thrust is negative for cases where $c_p^* \lesssim 0$

Calculating A_3 , A_4 , p_3 and p_4

These parameters can be calculated directly from the experimental data. The pressure taps along the center line of the duct are used to compute the pressure distributions on each surface. Because the spacing of these taps is known, the surface force contributions of each can be calculated as shown in Fig. B.17.

Checking the Thrust Estimate

The ideal power \dot{Q} can be estimated from the mass flow rate, velocity, effective area, and pressure estimates developed previously. Since the electrical input power is measured, this value can be compared to the flow of energy through the fan. The net efficiency of the fan system can be defined as the ratio of these power estimates

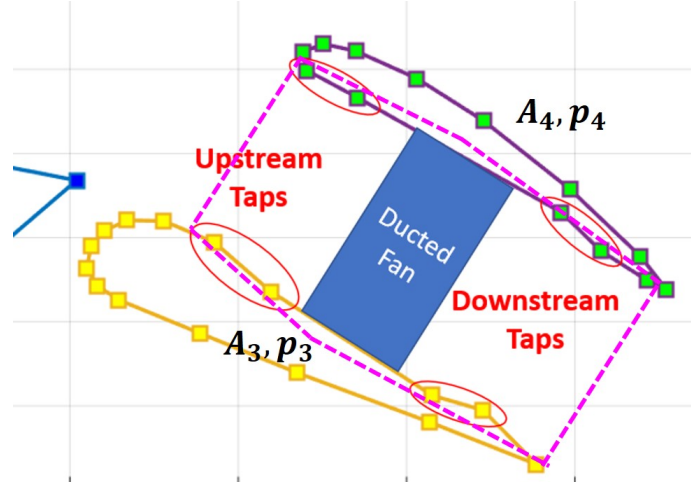


Figure B.17: The pressure distributions on surfaces ③ and ④ are measured and the areas of each surface is known.

$$\eta_{net} \equiv \frac{\dot{Q}}{P_{elec_{in}}} \quad (\text{B.99})$$

Since this is an efficiency, $\eta_{net} \leq 1$, and in practice with this system, $\eta_{net} \leq 0.60$ considering the electrical losses in the motor, motor controller (ESC), and primarily the fan.

The efficiency of each component in the system can be approximated as

$$\eta_{fan} \leq 0.7, \text{ typical total-to-total losses from fan and stator vanes} \quad (\text{B.100})$$

$$\eta_{motor} \leq 0.88, \text{ combined back EMF, ohmic, and eddy current losses} \quad (\text{B.101})$$

$$\eta_{esc} \leq 0.98, \text{ MOSFET switching losses} \quad (\text{B.102})$$

$$\boxed{\eta_{max} = \eta_{fan}\eta_{motor}\eta_{esc} \leq 0.604} \quad (\text{B.103})$$

Sample results from this estimation strategy are shown in Fig. B.18.

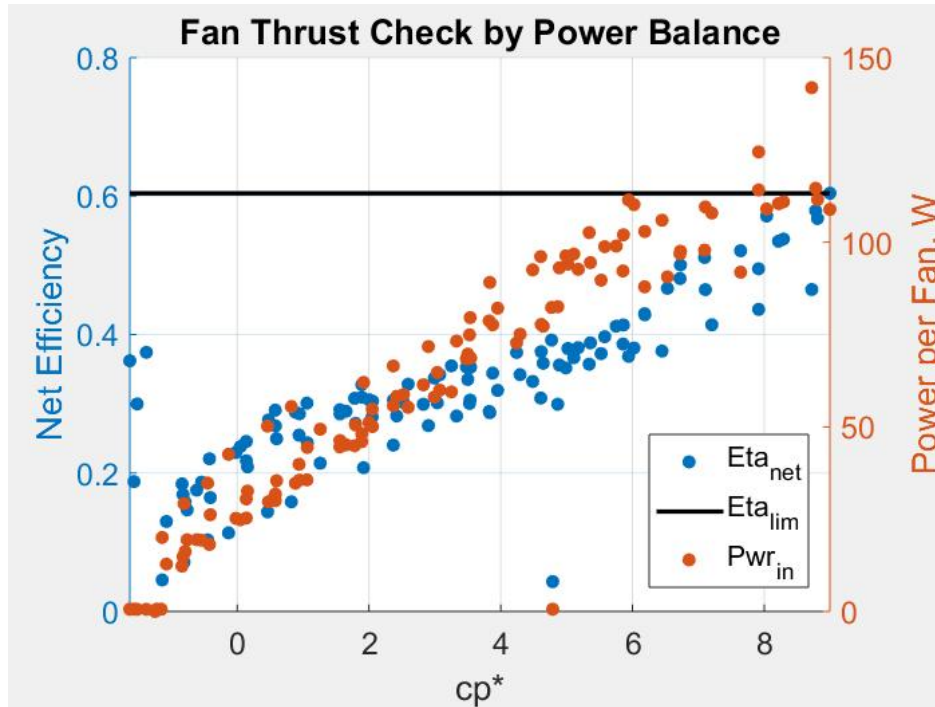


Figure B.18: Example showing a valid power balance for all conditions in a specific configuration, in this case ADP at $\alpha = 0$ deg. Also note that the high efficiency early in the test corresponds to zero electrical power input.

For the example shown in figure B.18 the maximum efficiency limit was not exceeded for any of the operating conditions. Exceeding this limit does not necessarily invalidate the force estimate. Rather, it provides information about the conditions under which the estimate is consistent with the other available data and conservative. Given the scope of this experimental effort, there are conditions where this estimate is likely to break down, particularly when operating with high α or θ .

Comments On Estimating Fan Thrust

The objective of this subsection is to show how the force contributions of the embedded propulsion systems can be estimated from the data collected during the wind tunnel experiments. Significant guidance is taken from CFD analysis of these systems when developing

this estimate. This analysis will be treated in detail in a later chapter. Additionally, the methods presented for checking the validity and conservatism of the thrust estimate are coarse estimates themselves. These are presented to show when the primary thrust estimate is consistent with other available data and thereby a conservative estimate, and when it is not - *either not a reliable estimate or not a conservative estimate* .

Estimates of the total force contributions for both the ADP and CDP propulsion systems could be improved by combining these results with particle image velocimetry (PIV) measurements at multiple planes along the span of the wind tunnel model. Such an effort should be considered as an extension of this initial exploration.

B.5 Wind Tunnel Corrections

B.5.1 3-D Blockage Correction

Several corrections are required to compensate for the bounded environment of a wind tunnel. These corrections compensate the free- stream velocity for the blockage effects of the model in the test section as well as the wake/jet blockage from the propulsion system embedded in the model. Also, the velocity measurements must be compensated for the presence of large circulation about the wind tunnel model. The objective of this section is to summarize these corrections and show how they are applied to this specific experiment.

The presence of the model in the wind tunnel causes a blockage that effectively reduces the cross-sectional area of the test section. This blockage increases the velocity in the test-

section near the model. To account for this a 3D solid blockage correction is applied [cite Barlow et. al. and Brandt-Selig]

$$\frac{\Delta V}{V_u} = \frac{K_1 \tau_1 \bar{V}_{model}}{C^{3/2}} \quad (\text{B.104})$$

$$V_{corr_B} = 1 + \frac{\Delta V}{V_u} \quad (\text{B.105})$$

For this experiment, this correction is a constant for both the CDP and ADP configurations.

$$\boxed{V_{corr_{B,CDP}} = 1.0159} \quad (\text{B.106})$$

$$\boxed{V_{corr_{B,ADP}} = 1.0021} \quad (\text{B.107})$$

where factors K_1 and τ_1 are developed in [Barlow et. al.], C and \bar{V}_{model} are the cross-sectional area of the wind tunnel and the volume of the model respectively.

B.5.2 Confined Flow Thrust Correction

The boundary correction used to account for the presence of the wind tunnel walls was developed by Glauert in [cite Glauert] and illustrated in [BrandtSelig]. Since the flow field is restricted by walls of the test-section, the static pressure in the fan slipstream as it develops downstream, beyond the constraints of the fan-ducts. Therefore, by continuity analysis, the streamwise thrust component would actually be produced by a lower freestream velocity if the flow were unrestricted. Shown in Figs. B.19 and B.20, These corrections are described by

$$\frac{V_{Thr_{corr}}}{V_{\infty}} = 1 - \frac{\tau_4 \alpha_1}{2\sqrt{1 + 2\tau_4}} = V_{corr_T} \quad (\text{B.108})$$

where,

$$\tau_4 = \frac{T_{u_{est}}}{\rho A_{fan} V_{\infty}^2} \quad (\text{B.109})$$

$$\alpha_1 = \frac{A_{fan}}{C} \quad (\text{B.110})$$

as developed in [cite Barlow et.al]

The interdependence of the thrust estimate and freestream velocity correction requires the development of an iterative process where this correction is at first neglected to develop a thrust estimate, then included in the second iteration to successively refine both the velocity correction and thrust estimate according to the algorithm show in A.7.

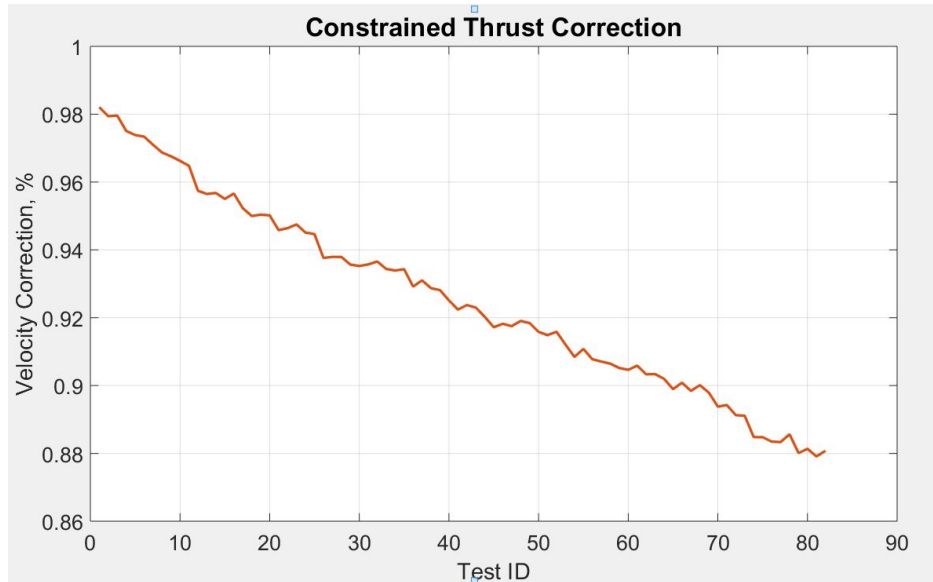


Figure B.19: Example showing the velocity correction due to the u-thrust component in a confined flow-field for a specific configuration, in this case ADP at $\alpha = 0$ deg.

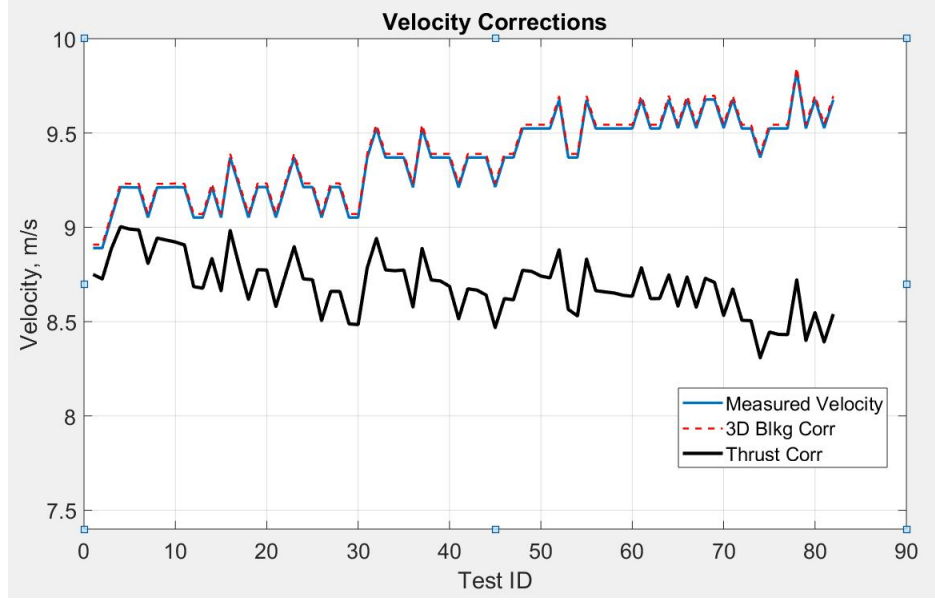


Figure B.20: Example showing the net velocity correction due to the 3D blockage and thrust u-thrust component in a confined flow-field for a specific configuration, in this case ADP at $\alpha = 0$ deg.

Algorithm 7: Iterative scheme for refining velocity and thrust estimates

Result: Refine the thrust estimate and corresponding velocity correction

```

78 Estimate  $V_{Thr_{corr}}$  assuming  $T_{u_{est}} = 0$ ;
79 Compute  $T_{u_{est}}$ ;
80 for  $iter = 1:m$  do
81   Estimate  $V_{Thr_{corr}}$  using new  $T_{u_{est}}$ ;
82   Refine  $T_{u_{est}}$ ;
83   Compute the residual;
84 end

```

The convergence history of this algorithm is shown in Fig. B.21.

The residual in this case is defined as

$$R_{V_{corr_T}} = V_{corr_T} - V_{corr_{T_{old}}} \quad (\text{B.111})$$

where V_{corr_T} is updated each iteration. Figure B.21 shows that this converges rapidly, typically within three to five iterations.

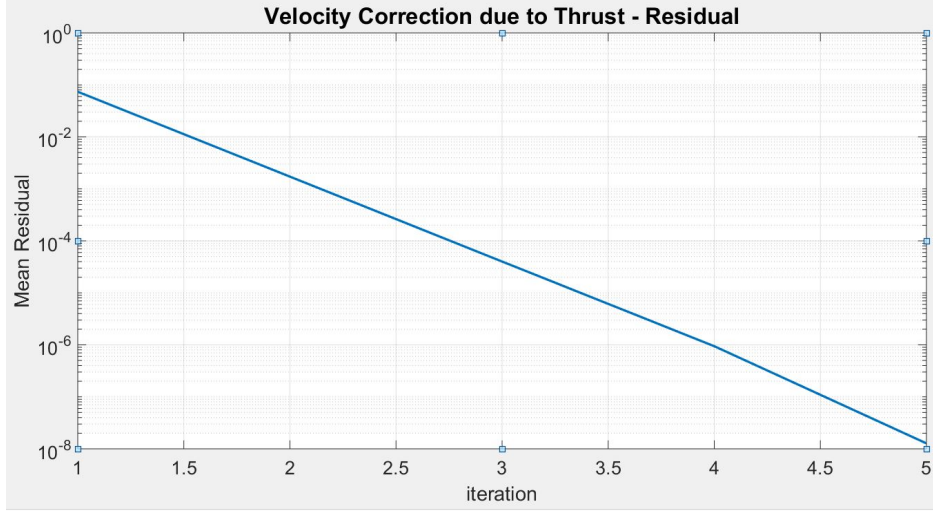


Figure B.21: Example showing the convergence of the velocity correction due to thrust in a specific configuration, in this case ADP at $\alpha = 0$ deg.

These corrections can then be applied sequentially as shown in figure B.20 according to

$$V_{\infty corr} = V_{corrT} V_{corrB} \quad (\text{B.112})$$

For the ADP configuration, V_{corrB} is negligible, correcting the measured velocity by only 0.21%. However, the 1.59% correction for the CDP configuration is not negligible, and so this correction is included for both ADP and CDP model configurations.

The corrected freestream velocity, $V_{\infty corr}$ will be used for computing the force and moment coefficients as well as the parameter, c_p^* , resulting from the wind tunnel measurements and estimates.

B.5.3 Circulation-Induced Velocity Correction

Though the circulation of the wing-bound vortex dominates the near-field region of the flow.

The wind tunnel inlet section is designed to enable a far-field free-stream velocity that is

nominally unaffected by the presence of this strong down-stream vortex. The induced u -component of velocity is computed for the primary bound vortex at this location as well as each image vortex, required by the symmetry conditions imposed at the upper and lower wall. This component is further minimized by placing the velocity measurement probe near the center of the test section on approximately the same water-line as the wind tunnel model. This correction is included in the calculations, though the contribution is negligible, with the maximum on the order 10^{-5} .

The methodology of this correction will be shown in the [code Appendix] but does not require further treatment in this context.

B.6 Calculation Summary

In this chapter, the system geometry was set in the proper reference frames to carry out this analysis, along with the transformation matrices between these frames. A dimensional analysis of the forces and moments as an additional function of power was presented and showed that an additional dimensionless parameter, c_p^* , is required to describe the dependence of the u and v force components and pitching moment on fan power. The methodology for computing the pressure contribution to these forces and moments from the wind tunnel measurements was shown, as were methods for estimating and checking the fan contributions as well. Finally, a set of wind tunnel corrections were developed to compensate for the wind tunnel blockage due to the CDP and ADP models, as well as the confined flow around the fan jet. These results are summarized for a sample ADP case shown in Fig. B.22.

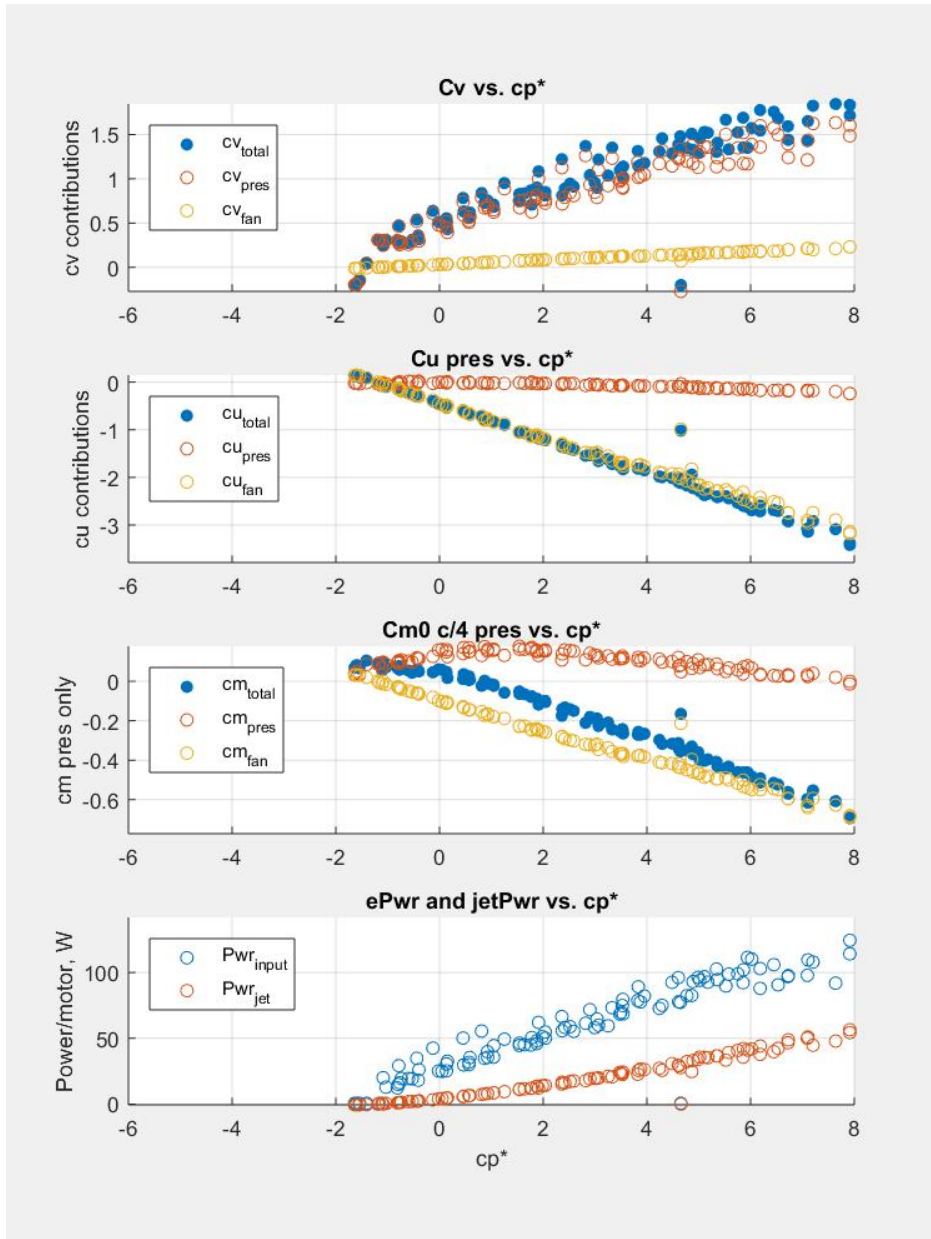


Figure B.22: Example showing the force and moment coefficients for a specific configuration, in this case ADP at $\alpha = 0$ deg.

The force and moment coefficients are calculated according to the methodology described earlier in this chapter, with contributions from the integrated pressure-forces and fan-forces considered separately in all cases. The coefficients associated with these forces are described as follows:

$$c_u = c_{u_{pres}} + c_{u_{fan}}, \text{ horizontal force coefficient} \quad (\text{B.113})$$

$$c_v = c_{v_{pres}} + c_{v_{fan}}, \text{ vertical force coefficient} \quad (\text{B.114})$$

$$c_{m,c/4} = c_{m,c/4_{pres}} + c_{m,c/4_{fan}}, \text{ moment coefficient, about } c/4 \quad (\text{B.115})$$

B.7 Conclusions

The analysis presented in this chapter provides a method for directly calculating and where necessary, for estimating significant contributions to the net force acting on the wind tunnel models. These sources include both the fan pressure and momentum flux contributions from a control volume analysis, and the integrated static pressure distributions around the aerodynamic surfaces. Generally, the pressure measurements and therefore the resulting force contributions are accurate for both the fan and aerodynamic surface components. However, the estimate of the fan force contribution due to momentum flux is somewhat unreliable.

For small angles of attack, $\alpha \leq 18 \text{ deg}$, the estimated momentum flux contribution to net force is reasonable, satisfying both the power balance and continuity tests. When the angle of attack increases to $27 \text{ deg} \leq \alpha \leq 67.5 \text{ deg}$, the momentum flux estimate is likely less accurate though still conservative, given the increasing prevalence of flow separation from the lower fan-inlet lip. However, when $\alpha \geq 72 \text{ deg}$, the momentum flux estimate appears to break down.

Typically, the momentum flux component accounts for approximately 30% of the total fan force contribution, which itself accounts for less than 30% of the total lifting force on the

model and about 70% of the total horizontal force on the model. Therefore, the net force on the ADP and CDP wind tunnel models is well represented by the data presented herein.

Appendix C

HEPS Experiment Development and Construction

C.1 Introduction

The objective of this chapter is to detail the design and construction of a lab-scale, internal combustion engine (ICE) based hybrid-electric power system (HEPS) for use in electric aircraft propulsion applications. This experiment was constructed to support the development of a detailed dynamical model in the Matlab Simulink environment, providing both quantitative and qualitative data for validating the model. Of primary concern to this research effort is the transient response of the power system to changes in load. The data gathered from this experiment will be used to identify critical, potentially aberrant, dynamic characteristics present in the real system that must be reflected in the model. Additionally, this data will be used for tuning a baseline model, from

which control improvements can be developed. Therefore, this experiment must be capable of repeatably applying a load profile to the power-system and recording both the mechanical and electrical response with a known controller applied. This data will then be used to tune the mechanical and electrical response of the computational model.

C.2 System Configuration

The hybrid topology proposed in this research is Direct Transmission to Multiple Loads (DTML). Where, as the name suggests, the electric power generated in the system is directly transmitted to the distributed electrical power system of the aircraft, as shown in Fig. C.1.

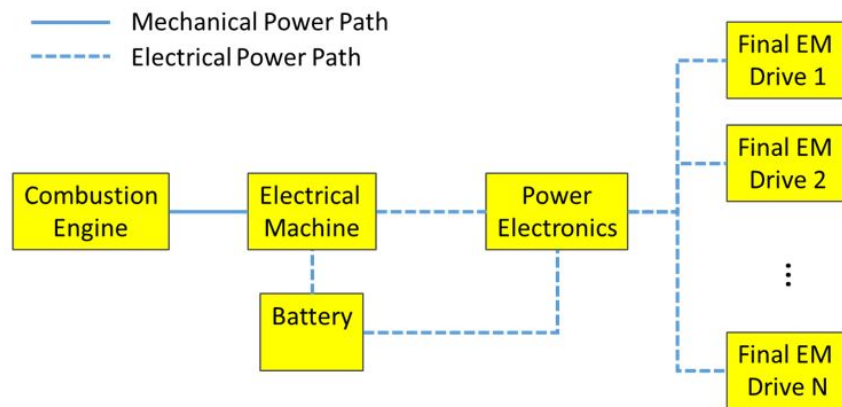


Figure C.1: This configuration applies to the power systems required for both the ADP and CDP propulsion configurations.

As shown in Fig. C.1, the output of the power system is transmitted electrically to a plurality of electrical loads in the propulsion system. This transmission can be accomplished using either AC or DC power, depending largely on the scale of the loads in the system. For

the distributed propulsion systems explored in this research, these loads are assumed to be small, typically less than 10kW per motor/fan system.

At this scale, brushless DC (BLDC) permanent magnet synchronous machines (PMSMs) will provide the maximum power density [cite motor paper] and will be used throughout this analysis. These loads require the use of a dedicated inverter to provide synchronous AC power to each motor based on its current speed and load. As MOSFET-based DC-AC controllers are widely available at this scale, this method of load control will be adopted for each load. Therefore, the electrical power will be transmitted using direct current.

Though each load can be controlled individually, the resulting load on the power system will be the sum of each individual load. Therefore, for the purposes of this experiment, only one load will be applied to the system, as shown in Fig. C.2.

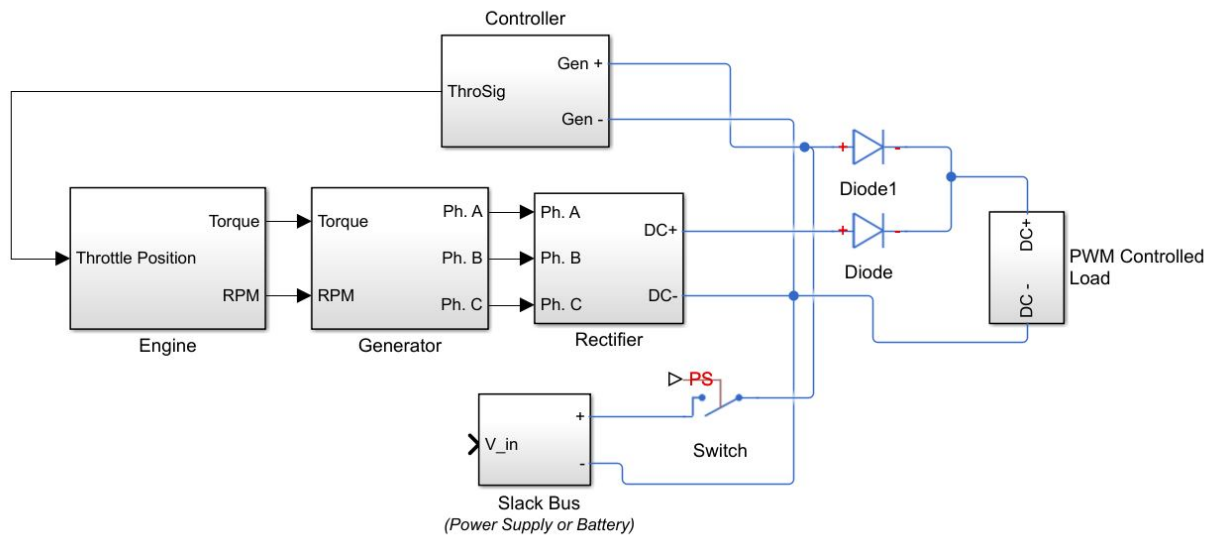


Figure C.2: For this experiment, only a single PWM controlled load is applied to the system. Also, note that the battery or slack-bus can be connect or removed from the system.

This experimental apparatus consists of five critical components that will be discussed in detail later in this chapter. These are

- Internal combustion engine
- Delta-connected three-phase BLDC generator
- Three-phase full-bridge diode rectifier
- PWM controlled load
- Voltage regulated slack bus

Though this experiment is designed for a peak power output of $\sim 2kW$, this configuration is generally scalable to $\sim 300kW$, essentially the viable power range of reciprocating internal combustion engines, with minimal changes to the topology. Thus, it is suitable for use in a broad array of airborne applications from small UAS to general aviation aircraft, which is the scope of the present research. Scaling considerations will be discussed in a later Chapter.

C.3 Power System Design and Construction

In order to ensure the consistency of the data, this experiment is conducted in an indoor laboratory environment. To mitigate challenges such as exposure to the toxic exhaust of the 2-stroke engine, the experiment is installed in a fume hood, as shown in Fig. C.3.

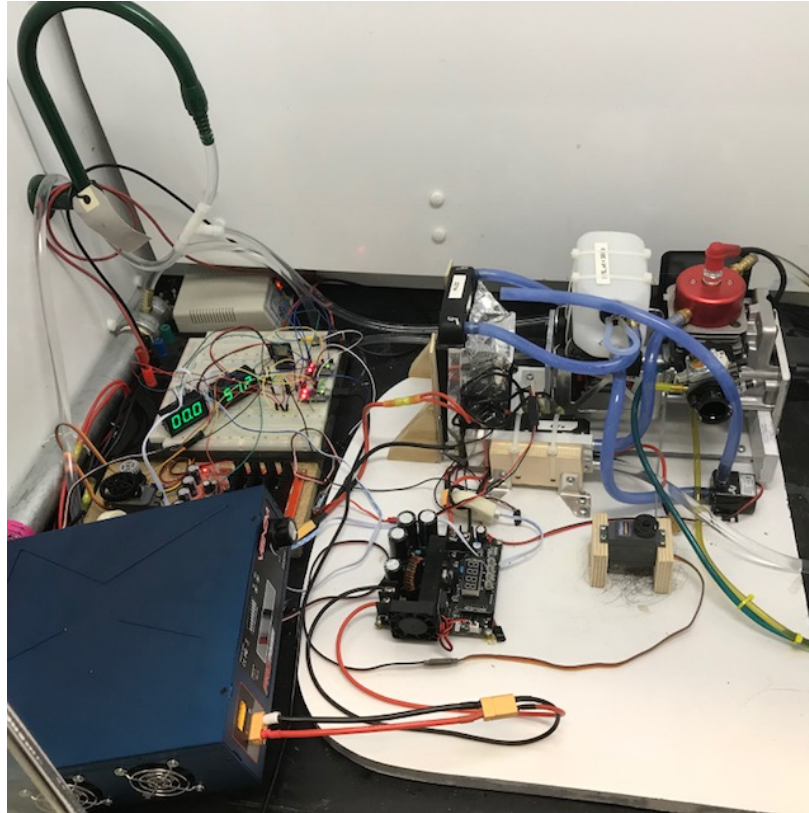


Figure C.3: Hybrid power system experiment installed in a fume hood in the Syracuse Center of Excellence.

C.3.1 Thermal and Exhaust Management Strategy

The volumetric flow rate of the fume hood used for this experiment is typically between 600-800scfm. This is sufficient for evacuating hazardous chemical vapors with minimal flow disturbances from the hood.

This power system is designed to operate in the fume hood as well as on board future test aircraft. Therefore, the heat load from the system must be sufficiently mitigated. The energy balance of this system can be summarized as

$$\dot{Q}_{fuel} = \dot{Q}_{exhaust} + \dot{Q}_{cyl} + \dot{Q}_{gen} + \dot{Q}_{rect} + \dot{Q}_{diodes} + \dot{W}_{elec} \quad (C.1)$$

With the exception of \dot{W}_{elec} The majority of the energy in the fuel is rejected from the system as heat, either directly through the combustion exhaust, heating the cylinder and engine block, indirectly through the ohmic losses incurred due to current flow through the system, or due to eddy currents and other losses in the generator. Ultimately, even \dot{W}_{elec} , the useful electrical power is dissipated as heat in this experiment. Therefore, an effective thermal management system is required. As a result, water cooling is used wherever possible. This cooling circuit is shown in Fig. C.4.

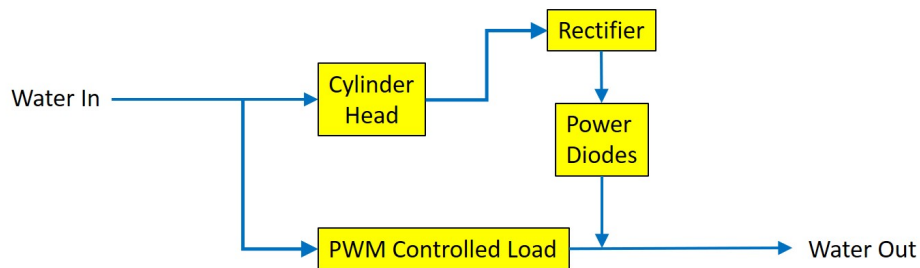


Figure C.4: Water cooling is used to remove heat from the engine as well as the power diodes, rectifier, and the primary system load.

C.3.2 Engine

The Zenoah G320PUM engine is a liquid-cooled, naturally aspirated two-stroke. This engine was selected for its robustness, built-in water-cooling compatibility, high power density and low cost, as shown in Fig. C.5.



Figure C.5: A Zenoah model G320PUM, liquid cooled engine is use as the prime-mover for this hybrid system.

The specification of this engine are provides in Table C.1.

The two-stroke engine is combined with a PMSM generator comprising the engine-generator system of the HEPS, as shown in Fig. C.6.

C.3.3 Generator

The generator used for this experiment is a three-phase PMSM BLDC. The Leopard Hobbies LC6362-10T 210kV motor was selected because its rated current capacity of 35A with a peak capacity of 70A with an operating voltage up to 54.6V, Fig. C.7. Given the peak voltage and voltage constant, the maximum operating speed for this motor is approximately 11,500rpm,

Zenoah G320PUM Specifications		
Engine Parameter	Value	Units
Cylinder Displacement	31.8	cm^3
Cylinder Bore	38	mm
Cylinder Stroke	28	mm
Peak Power Output	3.21	kW
Max. Power Speed	14000	rpm
Carburetor	Walbro	—
Carburetor Model No.	WT-1107	—
Specific Fuel Consumption	604	g/kWh
Ignition System	CDI	—
Idle Speed	4000	rpm
Spark Plug	NGK CMR7H	—
Starting System	Recoil	—
Weight	1.93	kg
Peak Specific Power	1.66	kW/kg

Table C.1: Zenoah G320PUM Specifications

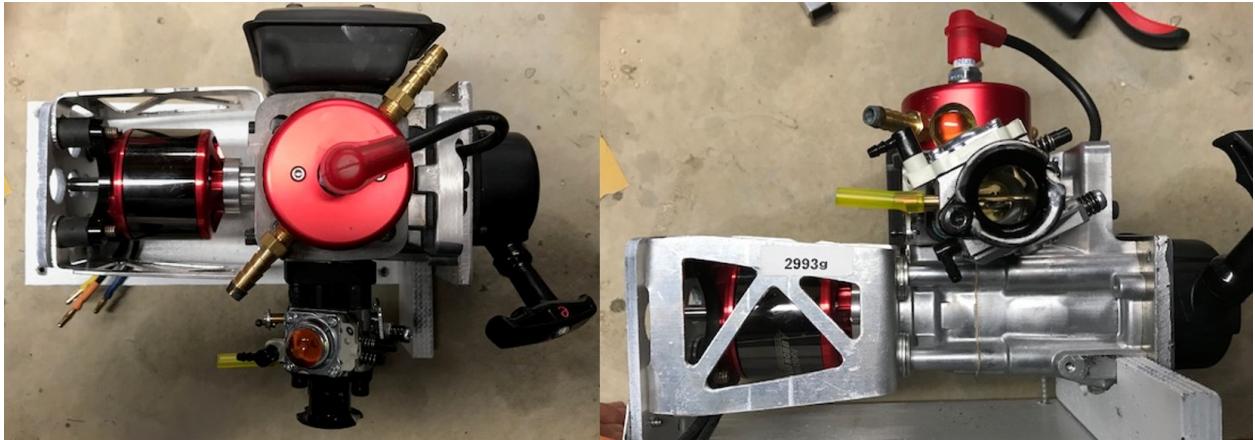


Figure C.6: The Zenoah G320PUM, is coupled directly to a three-phase BLDC generator. The generator is mounted rigidly to the output shaft of the engine, and supported by polymer vibration-absorbing mounts.

which pairs well with the Zenoah G320PUM. This generator is a Delta-wound PMSM, as shown in Fig. C.8. These specifications are further detailed in Table C.2.

Ideally, a generator would be specifically designed to operate with a specific engine, however due to budgetary constraints, selection from low cost, commercial-off-the-shelf (COTS)

parts is necessary. Additionally, since the primary objective of this experiment is to characterize the dynamic response of an ICE driven DTML-hybrid system to changes in loading, the overall efficiency of the system is of secondary concern.



Figure C.7: The Leopard Hobbies LC6362-10T is a three-phase PMSM motor with the phases connected in a delta configuration.

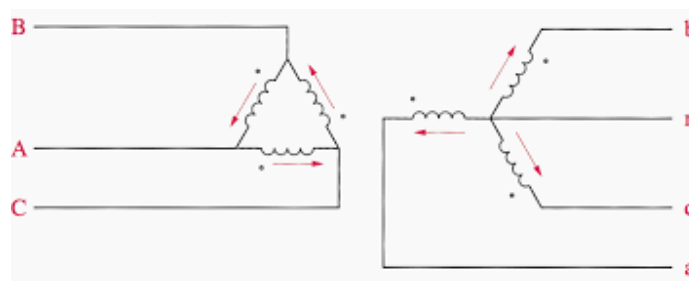


Figure C.8: A delta-connected generator is preferable for this airborne application, the neutral reference required for a wye connected system presents significant challenges for un-grounded systems. (<http://electrical-engineering-portal.com/3-phase-transformer-connections>.)

Leopard LC6362-10T 210kV Specifications		
PMSM Parameter	Value	Units
1/Voltage Constant	210	rpm/V
Phase Resistance	0.0328	ohm
Shaft Diameter	8	mm
No Load Current (20.0V)	1.8	Amps
Rated Current	35	Amps
Max. Current	70	Amps
Rated Voltage	54.6	V
Rated Power	1150	W
Max Power	2300	W
Weight	595	g
Specific Power	3.86	kW/kg

Table C.2: Leopard LC6362-10T 210kV Specifications

C.3.4 Power Electronics

Three-Phase Rectifier

A three-phase passive full-wave diode bridge rectifier is used for this experiment to convert the three-phase AC power from the generator into DC power, as shown in Fig. C.9. Though significant improvements in efficiency are realized by using active rectification by MOSFET full-bridge rectifiers, only COTS parts are selected for this experiment due primarily to budgetary constraints. Because overall efficiency is not a primary concern, the heat load generated by the diode bridge is mitigated by bonding the rectifier assembly to a water-cooled heat-sink. The specifications of this rectifier are given in Table C.3.

Power Diodes

As shown in Fig. C.10, a secondary set of power diodes is used to passively regulate current flow from the slack bus to the load and prevent this power from feeding back into the

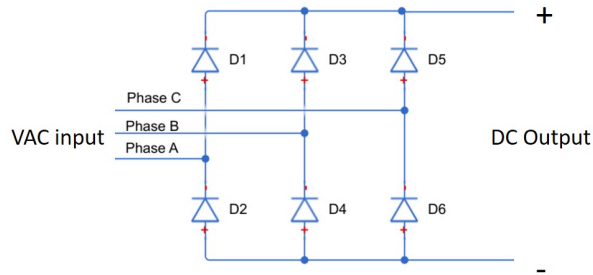


Figure C.9: The MDS-100A three-phase rectifier is a low cost COTS device capable of handling 100A forward rectified DC current.

MDS-100A Rectifier Specifications			
Parameter	Description	Value	Units
I_O	DC Output Current @ $T_j = 150^\circ C$	100	Arms
V_{RRM}	Max. Repeat Peak Reverse Voltage	1600	Vrms
I_{RRM}	Max. Repeat Reverse Current	10	mArms
V_{FM}	Forward Voltage Drop @ $I_{PK} = 150Arms$	1.35	Vrms
$V_{F(TO)}$	Voltage Threshold @ $150^\circ C$	0.81-0.99	Vrms
T_j	Junction Operating Temp.	-40 to 125	$^\circ C$

Table C.3: MDS-100A Rectifier Specifications

generator. The diodes selected for this application are the IXYS DSS2x101-015A Schottky Diodes, Fig. C.10.

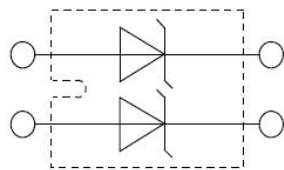


Figure C.10: The IXYS DSS2x101-015A Schottky Diode is a low cost COTS device capable of handling 100A forward DC current with the additional benefit of being packaged in a double configuration.

The specifications for these power diodes are given in Table C.4.

IXYS DSS2x101-015A Schottky Diode Specifications			
Parameter	Description	Value	Units
I_O	DC Output Current @ $T_{case} = 110^\circ C$	2 x 100	Arms
V_{RRM}	Max. Repeat Peak Reverse Voltage	150	Vrms
I_{RRM}	Max. Repeat Reverse Current	4	mArms
V_{FM}	Forward Voltage Drop @ $T_{vj} = 125^\circ C$	0.77	Vrms
$V_{F(TO)}$	Voltage Threshold @ $T_{vj} 150^\circ C$	0.53	Vrms
T_{vj}	Virtual Junction Operating Temp.	-40 to 150	$^\circ C$

Table C.4: IXYS DSS2x101-015A Schottky Diode Specifications

The complete specifications for both the rectifier and power diodes used in this experiment are provided in the Appendices to this document.

C.3.5 Load Design

The confines of the laboratory setting of this experiment required that certain safety precautions be addressed. This was particularly critical when designing a method for loading the hybrid power system. This load must be able to dissipate up to the $\sim 2kW$ output of the engine and generator, and must do it in a way that is controllable, repeatable, physically meaningful, and above all, safe to operate in the laboratory.

Laboratory Load Design

Water-cooled DC resistors are connected in parallel with each other and paired in series with a high-frequency PWM DC motor controller to create a variable DC load bank. The amount of power processed by this load is controlled by changing the duty cycle of the PWM signal output from the motor controller.

A controlled resistive dump load is used in this experiment for several reasons. First, this presents a controlled means of dissipating a large amount of power without exposing the operator to unnecessary risks, such as running a large fan or propeller to dissipate the power to the surrounding air. Second, since the DC voltage generated will be transmitted directly to the load, without first passing through a storage medium, like a battery, and without significant power conditioning, such as a boost converter or buck converter, the load needs to be compatible with a range of DC voltages. With a 100% duty cycle, The output voltage of the generator system is determined simply by

$$P_{max} = I_{d=1}^2 R_{tot} \quad (C.2)$$

where,

$$I_{d=1} = \frac{V_{DC_{out}}}{R_{tot}} \quad (C.3)$$

For a given generator output voltage, the power dissipated by the load is

$$0 \leq P_{load} \leq P_{max} \quad (C.4)$$

and can be achieved by varying the PWM duty cycle from 0 to 1, through in practice this is limited to $0 \leq D \leq 0.9$. This load configuration is shown in Fig. C.11.

The resistive load used in the laboratory is constructed using two, parallel DC water heaters, each with a 1500W rated capacity with a 48VDC input, for a maximum power dissipation capacity of 3000W. These heaters are placed into either end of a tubular heat exchanger, Fig. C.12. Cold water is fed into one end, heated by the DC heating elements,

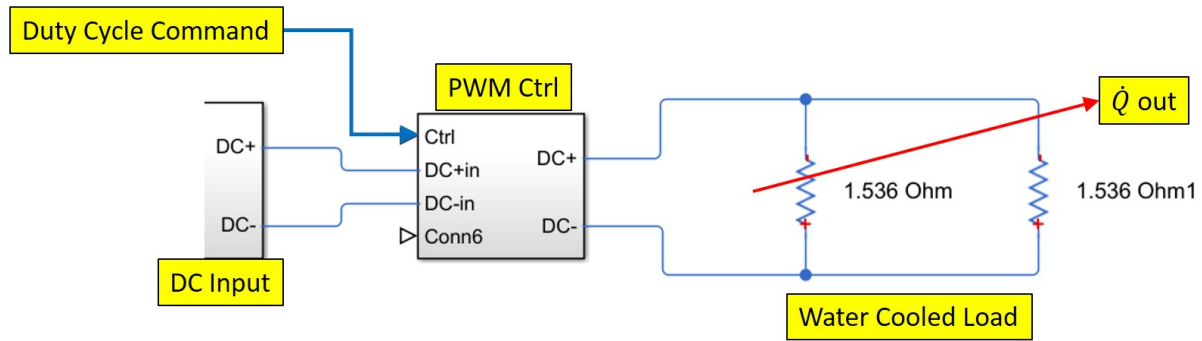


Figure C.11: The DC load consists of two water heating elements, each with a resistance of 1.536Ohms, connected in parallel.

and warm water is discharged from the system. This system was designed with a limit power loading of 2000W, thereby yielding a factor of safety of 1.5.

$$\text{Factor of Safety, } F.S. = \frac{P_{maxload}}{P_{limitload}} \quad (C.5)$$

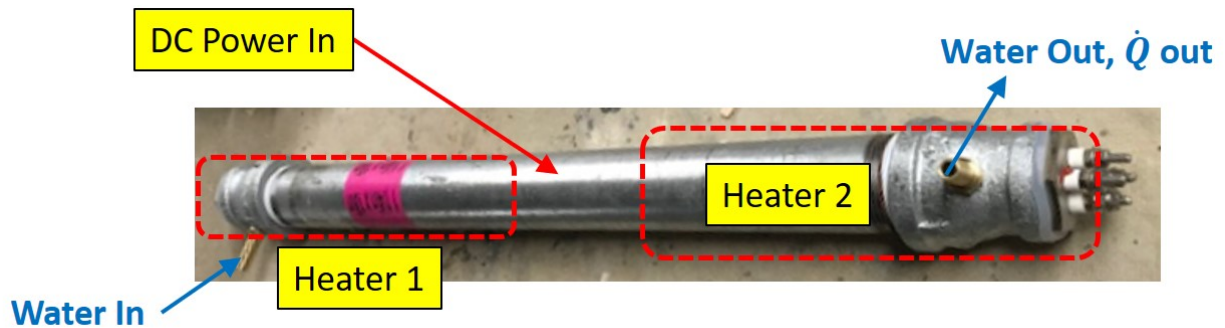


Figure C.12: The tubular heat exchanger constructed for this experiment provided a safe, compact design, where heating elements were shielded from contact with any external surface.

PWM DC Controller

In order to regulate the power input to the load for a given generator output voltage, a PWM dc motor controller, Fig. C.14, is used to regulate the system. The PWM response of the controller at two different duty cycles is shown in Fig. C.13.

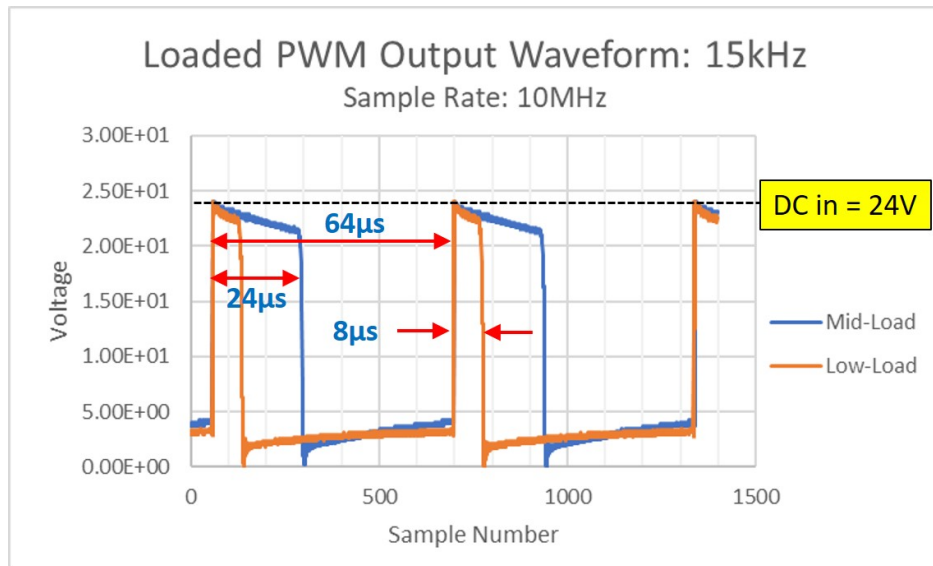


Figure C.13: The PWM motor controller breaks the DC input voltage into discrete square wave pulses in order to control power output. Shown here are the measured waveforms at duty cycles of $D_{mid} = 0.375$ and $D_{low} = 0.125$.

This controller is regulated using a potentiometer input to control the duty cycle as shown in Fig. C.14, though for future experiments this could be connected to a microcontroller as well. For simplicity and reliability, this potentiometer was operated mechanically using a position-controlled servo. The specifications for this controller are given in Table C.5.

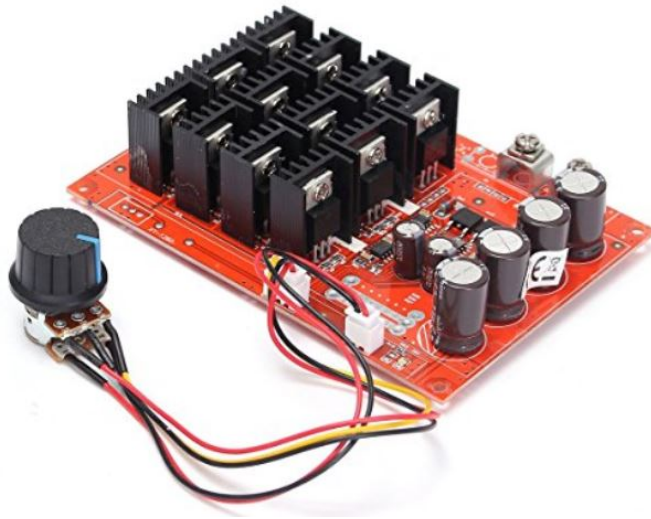


Figure C.14: The PWM controller used in this experiment uses an array of MOSFETs operating at a constant switching frequency of 15kHz to generate the controlled square wave pulses required for regulating the DC load.

PWM Switching DC Motor Controller Specifications			
Parameter	Description	Value	Units
P_{max}	Max. Output Power	3000	W
V_{in}	Input Voltage Range	12-48	VDC
$V_{out_{eff}}$	Effective Output Voltage	$0-V_{in}$	VDC
I_{out}	Max. Output Current	62.5	A
—	Control Signal	Potentiometer	—
—	Cooling	Convection	—

Table C.5: PWM Switching DC Motor Controller Specifications

C.3.6 Slack Bus

For this experiment, the performance of the hybrid power system is tested with and without a slack bus. Therefore, the slack bus must be easily added or removed from the system. The slack bus consists of a DC power supply and a buck-boost converter, shown in Fig. C.15. This enables the slack bus to operate at an arbitrary fixed voltage. Typically, the experiment is controlled to produce a specific voltage, which can be changed according to the control software. The addition of the buck-boost controller allows the slack bus voltage to be maintained at a near constant level up to its limit output current.

The buck-boost controller software limits the output current to a maximum of 15A, while the input current is fuse-limited to 20A.

Power Supply

A Venom ProPower DC power supply is used in this experiment. The output voltage is variable between 12V and 24V, with current limited to 60A. The specifications for this system are given in Table C.6.

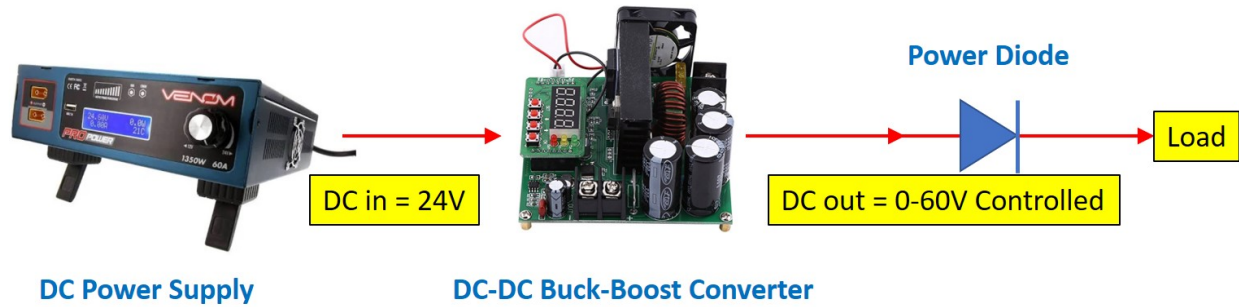


Figure C.15: The slack bus used in this experiment consists of COTS power supply and conditioning equipment. The Output voltage from DC power supply is boosted to the working voltage of the system.

Venom ProPower DC Power Supply Specifications			
Parameter	Description	Value	Units
P_{max}	Max. Output Power	1350	W
V_{in}	Input Voltage	120	VAC
V_{out}	Output Voltage Range	12-24	VDC
I_{out}	Max. Output Current	60	A
—	Control Signal	Potentiometer	—
—	Cooling	Case Fans	—

Table C.6: Venom ProPower DC Power Supply Specifications

Buck-Boost Converter

A DROK DC-DC Buck-Boost Converter is used in this experiment. Since the maximum output voltage of the power supply is 24V and the power system will operate in excess of 30V, a boost converter is required. Also, multiple operating voltages will be used during the experiment to more fully characterize the system behavior. As such, the ability to control the output voltage of the slack bus is also required.

The specifications of the buck-boost converter used in this system are given in Table C.7.

DROK DC-DC Buck-Boost Controller			
Parameter	Description	Value	Units
P_{max}	Max. Output Power	900	W
V_{in}	Input Voltage	0-60	VDC
V_{out}	Output Voltage Range	0-60	VDC
I_{out}	Max. Output Current (software)	15	A
I_{in}	Max. Output Current (fused)	20	A
V_{out} or I_{out}	Control Signal (actively controlled)	User Input	VDC or A
—	Cooling	Case Fans	—

Table C.7: DROK DC-DC Buck-Boost Controller

C.4 Data Acquisition System

C.4.1 Architecture

The data logger developed for this experiment needed to be low cost and capable of logging both digital and analog data streams very rapidly. Again, the rapid serial data logging capability of the ATmega32u4 16MHz processor and the analog and digital I/O capability of the Arduino ProMicro microcontroller board is used. This system is capable of accurately logging data to the SD card in excess of 400Hz. This is sufficient for this application as the servos controlling the load variation and the throttle position are updated at 50Hz. This system is required to store the following analog data streams.

V_{gen} Analog Input - The generator output voltage measured between the DC terminals of the rectifier

V_{load} Analog Input - The system voltage at the input terminals of the PWM load controller

I_{load} Analog Input - The voltage output from the hall-effect DC current sensor located at the input to the restive load.

I_{slk} Analog Input - The voltage output from the hall-effect current sensor located at the output from the slack bus boost controller.

The architecture of this system is shown in Fig. C.16.

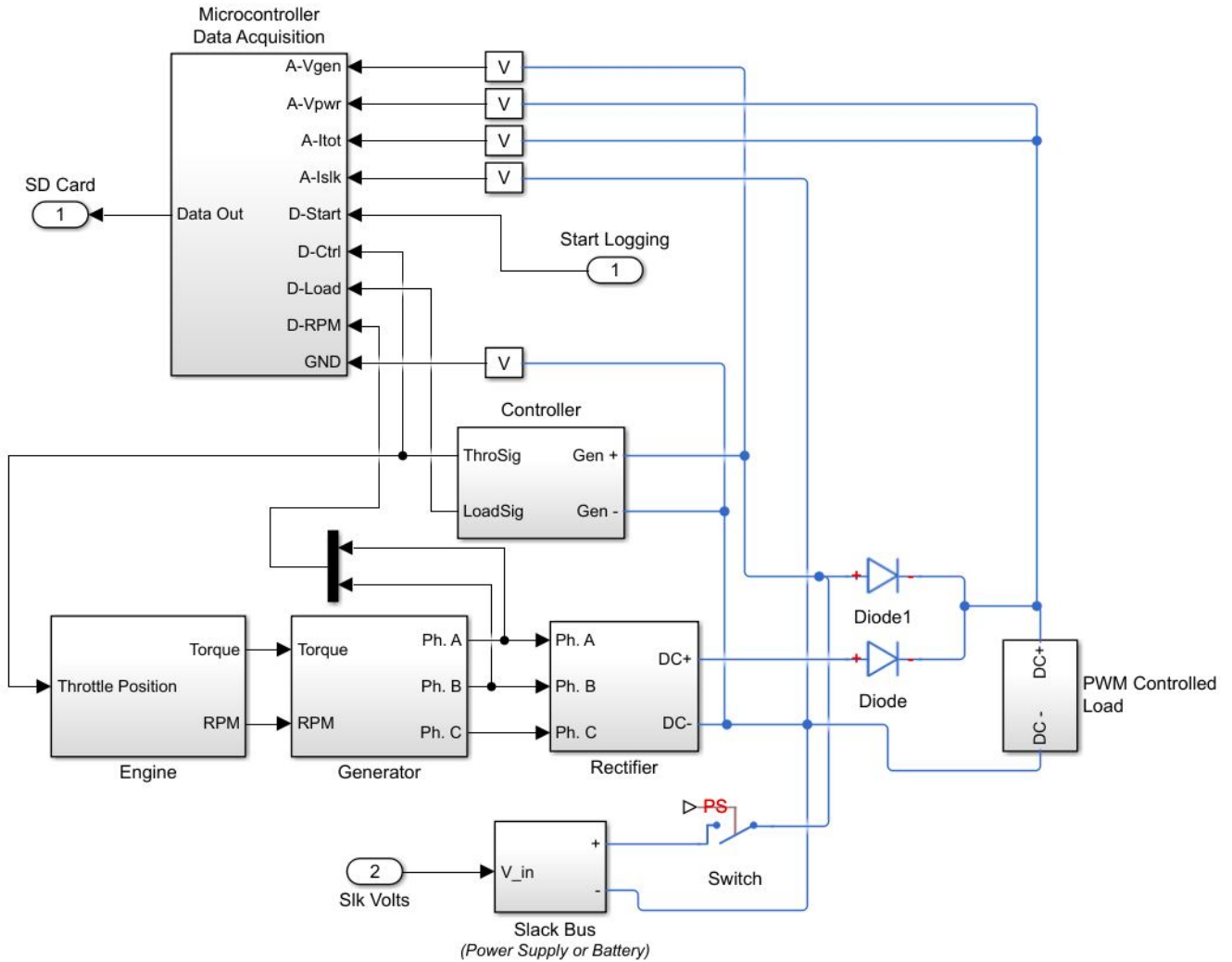


Figure C.16: The data acquisition system developed for this experiment is based on the same microcontroller and SD card data logging as the wind tunnel data acquisition system.

Additionally, the system is also requires to store the following digital data streams.

Cmd_{thr} Digital Signal - The PWM control signal sent to the throttle control servo, computed by a parallel microprocessor running the control algorithms. This PWM signal varies

in pulse-width from $800\mu s$ to $2200\mu s$, and are measured by marking the time between input pin state changes on the data logging processor.

Cmd_{load} Digital Signal - PWM control signal sent to the load control servo according to the load profile for a certain test. Again this signal varies from $800\mu s$ to $2200\mu s$ and are measured in the same way as *Cmd_{thr}*.

RPM Digital signal, The signal generated by passing the potential between generator phase A and phase B through a digital filter circuit. The rotational speed of the generator is a multiple of the time measured between these pulses.

Also, given the rapid data logging rate, in order to reduce the file size and clearly delineate between separate tests, a start/stop command is also monitored using a digital pin state on the micro-processor. When given the command, the data logger begins recording data while the control processor executes the specified test protocol in parallel.

C.4.2 Uncertainty Analysis

Due to the Datalogger ADC

As discussed in a previous chapter, the ATmega32u4 processor uses a 10-bit, 0-5V unipolar analog to digital converter. The resolution of the measurement is the least significant bit (LSB). With a 5V analog reference voltage, e.g. $V_{AREF} = 5V$ and a ground reference voltage $V_{SSA} = 0V$, the resolution of the voltage measurement is

$$1LSB = \frac{V_{AREF} - V_{SSA}}{2^n - 1} = \frac{5}{1023} = 4.89mV \cong 0.1\% \text{ of full range} \quad (C.6)$$

The $\sigma = 1$ boundary for this resolution is

$$u_{ACD:\sigma=1} = \frac{4.89mV}{2\sqrt{3}} = \pm 1.41mV \quad (C.7)$$

Here, we will use the $\sigma = 2$ boundary which represents a confidence interval of $\sim 95\%$.

$$u_{ADC:\sigma=2} = \pm 2.82mV = 0.0577\% \text{ of the full } 0\text{-}5V \text{ range} \quad (C.8)$$

The high voltage generated by the experiment must be reduced to a 0-5V analog logic signal in order to be read by the ADC. This is accomplished using the simple voltage divider circuit shown in Fig. C.16. Although the resistors used in this circuit have resistance uncertainties of $\pm 5\%$, the circuit was calibrated using a TekPower 3005T DC power supply. This power supply has a combined voltage output and read-back uncertainty of

$$u_{VD} = u_{PS} \cong \pm 0.1\% \quad (C.9)$$

This calibration uncertainty will be used for the uncertainty of the voltage divider output, since the resistance of this circuit remains constant throughout the experiment. These uncertainties apply to the voltages measured by microcontroller at both the rectifier DC output as well as the total system output to the PWM load controller.

Due to the Current Sensor

Unlike in the wind tunnel portion of this thesis, the hybrid output current was measured using the Bayite $\pm 100A$ Digital Current Ammeter, as shown in Fig. C.17.



Figure C.17: This current sensor is designed to measure AC, DC and Pulsed current. The digital display provides a convenient means of visual feedback during testing.

This device uses a Hall Effect Transformer to measure the DC current output from the boost converter as well as the pulsed DC current output from the PMW load controller. The manufacturer estimates the accuracy of this sensor to be

$$u_{HS} = \pm 1\% \text{ of full range} \approx \pm 1 \text{ Amp} \quad (\text{C.10})$$

The full range analog voltage output from this sensor is $\pm 1.25V$ and is read by the microcontroller ADC. Therefore the uncertainty of the current measurement is

$$u_{HS} = \pm 1\% \rightarrow u_{HSV} = \pm 0.0125V$$

$$u_{ADC:\sigma=2} = \pm 0.00282V$$

$$u_I = \sqrt{u_{HS}^2 + u_{ADC}^2} = \pm 0.0128V = \pm 1.03A \quad (\text{C.11})$$

This uncertainty is quite large when compared to the values of currents measured in this experiment, particularly from the slack bus. Therefore, the conductors are looped twice through the sensor, doubling the signal measurement and reducing the measurement

uncertainty to

$$u_I \approx \pm 0.51A. \quad (\text{C.12})$$

The characteristic response time of this type of sensor is approximately $3 - 16\mu s$ or $\geq 62.5kHz$, given that the maximum logging frequency of the data acquisition system is $\sim 400Hz$, no additional considerations need to be made for the dynamics of this sensor.

C.5 Control System

C.5.1 Architecture

This experiment uses two microcontrollers each running dedicated control or datalogging software in parallel. This maximizes the performance of both the control system and the data logging system.

The dedicated control microprocessor is responsible for managing each consecutive experiment, as well as for controlling the engine and generator throttle during the experiment, as shown in Fig. C.18. Both controllers receive the same input start command such that the test profile and data recording software begin simultaneously. For a given battery of test, each concurrent run is assigned a unique integer identifier in the logfile for each test comparison and data reduction. Automating the test protocols in this manner enables each test to be repeated precisely, thus providing clean repeatable data.

For each test, the experiment controller has a pre-programmed load profile that it executes in time, by changing the PWM duty cycle of the load controller. There are two load profile types applied to the system.

- **Step Response** The controller will proceed from zero power to full power in a series of discrete step-changes in load. The change in load controller duty cycle is the same for each step. Once full power is reached, the load will be reduced to zero-power in a series of discrete steps.
- **Ramp Response** The controller will ramp from zero power to full power at a prescribed rate, hold for a certain duration, then ramp back to zero power.

These profiles will be discussed in detail in the next Chapter.

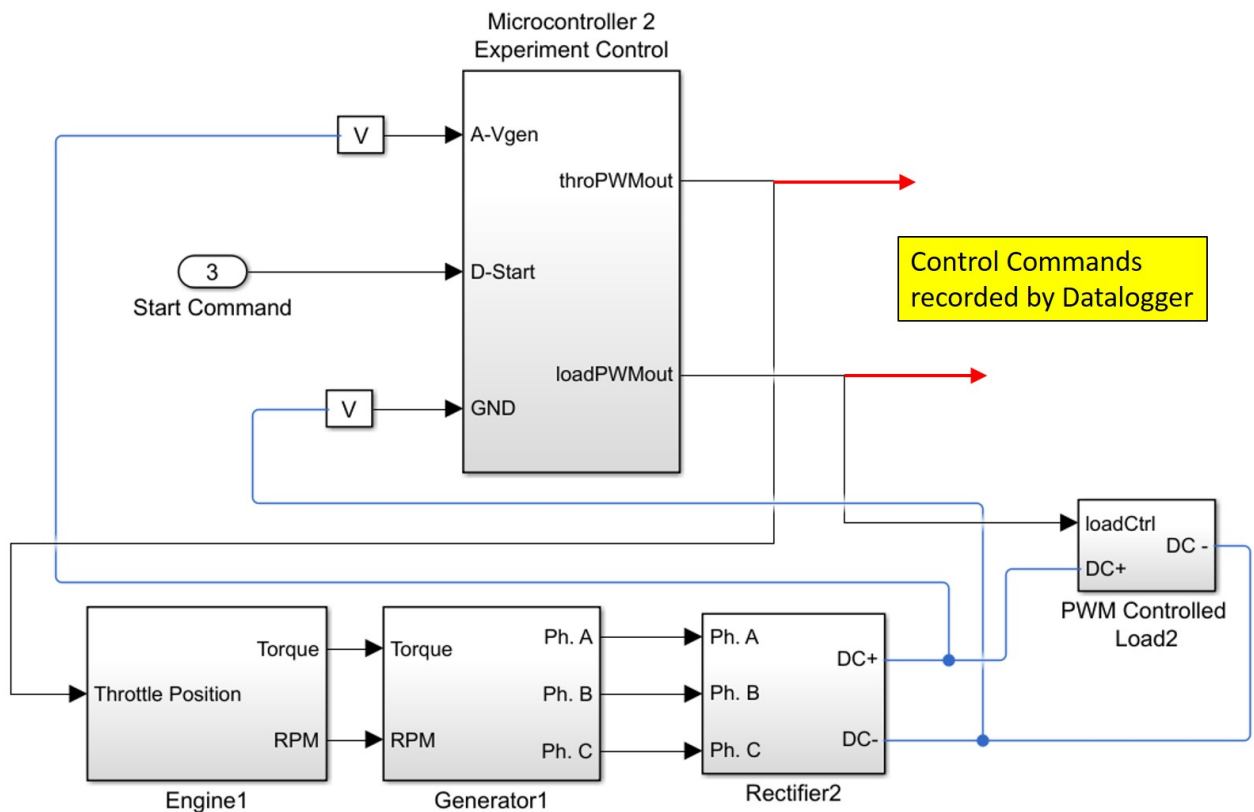


Figure C.18: The experiment control software runs on a dedicated microcontroller, in parallel with the data logging microcontroller. Shown here is the architecture of the system as it pertains to the experiment controller only.

C.5.2 Preliminary Linear Controls and Implementation

Since the primary objective of this experiment is to provide a reference data set for the development of a detailed dynamical model, the controller applied to the experiment must be mathematically simple and easily replicated in the simulation software, and robust enough to control the experiment during testing. For this experiment, a proportional, integral, and derivative (PID) controller was designed for the experiment. The basic formulation for this controller is

$$u(y) = k_p e(t) + k_i \int_0^t e(t) dt + k_d \frac{de(t)}{dt} \quad (\text{C.13})$$

where u is the controller output, e is the measured signal error from the controller set point,

$$e = \text{Setpoint} - \text{Input} \quad (\text{C.14})$$

and k_p , k_i , and k_d are the proportional, integral, and derivative gains respectively.

This controller is implemented in the experiment using the `PID_v1.h` header and associated libraries licensed for Arduino devices by MIT [12]. This C++ implementation is

```
/*working variables*/  
  
unsigned long lastTime;  
  
double Input, Output, Setpoint;  
  
double errSum, lastErr;  
  
double kp, ki, kd;  
  
void Compute()  
  
{
```



```

/*How long since we last calculated*/

unsigned long now = millis();

double timeChange = (double)(now - lastTime);

/*Compute all the working error variables*/

double error = Setpoint - Input;

errSum += (error * timeChange);

double dErr = (error - lastErr) / timeChange;

/*Compute PID Output*/

Output = kp * error + ki * errSum + kd * dErr;

/*Remember some variables for next time*/

lastErr = error;

lastTime = now;
}

void SetTunings(double Kp, double Ki, double Kd)
{
    kp = Kp;

    ki = Ki;

    kd = Kd;
}

```

As can be seen from the implementation example, the PID formulation used here is

$$u_k = k_p e + k_i * \sum_{k=0}^k e \Delta t + \frac{e_k - e_{k-1}}{\Delta t} \quad (\text{C.15})$$

where k is the current sample.

The implementation of PID control in MATLAB Simulink is straightforward and will be discussed in detail in a later chapter.

C.6 Conclusions

The hybrid power system and associated control and data acquisition systems presented in this chapter are capable of safe, automated test operation in a laboratory setting. The thermal and exhaust hazards are mitigated by the use of water cooling as well as installation in a fume ventilation hood.

The data acquisition system is capable of resolving the long time-scale dynamics of the mechanical and electrical systems in the experiment, while the high frequencies, $\geq 15kHz$, associated with the operation of the PWM load controller as well as the dynamics of the current sensors, may appear as a noise source in the data. These can be removed during post-processing through the use of a low-pass filter.

The uncertainties associated with the microcontroller ADC are negligible, though the uncertainties associated with current measurement must be carefully considered and mitigated. The current measurement uncertainty $u_I \approx \pm 0.51A$. is deemed acceptable in this

case given the large load currents expected, $\geq 30A$, and the system reliability gained by eliminating terminal connections to a series-connected current sensor.

Bibliography

- [1] I.H. Abbot. *Theory of Wing Sections, Including a Summary of Airfoil Data*. Dover Publications, 1959.
- [2] Airbus. *e-Thrust Project Page*. accessed April 25, 2017. URL: <http://www.airbusgroup.com/int/en/corporate-social-responsibility/airbus-e-fan-the-future-of-electric-aircraft/technology-tutorial/E-Thrust.html>.
- [3] vans aircraft. *Vans RV-10*. 2018. URL: <https://www.vansaircraft.com/public/rv10.htm>.
- [4] Airliners.net. *v22*. accessed Aug. 2018. URL: <http://imgproc.airliners.net/photos/airliners/8/7/4/2323478.jpg?v=v40>.
- [5] Inc. Allegro MicroSystems. *Current Sensor Specifications*. 2018.
- [6] John D. Anderson. *Fundamentals of Aerodynamics, 5th Ed*. McGraw Hill Companies, Inc., 2007.
- [7] John D. Anderson. *Introduction to Flight, 5th Ed*. McGraw Hill, 2005.

- [8] M.J. Armstrong, M. Blackwelder, and et. al. “Architecture Voltage and Components for a Turboelectric Distributed Propulsion Electric Grid”. In: *NASA Self Published* (2015).
- [9] J. B. Barlow, W. H. Rae, and Alan Pope. *Low Speed Wind Tunnel Testing*. John Wiley and Sons, Inc., 1999.
- [10] E.A. Basso and et. al. “IEEE 1547 Standards for Advancing Grid Modernization”. In: *IEEE Standard* (2015).
- [11] B.M. Baumann et al. “Mechatronic Design and Control of Hybrid Electric Vehicles.” In: *IEEE/ASME Transactions on Mechatronics* 5.1 (2000), pp. 53–72.
- [12] Brett Beaugard. *PID Library*. URL: <http://playground.arduino.cc/Code/PIDLibrary>.
- [13] Bombardier. *Rotax 582 Performance Data*. accessed April 24, 2017. URL: <http://www.flyrotax.com>.
- [14] A.R.S Bramwell, David Balmford, and George Done. *Helicopter Dynamics, Second Ed.* Elsevier, 2001.
- [15] T. Bujanovic. *Power System: State of Technology and Future Research Directions[Lecture]*. 2017.
- [16] Universita’ Degli Studi di Cagliari. “A quick introduction to sliding mode control and its applications.” In: *Self Published; Universita’ Degli Studi di Cagliari, Cagliari, Italy* (accessed 2018).

- [17] A. Damiano et al. “Sliding Model Control Design Principles and Applications to Electric Drives”. In: *IEEE Transactions on Industrial Electronics* 51.2 (2004), pp. 364–373.
- [18] John Dannenhoffer. *LiftingLine.m*. accessed 2018. URL: <http://www.ecs.syr.edu/Faculty/dannenhoffer/AEE342/LiftingLine.m>.
- [19] J.H Diekmann and K.-U Hahn. “Effect of an Active High-Lift System Failure During Landing.” In: *CEAS Aeronautic Journal* 6 (2015), pp. 181–196.
- [20] DYS. *drone*. accessed Aug. 2018. URL: https://cdn8.bigcommerce.com/s-xkoep7/images/stencil/1280x1280/products/883/4050/D400_X4_1__44137.1448912930.jpg?c=2&imbyypass=on.
- [21] FAA. *CFR Title 14 Part 23 - Airworthiness Standards for Normal Category Aircraft*. 2017. URL: ecfr.gov.
- [22] FAA. *CFR Title 14 Part 25 - Airworthiness Standards for Transport Category Aircraft*. 2017. URL: ecfr.gov.
- [23] FAA. *CFR Title 14 Part 27 - Airworthiness Standards for Normal Category Rotorcraft*. 2017. URL: ecfr.gov.
- [24] FAA. *CFR Title 14 Part 29 - Airworthiness Standards for Transport Category Rotorcraft*. 2017. URL: ecfr.gov.
- [25] Robert W. Fox, Alan T. McDonald, and Philip J. Pritchard. *Introduction to Fluid Mechanics*. John Wiley Sons, Inc, 2006.

- [26] W. Fredricks, M. Moore, and R. Busan. “Benefits of Hybrid Electric Propulsion to Achieve 4x Increase in Cruise Efficiency for a VTOL Aircraft”. In: *NASA Langley Research Center, Self published* (2014, accessed 2016).
- [27] C. Friedrich and R. Robertson. “Hybrid-Electric Propulsion for Aircraft.” In: *Journal of Aircraft* 52.1 (2015), pp. 176–189.
- [28] A.S Gohardani, G. Doulgeris, and R. Singh. “Challenges of Future Aircraft Propulsion: a review of distributed propulsion technology and its potential application for the all electric commercial aircraft”. In: *Progress in Aerospace Sciences* (2010).
- [29] robinson helicopters. *Robinson R22*. 2018. URL: www.robinsonheli.com.
- [30] H.G. Hill and C.R. Peterson. *Mechanics and Thermodynamics of Propulsion, 2nd ed.* Addison-Wesley Publishing Company, 1992.
- [31] J.G. E.A. Kassakian. “The future of the electric grid: an interdisciplinary MIT study”. In: *Massachusetts Institute of Technology, self published* (retrieved February 8, 2017).
- [32] Ali Keyhani, Mohammad N Marwali, and Min Dai. *Integration of Green and Renewable Energy in Electric Power Systems*. John Wiley and Sons, 2010.
- [33] Kittyhawk. *Kittyhawk, Cora*. accessed Aug. 2018. URL: https://kittyhawk.aero/wp-content/uploads/2018/03/core_tile_KH-630x374.jpg.
- [34] J.P. Kleijnen. “Kriging Metamodeling in Simulation: A Review.” In: *European Journal of Operational Research* 192 (2009), pp. 707–716.
- [35] T. Kummer J. Dang. “High-lift Propulsive Airfoil with Integrated Cross-flow Fan”. In: *AIAA Journal of Aircraft* 43.4 (2015).

- [36] G. Lei, T. Wang, and Y. Guo. “System-Level Design Optimization Methods for Electric Drive Systems: Deterministic Approach”. In: *IEEE Transactions on Industrial Electronics* 61.12 (2014), pp. 6591–6602.
- [37] Lilium. *Lilium Jet*. accessed Mar. 2017. URL: www.lilium.com.
- [38] A.G. Loukianoc et al. “Discontinuous Controller for Power Systems: Sliding-Mode Block-Control Approach”. In: *IEEE Transactions on Industrial Electronics* 51.2 (2004), pp. 340–352.
- [39] MIT. “MIT Lecture Notes of Vorticity”. In: *MIT Open Courseware* (accessed 2018).
- [40] Ned Mohan. *Electric machines and drives: a first course*. Wiley, 2012.
- [41] Daniel Mueller. *Battery Comparisons*. accessed Aug. 2018. URL: https://www.researchgate.net/profile/Daniel_Mueller11/publication/257984459/figure/fig1/AS:297680254324736@1447983911716/Specific-power-and-specific-energy-of-different-battery-types-3.png.
- [42] D. Nalianda and R. Singh. “Turbo-Electric Distributed Propulsion-.” In: *Aircraft Engineering and Aerospace Technology: An International Journal* 86.6 (2014), pp. 543–549.
- [43] Norman S. Nise. *Control systems engineering*. Wiley, 2008.
- [44] S. Orr. “Integrated Aerodynamic and Dynamic Optimization of.” In: *Rensselaer Polytechnic Institute, Troy, NY* (2004).

- [45] R. Patil, Z. Filipi, and H. Fathy. “Computationally Efficient Combined Plant Design and Controller Optimization Using a Coupling Measure.” In: *Journal of Mechanical Design* 134 (2012), 071008-1 through -8.
- [46] Nhan Huu Phan. “Leading Edge Embedded Fan Airfoil Concept - A New Powered Lift Technology”. In: *Syracuse University, PhD Thesis* (2015).
- [47] Sho Sato. “The Power Balance Method for Aerodynamic Performance Assessment”. In: *Massachusetts Institute of Technology, PhD Thesis* (2012).
- [48] Aurora FLight Sciences. *Aurora FLight Sciences*. accessed Mar. 2017. URL: www.aurora.aero.
- [49] Professional Helicopter Services. *R22*. accessed Aug. 2018. URL: <https://www.phs.com.au/wp-content/uploads/2016/08/Robinson-R22.jpg>.
- [50] Y Shtessel and et. al. *Sliding Mode Control and Observation*. Springer Science+Business Media, 2013.
- [51] E. Silvas et al. “Review of Optimization Strategies for Systems Level Design in Hybrid Electric Vehicles.” In: *IEEE Transactions on Vehicular Technology* 66.1 (2017), pp. 57–70.
- [52] American Helicopter Society. *AHS VTOL Info*. accessed Aug. 2018. URL: www.vtol.org.
- [53] W. Soong. “Sizing of Electrical Machines.” In: *Power Engineering Briefing Note Series; University of Adelaide, Adelaide, Australia* (2008).

- [54] A.M. Stoll et al. “Drag Reduction Through Distributed Electric.” In: *Aviation Technology, Integration, and Operations Conference, Atlanta, GA* (2014).
- [55] COBB Tuning. *COBB Tuning Dynamometer Database*. accessed April 24, 2017. URL: <http://www.cobbtuning.com/dyno-database/>.
- [56] Vadim I. Utkin. “Sliding Model Control Design Principles and Applications to Electric Drives”. In: *IEEE Transactions on Industrial Electronics* 40.1 (1993), pp. 23–35.
- [57] T. Welles and J. Ahn. “Novel Piston Engine and Electrochemical Hybrid System for Unmanned Aerial Systems”. In: *forthcoming* (2018).
- [58] S.L. Yechout T.R. Morris, D.E. Bossert, and W.F. Hallgren. *Introduction to Aircraft Flight Mechanics: Performance, Static Stability, Dynamic Stability, and Classical Feedback Control*. AIAA, 2003.
- [59] S. Yoon, H.C. Lee, and T.H. Pulliam. “Computational Analysis of Multi-Rotor Flows.” In: *NASA Ames Research Center* (2015).
- [60] L. Young et al. “Insights into Airframe Aerodynamics and Rotor-on-Wing Interactions from a 0.25-.” In: *Army/NASA Rotorcraft Division* (2003).
- [61] B. Yuksek et al. “Transition Flight Modeling of a Fixed-Wing VTOLL UAV.” In: *Journal of Intelligent Robotic Systems* 84 (2016), pp. 83–105.
- [62] Z. Zhu and D. Howe. “Electrical Machines and Drives for Electric, Hybrid and Fuel Cell Vehicles.” In: *Proceedings of the IEEE* 95.4 (2007), pp. 746–765.

Andrew Voss Welles

Cell Phone: 607-425-7194

Personal Email: Andy.Welles@Gmail.com

Permanent Address: 18 High View Circle Horseheads, NY 14845

Education

- Syracuse University, Doctor of Philosophy in Mechanical and Aerospace Engineering**, Aug. 2018 GPA 3.89 of 4.0
- **Dissertation Topic** – Hybrid Electric Distributed Propulsion for Vertical Takeoff and Landing (VTOL) Aircraft: a computational and experimental investigation and feasibility study of the demands of VTOL flight on the dynamic stability of internal combustion-electric hybrid powertrains for VTOL flight applications
 - **Teaching Assistantship** – Applications of Computational Fluid Dynamics, Aircraft Performance and Dynamics, and Aerodynamics
 - **Qualifying Exam Topics** – Combustion, Fluid Mechanics, Mathematics
- Syracuse University, Master of Science in Mechanical and Aerospace Engineering**, May 2009 GPA 3.56 of 4.0
- Research Assistantship
- Syracuse University, Bachelor of Science in Aerospace Engineering**, May 2008 GPA 3.32 of 4.0
- Dean's Scholarship and Founder's Scholarship

Relevant Coursework

- Ph.D. – Courses in Turbulence, Fuel Cell Systems, Combustion, Electric Power Systems and Control, and Machine Learning
- B.S. and M.S. - Research and coursework focused on applying Computational Fluid Dynamics (CFD) to aerodynamic and thermodynamic design projects.

General Technical Skills

AutoCAD Catia V5 Maple MathCAD MATLAB and Simulink Microsoft Access Microsoft Office
Microsoft Project PI Pro-E/Creo Solidworks Linux and Embedded Linux NI Labview
Visual Studio Emacs Sublime Text Ladder Logic Arduino IDE

Analysis and Modeling Skills

ANSYS Fluent Star CCM+ Pointwise ICEM Gambit NASTRAN Abaqus Cantera NASA CEA

Statistics and Machine Learning

Minitab R Weka MATLAB

Computing Languages

C++ FORTRAN Java Script Python

Industry Experience

- Manager of Welles Group, LLC; Engineering and Product Development Consulting Services** Sept. 2017 – Present
- Provide CFD/FEA analysis for commercial clients across a broad range of industries including military aerospace, consumer products, and outdoor recreation industries
 - Develop numerical software tools for efficient product development
 - Create metrology and instrumentation systems based on machine vision and machine learning algorithms
 - Develop microcontroller-based embedded systems for experimental control and data acquisition
- Development Engineer: Corning Incorporated; Develop and Deploy New Glass Forming Technologies** Oct 2011 – Jan 2015
- Lead engineer for multiple business-critical technology development projects
 - Responsible for leading multiple cross-functional engineering teams through building fundamental understanding, concept design, production trials and initial manufacturing deployment for Corning's global LCD Substrate, High Performance Displays, and Gorilla® Glass Manufacturing Enterprises
 - Principle and contributing author of multiple patents, invention disclosures and internal publications
 - Led efforts to evaluate competitor process technology and improve commercial strategy
- Reliability Engineer: World Kitchen; Product and Process Reliability Management** Aug 2011 – Oct 2011
- Deployed CFD/FEA software for improving existing process equipment for new applications.
- Lead Systems Engineer: Sikorsky Aircraft; Aircraft Systems Performance Management** Aug. 2010 – Aug. 2011
- Responsible for managing engineering-specific contract deliverables
 - Ensure all key performance parameters for the aircraft are met and potential risks are mitigated
- Aero-Thermo Engineer/MCSA Lead Engineer: Sikorsky Aircraft; Aircraft Design and Analysis** May 2009 – Aug. 2011
- Managed the integration of CFD numerical simulation software into the engineering department
 - Utilized CFD/FEA analysis capability to guide design structural and aerodynamic design decisions
 - Presented design and analysis for military customers and the FAA
 - Led the design of an infrared signature suppressing exhaust system for a turboprop engine
 - Provided engineering support for the assembly of aircraft primary structure
- Graduate Research: Magna Powertrain, Syracuse University; Automotive Advanced Design** Jan. 2009 – May 2009
- Research collaborator in the development of an automotive waste heat recovery system
 - Designed high efficiency turbomachine components utilizing parametric CFD results
- Graduate Research: Welch Allyn, Syracuse University; Infrared Thermometry System Design** May 2008 – Dec. 2008
- Performed detailed parametric CFD heat flow analysis of a new infrared thermometer
 - Collaborated with the Welch Allyn IR Thermometry Team in product development and testing
- Aerospace Senior Design Team Captain: Syracuse University; Aircraft Design, Analysis, and Fabrication** Jan. 2008 – May 2008
- Designed an aircraft optimized for a specific mission
 - Designed, built, and tested the final aircraft, winning the competition and setting several new records
- Undergraduate/Graduate Research: Syracuse University; CFD Based Wind Turbine Design** Aug. 2007 – May 2009

- Collaborated with architecture faculty to integrate wind turbine into the urban environment
- Performed CFD analysis of new wind turbine concepts

Undergraduate Research: Syracuse University; HVAC System Design

May 2007 – Aug. 2007

- Developed new HVAC and Personal ventilation concepts
- Performed a detailed 3D CFD parametric study and designed an experiment to validate results

Engineering Internship: Allred and Associates Inc.; Composites Design and Manufacturing

June 2006 – Feb. 2007

- Designed, built, and tested composite parts and developed potential new products

Undergraduate Research: Syracuse University; Aircraft Integrated Propulsion System Design

Aug. 2004 – June 2006

- Designed, built, and tested three generations of Propulsive Wing prototype aircraft

Entrepreneurial Experience

Founder and CEO: Voss Aerospace, Inc.; Developing and Proliferating Advanced VTOL Technology

Mar 2015 – Dec. 2016

- Founded in conjunction with Ph.D. research to enable fund development and direct technology commercialization
- Led the invention and development of a safe and scalable vertical takeoff and landing (VTOL) integrated aircraft system
- Developed a small scale, high power density hybrid-electric powertrain for unmanned aircraft
- Provide strategic leadership during the formation of a new aerospace technology venture
- Secured seed funding to begin building a business around our core technologies

Additional Skills

Composite Design and Fabrication CNC Machining and Programming Carpentry MIG, TIG, Stick Welding
 Plumbing Machining and Metal Fabrication Electrical Masonry Sheet Metal Design and Fabrication

Activities

AIAA SAE SAE Mini Baja Design Build Fly Engineering Honors Society Skiing Rock Climbing